

Space Weather



RESEARCH ARTICLE

10.1029/2020SW002712

Key Points:

- Correction of meteorological effects on muon component of secondary cosmic rays significantly extends the usability of muon monitors
- A new method for modeling of meteorological effects utilizing multivariate analysis and machine learning techniques is presented
- Correction efficiency of the best performing algorithm is greater than for other commonly used methods

Correspondence to:


M. Savić,
msavic@ipb.ac.rs

Citation:

Savić, M., Maletić, D., Dragić, A., Veselinović, N., Joković, D., Banjanac, R., et al. (2021). Modeling meteorological effects on cosmic ray muons utilizing multivariate analysis. *Space Weather*, 19, e2020SW002712. <https://doi.org/10.1029/2020SW002712>

Received 30 DEC 2020
 Accepted 13 JUL 2021

Modeling Meteorological Effects on Cosmic Ray Muons Utilizing Multivariate Analysis

M. Savić¹ , D. Maletić¹, A. Dragić¹, N. Veselinović¹, D. Joković¹, R. Banjanac¹, V. Udovičić¹, and D. Knežević¹

¹Institute of Physics Belgrade, University of Belgrade, Belgrade, Serbia

Abstract Correction of meteorological effects on muon component of secondary cosmic rays significantly extends the usability of muon monitors. We propose a new data driven empirical method for correction of meteorological effects on muon component of secondary cosmic rays, based on multivariate analysis. Several multivariate algorithms implemented in Toolkit for Multivariate Data Analysis with ROOT framework are trained and then applied to correct muon count rate for barometric and temperature effects. The effect of corrections on periodic and aperiodic cosmic ray variations is analyzed and compared with integral correction method, as well as with neutron monitor data. The best results are achieved by the application of linear discriminant method, which increases sensitivity of our muon detector to cosmic ray variations beyond other commonly used methods.

Plain Language Summary Primary cosmic rays are energetic particles that arrive at Earth from space. On their journey toward Earth they are affected by the solar wind (a stream of charged particles emanating from the sun), which has information about various solar processes embedded in it. In top layers of the atmosphere primary cosmic rays interact with nuclei of air molecules and produce large number of secondary particles that propagate toward Earth's surface. These secondary particles preserve information about variations of primary cosmic rays, which allows for the study of solar processes using Earth based detectors. One type of secondary particles that can be detected on the ground are muons. However, muons are affected by the conditions in the atmosphere, which can disturb the information about variations of primary cosmic rays. That is why it is important to model these atmospheric effects on cosmic ray muons as well as possible so they can be corrected for. In this study, we present a new method for modeling and correction of atmospheric effects on cosmic ray muons, that is based on multivariate analysis utilizing machine learning algorithms. This method increases sensitivity of our muon detector to cosmic ray variations beyond other commonly used methods.

1. Introduction

Meteorological effects on muon component of secondary cosmic rays have been known and studied for almost a century. A number of meteorological parameters contribute to variation of muon flux in the atmosphere, but two are the most significant: atmospheric pressure and atmospheric temperature.

Aperiodic fluctuations of intensity, discovered in the very early cosmic ray measurements, were eventually attributed to the variation of atmospheric pressure by Myssowsky & Tuwim (1926) (associated effect dubbed *barometric*), while *temperature effect* has been discovered more than a decade later and has two components: *negative* (first quantitatively described by Blackett, 1938) and *positive* (suggested by Forró, 1947). Barometric effect represents variation of muon flux due to variation of the mass of the absorber (air column) above the detector. Negative temperature effect is a consequence of dependence of effective height of muon generation level on the atmospheric temperature, resulting in longer muon path and increased probability of decay with higher temperature. Positive temperature effect has to do with positive correlation between atmospheric temperature and air density, decreasing the probability of nuclear interactions and increasing the probability of decay of muon-generating pions with the increase of temperature.

In order to study variations of primary cosmic rays (CR) using Earth based muon detectors, it is of the utmost importance to describe these meteorological effects as precisely as possible so they can be corrected for. A precise correction for meteorological effects significantly increases sensitivity of muon detectors to CR variations, making them a more usable counterpart to neutron monitors (the other widely used type of

© 2021. The Authors.

This is an open access article under the terms of the [Creative Commons Attribution-NonCommercial-NoDerivs License](https://creativecommons.org/licenses/by-nc-nd/4.0/), which permits use and distribution in any medium, provided the original work is properly cited, the use is non-commercial and no modifications or adaptations are made.

ground based cosmic ray detectors), as muon detectors are normally responsive to higher energy primary cosmic rays. Additionally, muon monitors have a unique application in diagnostics of the atmosphere, allowing for prediction of atmospheric temperatures provided a good model of meteorological effects is available (Belov et al., 1987; Kohno et al., 1981).

Several empirical and theoretical models of meteorological effects have been proposed over the years, based on which corrections can be performed. Even though full set of meteorological effects is larger, in this analysis we will concentrate on the correction of temperature and barometric effect only, so results can be more easily compared to other methods.

Some of the most commonly used methods for temperature correction are: method of effective level of generation, introduced by Duperier (1949), integral method, developed by Feinberg (1946), Dorman (1954), and others (Maeda & Wada, 1954; Wada, 1962), method of mass-averaged temperature developed by Dvornikov et al. (1976), and method of effective temperature (mostly applicable to underground detectors) (Barrett et al., 1952).

Each of these methods have their own advantages, but in this study, we have decided to use the integral method as a reference against which to compare the results of our analysis. Main reason being is that it is derived from the theory of meteorological effects, which involves the most detailed analysis, as well as it being the least approximative. According to this approach, relative variation of muon count rate due to the temperature effect can be expressed as:

$$\left(\frac{\delta I}{I}\right)_{temp} = \int_0^{h_0} \alpha(h) \cdot \delta T(h) \cdot dh, \quad (1)$$

where α is temperature coefficient density function, δT is temperature variation and h_0 is atmospheric depth of the observation level expressed in g/cm^2 . Temperature coefficient density function is calculated theoretically, while temperature variation is calculated relative to some reference temperature for the period, usually mean temperature. In practical application, integration in Equation 1 is substituted with a sum, taking into account some finite number of isobaric levels.

Analysis of barometric effect is also included in the theory of meteorological effects, but barometric coefficient is rarely calculated theoretically. Most commonly it is determined using linear regression, assuming linear dependence between atmospheric pressure and muon flux:

$$\left(\frac{\delta I}{I}\right)_{pres} = \beta \cdot \delta P, \quad (2)$$

where β is barometric coefficient, and δP represents atmospheric pressure variation.

Each of the mentioned methods is at least in some part approximative, so the idea behind this work is to introduce a new empirical method for correction of meteorological effects that would be data driven, assuming as little as possible upfront. Other advantages of such approach are that it does not depend on the design of the detector, location of the site or topology of the surrounding terrain (as these would ideally be factored in by the model), and that it can be applied in near-real time. Additionally, proposed method can be used in the analysis and potential correction of temperature effect of neutron component of cosmic rays, as part of detected neutrons can originate from cosmic ray muons captured in the nuclei of the shielding of a neutron monitor detector (Dorman, 2004). Finally, in principle it can easily be generalized to take wider set of meteorological parameters into account.

As the presented problem is multidimensional, involving a relatively large number of correlated variables, we have decided to employ multivariate analysis, relying on machine learning techniques. In some recent work (Morozova et al., 2017; Savic et al., 2019) decorrelation of atmospheric variables and numerical modeling has been successfully applied to the study of interaction of cosmic rays with Earth's atmosphere, so utilizing adaptive and flexible machine learning methods could possibly yield further improvement, potentially revealing additional dependencies and taking higher order effects into account. This approach involves application of a number of multivariate algorithms, more or less rooted in statistical machine learning, to our problem and comparing their consistency and effectiveness with selected reference results.

Large part of variations observed in continuous cosmic ray measurements can be attributed to different space weather phenomena, due to modulation of primary cosmic rays in the heliosphere. In terms of temporal properties, they can be classified as periodic or aperiodic. We will test how newly introduced methods for correction of meteorological effects affect the sensitivity for detection of both periodic as well as aperiodic variations of muon flux of nonterrestrial origin, and how it ultimately compares to the sensitivity of neutron monitors.

2. Data

For the analysis of meteorological effects both muon flux and meteorological data are needed. Muon flux was measured experimentally in the Low Background Laboratory at the Institute of Physics Belgrade, while meteorological data is a combination of modeled atmospheric temperature profiles, and atmospheric pressure and ground level temperature measured locally.

2.1. CR Muon Data

Low Background Laboratory (LBL) is located on the grounds of the Institute of Physics Belgrade. Geographical coordinates for the laboratory are $44^{\circ}51'N$ and $20^{\circ}23'E$, with elevation of 75 m and geomagnetic cutoff rigidity of 5.3 GV. Detector system is comprised of a $100 \times 100 \times 5$ cm plastic scintillator with accompanying read-out electronics. Median energy for the detector system is (59 ± 2) GeV (Veselinović et al., 2017), with muon flux of $(1.37 \pm 0.06) \times 10^{-2}$ per cm^2 s. Electron contamination determined for a previously used experimental setup was $\sim 24\%$ (Dragić et al., 2008), and is assumed to be comparable for the current one (Joković, 2011). More detailed description of the laboratory and the experimental setup can be found elsewhere (Dragić et al., 2011). Native muon count rate data has time resolution of 5 min, but hour sums are also frequently used in analysis.

Continuous cosmic ray muon flux measurements have been ongoing in LBL since 2002, current setup being utilized since 2009. Data are available to public via an online interface on the Belgrade Cosmic Ray Station internet site (Low Background Laboratory for Nuclear Physics, 2020).

As with any long-term measurement, some shorter interruptions and inconsistencies are unavoidable, hence when choosing the interval to be used for the analysis we decided to use a one-year period from June 1, 2010 to May 31, 2011, where measurements had the most continuity and consistency. Additionally, using a one-year period should remove any potential bias, primarily due to annual temperature variation.

2.2. Meteorological Data

Meteorological parameters needed for the analysis come from two sources: Atmospheric temperature profile data are produced by an atmospheric numerical model, while atmospheric pressure and ground temperature data come from local measurements.

Meteorological balloon soundings above Belgrade done by Republic Hydro-meteorological Service of Serbia (RHMZ, 2020) are not frequent enough for the purposes of this analysis, so modeled data for atmospheric temperature profile are used instead. Several numerical atmospheric models can provide such data. In this work, we have chosen Global Forecast System (GFS) produced by National Centers for Environmental Prediction (GFS, 2020), which has been found to be in best agreement with balloon soundings done above Belgrade. Comparison was done where soundings data were available, as described in our previous study (Savić et al., 2019). GFS provides a large number of modeled atmospheric parameters among which are atmospheric temperatures for different isobaric levels. Modeled data sets are being produced four times per day (at hours 00:00, 06:00, 12:00, and 18:00). In addition, analysis data are also available, reprocessed *post festum* and taking into account real data measured by world network of meteorological services. In this analysis, we have been using such reprocessed atmospheric temperatures for the following isobaric levels: 10, 20, 30, 50, 70, 100, 150, 200, 250, 300, 350, 400, 450, 500, 550, 600, 650, 700, 750, 800, 850, 900, 925, and 975 mb. Data are available with spatial resolution of 0.5° of geographical longitude/latitude, so coordinates closest to the laboratory coordinates were chosen. Data were then interpolated with cubic spline, similar as in Berkova et al. (2012), and sampled in finer time resolution needed for the analysis.

Atmospheric pressure and ground temperature data are compiled from different meteorological stations in and around Belgrade, and then interpolated as described in more detail elsewhere (Savic et al., 2016). Finally, unique time series of combined modeled and measured meteorological data, with finest time resolution of 5 min, is assembled to be used in the analysis.

3. Methodology

The use of machine learning has seen an unprecedented expansion in the last decade. The main strength of such approach being that it does not assume any a priori model, but is data driven and thus able to potentially discover hidden dependencies. This is especially true when applied to large data sets with many correlated variables. In this study, we want to establish whether such approach would yield any improvements when applied to the problem of meteorological effect on cosmic ray muons.

To test this, we have decided to use toolkit for multivariate analysis (TMVA) package which provides a ROOT-integrated environment for application of multivariate classification and regression techniques (Hoecker et al., 2007). The package has been developed for the use in high-energy physics and contains implementation of a number of supervised learning algorithms, which utilize training and testing procedures on a sample data set to determine the mapping function. Mapping function maps the input parameters to output target value, trying to model the actual functional dependence (“target” function) as accurately as possible. The structure of the mapping function is algorithm specific, and can be a single global function or a set of local models. Trained algorithm is then applied to the full data set and provides either a signal/background separation (in case of classification) or prediction of target value (in case of regression).

For us, the later application is especially interesting. The idea is to train the mapping function, using meteorological parameters as input variables, and muon count rate as the regression target, and use trained function to produce the predicted target output for a larger data set. In principle, implementation of this procedure is specific for different analysis frameworks. TMVA provides template code for the training and application of multivariate methods, where optimal parameters obtained in the training/testing phase are stored in “weight” files to be used in the application phase. Thusly predicted muon count rate would ideally contain only variations related to meteorological effects, while the residual difference between modeled and measured muon count rate would contain variations of non-meteorological origin. We would apply this procedure for a number of algorithms implemented in TMVA, compare their performance and efficiency based on several criteria, and finally suggest the methods best suited for the modeling, and ultimately the correction, of meteorological effects.

Corrected muon count rate would be calculated according to the following equation:

$$N_{\mu}^{(corr)} = \Delta N_{\mu} + \langle N_{\mu} \rangle, \quad (3)$$

where

$$\Delta N_{\mu} = N_{\mu}^{(mod)} - N_{\mu} \quad (4)$$

is the difference between the modeled and measured muon count rate.

Not all machine learning methods are equally suited for all types of problems and selection of the optimal method for a particular application is rarely straightforward. The efficiency of different algorithms depends on a number of factors: Whether they are used for classification or regression, is correlation between parameters linear or nonlinear, what is the general complexity of the problem and required level of optimization, and so on. One can only assume the efficiency of any given algorithm upfront but there is no clear general rule which one will perform best in a particular situation. Often, several algorithms with specific strengths and weaknesses can be applied to the same problem and only through analysis of the final result the optimal one can be determined. For this reason, in our analysis we have decided to indiscriminately include the largest number of algorithm classes available in TMVA, and only after extensive parallel testing narrow the selection down to the optimal one.

We will briefly describe different classes of multivariate methods available in TMVA, as well as list specific algorithms that were chosen as representative for each class. First class are methods based on probability

density estimation (PDE) techniques, where actual probability density function is estimated based on the available data. Here we have selected to test two specific multidimensional implementations, somewhat similar in nature: PDE range-search (PDE-RS) and k-nearest neighbor (KNN) algorithms. Examples of use of this approach for multivariate regression are scarce, but the success with which PDERS was applied in classification problems in high-energy physics (Carli & Koblitz, 2003) motivated its use here. Second class are methods based on function discriminant analysis. These methods are widely used for dimensionality reduction and classification. Here, we selected the linear discriminant (LD) algorithm which shares some similarities in the approach with principal component analysis (PCA), in that it maps a space of potentially correlated input variables onto a smaller space of uncorrelated variables, but in addition to PCA it also maximizes the separation between output classes, making it a natural choice for application to our problem. Algorithms that employ higher order functions were also tested, but as could be expected performed more poorly. Application of artificial neural networks (ANN) to multivariate regression problems has seen expansion in recent years, where ANN methods often perform better than more straightforward regression techniques, especially if some degree of nonlinearity is present. Even though the dependence of cosmic ray muon flux on atmospheric temperatures is linear, we felt it is certainly worth investigating how ANN methods would perform when applied to this problem, and if any additional hidden dependence would be revealed. We have chosen to apply the MLP, as it is the fastest and most flexible available ANN algorithm in TMVA. Finally, method of boosted regression trees (BDT) employs a larger number (*forest*) of binary decision trees, which split the phase space of input variables based on a yes/no decision to a series of sequential cuts applied, so to predict a specific value of the output variable. They have been very successfully applied to classification problems in high-energy physics (Lalchand, 2020), but can also be used for multivariate regression with the similar rationale as for the ANN. We have selected two representative algorithms for testing: boosted decision tree (BDT) and gradient boosted decision tree (BDTG).

In this analysis, the procedure is applied to correction of barometric and temperature effect but it is easy to see how it can be extended to include more atmospheric variables, especially as such data is readily available from atmospheric numerical models.

3.1. Training Procedure

For the training/testing data subset we have selected data for the 10 geomagnetically quietest days of each month (list provided by GFZ German Research Center for Geosciences, GFZ Potsdam, 2020), as we expect variations due to meteorological effects to be more pronounced here. This subset was then further split into training and testing data set, where 70% of randomly selected data was used for training while remaining 30% was used for testing. Data time resolution used was 5 min as it gave us a larger statistics for training.

There is a number of settings that can be manipulated for each of the multivariate algorithms used. They vary from some basic parameters, to selection of different subalgorithms or various options that can be turned on or off. For each algorithm, we have selected the optimal set of parameters. The criterium for optimal performance was minimizing the average quadratic deviation of the modeled output versus the target value. Also, where allowed by the algorithm, input variables were decorrelated prior to further processing.

Table 1 shows the values of average quadratic deviation for the modeled output (modeled muon count rate) versus the target value (measured muon count rate) for different algorithms. First two columns refer to the training data subset while second two columns refer to the testing data subset. First and third column represent average quadratic deviation defined as $(\sum(f_{MVA} - f_{target})^2)^{1/2}$ (where f_{MVA} and f_{target} represent modeled and measured count rates, respectively), while second and fourth columns represent truncated average quadratic deviation which takes into account 90% of data with least deviation. As previously mentioned, the criterium for selection of optimal parameters for every algorithm is the minimal value of average quadratic deviation for the test data subset.

3.2. Algorithm Performance Analysis

All presented multivariate algorithms have no built in knowledge about the studied effect, so in addition to quantitative test mentioned in the section above, we introduce some qualitative analysis designed to estimate the integrity of modeled data. Prime concern here would be to test whether the suggested procedure

Table 1
Average Quadratic Deviation for Selected Multivariate Methods

Method	Training		Testing	
	Average deviation (counts/5 min)	Truncated deviation (counts/5 min)	Average deviation (counts/5 min)	Truncated average (counts/5 min)
PDERS	234	185	258	201
KNN	224	177	233	185
LD	286	225	284	223
MLP	228	180	234	186
BDT	219	182	237	188
BDTG	223	174	236	187

Abbreviations: BDT, boosted decision tree; BDTG, gradient boosted decision tree; KNN, k-nearest neighbor; LD, linear discriminant.

for the correction of barometric and temperature effect (PT correction) removes these meteorological effects only, while leaving all other features nonperturbed. To this end, we will analyze several distributions of modeled data, compare them with raw and reference PT corrected data (obtained using the integral method) and look for possible anomalous features.

First, we will look into structure of distributions of difference between modeled and measured muon count rate as a function of measured count. We want to make comparison between these distributions in the training phase (for the test data subset) and after the trained algorithm was applied to the full data set. We would expect these distributions to be consistent, and appearance of some new structures or strong trends would point to some perturbation in the application phase. We have selected two examples to illustrate the difference in consistency of application of trained algorithms—BDTG and PDERS, their distributions shown in Figure 1.

We can see that distributions for BDTG algorithm for test data subset (Figure 1a) and full data set (Figure 1b) are fairly similar, and any structures and trends in the test distributions are mostly well replicated in the full data set distributions (different statistics taken into account). This is the case for most applied algorithms except for PDERS, where some dependence of the count rate, negligible for the test data distribution (Figure 1c), exists for the full data set distribution (Figure 1d).

Another, more important feature, is that for some algorithms distributions we analyzed in the previous paragraph are not smooth, but rather display some structures. To get further insight into these structures, for all featured methods we plotted distributions of modeled muon count rate along with the distribution of raw count rate on the same graph, as shown in Figure 2.

In order to better understand shapes of distributions and any structures observed in plots in Figure 2, it would be helpful to compare them to equivalent plots for muon count rates corrected for pressure and temperature effects using a well-established reference method. However, before we take a look at these distributions, we will first briefly describe procedures used to obtain reference PT correction.

Temperature and barometric effect are typically corrected for independently, where one of several methods mentioned in Section 1 is used for temperature correction, and barometric coefficient for pressure correction is determined empirically. Integral method for correction of temperature effect is widely accepted as the most accurate one. It is based on the theory of meteorological effects and takes complete atmospheric temperature profile and relevant processes into account. Most thorough description of the theory of meteorological effects is given by Dorman (2004), where temperature coefficient density function $\alpha(h)$ in Equation 1 is given in its integral form. In order to be applied, this function is then calculated through integration, substituting parameters specific to the location of the experiment. Temperature coefficient density functions for the location of Low Background Laboratory for Nuclear Physics were calculated using Monte Carlo integration technique. In order to determine barometric coefficient, temperature corrected muon data were plotted as a function of atmospheric pressure (using entries for 10 geomagnetically quietest days

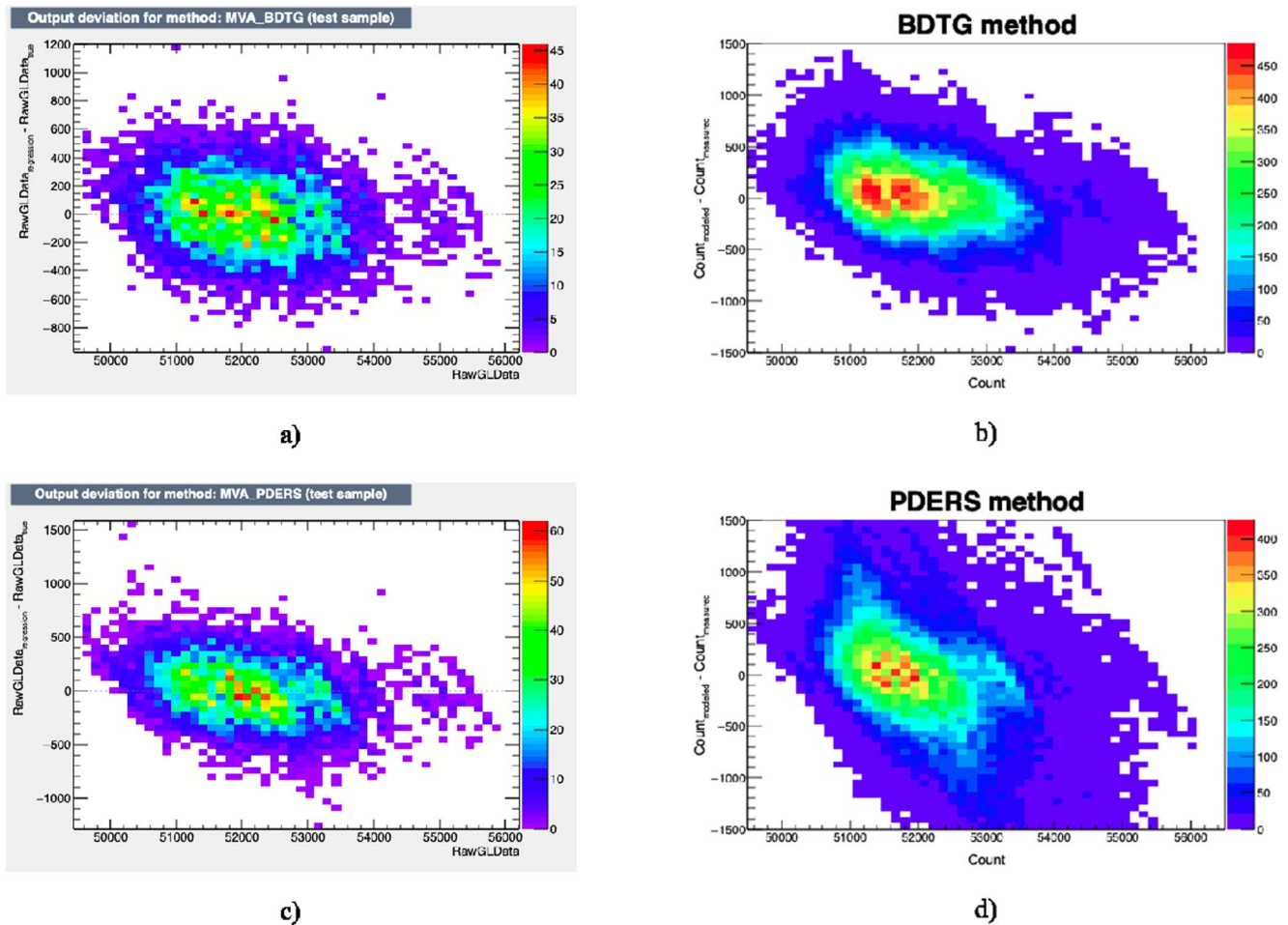


Figure 1. Distribution of difference between modeled (regression) and measured (true) muon count rate as a function of measured muon count rate for: (a) gradient Boosted decision tree (BDTG)—test data set, (b) BDTG—full data set, (c) PDERS—test data set, and (d) PDERS—full data set.

of each month only), coefficient determined via linear regression separately for each calendar year. Both procedures are presented in greater detail in our previous work (Savic et al., 2016).

Distributions equivalent to ones shown in Figures 1 and 2 were plotted for reference pressure and temperature corrected data, as shown in Figure 3. The analog for the modeled muon count rate is calculated from the variation due to pressure and temperature effects calculated based on the integral method. It is worth pointing out that distributions for reference PT corrected data are noticeably less smooth, which can be mostly attributed to lower statistics used as only hour summed data was available for this correction.

Based on these plots, we can conclude that we should not expect a significant deviation between raw and corrected data and that corresponding distributions should not have any characteristic structures. Most plots in Figure 2 are consistent with this expectation, however, some structures can be observed in KNN plots, and to a degree in BDT plots, while distribution plotted for PDERS algorithm does not have these structures but appears to somewhat deviate from raw data distribution.

Another insight into performance and consistency of different multivariate algorithms when applied to the modeling of meteorological parameters can be gathered by the way of spectral analysis of PT corrected data. Pressure and temperature corrected muon count rate was determined for all selected algorithms using modeled data, as described in Section 3. Since some gaps exist in our muon data, Lomb-Scargle algorithm was used to obtain the power spectra, as it is less sensitive to uneven data sampling (Press et al., 2007). Figure 4 shows power spectra for raw and muon count rates corrected for pressure and temperature effects using integral and two illustrative examples of multivariate methods. Full spectrum as well as selected interval

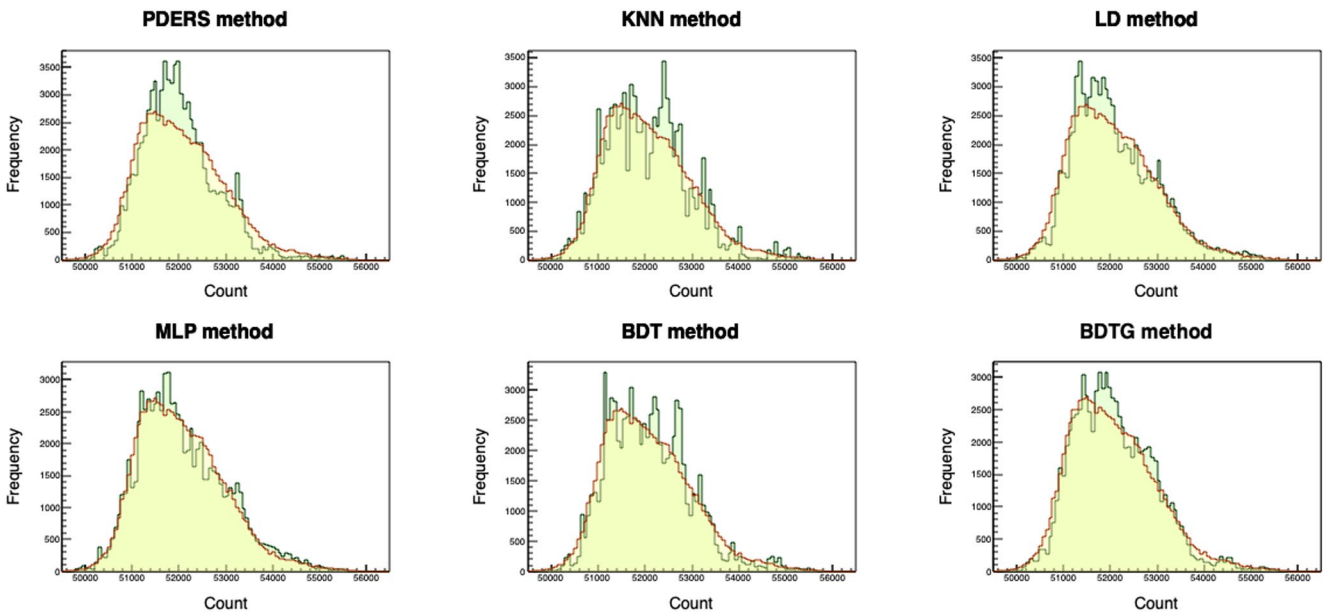


Figure 2. Comparison between distributions of raw (yellow) and muon count rate modeled by selected multivariate methods (green).

of frequencies around the periodicity of one day are shown, red dashed line indicating significance level of 0.01.

If integral method is again used as a reference, we can see that thus obtained PT correction does not remove daily variation, but rather makes it more pronounced. This should not come as a surprise, as only smaller part of the diurnal variation can be attributed to meteorological effects (Quenby & Thambyahpillai, 1960), while larger part is of nonmeteorological origin. Hence, removing variation due to atmospheric pressure would make daily variation more prominent. LD, and to a degree BDT/BDTG methods, have an effect on daily variation similar to the integral method, but for BDT method (bottom right in Figure 4) we observe emergence of some frequencies with significant power that cannot be associated with any known periodicity of cosmic rays, and probably have artificial origin. Such features are even more pronounced for the remaining multivariate algorithms, where in addition an over-reduction of power frequency corresponding to diurnal variation to can be observed. Over-reduction of daily variation coupled with introduction of artificial variations with significant powers points to possible inadequateness or overtraining of some of the multivariate methods.

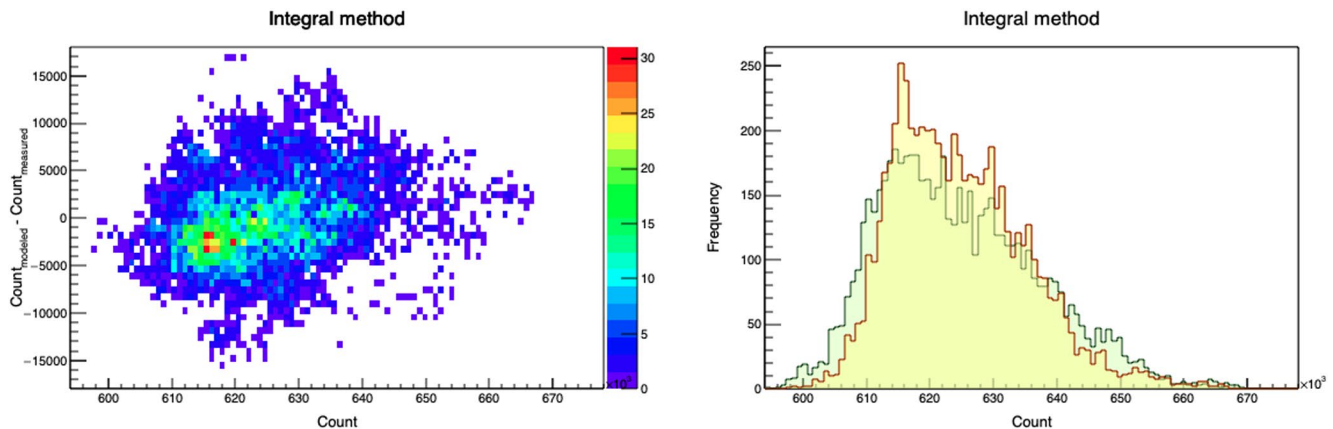


Figure 3. Distribution of difference between muon count rate calculated from the variation due to pressure and temperature effect using integral method and measured muon count rate as a function of measured muon count rate (left), and comparison between distributions of raw (yellow) and calculated muon count rate (green) shown on the right.

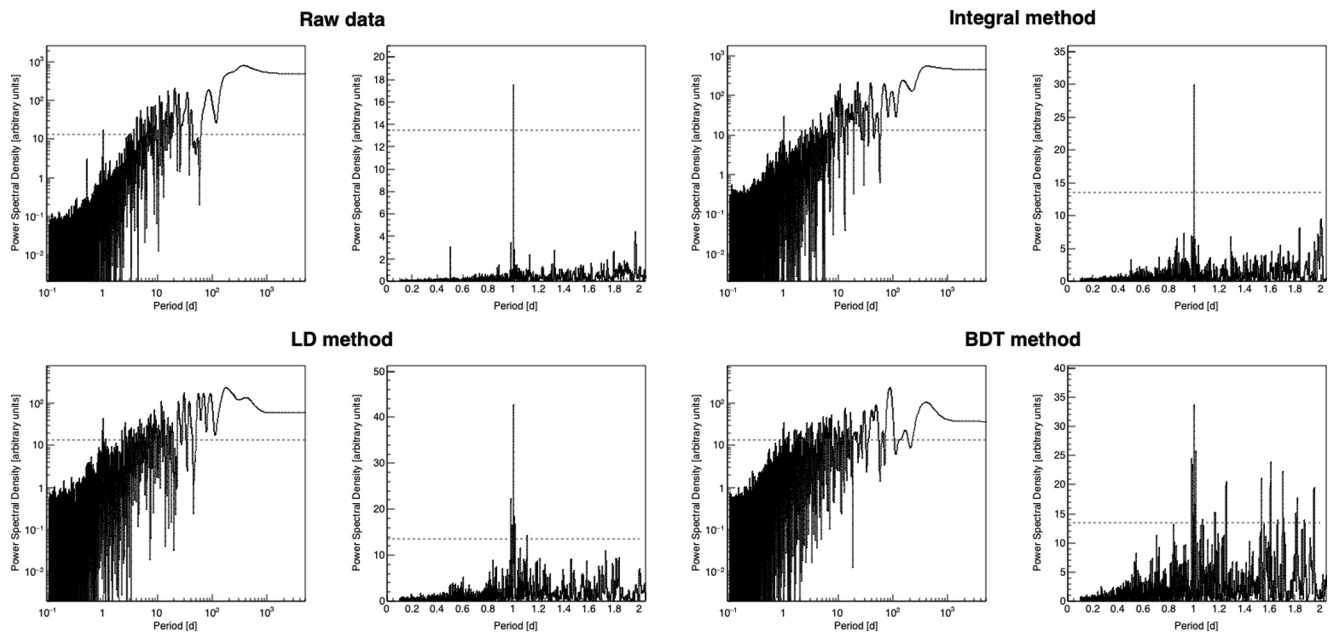


Figure 4. Power spectra for raw data (top left), PT corrected data using integral method (top right), and PT corrected data using selected multivariate methods (second row). For each method, both full spectrum and a range of frequencies around periodicity of one day are shown. Significance level of 0.01 is indicated by the red dashed line.

The effect on annual variation is difficult to determine based on the spectral analysis as period of only one year is analyzed, but we will introduce some quantitative tests in the next section that will help us with this estimate.

4. Results

We will use two criteria to estimate the efficiency of newly introduced methods for PT corrections. One will rely on the effectiveness with which the multivariate algorithms remove the annual variation and reduce variance, while the other will be based on the effect the correction has on detection sensitivity for aperiodic events, such as Forbush decreases (Forbush, 1937). In both cases, we will compare the results with the ones obtained by the integral method.

4.1. Effects of PT Correction on Periodic CR Variations

Significant part of the annual variation of cosmic ray muon flux can be attributed to the variation of atmospheric temperature (Hess, 1940). As mentioned before, the effectiveness with which this effect is corrected for will affect the detector sensitivity to variations of primary cosmic rays of non-atmospheric origin.

We will examine time series for pressure and temperature corrected data and compare them with raw and pressure corrected time series, especially taking note of how PT correction affects the annual variation. In order to estimate this effect, we fit the time series (except for raw data) with sine function with a period of one year. The amplitude of pressure corrected data determined from such fit will be used as an estimate of the annual muon flux variation, and serve as a reference against which to compare the effect of PT correction by different methods. In Figure 5 time series for raw, pressure corrected and pressure and temperature corrected data are shown. For the sake of simplicity, not all time series for data PT corrected using multivariate algorithms are shown, but rather only characteristic ones. Table 2 shows values for the annual variation amplitude for pressure and PT corrected time series, as well as possibly more informative reduction of annual variation calculated relative to the amplitude of the pressure corrected muon flux.

While, time series in Figure 5 for data PT corrected using integral, LD and BDTG methods do not seem to have some unexpected fluctuations, that is not the case for MLP method, where one can observe some

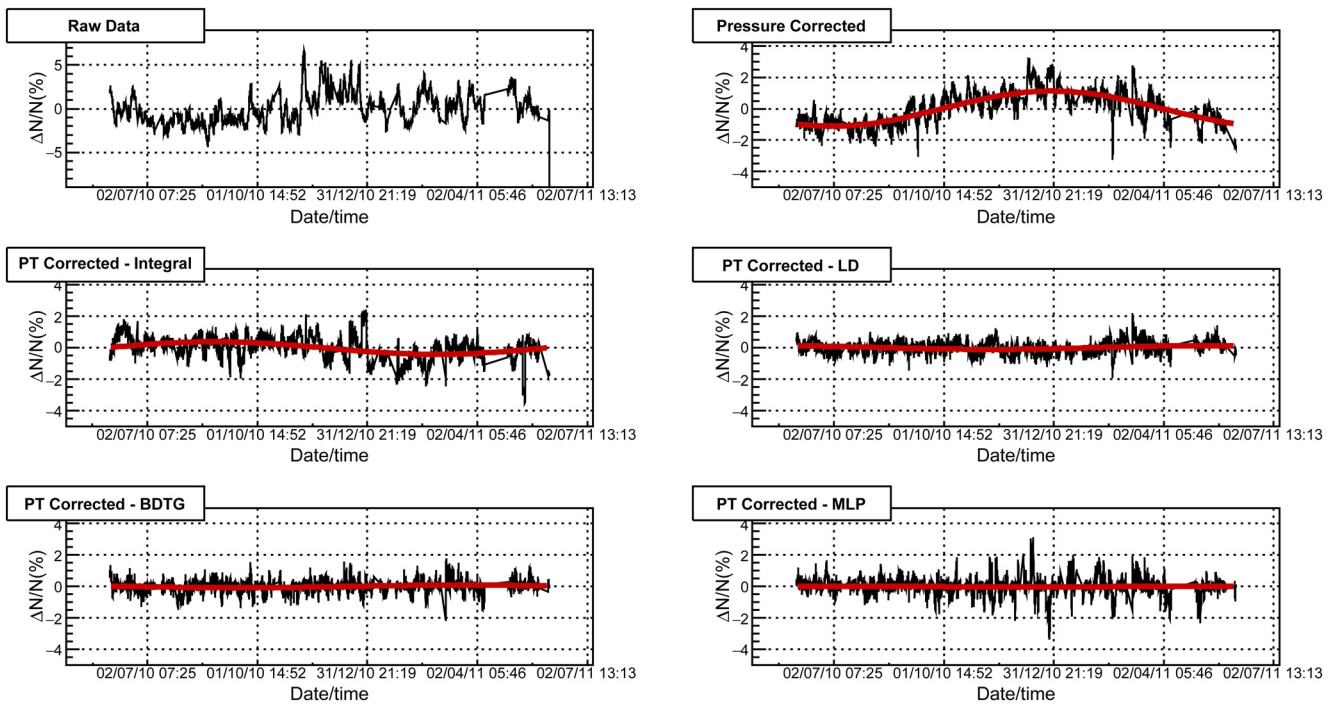


Figure 5. Muon count rate time series for the period from June 1, 2010 to May 31, 2011: raw data (top left), pressure corrected data (top right), PT corrected data using integral method (second row left) and data PT corrected using selected multivariate methods.

data that appears to deviate from the mean more significantly than what would be intuitively expected. For remaining multivariate algorithms this is even more the case. In order to try and quantify this visual comparison, we will analyze the effect corrections have on standard deviation of the data. If calculated relative to the mean muon flux for the whole period, standard deviation would be sensitive to the residual annual variation. To make standard deviation independent of the seasonal variation, we used a moving ten-day window to determine the mean value and then calculated the standard deviation relative to it.

Figure 6 shows distributions of relative variation of muon flux in respect to the moving window mean value for raw data and PT corrected data using integral, LD and MLP methods. It is based on these distributions that standard deviation was determined and results are presented in Table 3. Comparing standard deviations for PT corrected muon flux obtained by multivariate methods with the one obtained by the integral method, we can see that for LD, BDT, and BDTG algorithms they have comparable values. The difference is somewhat larger in the case of MLP, which is in accordance with features observed in Figure 6, while it is significantly larger for the remaining algorithms. This indicates that PT correction performed using KNN and PDERS (and possibly MLP) algorithms probably introduces some artificial features into PT corrected muon flux data.

One way to evaluate the effectiveness of different algorithms in reduction of the seasonal variation even better, would be to compare the PT corrected muon data to pressure corrected time series for selected neutron monitor detectors. The reasoning is based on a well-known fact that meteorological effects on the neutron component of secondary cosmic rays are dominated by the barometric effect. Temperature effect does exist for the secondary cosmic ray neutrons, but whether calculated theoretically (Dorman, 2004) or determined experimentally (Kaminer et al., 1965), it is still an order of magnitude smaller than for the muon component and typically not corrected for in neutron monitor data. Based on this, we

Table 2
Amplitude and Reduction of the Amplitude of Annual Variation Relative to Pressure Corrected Data (P Corrected) for PT Corrected Data (Using Integral and Selected Multivariate Methods)

Method	Amplitude (%)	Relative reduction (% of P corrected)
P corrected	1.11 ± 0.09	/
Integral	0.40 ± 0.03	64 ± 6
PDERS	0.09 ± 0.02	92 ± 3
KNN	0.24 ± 0.04	79 ± 5
LD	0.11 ± 0.03	90 ± 4
MLP	0.03 ± 0.01	98 ± 2
BDT	0.12 ± 0.03	89 ± 4
BDTG	0.086 ± 0.009	92 ± 2

Abbreviations: BDT, boosted decision tree; BDTG, gradient boosted decision tree; KNN, k-nearest neighbor; LD, linear discriminant.

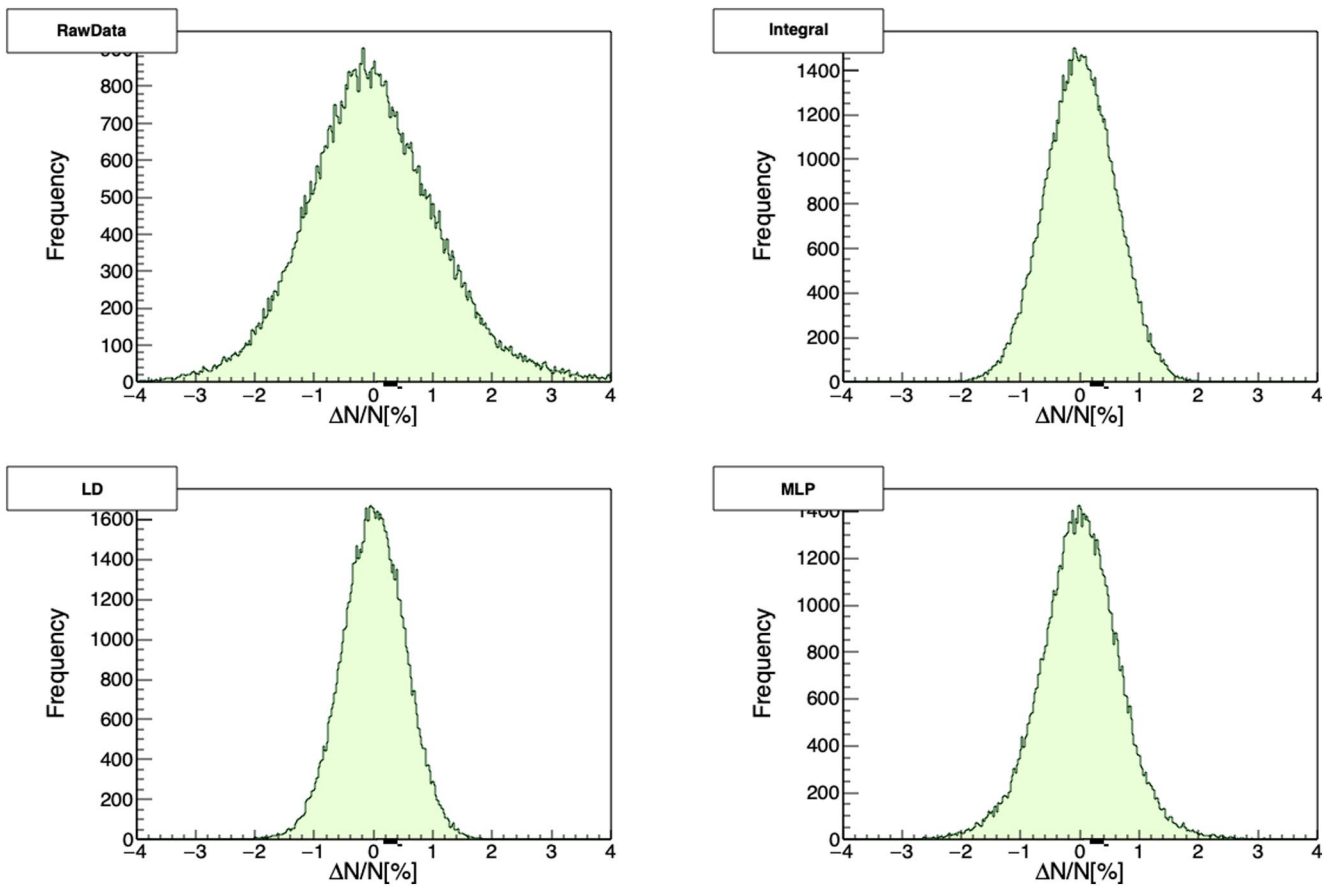


Figure 6. Relative variation of muon count rate calculated in respect to mean count in the ten-day moving window, for raw data (top left), PT corrected using integral method (top right), and data PT corrected using selected multivariate methods (second row).

believe pressure corrected neutron monitor data to be (in the first approximation) independent from meteorological effects, and hence a good reference for the evaluation of effectiveness of different methods for PT corrections of muon flux data.

For this comparison, we have chosen neutron monitors located in Athens and Rome, as they had the most consistent operation in the period we use for the analysis. Respective geomagnetic cutoff rigidities for these neutron monitors are 8.53 and 6.27 GV. Pressure and efficiency corrected relative neutron count rate was acquired via Neutron Monitor Database (NEST, 2020), presented for the said period in Figure 7. As for the muon flux data, relative neutron count rate time series were fitted with sinusoidal function, with a period of one year, to obtain the amplitude used as an estimate of the annual variation. Neutron monitors are more sensitive to lower energy secondaries than muon detectors so their time series can exhibit larger variations, which in turn can affect the fitting algorithm. However, in this case the fits seem to be dominantly affected by the relatively stable period between June and November 2010, hence we believe them to be a reliable estimate of the seasonal variation amplitude. Thus acquired annual variation amplitude for Rome neutron monitor is $(0.29 \pm 0.01)\%$, while for the Athens neutron monitor it is $(0.17 \pm 0.05)\%$.

Table 3
Standard Deviation of Relative Variation of Muon Count Rate for Raw and Data Corrected for Pressure and Temperature Effect (Using Integral and Selected Multivariate Methods)

Method	Raw	Integral	PDERS	KNN	LD	MLP	BDT	BDTG
Relative deviation (%)	1.117	0.592	0.990	0.785	0.533	0.687	0.607	0.551

Abbreviations: BDT, boosted decision tree; BDTG, gradient boosted decision tree; KNN, k-nearest neighbor; LD, linear discriminant.

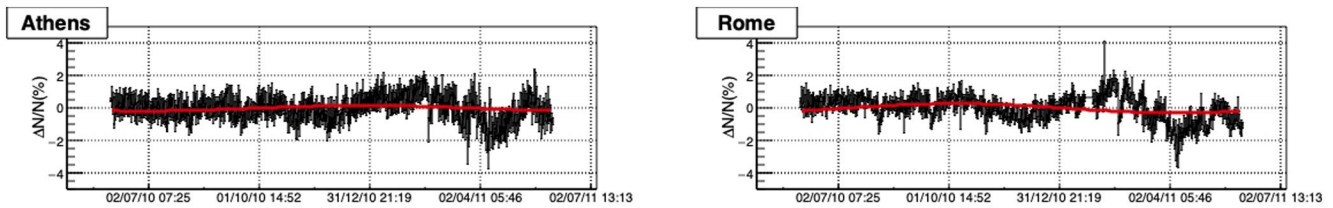


Figure 7. Relative neutron count rate time series for the period from June 1, 2010 to May 31, 2011 for Athens (left) and Rome (right) neutron monitors.

Comparing these values with the ones in Table 2, we see that methods KNN, LD, and BDT yield the most similar results. PDERS and MLP seem to underestimate the annual variation, while the integral method estimates a somewhat larger value.

Observed overall poor performance of KNN and PDERS algorithms could possibly be explained by the fact that these algorithms perform best when applied to problems involving strong nonlinear correlations, and are less efficient when dependencies between variables are dominantly linear (Hoecker et al., 2007). Additionally, these algorithms typically need a large training sample, so possibly statistics in our analysis was inadequate. However, artificial neural networks (such as MLP) should in principle be well suited for multivariate linear regression, and perform better than observed results suggest. Most likely, using minimization of the average quadratic deviation as a sole criterium for the selection of optimal parameters in the training phase may lead to overtraining (Montgomery et al., 2006), and additional qualitative criteria (i.e., ones introduced here) and more careful parameter control should also be used. BDT and BDTG algorithms performed reasonably well even though they are not optimized for treatment of linear multivariate problems, however, spectral analysis indicates a further improvement can be made. Additionally, all algorithms would probably benefit from a longer data interval of several years being used.

4.2. Effects of PT Correction on Aperiodic CR Variations

As mentioned before, apart from increasing sensitivity of muon detectors to periodic variations of primary cosmic rays, correcting raw muon flux data for meteorological parameters also affects detector sensitivity to aperiodic events which occur due to heliospheric modulation of primary cosmic rays. Here, we will analyze the effect PT correction, performed by application of different multivariate algorithms, has on detection of Forbush decrease events. We have chosen to concentrate on Forbush decreases as our muon detector is much less sensitive to other aperiodic events, such as ground level enhancements (GLE).

Forbush decrease (FD) events are typically characterized by their amplitude, so it could be a natural choice for a parameter to be used as a measure of detection sensitivity. However, another requirement for definition of sensitivity could be that detected signal significantly deviates from random fluctuations. That is, why we have decided to use the ratio of the amplitude to the standard deviation of muon flux, or relative amplitude, as an estimate of sensitivity to aperiodic events, rather than the actual amplitude. As we primarily focus on the magnitude of Forbush decreases, when we mention an FD event in the following text it mainly refers to the decrease phase and not the recovery phase.

To determine the amplitude, we have used a method proposed by Barbashina et al. (2009). The idea is to make the result independent from different trends leading up to, and following the actual FD. To do this, two intervals are defined: one i days before the onset of the FD, where i can have value $(1, \dots, n)$ days, and the other p days after the end of the decrease, where p can have value $(1, \dots, m)$ days. These intervals are then detrended using fit parameters obtained from linear regression. Mean count is determined for the detrended time series before the onset of FD for j days (where $j = 1, \dots, i$), and for the detrended time series during recovery stage for q days (where $q = 1, \dots, p$). Thus, in total we obtain $n!$ values for mean detrended count before the onset of FD, and $m!$ values for mean detrended count for the recovery stage. FD amplitude estimate is then calculated for each combination of “before” and “after” values according to the following formula:

$$A_{ij}^{pq} = \frac{\langle I_{before}^{(i,j)} \rangle - \langle I_{after}^{(p,q)} \rangle}{\langle I_{before}^{(i,j)} \rangle} \times 100\%, \quad (5)$$

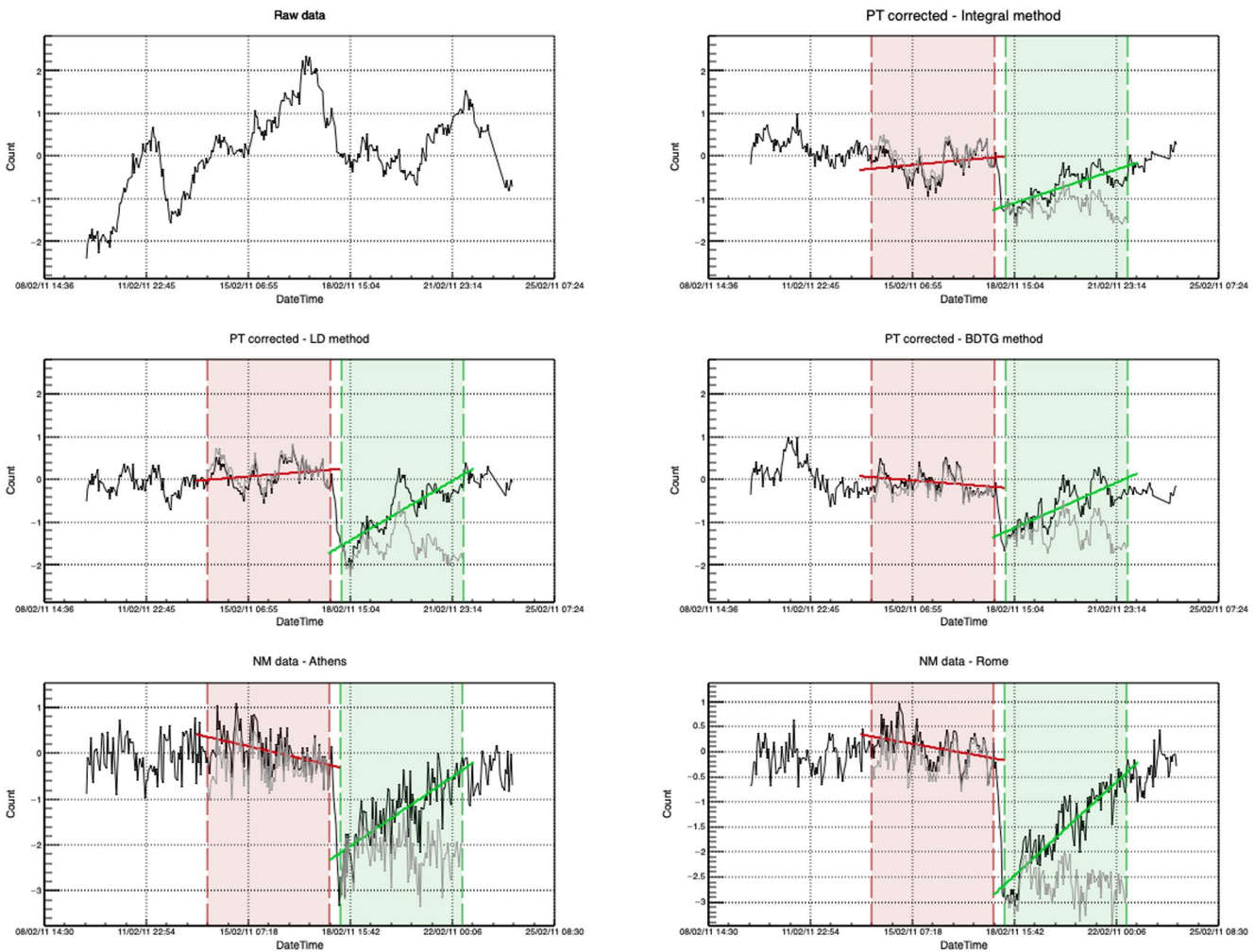


Figure 8. Time series for the interval around Forbush decrease of February 18, 2011: raw muon data (top left), PT corrected muon data using integral (top right), linear discriminant (center left) and gradient boosted decision tree (center right) methods, and neutron monitor data for Athens (bottom left) and Rome (bottom right) neutron monitors. Interval leading into (red) and following the Forbush decrease (FD) (green) are highlighted, as well as detrended intervals used to determine FD amplitude (gray).

where I_{before} and I_{after} are respective values for mean detrended count for intervals before the onset and after the end of the Forbush decrease. Finally, FD amplitude is calculated as the average of individual A_{ij}^{pq} values, rms deviation from the mean of the distribution used as an error estimate.

During the one-year period we used for the analysis there was a large number of Forbush events, but most of them had rather small amplitudes. We have analyzed several, however, here we will focus on the one with the largest magnitude as the results are most easily interpreted. The event is a Forbush decrease that occurred on February 18, 2011 in relation to X2.2 solar flare, and according to IZMIRAN space weather database (IZMIRAN, 2020) had 10 GV rigidity particle variation magnitude of 5.4. In Figure 8, we have shown plots that represent procedure described in the previous paragraph, applied to PT corrected datasets using integral method and selected multivariate algorithms. Procedure is also applied to pressure and efficiency corrected data for Athens and Rome neutron monitors, raw data also presented for reference. On the plots, interval leading into the onset of FD is indicated by red dashed lines, while recovery interval after the decrease is indicated by green dashed lines. We have chosen the lengths of both intervals to be four days ($n = m = 4$). Linear fits are represented by solid red and green lines, respectively, while detrended intervals are plotted using gray lines. Amplitudes and relative amplitudes calculated from the differences of means of detrended intervals are shown in Table 4.

Table 4
Amplitudes and Relative Amplitudes for the Forbush Decrease of February 18, 2011 for PT Corrected Muon Data and Selected Neutron Monitors

Method/NM monitor	Integral	LD	BDTG	Athens	Rome
FD amplitude (%)	1.38 ± 0.14	1.96 ± 0.18	1.10 ± 0.13	1.97 ± 0.15	2.68 ± 0.15
Relative FD amplitude	4.31 ± 0.44	7.09 ± 0.65	4.78 ± 0.56	5.30 ± 0.40	8.65 ± 0.48

Abbreviations: BDTG, gradient boosted decision tree; FD, Forbush decrease; LD, linear discriminant.

We see that relative amplitudes for this Forbush decrease, calculated based on data corrected for pressure and temperature using LD and BDTG algorithms, have sensitivity that is comparable or better than the sensitivity of integral method, even approaching the sensitivity of reference neutron monitors in the case of LD algorithm. However, when LD algorithm is concerned, such result can be at least in part explained by the fact that the calculated absolute FD amplitude is larger than expected for a muon detector. We would expect this value to be comparable to the value calculated based on the integral method. The reason for this discrepancy could be systematic, but also could be somewhat related to features of the studied FD event. Ideally, we should extend this analysis to more events, but selected time period was relatively calm in terms of solar activity, and February 2011 event was the only significant one with magnitude for 10 GV rigidity particles larger than five. Preliminary analysis done on Forbush decrease events of larger magnitude, that are outside the period used for analysis in this work, does show somewhat smaller effect for LD method, so that could be one of the focuses in the continuation of this work. We have excluded plots for the remaining multivariate algorithms as the results were either poorer (in the case of BDT and MLP) or inconsistent (in the case of PDERS and KNN).

5. Conclusions

We have selected a number of multivariate algorithms included in the TMVA package to apply for the correction of barometric and temperature effect on cosmic ray muons. Optimal parameters were determined for each algorithm based on the average quadratic deviation of modeled from measured data. Different distributions of modeled data for training phase and after the application of trained methods were compared to estimate the performance of selected algorithms. Pressure and temperature correction was done and spectral analysis performed to further test the algorithm consistency. The effect of the correction was analyzed for long-term (annual) and short-term (Forbush decrease) cosmic ray variations. In both cases, the efficiency of multivariate algorithms was compared to integral method and pressure corrected neutron monitor data.

Multidimensional probability density estimator algorithms (PDERS and KNN) appear not to be well suited for the modeling of pressure and temperature effect, most likely due to highly linear correlations between variables. MLP seems to have underperformed, while methods based on boosted decision trees (particularly BDTG) proved to be more successful, especially when effect on aperiodic variations was concerned. It should be expected that both MLP and BDT(G) methods can be improved if a longer period is used for analysis and parameters beyond average quadratic deviation of modeled data are used for algorithm optimization during training phase. Out of presented algorithms, LD proved to be the most consistent and effective in removing the pressure and temperature effects. In terms of the effect of PT correction on annual and aperiodic variations, this method matched or outperformed the integral method, while the effect it had on aperiodic effects was somewhat overestimative. This could give us grounds to assume at least part of the temperature effect is not taken into account by the integral method, and that there could be room for further improvement in modeling of meteorological effects beyond what theory currently provides.

Data Availability Statement

Raw muon count rate data set used in this study are publicly available online on the Belgrade Cosmic Ray Station site (<http://www.cosmic.ipb.ac.rs/>). Modeled atmospheric temperature data are available online on the NOAA GFS page (<https://www.ncdc.noaa.gov/data-access/model-data/model-datasets/global-forecast>).

system-gfs). Latest atmospheric pressure and ground temperature data are available online on the site of Republic Hydro-meteorological Service of Serbia (<http://www.hidmet.gov.rs/>). List of international geomagnetically quiet days can be downloaded from the GFZ site (<https://www.gfz-potsdam.de/en/kp-index/>). Neutron monitor data can be accessed online via NEST browser interface (<http://www01.nmdb.eu/nest/>).

Acknowledgments

The authors acknowledge funding provided by the Institute of Physics Belgrade, through the grant by the Ministry of Education, Science and Technological Development of the Republic of Serbia.

References

- Barbashina, N., Dmitrieva, A., Kompaniets, K., Petrukhin, A., Timashkov, D., Shutenko, V., et al. (2009). Specific features of studying Forbush decreases in the muon flux. *Bulletin of the Russian Academy of Sciences: Physics*, 73, 343–346. <https://doi.org/10.3103/S1062873809030198>
- Barrett, P. H., Bollinger, L. M., Cocconi, G., Eisenberg, Y., & Greisen, K. (1952). Interpretation of cosmic-ray measurements far underground. *Reviews of Modern Physics*, 24, 133–178. <https://doi.org/10.1103/RevModPhys.24.133>
- Belov, A., Blokh, Y., Dorman, L., & Rogovaya, S. (1987). The temperature diagnostics of the atmosphere allowing for the temperature of the near-surface layer. *International Cosmic Ray Conference*, 4, 263.
- Berkova, M., Belov, A., Eroshenko, E., & Yanke, V. (2012). Temperature effect of muon component and practical questions of how to take into account in real time. *Astrophysics and Space Sciences Transactions*, 8, 41–44. <https://doi.org/10.5194/astra-8-41-2012>
- Blackett, P. M. S. (1938). On the instability of the Barytron and the temperature effect of cosmic rays. *Physical Review*, 54, 973–974. <https://doi.org/10.1103/PhysRev.54.973>
- Carli, T., & Koblitz, B. (2003). A multi-variate discrimination technique based on range-searching. *Nuclear Instruments and Methods in Physics Research Section A: Accelerators, Spectrometers, Detectors and Associated Equipment*, 501, 576–588. [https://doi.org/10.1016/S0168-9002\(03\)00376-0](https://doi.org/10.1016/S0168-9002(03)00376-0)
- Dorman, L. I. (1954). On the temperature effect of the hard component of cosmic rays. *Reports of Academy of Sciences of USSR (DAN SSSR)*, 95, 49–52.
- Dorman, L. I. (2004). *Cosmic rays in the Earth's atmosphere and underground*. Springer. Retrieved from <https://books.google.rs/books?id=mKlv68WBU5kC>
- Dragić, A., Joković, D., Banjanac, R., Udovičić, V., Panić, B., Puzović, J., & Aničin, I. (2008). Measurement of cosmic ray muon flux in the Belgrade ground level and underground laboratories. *Nuclear Instruments and Methods in Physics Research Section A: Accelerators, Spectrometers, Detectors and Associated Equipment*, 591(3), 470–475.
- Dragic, A. L., Udovicic, V. I., Banjanac, R., Jokovic, D. R., Maletic, D. M., Veselinovic, N. B., et al. (2011). The new set-up in the Belgrade low-level and cosmic-ray laboratory. *Nuclear Technology & Radiation Protection*, 26(3), 181–192. <https://doi.org/10.2298/NTRP1103181D>
- Duperier, A. (1949). The meson intensity at the surface of the Earth and the temperature at the production level. *Proceedings of the Physical Society Section A*, 62(11), 684–696. <https://doi.org/10.1088/0370-1298/62/11/302>
- Dvornikov, V. M., Krestyannikov, Y. Y., & Sergeev, A. (1976). Determination of the mass-average temperature on the cosmic ray intensity data. *Geomagnetism and Aeronomy*, 16, 923–925.
- Feinberg, E. L. (1946). On the nature of cosmic ray barometric and temperature effects. *Reports of Academy of Sciences of USSR (DAN SSSR)*, 53, 421–424. <https://doi.org/10.1038/157421a0>
- Forbush, S. E. (1937). On the effects in cosmic-ray intensity observed during the recent magnetic storm. *Physical Review*, 51, 1108–1109. <https://doi.org/10.1103/PhysRev.51.1108.3>
- Forró, M. (1947). Temperature effect of cosmic radiation at 1000-m water equivalent depth. *Physical Review*, 72, 868–869. <https://doi.org/10.1103/PhysRev.72.868>
- GFS. (2020). Retrieved from <https://www.ncdc.noaa.gov/data-access/model-data/model-datasets/global-forecast-system-gfs>
- GFZ Potsdam. (2020). Retrieved from <https://www.gfz-potsdam.de/en/kp-index/>
- Hess, V. F. (1940). On the seasonal and the atmospheric temperature effect in cosmic radiation. *Physical Review*, 57, 781–785. <https://doi.org/10.1103/PhysRev.57.781>
- Hoecker, A., Speckmayer, P., Stelzer, J., Therhaag, J., von Toerne, E., Voss, H., & Zemla, A. (2007). *Tmva—Toolkit for multivariate data analysis*. Ithaca, NY: Cornell University.
- IZMIRAN. (2020). Retrieved from <http://spaceweather.izmiran.ru/eng/dbs.html>
- Joković, D. (2011). *Detekcija i spektroskopija miona iz kosmičkog zračenja plastičnim scintilacionim detektorima (Detection and spectroscopy of cosmic ray muons with plastic scintillation detectors) (Doctoral dissertation)*. Faculty of Physics, University of Belgrade. Retrieved from <http://www.cosmic.ipb.ac.rs/documents/jokovic-thesis.pdf>
- Kaminer, N. S., Ilgatch, S. F., & Khadakhanova, T. S. (1965). Temperature effect of the cosmic ray neutron component. In *Proceedings of the 9th International Cosmic Ray Conference* (Vol. 1, p. 486).
- Kohno, T., Imai, K., Inue, A., Kodama, M., & Wada, M. (1981). Estimation of the vertical profile of atmospheric temperature from cosmic-ray components. In *Proceedings of the 17th International Cosmic Ray Conference* (Vol. 10, p. 289).
- Lalchand, V. (2020). Extracting more from boosted decision trees: A high energy physics case study. In *33rd Annual Conference on Neural Information Processing Systems* (Vol. 1).
- Low Background Laboratory for Nuclear Physics. (2020). Retrieved from <http://www.cosmic.ipb.ac.rs/>
- Maeda, K., & Wada, M. (1954). Atmospheric temperature effect upon the cosmic ray intensity at sea level. *Journal of the Scientific Research Institute*, 48, 71–79.
- Montgomery, D. C., Peck, E. A., & Vining, G. G. (2006). *Introduction to linear regression analysis* (4th ed.). Hoboken, NJ: Wiley & Sons.
- Morozova, A. L., Blanco, J. J., & Ribeiro, P. (2017). Modes of temperature and pressure variability in midlatitude troposphere and lower stratosphere in relation to cosmic ray variations. *Space Weather*, 15(5), 673–690. <https://doi.org/10.1002/2016SW001582>
- Myssowsky, L., & Tuwim, L. (1926). Unregelmäßige intensitätsschwankungen der höhenstrahlung in geringer seehöhe. *Zeitschrift für Physik*, 39, 146–150. <https://doi.org/10.1007/BF01321981>
- NEST. (2020). Retrieved from <http://www01.nmdb.eu/nest/>
- Press, W. H., Teukolsky, S. A., Vetterling, W. T., & Flannery, B. P. (2007). *Numerical recipes 3rd edition: The art of scientific computing* (3rd ed.). New York: Cambridge University Press.
- Quenby, J. J., & Thambyahpillai, T. (1960). Atmospheric temperature effects on the solar daily variation of cosmic ray intensity. *The Philosophical Magazine: A Journal of Theoretical Experimental and Applied Physics*, 5(54), 585–600. <https://doi.org/10.1080/14786436008241210>
- RHMZ. (2020). Retrieved from <http://www.hidmet.gov.rs/index-eng.php>

- Savic, M., Dragic, A., Veselinovic, N., Udovicic, V., Banjanac, R., Jokovic, D., & Maletic, D. (2016). Effect of pressure and temperature corrections on muon flux variability at ground level and underground. In *25th European cosmic ray Symposium*.
- Savic, M. R., Dragic, A. L., Maletic, D. M., Veselinovic, N. B., Banjanac, R. M., Jokovic, D. R., & Udovicic, V. I. (2019). A novel method for atmospheric correction of cosmic-ray data based on principal component analysis. *Astroparticle Physics*, *109*, 1–11. <https://doi.org/10.1016/j.astropartphys.2019.01.006>
- Veselinović, N., Dragić, A., Savić, M., Maletić, D., Joković, D., Banjanac, R., & Udovičić, V. (2017). An underground laboratory as a facility for studies of cosmic-ray solar modulation. *Nuclear Instruments and Methods in Physics Research Section A: Accelerators, Spectrometers, Detectors and Associated Equipment*, *875*, 10–15. <https://doi.org/10.1016/j.nima.2017.09.008>
- Wada, M. (1962). Atmospheric effects on the cosmic-ray meson intensity. *Journal of the Physical Society of Japan Supplement*, *17*, 508. <https://doi.org/10.1143/jpsj.17.1805>

Accepted Manuscript

Rigidity dependence of Forbush decreases in the energy region exceeding sensitivity of neutron monitors

M. Savić, N. Veselinović, A. Dragić, D. Maletić, D. Joković, R. Banjanac, V. Udovičić

PII: S0273-1177(18)30749-X

DOI: <https://doi.org/10.1016/j.asr.2018.09.034>

Reference: JASR 13947

To appear in: *Advances in Space Research*

Received Date: 2 May 2018

Revised Date: 14 September 2018

Accepted Date: 24 September 2018

Please cite this article as: Savić, M., Veselinović, N., Dragić, A., Maletić, D., Joković, D., Banjanac, R., Udovičić, V., Rigidity dependence of Forbush decreases in the energy region exceeding sensitivity of neutron monitors, *Advances in Space Research* (2018), doi: <https://doi.org/10.1016/j.asr.2018.09.034>

This is a PDF file of an unedited manuscript that has been accepted for publication. As a service to our customers we are providing this early version of the manuscript. The manuscript will undergo copyediting, typesetting, and review of the resulting proof before it is published in its final form. Please note that during the production process errors may be discovered which could affect the content, and all legal disclaimers that apply to the journal pertain.



Rigidity dependence of Forbush decreases in the energy region exceeding sensitivity of neutron monitors

M. Savić, N. Veselinović*, A. Dragić, D. Maletić, D. Joković, R. Banjanac, V. Udovičić

Institute of physics, University of Belgrade, Pregrevica 118, 11080 Zemun, Serbia

*Corresponding author: veselinovic@ipb.ac.rs

Keywords: Forbush decrease; Muon CR station; Median rigidity

Abstract

Applicability for solar modulation studies of our present setup in a shallow underground laboratory is tested on four prominent examples of Forbush decrease during solar Cycle 24. Forbush decreases are of interest for space weather application as well as study of energy dependent solar modulation and they have been studied extensively. The characteristics of these events, as recorded by various neutron monitors and our detectors, were compared and rigidity spectrum was found. Linear regression was performed to find power indices that correspond to each event. As expected, steeper spectrum during more intense extreme solar events with strong X-flares shows greater modulation of galactic cosmic rays. Presented comparative analysis illustrates applicability of our setup for studies of solar modulation process in the energy region exceeding sensitivity of neutron monitors.

1. Introduction

Galactic cosmic rays (GCR) traverse the heliosphere which leads to variation of cosmic ray flux due to solar activity. The influence of solar and heliospheric modulation is pronounced for primary cosmic rays' particles with low rigidity or momentum over unit charge. Cosmic rays (CR) interact, upon arrival, with Earth's atmosphere causing electromagnetic and hadronic showers. Network of ground based CR detectors, neutron monitors (NM) and muon detectors, located at various locations around the globe, as well as airborne balloons and satellites provide valuable data to study time variation of the integrated CR flux affected by these modulations. Energies of the primary particles NMs are sensitive to, depending on the state of solar activity, are up to 40 GeV. Muon detectors have significant response from 10 GeV up to several hundred GeV for surface, and one order of magnitude greater for underground detectors, depending on the depth (Duldig, 2000). This energy interval allows muon detectors to monitor modulation effect for lower energy CRs but also galactic effects for primaries with higher energy where solar modulation is negligible. Because of the sensitivity to different energies of primary particle flux, observations of muon detectors complement NM observations in studies of long-term CR variations, CR anisotropy and gradients or rigidity spectrum of Forbush decreases.

Forbush decreases (Forbush, 1954) represent decreases of the observed galactic cosmic rays intensity under the influence of coronal mass ejections (CMEs) and interplanetary counterparts of coronal mass ejections (ICMEs) and/or high speed streams of solar wind (HSS) from the coronal holes (Belov, 2008). Forbush decreases (FD) belong to two types, depending on the drivers: non-recurrent and recurrent decreases. This work will address several non-recurrent FD.

These sporadic FD are caused by ICMEs. As the matter with its magnetic field moves through Solar system it suppresses CR intensity. FDs of this kind have asymmetric profile and intensity of galactic cosmic rays has sudden onset and recovers gradually. Sometimes an early phase of FD prior the dip (precursor of FD) has increase of CR intensity. These precursors of FDs are caused by galactic cosmic ray acceleration at the front of the advancing disturbance on the outer boundary of the ICME, as the primary cosmic rays' particles are being reflected from the approaching shock (Papailiou et al., 2013). Profile of the FD depends on the area, velocity and intensity of CME magnetic field produced in extreme events that originate at the Sun (Chauhan et al., 2008).

Data from observed modulation of GCR intensity contain information regarding their transport through interplanetary environment. GCR transport parameters are connected with interplanetary magnetic field (IMF) in the heliosphere. It is empirically established that radial diffusion coefficient is proportional to the rigidity of CR (Ahluwalia, 2005). In this article we present analysis of the amplitude of the FD during four events which were recorded by plastic scintillator muons detectors, located at Belgrade muon station, as well as by network of NMs.

2. Belgrade CR station

The Low-Background Laboratory for Nuclear Physics (LBLNP) is a part of the Institute of Physics, University of Belgrade. It is composed of two separate laboratory facilities, ground level laboratory (GLL) and underground laboratory (UL), dug into the cliff. The overburden of the UL is about 12 meters of loess soil, which is equivalent to 25 meters of water (m.w.e). Laboratory is dedicated to measurements of low radiation activities and studies of muon and electromagnetic components of cosmic rays at ground and shallow underground level. Geographic position of the laboratory is at 75 m a.s.l., at 44° 51' N latitude and 20° 23' E longitude; geomagnetic vertical rigidity cut-off is 5.3 GV at the surface. The equipment was upgraded in 2008, and now consists of two identical sets; one situated in GLL the other in UL, of detectors and accompanying data processing electronics. Detectors are a pair of plastic scintillator detectors, dimensions being 100cm x 100cm x 5cm, with four PMTs directly coupled to the corners. Signal from Two opposite PMTs on a single detector is summed and coincidence of two diagonals is found. Figure 1 presents the coincident sum spectra of two diagonals of the large scintillator detector.

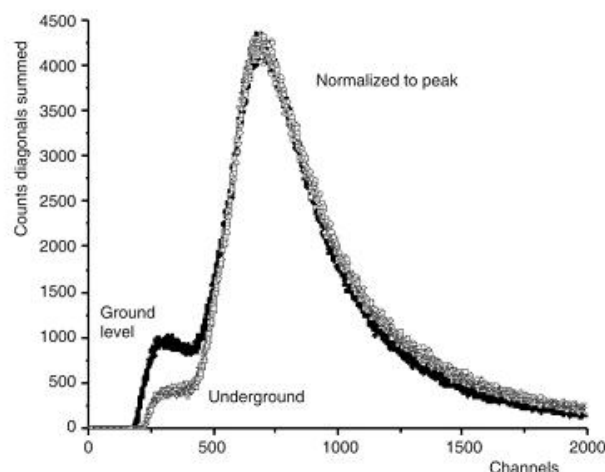


Figure 1. The coincident spectra of two diagonals of the large plastic detectors in the UL and GLL normalized for comparison.

Summing over diagonals suppresses acquisition of electromagnetic component of the secondary cosmic rays shower and collects mainly muon component of secondary CR. Well defined peak in the energy spectra corresponds to the muon energy loss of ~ 11 MeV. Average muon flux measured in the laboratory is 137(6) muons/m²s for GLL and 45(2) muons/m²s for UL. For more detailed description see (Dragić, et al. 2011). Integral of this distribution, without low energy part, is used to form time series of this CR muons spectrum integrated over different time intervals. This time series is then corrected for efficiency, atmospheric pressure and temperature (Savic et al, 2015).

There is a variation of CR flux, measured at the ground level, due to conditions in the atmosphere. Effects of atmospheric pressure can be easily accounted for, similar like for NMs, but the temperature effect is somewhat more difficult to treat. The difficulties arise from interplay of positive and negative temperature effects. With temperature increase, atmospheric density is reduced hence less pions interact and more muons are created from decay. The result is positive

effect of more muons at the ground level. On the other hand, altitude of muon production level is higher due to expansion of the atmosphere when the temperature is higher, muon path length is longer and there is higher decay probability for muons before they reach ground level. Negative effect is dominant for low energy muons (mostly detected in GLL) and positive for higher energy muons. The proper treatment of the temperature effect requires knowledge of the entire temperature profile of the atmosphere. This meteorological variation must be corrected for in order to study CR variations originating outside of the atmosphere.

For ground (and underground) based CR detectors, response function, the relation between particles of GCR spectra at the top of the atmosphere and recorded secondary particles at surface level should be accurately known. The total detector count rate can be expressed as (Caballero-Lopez and Moraal, 2012):

$$N(R_0, h, t) = \sum_i \int_{R_0}^{\infty} (S_i(R, h) j_i(R, t)) dR = \int_{R_0}^{\infty} W(R, h, t) dR, \quad (1)$$

Where $N(R_0, h, t)$ is detector counting rate, R_0 is geomagnetic cut-off rigidity, h is atmospheric depth and t represents time. $S_i(R, h)$ represent detector yield functions for primary particles type i , and $j_i(R, t)$ represent the primary particle rigidity spectrum of type i at time t . Total response function $W(R, h, t)$ is defined as a summed product of $S_i(R, h)$ and $j_i(R, t)$. Maximum value of this function is in the range of 4-7 GV at sea level, depending on the solar modulation epoch at time t (Clem and Dorman, 2000). One of the methods to find this response function is to use numerical simulation of propagation of cosmic rays through the atmosphere. CORSIKA simulation package (Heck et al., 1998) was used for CR transport through the atmosphere as well as GEANT4 (Agostinelli et al., 2003) for simulation of propagation of secondary CR through overburden and response of the detectors in order to find relation between the count rate at our site and flux of primary particles on top of the atmosphere.

The excellent agreement of the simulated and measured flux (figure 2), allows us to establish that cut-off energy for primary CR protons for showers detected in GLL is caused with its geomagnetic rigidity and median energy ~ 60 GeV. For UL, cut-off due to earth overburden is 12GeV and median energy is ~ 120 GeV. These values give us opportunity to study solar modulation at energies exceeding energies detected with neutron monitor. Observation of the solar activity and related magnetic disturbances in the heliosphere that create transient CR intensity variation at several different energies can provide an energy dependent description of these phenomena.

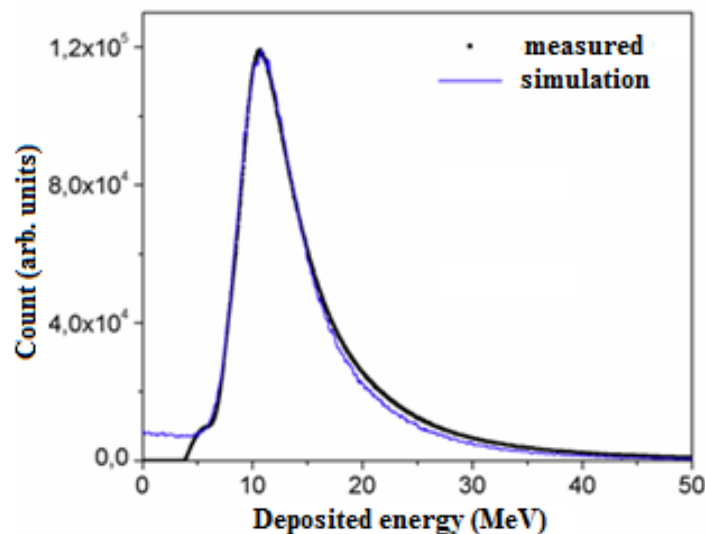


Figure 2: Simulated (blue line) and measured spectra (black line) for muon detector in UL.

3. Data analysis

The new setup in LBLNP, presented in (Dragić et al., 2011), coincides with the start of the 24th solar cycle, thus allowing us to observe rise and fall of solar activity and the effect of solar modulation at energies higher than ones studied using neutron monitors.

Muon time series were searched for days where the average muon flux was significantly lower than background level. Background level was determined from moving averages of hourly count rates 10 days before the event. These drops in count rate, in GLL and UL, are then compared with space weather events of the solar cycle 24. Data collected in UG and GLL has been compared with four neutron monitor station (NM) from Neutron monitor database [http://www.nmdb.eu/]. Three of these neutron monitors (Athens, Rome and Jungfrauoch) have similar cut-off rigidity and geographic proximity to Belgrade CR station.

Correlation between count rates during March 2012 measured in LBLNP and NMs (table 1) is very high between NMs but for GLL and UL, as the cut-off energy of the primary flux increases, the correlation is slightly lower.

UL_tpc	75	81	80	81	76	73	78	86	97	100
UL_pc	77	83	83	83	73	78	72	84	100	97
UL_raw	57	71	70	74	94	49	51	100	84	86
GLL_tpc	86	86	84	83	59	90	100	51	72	78
GLL_pc	90	92	90	89	56	100	90	49	78	73
GLL_raw	63	79	78	81	100	56	59	94	73	76
Oulu	90	98	98	100	81	89	83	74	83	81
Jung.	91	98	100	98	78	92	84	70	83	80
Rome	91	100	98	98	79	92	86	71	83	81
Athens	100	91	91	90	63	90	86	57	77	75
	Athens	Rome	Jung.	Oulu	GLL_raw	GLL_pc	GLL_tpc	UL_raw	UL_pc	UL_tpc

Table 1: Correlation matrix of linear correlation coefficient (in %) for recorded hourly flux at Belgrade cosmic ray station with its temperature and pressure corrected underground and ground level detectors (UL_tpc, GLL_tpc), only pressure corrected (UL_pc, GLL_pc), raw data(UL_raw, GLL_raw) and recordings at Rome, Oulu, Jungfrauoch (Jung.) and Athens NMs for March 2012.

Selected Forbush decreases

Belgrade CR station has detected, both in GLL and UL, several significant structures connected to some extreme solar effects. Several, more prominent, Forbush decreases happened on March 2012, September 2014, June 2015 and latest in September 2017.

Forbush decrease that occurred on 8 of March 2012 was recorded at Belgrade CR station as well as other stations (Figure 3). This FD is separated into two decreases following two CME. These CMEs produced intense disturbance in the interplanetary space and caused severe geomagnetic storm when the shockwave reached Earth on March 8, 2012. In this event a very complex combination of modulation occurs (Lingri et al., 2016). Two coronal mass ejections from the same active region as the Sept. 10 (X1.6) flare produced FD occurred on September 12, 2014. There was a relatively fast Partial Halo CME and a larger and faster moving Halo CME trailing behind the first one on 10th of September. These two gave rise to the FD that was first detected by neutron monitors on 12th of September 2014. This FD is not classical two steps FD as expected, probably due to the interaction of slower and faster CME. It is reflected in the profile of the FD (Figure 3) with small second step several hours after the first, similar to FD happened on February 2011 (Papaioannou et al., 2013). During June 2015 a large activity happen on the Sun from powerful AR 2371 that produced several CMEs emerging from the Sun. These CMEs induced complex modulation of galactic cosmic rays that leads to FD recorded on June 22, 2015 with unusual structure (Samara et al., 2018).

A sudden burst of activity from the Sun early in September 2017, after prolonged period of low solar activity, produced several flares, including largest solar flare seen from Earth since 2006, an X9.3 flare. This activity produced several CMEs that were Earth-directed. Throughout this time Earth experienced a series of geomagnetic storms, starting promptly after the first CME. This unusual activity produced FD recorded with the detectors and a ground level enhancement (GLE) on Earth and Mars (Guo et al., 2018)

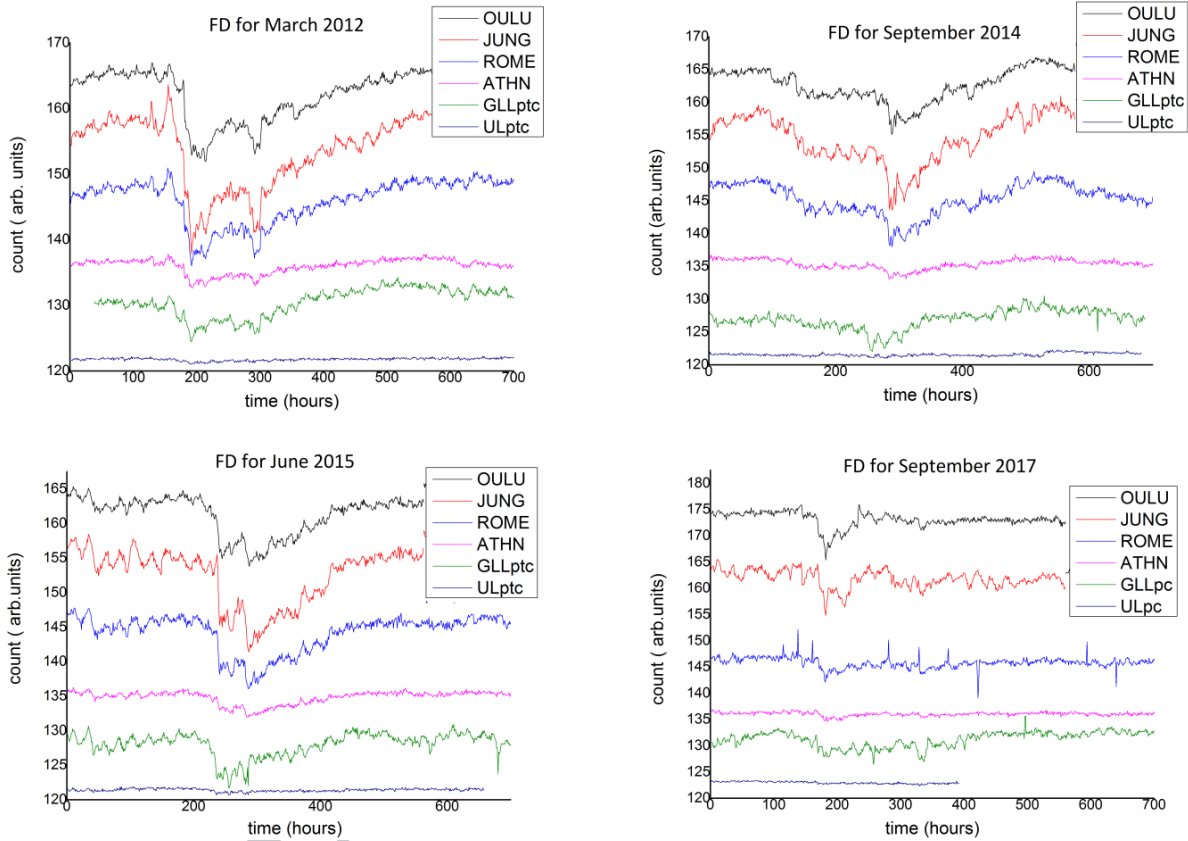


Figure 3: Comparison of hourly time series over one month period for pressure and temperature corrected count rates of Belgrade muon monitor station (GLLptc and ULptc) and neutron monitors: Athens (ATHN), Rome (ROME), Jungfrauoch (JUNG), Oulu (OULU) for extreme solar event in March 2012, September 2014, June 2015. Count rates are shifted for comparison. For extreme solar event in September 2017 for GLL and UL count rate are pressure corrected only.

4. FD and median rigidity

For each event we study the energy dependence of the amplitude. Energy dependence of FD amplitude is expected to follow the power law: $\Delta N/N \sim R^{-\gamma}$ (Cane, 2000). In order to obtain reliable values of amplitudes, we defined amplitude as a relative decrease of hourly count rate of the minimum compared with average from seven days count rate before FDs (not including possible precursory increases). Base period this long was used due to higher activity of the Sun prior to registered FDs and sensitivity of the muon detectors.

Amplitudes have been determined for two of our detectors as well as for 12 NMs. In order to investigate the rigidity spectrum of mentioned FDs median rigidity, R_m , is defined. R_m is the rigidity of the response of the detector to GCR spectrum where 50% of detector counting rate lies below R_m (Ahluwalia and Fikani, 2007). For this study we used a list of R_m for 12 NM station given by (Minamino et al., 2014). For a NM, median rigidity can be computed from the detector response function

derived from surveys for particulate station, usually around minima of solar activity as the intensity of lowest-rigidity GCRs is maximal then.

For Belgrade muon station R_m was found using response function acquired with Monte Carlo method of CR transport. Approximate values of R_m for the detectors used in this study are listed in table 2.

Stations	Median rigidity R_m (GV)	Min. rigidity R_0 (GV)
Athens	25,1	8,53
Mexico	25,1	8,28
Almaty	15,8	6,69
Lomnický štít	12,6	3,84
Moscow	15,8	2,43
Kiel	15,8	2,36
Yakutsk	12,6	1,65
Apatity	12,6	0,65
Inuvik	12,6	0,3
Mc Murdo	12,6	0,3
Thule	12,6	0,3
South Pole	10	0,1
UL	122	12,3
GLL	63	5,3

Table 2: Median and cut-off rigidity for several stations

For every selected event a scatter plot is drawn (Figure 4). All plots show, plotted in log-log scale, clear median rigidity dependence of the amplitude of the decrease of FD.

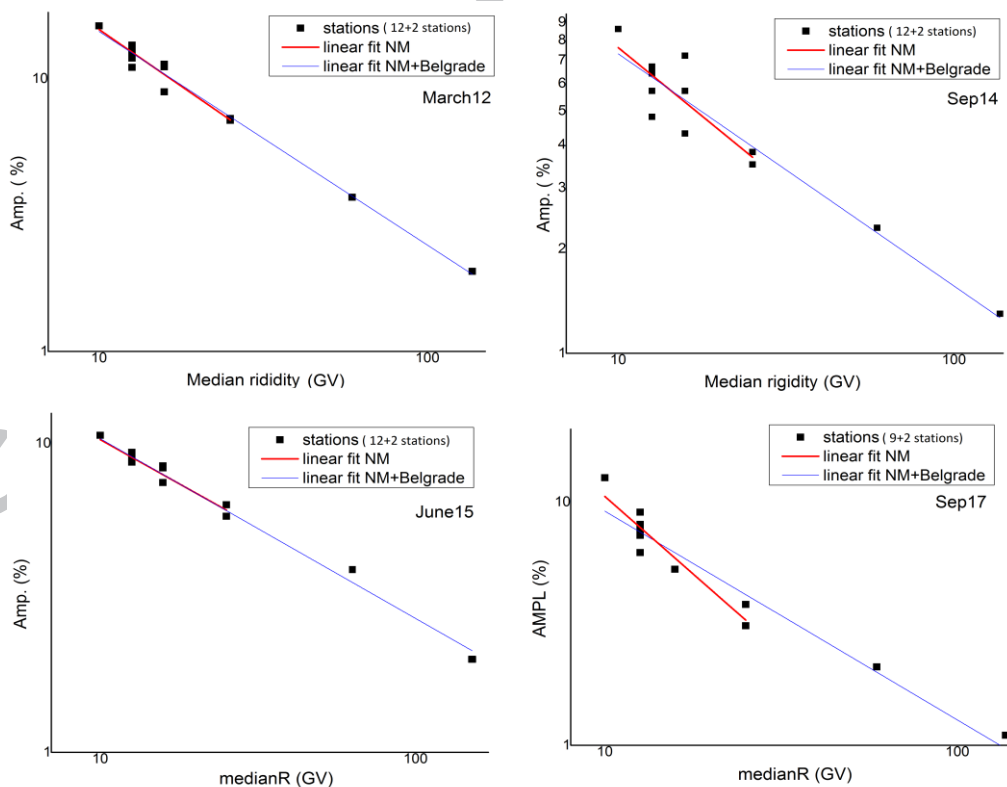


Figure 4: Rigidity spectrum of FD from March 8, 2012, September 12, 2014, June 22, 2015 and September 8, 2017. Points represent the amplitude of the event as seen by NMs and Belgrade CR station.

Linear regression is performed to find power indices corresponding to each event. Power indices are given in table 3.

γ	NM	NM+Belgrade	Belgrade stat. only
March 2012.	0,82±0,08	0,78±0,03	0.715
Sept. 2014.	0,79±0,16	0,67±0,06	0.744
June 2015.	0,57±0,05	0,58±0,02	0.764
Sept. 2017.	1,27±0,16	0,86±0,07	0.739

Table 3: Power indices of median rigidity dependence of the dip of the FD. Power indices are obtained for NM only and for NMs and Belgrade muon station.

Higher power indices can be due to more complex variation of GCR. This more complex variation is a result of series of CMEs during this event that leads to large compound ICME structure with multiple shocks and transient flow (Zhao and Zhang, 2016). Results for power law are generally consistent with previous studies (Ahluwalia and Fikani, 2007, Lingri et al., 2016, Klyueva et al., 2017) conducted for NMs only.

More significant difference observed for indices during the 2017 event is because we used only pressure corrected data for muon flux recorded at Belgrade station. For all other events and data we performed both pressure and temperature correction. Without temperature corrections variation of the count rate in muon detectors is higher and it can affect the results.

We expect when implementation of newly improved, internally developed technique for temperature correction of CR flux is performed, amplitude of the FD measured at Belgrade muon station will be more consistent with other events and measurements. More data points on the graphs are needed to understand indices better, particularly in an energy region between NM and our lab. Similar work (Braun et al., 2009) discussed the extension up to 15 GeV and 33 GeV but there is no data available for FDs during Cycle 24 and cannot be incorporated into this work. As for other operating muon telescopes, there is an agreement between our stations data and URAGAN data for FD in June 2015 (Barbashina et al., 2016) but we have no data for other FDs and/or median energies of other stations. Our new experimental setup described elsewhere (Veselinović et al. 2017) will provide, two extra median energies (121 GeV and 157 GeV) to monitor variations of CR flux.

Conclusion

Belgrade CR station, with both ground level and underground setups, monitors effect of solar modulation on cosmic ray flux since 2008. Extreme solar events, like Forbush decreases, during Solar cycle 24 have been detected at the site, suggesting these phenomena can be studied at higher energies than typical energies detected with NM. GLL and UL data, as well as data from several neutron monitor stations, are used to analyze four intense Forbush decreases. The magnitude of FD events is energy (rigidity) dependant and follows the power law. Data used to find rigidity dependence of these transient solar modulation of GCR are obtained over much higher range of rigidities than region NMs are sensitive in, thus allowing more extensive studies of cosmic-ray solar modulation processes.

Acknowledgments

We acknowledge the NMDB database (www.nmdb.eu), founded under the European Union's FP7 programme (contract no.213007) for providing data. We acknowledge individual monitors following the information given on the respective station information page. *Athens neutron monitor data were kindly provided by the Physics Department of the National and Kapodistrian University of Athens.*

Jungfrau neutron monitor data were kindly provided by the *Physikalisches Institut, University of Bern, Switzerland*. For Oulu NM data were kindly provided by <http://cosmicrays oulu.fi> and Sodankyla Geophysical Observatory. Rome neutron monitor data were kindly provided by SVIRCO NM, supported by INAF/IAPS-UNIRoma3 COLLABORATION. We thank the anonymous referees for useful advices.

The present work was funded by the Ministry of Education, Science and Technological Development of the Republic of Serbia, under the Project No. 171002.

References

1. Ahluwalia, H. S. (2005), "Cycle 20 solar wind modulation of galactic cosmic rays: Understanding the challenge", *Journal of Geophysical Research*, Vol.110, A10106, doi:10.1029/2005JA011106.
2. Ahluwalia, H.S. and Fikani, M.M. (2007) "Cosmic ray detector response to transient solar modulation: Forbush decreases". *Journal of Geophysical Research*, Vol. 112, Issue A8, A08105, doi: 10.1029/2006JA011958
3. Barbashina, N. S., Ampilogov N. V., Astapov I. I., Borog V. V., Dmitrieva A. N., Petrukhin A. A., Sitko O. A., Shutenko V. V. and Yakovleva E. I. (2016) "Characteristics of the Forbush decrease of 22 June 2015 measured by means of the muon hodoscope URAGAN." *Journal of Physics: Conference Series*. Vol. 675. No. 3., article id. 032038, doi: 10.1088/1742-6596/675/3/032038
4. Belov, A. V. (2008) "Forbush effects and their connection with solar, interplanetary and geomagnetic phenomena" *Proceedings of the International Astronomical Union* 4.S257: pp. 439-450, doi:10.1017/S1743921309029676
5. Braun I., Engler J., Hörandela J.R., Milke J. (2009) "Forbush decreases and solar events seen in the 10–20 GeV energy range by the Karlsruhe Muon Telescope", *Advances in Space Research*, Volume 43, Issue 4, pp. 480-488, doi: 10.1016/j.asr.2008.07.012
6. Caballero-Lopez, R. A., and H. Moraal. (2012) "Cosmic-ray yield and response functions in the atmosphere.", *Journal of Geophysical Research: Space Physics*, Volume 117, Issue A12, pp. 7461-7469, doi: 10.1029/2012JA017794
7. Cane, H.V. (2000) "Coronal Mass Ejections and Forbush Decreases", *Space Science Reviews*, Volume 93, Issue 1–2, pp. 55–77, doi:10.1023/1026532125747
8. Chauhan, M.L., Jain Manjula, S K Shrivastava S.K., (2008) "Study of two major Forbush decrease events of 2005", *Proceedings of the 30th International Cosmic Ray Conference*, Mexico City, Vol. 1 (SH), pp. 307–310, doi: 10.7529/ICRC2011/V10/0097
9. Clem J.M., Dorman L.I. (2000) "Neutron Monitor Response Functions, Cosmic Rays and Earth", *Space Science Reviews*, v. 93, Issue 1/2, pp. 335-359, doi: 10.1023/A:1026515722112
10. Dragić A., Udovičić V., Banjanac R., Joković D., Maletić D., Veselinović N., Savić M., Puzović J., Aničin I.V. (2011) "The New Setup in the Belgrade Low-Level and Cosmic-Ray Laboratory", *Nuclear Technology & Radiation Protection* Vol. 26, No. 3, pp.181-192, doi: 10.2298/NTRP1101064N
11. Duldig M.L. (2000) "Muon Observations". In: Bieber J.W., Eroshenko E., Evenson P., Flückiger E.O., Kallenbach R. (eds) *Cosmic Rays and Earth*. Space Sciences Series of ISSI, vol 10., pp. 207-226, Springer, Dordrecht, doi:10.1007/978-94-017-1187-6_1
12. Forbush S.E.(1954) "World-wide cosmic ray variations, 1937–1952", *Journal of Geophysical Research*, vol. 59, issue 4, pp. 525-542, doi: 10.1029/JZ059i004p00525
13. Guo J., Dumbović M., Wimmer-Schweingruber R.F., Temmer M., Lohf H., Wang Y., Veronig A., Hassler D.M., Leila M., Mays L.M., Zeitlin C., Ehresmann B., Witasse O., Freiherr von Forstner

- J.L., Heber B., Holmström M., Posner A. (2018) "Modeling the evolution and propagation of the 2017 September 9th and 10th CMEs and SEPs arriving at Mars constrained by remote-sensing and in-situ measurement." arXiv preprint arXiv:1803.00461
14. Klyueva A.I., Belov A.V., Eroshenko E.A. (2017) "Specific features of the rigidity spectrum of Forbush effects" *Geomagnetism and Aeronomy*, Volume 57, Issue 2, pp. 177–189, doi: 10.1134/S0016793217020050
 15. Lingri D., Mavromichalaki H., Belov A., Eroshenko E., Yanke V., Abunina A., Abunina M., (2016) "Solar Activity Parameters and Associated Forbush Decreases During the Minimum Between Cycles 23 and 24 and the Ascending Phase of Cycle 24", *Solar Physics* 291(3), pp.1025-1041, doi:10.1007/s11207-016-0863-8
 16. Minamino, Mohanty, Morishita, et al. for the GRAPES-3 Collaboration (2014) "Rigidity Dependence of Forbush Decreases", Poster #654, pp. 3612-3615 Proceedings of the 33rd International Cosmic Ray Conference, Rio de Janeiro, Brazil
 17. Papailiou, M., Mavromichalaki H., Abunina M., Belov A., Eroshenko E., Yanke V., Kryakunova O. (2013) "Forbush decreases associated with western solar sources and geomagnetic storms: A study on precursors." *Solar Physics* 283.2, pp.557-563. doi: 10.1007/s11207-013-0231-x
 18. Papaioannou, A., A Belov A., Mavromichalaki H., Eroshenko E., Yanke V., Asvestari E., Abunin A. and Abunina M. (2013) "The first Forbush decrease of solar cycle 24", *Journal of Physics: Conference Series*, Volume 409, Issue 1, article id. 012202, doi:10.1088/1742-6596/409/1/012202
 19. Samara, E., Smpontas I. A., Lytrosyngounis I., Lingri D., Mavromichalaki H., Sgouropoulos C. (2018): "Unusual Cosmic Ray Variations During the Forbush Decreases of June 2015" *Solar Physics* 293: 67. DOI:10.1007/S11207-018-1290-9
 20. Savić M., Maletić D., Joković D., Veselinović N., Banjanac R., Udovičić V. and Dragić V. (2015) "Pressure and temperature effect corrections of atmospheric muon data in the Belgrade cosmic-ray station", *Journal of Physics: Conference Series*, Volume 632, Issue 1, article id. 012059, doi:10.1088/1742-6596/632/1/012059
 21. Veselinović N., Dragić A., Savić M., Maletić D., Joković D., Banjanac R. and Udovičić V. (2017) "An underground laboratory as a facility for studies of cosmic-ray solar modulation", *Nucl.Instrum.Meth.* A875 p.10-15, doi:10.1016/j.nima.2017.09.008
 22. Zhao L.-L., Zhang H. (2016) "Transient Galactic Cosmic-ray Modulation during Solar Cycle 24: A Comparative Study of Two Prominent Forbush Decrease Events", *The Astrophysical Journal* 827 (1), article id. 13, DOI:10.3847/0004-637X



New insights from cross-correlation studies between solar activity indices and cosmic-ray flux during Forbush decrease events

Mihailo Savić, Nikola Veselinović*, Aleksandar Dragić, Dimitrije Maletić, Dejan Joković
Vladimir Udovičić, Radomir Banjanac, David Knežević

Institute of Physics Belgrade, University of Belgrade, Pregrevica 118, 11080 Belgrade, Serbia

Received 1 April 2022; received in revised form 12 September 2022; accepted 27 September 2022

Abstract

Observed galactic cosmic ray intensity can be subjected to a transient decrease. These so-called Forbush decreases are driven by coronal mass ejection induced shockwaves in the heliosphere. By combining in situ measurements by space borne instruments with ground-based cosmic ray observations, we investigate the relationship between solar energetic particle flux, various solar activity indices, and intensity measurements of cosmic rays during such an event. We present cross-correlation study done using proton flux data from the SOHO/ERNE instrument, as well as data collected during some of the strongest Forbush decreases over the last two completed solar cycles by the network of neutron monitor detectors and different solar observatories. We have demonstrated connection between the shape of solar energetic particles fluence spectra and selected coronal mass ejection and Forbush decrease parameters, indicating that power exponents used to model these fluence spectra could be valuable new parameters in similar analysis of mentioned phenomena. They appear to be better predictor variables of Forbush decrease magnitude in interplanetary magnetic field than coronal mass ejection velocities.

© 2022 COSPAR. Published by Elsevier B.V. All rights reserved.

Keywords: Cosmic rays; Forbush decrease; Solar energetic particles; Solar activity

1. Introduction

Cosmic rays (CRs) are high-energy charged particles that arrive at Earth from space, mainly originating from outside of our Solar system. CRs are modulated in the heliosphere (Heber et al., 2006) due to interaction with the interplanetary magnetic field (IMF) frozen in a constant stream of charged particles from Sun - the solar wind (SW). Transients in the heliosphere additionally modulate CRs. One type of transients are interplanetary coronal mass ejections (ICMEs), closely related to coronal mass ejections (CMEs).

ICMEs interact with SW, and as the speed of particles in ICME is different than the speed of SW particles, a bow shock can be created, affecting the CR flux (Belov et al., 2014). This interaction between ICMEs and residual solar wind can be one of the causes of short-term depression in CR flux, detectable at Earth (Subramanian et al., 2009). Such transient decrease in observed flux is known as a Forbush decrease (FD), a type of CR flux modulation that has been studied extensively since its initial discovery in the 1930s (Gopalswamy (2016) and references therein). There are two clearly distinguishable classes of Forbush decreases: recurrent and non-recurrent. Non-recurrent FDs, typically caused by ICMEs (Dumbovic et al., 2012), are mostly characterized by a sudden offset, which lasts about a day, followed by a gradual recovery phase within several days (Cane, 2000). Due to ICME sub-structures

* Corresponding author.

E-mail address: veselinovic@ipb.ac.rs (N. Veselinović).

(the sheath and the associated shock and magnetic cloud) FD can have one or two-step profile, which depends on transit of one or both structures to the observer (Richardson and Cane, 2011). Recurrent FDs have different profile, with gradual onset and decrease and symmetrical recovery caused by high-speed streams from coronal holes (Melkumyan et al., 2019). In this paper we will focus on non-recurrent ICME induced FDs.

Apart from FD profile, one of the main parameters that is used to describe a Forbush decrease is its magnitude. The effect is not the same for all CR particles, as it depends on their rigidity. Rigidity is defined as $R \equiv B\rho = p/q$, where ρ is gyroradius of the particle due to magnetic field B , p is particle momentum, and q is its charge. The higher the rigidity of a particle, the less it is affected by heliospheric inhomogeneities, hence the reduction in flux is less pronounced.

Another phenomenon that can accompany violent events on the Sun is emission of fast-moving particles, commonly known as solar energetic particles (SEP). The occurrence of such particles is typically related to eruptions on the surface of the Sun, which can be characterized by bursts of X-rays - solar flares (SF), and/or emission of coronal plasma - already mentioned CMEs. When excess of these solar energetic particles with high energy penetrates the geomagnetic field, it can cause a sudden and brief increase in measured CR flux at Earth - a ground level enhancement (GLE). Because GLEs can be harmful to human infrastructures (potentially damaging power lines, satellites in orbit, etc.), they have been studied in detail for decades.

Variations of CR flux have been monitored at Earth for decades using ground and underground-based detectors, primarily neutron monitors (NM) (Belov et al., 2000; Koldobskiy et al., 2019) and muon detectors (Mendonça et al., 2016; Veselinović et al., 2015). Different types of ground-based detectors complement each other in terms of their CR energy domain (Veselinovic et al., 2017), muon detectors being sensitive to energies higher than those detectable by NMs. In addition, CR flux is also (especially in the last couple of decades) directly measured in space using space-borne instruments (Dumbovic et al., 2020; von Forstner et al., 2020). In the MeV energy range most space probe particle detectors are sensitive to, enhancement of SEP flux can enshroud CR flux, thus making a task of establishing decoupled event-integrated energy spectra (or spectral fluences) for SEP and CRs a laborious task (Koldobskiy et al., 2021; Bruno and Richardson, 2021).

Many authors have studied the connection between SFs, CMEs/ICMEs and SEP, consequential effects on the geomagnetic field and compound effect of the IMF and geomagnetic field disturbances on CRs. Most relevant for our analysis is work that studied connection between different FD and ICME parameters (Belov et al. (2000), Belov (2008), Papaioannou et al. (2020) and references therein), which has among other, shown significant correlation between CME speeds and FD magnitudes. More precisely, CME speeds have been established as the best predictor

variables of FD magnitudes for primary CR particles with 10GV rigidity detected at Earth. Also of interest is the work that studied the connection between the disturbance of geomagnetic field and CR flux measured at Earth (Alhassan et al., 2021; Badruddin et al., 2019), where a significant correlation between FD magnitude and different geomagnetic parameters due to common solar or interplanetary origin has been established.

SF, CME/ICME, SEP and FD events are very often related processes that occur either simultaneously or in succession, in which case can be thought of as different components of one more complex event. CMEs (along with their interplanetary counterparts ICMEs) have been recognized as the main driver of FDs, while on the other hand there has been plenty of evidence for the relationship between CMEs with SEP. Namely, there are two different known mechanism for SEP acceleration: acceleration during magnetic-reconnection events usually resulting in solar flares (which produce short impulsive SEP events), and acceleration caused by CME induced shock waves (which result in gradual SEP events) (Reames, 1999). For this study the second class is of interest. Another type of closely related events that are important for this analysis are energetic storm particle (ESP) events, which represent particles accelerated locally by interplanetary shocks driven by fast CMEs (Desai and Giacalone, 2016). Even though details of the mechanism and the precise role of CME induced shock in the evolution of SEP events are not fully understood (Anastasiadis et al., 2019), we believe that analysis of how SEP/ESP events relate to CME, geomagnetic and FD events could provide some valuable new insight. We are especially interested in, and will concentrate the most on, the possibility of the last of these connections. To do so, we have decided to look into the shape of SEP/ESP fluence spectra and analyze how it relates to different CME, geomagnetic and especially FD parameters.

It should be noted that different mentioned types of events, even when related, do not need to occur at the same place nor at the same time. This is due to the fact that SEP travel along magnetic field lines, while CME/ICME shocks travel mostly directly away from the Sun. Furthermore, modulation of primary CR, detected as FD upon their arrival at Earth, can happen anywhere in the heliosphere. Hence, in general case, detection of these events should not necessarily be simultaneous. However, we believe that for the class of events selected for this analysis we can assume that they occur and are detected within a certain time window. We will elaborate more on this in Section 2.3.

The article is structured as follows: first we list various sources of data and justify the selection of solar cycle 23 and 24 FD events to be used in the analysis; then we describe parametrization of SEP events (involving calculation and parametrization of SEP fluence spectra); finally we perform correlative analysis between established SEP parameters and various CME, FD and geomagnetic indices and discuss the observed dependencies.

2. Data

Sources of SEP proton flux, various solar and space weather parameters, as well as ground CR measurements and different FD parameters used in this study are listed below. Different criteria for FD event selection are also described.

2.1. Solar energetic particle flux data

The source for SEP flux data was the ERNE instrument (Torsti et al., 1995) onboard the Solar and Heliospheric Observatory (SOHO). Instrument consists of two separate particle detectors. The Low-Energy Detector (LED) and the High-Energy Detector (HED). Former covers ion fluxes and count rates in the 1.3 – 13 MeV/nucleon energy range, and latter ion fluxes and count rates in the 13 – 130 MeV/nucleon energy range. Both ranges are separated in ten energy channels. SOHO has been making in situ observation from Lagrangian point L1 for the last three solar cycles (data available at https://omniweb.gsfc.nasa.gov/ftpbrowser/flux_spectr_m.html). ERNE data for solar cycles 23, 24 and current cycle 25 allows the study of variations of proton fluences in SEP events during this period (Paassilta et al., 2017; Belov et al., 2021). Higher channels are more correlated with measured CR flux (Veselinovic et al., 2021) and it appears as if flux in these channels is a mixture of CR and energetic proton fluxes of particles with the same energy. Important feature of HED detector is that, due to rather large geometric factor, during large intensity proton events SOHO/ERNE data have been subject to saturation effects in higher energy channels (Valtonen and Lehtinen, 2009; Miteva et al., 2020).

2.2. IZMIRAN directory of Forbush decreases

IZMIRAN database is an online repository developed at the Institute of Terrestrial Magnetism, Ionosphere and Radiowave Propagation (IZMIRAN) at Moscow Troitsk, Russia. It contains an extensive list of Forbush decreases and various parameters from solar, space weather, cosmic ray and geomagnetic measurements, spanning from the late 1950s (<http://spaceweather.izmiran.ru/eng/dbs.html>). Database has been compiled from a number of sources, such as measurements by ground-based detectors, instruments mounted on various satellites, as well as public data provided by different agencies specializing in monitoring solar, space and atmospheric weather and geomagnetism. Extensive list of sources and data repositories used to compile this database are referenced in a number of publications listed on the IZMIRAN internet site (IZMIRAN Space Weather Prediction Center, 2016).

We have decided to use IZMIRAN database as our primary source of data for Forbush decrease parameters as well as for selected variables, parameters and indices that describe associated space weather and geomagnetic

phenomena. Selection of parameters pertinent to our analysis was mostly based on previous work by other authors (i.e. Belov (2008), Lingri et al. (2016)), where they established which quantities are most relevant in these types of studies.

Chosen parameters fall into three categories (abbreviations to be used throughout the text are given in parentheses). First category are FD related parameters - Forbush decrease magnitude for 10GV rigidity primary particles (M) and Forbush decrease magnitude for 10GV rigidity primary particles corrected for magnetospheric effect using Dst index (M_M). These magnitudes are determined using global survey method (GSM). GSM combines measurements from a world-wide network of neutron monitors (NMs), takes into account different anisotropies, disturbances of atmospheric and geomagnetic origin, as well as apparatus-specific features, and produces an estimated hourly variation of CR flux outside Earth's atmosphere and magnetosphere (Belov et al., 2018). Specifically, correction for magnetospheric effect takes into account the fact that geomagnetic disturbances affect the effective cutoff threshold rigidities and effective asymptotic directions of primary particles for different NM stations (Belov et al., 2005).

Second group of parameters used from IZMIRAN database are CME and SW related parameters - the average CME velocity between the Sun and the Earth, calculated using the time of the beginning of the associated X-ray flare (V_{mean}), the average CME velocity between the Sun and the Earth, calculated using the time of the beginning of the associated CME observations (V_{meanC}) and maximal hourly solar wind speed in the event (V_{max}). Izmiran DB authors have matched detected FD events with associated CMEs using a SOHO LASCO CME catalog (Belov et al., 2014). Catalog includes a comprehensive list of CME events along with some of most relevant parameters, i.e. speeds calculated by tracking CME leading edge (as described in Yashiro et al. (2004), further sources available at https://cdaw.gsfc.nasa.gov/CME_list/catalog_description.htm).

Final group of parameters from IZMIRAN database used in this analysis are related to geomagnetic field - maximal Kp index in the event (Kp_{max} - based on data from NOAA Space Weather Prediction Center, <https://www.swpc.noaa.gov/products/planetary-k-index>), maximal 3-h Ap index in the event (Ap_{max} - defined as the mean value of the variations of the terrestrial magnetic field, derived from Kp index) and minimal Dst index in the event (Dst_{min} - calculated using data provided by World Data Center for Geomagnetism, Kyoto, <http://wdc.kugi.kyoto-u.ac.jp/dst/dir/index.html>).

2.3. Selection of FD events

Time interval used for this analysis was dictated by the period of operation of SOHO/ERNE device, which was commissioned in December 1995 (data available from June 1996) and is still operational. That coincides with the

beginning of solar cycle 23 and lasts through cycle 24, so we considered all FD events that occurred in this period, concentrating on events with magnitudes for 10GV particles larger 4% in the analysis. There are several reason for such magnitude cut, primary reason being that even though we often reference neutron monitor data in the analysis, CR related research in our laboratory is mainly based on muons detectors, which are generally less sensitive to FDs of smaller magnitude and GLE events. Additionally, it is known that all larger FDs (i.e. with magnitudes greater than 5%) are caused by CMEs (Belov, 2008). Since we use CME speed as a reference parameter in the analysis, introducing such cut made event selection simpler, as practically all considered FD events would have an associated CME. Finally, CME speed is less reliably determined in the case of weaker CME events (Yashiro et al., 2004).

One important step in the event selection procedure is to make sure that for each global event both proton flux increase detected by SOHO/ERNE and FD are related to the same CME. As mentioned in the introduction, detection of these separate events is not necessarily simultaneous. However, we have checked the direction of CMEs/ICMEs for all events for which such information was available, and in all these cases they moved directly toward Earth. This would imply that detection of the increase of energetic particles, Forbush decrease and geomagnetic storm associated with a given CME should be detectable within a relatively small time window. To illustrate this, on Fig. 1 we have shown time series for proton flux (in

one selected energy channel), CR flux and Dst index for one such event. Furthermore, because of large magnitudes of FDs selected for the analysis, we believe it to be the case for all events.

Another important point is that we cannot say with certainty what is the exact origin of detected proton flux solely based on SOHO/ERNE data. They could be of solar origin (SEP), particles accelerated locally at shock in interplanetary space (ESP), or combination of both. For the sake of simplicity we have decided to use the somewhat more general term SEP for these energetic particles, having mentioned limitation of its use in mind.

As determination of SEP fluence is not a straightforward procedure (as explained in more detail in Section 3.1), from the initial set of events we discarded all for which fluence value was difficult to determine or had a large uncertainty due to overlap and unclear separation of proton flux time series of successive events. That set was then further reduced based on the quality of FD identification flag assigned to each event in the IZMIRAN database, taking into account only events where identification was confident or reliable enough. Applying mentioned selection criteria resulted in the final set of 21 events, presented in Table 1 with some of the parameters of interest.

3. Parametrization of SEP fluence energy spectra

Parametrization procedure for any of the selected FD events can be broken down into two steps: 1 - calculation

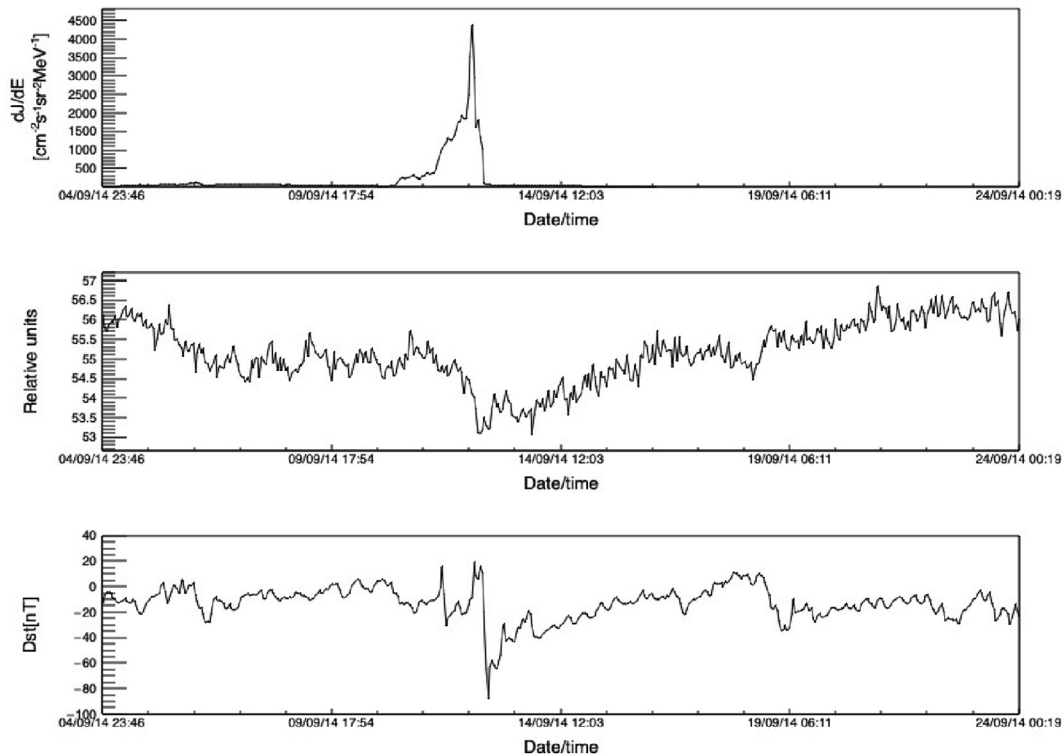


Fig. 1. Time series of hourly data for the same time interval around FD event of 12 September 2014: proton flux in the 1.3 – 1.6MeV channel (top), Athens neutron monitor count rate (middle), and Dst index (bottom).

Table 1

Forbush decrease events from solar cycles 23 and 24 selected for the analysis, along with some of the FD, CME and geomagnetic field parameters of interest.

Date/Time	M [%]	M_M [%]	X flare	V_{mean} [km s ⁻¹]	V_{meanC} [km s ⁻¹]	V_{max} [km s ⁻¹]	Kp_{max}	Ap_{max}	Dst_{min} [nT]
2001.09.29 09:40:00	4.3	4.4	M 1.0/	852.0	831	694.0	5.33	56.0	-56.0
2001.10.11 17:01:00	7.0	6.9	M 1.4/2F	766.0	769	572.0	6.0	80.0	-71.0
2001.10.21 16:48:00	5.4	7.3	X 1.6/2B	855.0	858	677.0	7.67	179.0	-187.0
2001.11.24 05:56:00	9.2	9.8	M 9.9/	1323.0	1366	1024.0	8.33	236.0	-221.0
2002.04.17 11:07:00	6.2	7.0	M 1.2/SF	742.0	745	611.0	7.33	154.0	-127.0
2002.09.07 16:36:00	4.6	5.1	C 5.2/SF	860.0	863	550.0	7.33	154.0	-181.0
2003.10.30 16:19:00	14.3	9.4	X10.0/2B	2109.0	2140	1876.0	9.0	400.0	-383.0
2003.11.20 08:03:00	4.7	6.8	M 3.2/2N	854.0	872	703.0	8.67	300.0	-422.0
2004.07.26 22:49:00	13.5	14.4	M 1.1/1F	1279.0	1290	1053.0	8.67	300.0	-197.0
2004.09.13 20:03:00	5.0	5.3	M 4.8/SX	945.0	948	613.0	5.33	56.0	-50.0
2005.05.15 02:38:00	9.5	12.2	M 8.0/SX	1207.0	1231	987.0	8.33	236.0	-263.0
2006.12.14 14:14:00	8.6	9.6	X3.4/4B	1154.0	1165	955.0	8.33	236.0	-146.0
2011.02.18 01:30:00	5.2	4.7	X2.2/	579.0	579	691.0	5.0	48.0	-30.0
2011.08.05 17:51:00	4.3	4.8	M 9.3/	1089.0	1104	611.0	7.67	179.0	-115.0
2011.10.24 18:31:00	4.9	6.5	-	-	633	516.0	7.33	154.0	-147.0
2012.03.08 11:03:00	11.7	11.2	X5.4/	1187.0	1188	737.0	8.0	207.0	-143.0
2012.07.14 18:09:00	6.4	7.6	X 1.4/	822.0	834	667.0	7.0	132.0	-127.0
2013.06.23 04:26:00	5.9	5.3	M 2.9/	832.0	844	697.0	4.33	32.0	-49.0
2014.09.12 15:53:00	8.5	5.9	X1.6/2B	893.0	897	730.0	6.33	94.0	-75.0
2015.06.22 18:33:00	8.4	9.1	M2.6/	1027.0	1040	742.0	8.33	236.0	-204.0
2017.09.07 23:00:00	6.9	7.7	X9.3/	-	1190	817.0	8.33	236.0	-124.0

of SEP fluence in different energy channels and 2 - determination of power exponents for SEP fluence spectra.

3.1. SEP fluence calculation

SEP fluence is calculated by integrating SOHO/ERNE proton flux time series in separate energy channels over time period associated with a given FD event. First step in this procedure is to determine this time period (and hence integration boundaries) as precisely as possible. Most more energetic events we considered for this analysis have a strong SF associated with them. This may lead to a complex picture, as FD event of interest often occurs in the middle of a turbulent period where additional FDs (sometimes associated with other CMEs) precede or follow it. As a consequence, clear separation of successive events and determination of optimal integration boundaries may not be simple nor straightforward. To make this procedure more reliable, we have used IZMIRAN database and neutron monitor data (courtesy of the Neutron Monitor Database ([Neutron Monitor Database, 2022](#))) in parallel with SOHO/ERNE proton time series, trying to identify prominent features in all three sources, so we could separate events of interest in all energy channels as clearly as possible.

Baseline for integration was determined based on a data interval of at least one (but preferably several) days, where proton flux was negligibly different from zero relative to the flux during the event. If possible, time interval before the event was taken for the calculation of baseline unless there was a preceding disturbance, in which case quiet interval following the event was taken instead. Integration of fluence for several selected SOHO/ERNE energy channels

for the event of 12 September 2014 is shown on [Fig. 2](#). Integration interval is indicated with vertical dashed lines and baseline value with a horizontal dashed line.

One interesting feature that can be observed in SOHO/ERNE data time series is that in some cases proton flux in the highest energy channels can dip below the baseline after the initial increase. For a number of events such behavior is even more pronounced, where in extreme cases it can happen that no flux increase is observed, but rather just the decrease. We believe this indicates that the highest energy channels have non-negligible contribution of low-energy cosmic rays, which can increase uncertainty for fluence calculation. We will refer to this again when discussing fluence spectra in [Section 3.2](#).

To make fluence calculation procedure more reliable we have assigned a quality flag to each event, based on our estimate of the uncertainty of integration, and decided on a quality cut we deemed acceptable for further analysis. As mentioned in [Section 2.3](#), 21 events have passed this criterion. Even then, for a number of events calculated fluence proved to be sensitive to small variations of integration boundaries, which makes it especially difficult to give a reliable estimate of the error for the integration procedure and should be kept in mind when discussing the results.

3.2. Determination of SEP fluence spectra power exponents

Fluence energy spectra for all selected events were formed using values for different energy channels, calculated as explained in the previous section. The choice of parameters to be used to describe their shape and characteristics depends on the analytic expression used to model

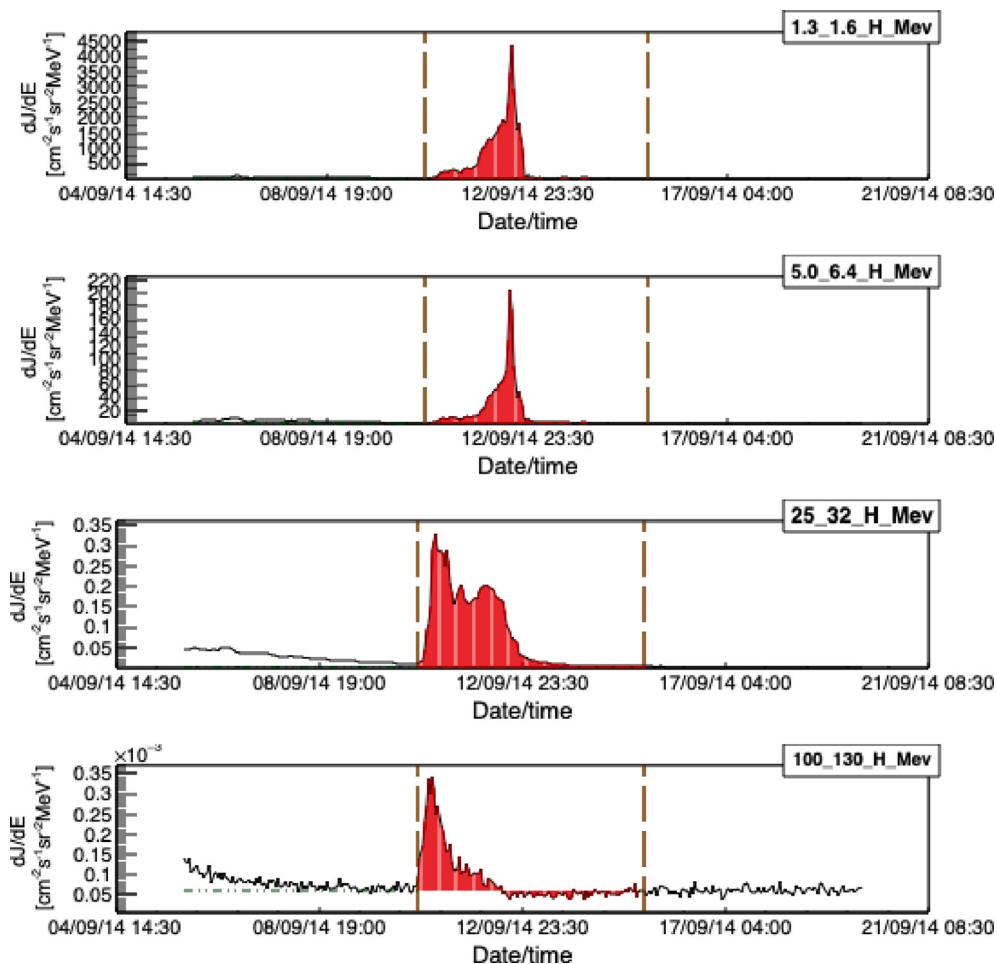


Fig. 2. Solar proton flux for four selected energy channels during FD event of 12 September 2014. Vertical dashed lines indicate integration interval, horizontal dashed line indicates the baseline value, while areas shaded red correspond to result of the integration used to calculate the SEP fluence.

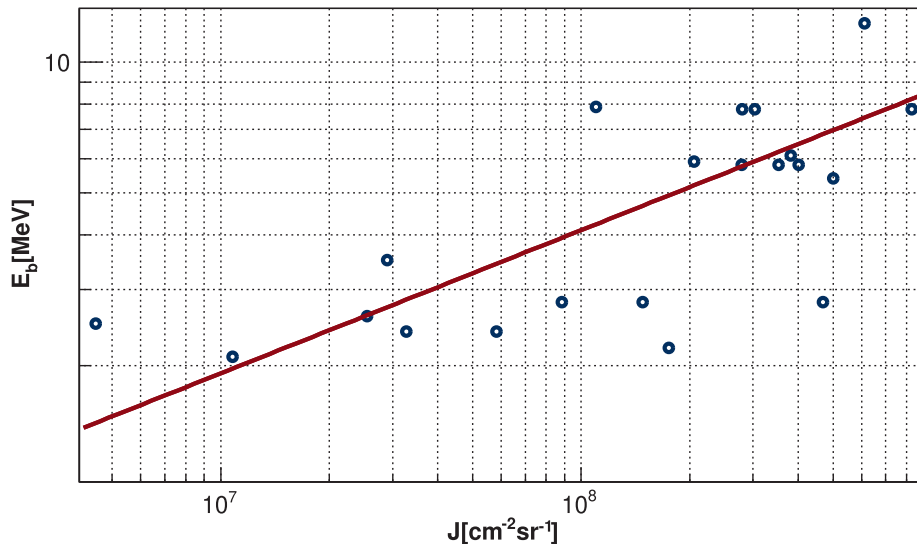


Fig. 3. "Knee" energy dependence on SEP fluence (integrated over full energy range) for selected events. Power function fit is indicated by the red line.

the spectrum. In general, during a SEP event spectra exhibit a characteristic “bend” or a “knee”, which is not so straightforward to describe theoretically. Various expressions were proposed to model this observed feature (Ellison and Ramaty, 1985; Mottl et al., 2001), out of which we have decided to use the following double power law one (Band et al., 1993; Zhao et al., 2016), as we feel it is well suited for our analysis:

$$\frac{dJ}{dE} = \begin{cases} E^{-\alpha} \exp\left(-\frac{E}{E_b}\right) & E \leq (\beta - \alpha)E_b, \\ E^{-\beta} [(\beta - \alpha)E_b]^{\beta - \alpha} \exp(\alpha - \beta) & E > (\beta - \alpha)E_b, \end{cases} \quad (1)$$

where E_b is knee energy at which the break occurs, while α and β are power-law exponents that describe energy ranges below and above the break respectively, and consequently are variables we chose to parametrize the SEP event.

These power-law exponents obtained by fitting fluence spectra with Expression 1 can be very sensitive to variation of knee energy, so some care needs to be taken in order to determine E_b as accurately as possible.

Determination of knee energy using “by eye” method proved to be uncertain enough for us to decide on using a more quantitative approach, which is based on the fact that knee energy generally depends on the integral fluence of the event (as described in Nymmik (2013) and Miroshnichenko and Nymmik (2014)). In accordance with this, we firstly determined the knee energy “by eye”, plotted it against integral fluence and then fitted this dependence with a power function in the form of $E_b = aJ^b$ (Fig. 3), where E_b is the knee energy, J integral fluence, and a and b are fit parameters. We then used these fit parameters to determine E_b for each event. In several cases where there has been some overlap of proton flux time series profiles associated with different successive events, small correction for integral fluence was introduced, which also affected the knee energy value.

Fluence spectra were then fitted with expression given in Eq. 1, using thusly calculated knee energy. On Fig. 4 we can see two characteristic examples that illustrate how well this expression actually models the fluence spectrum during a SEP event. In case of 11 October 2001 event (Fig. 4a) we see that the theoretical model fits the experimental data reasonably well, except for some small disagreement in the highest energy channels (feature we believe can be explained by our assumption that there is a non-negligible contribution of low-energy CR in this energy range). On the other hand, for a number of events with greater SEP flux higher energy channels tend to get saturated (as mentioned in Section 2.1). This in turn leads to an underestimated fluence and consequently poorer fit in this energy range, as can be seen for the 24 November 2001 event shown on Fig. 4b. Contribution of flux in these high-energy channels to integral fluence is very small, so this underestimated value does not significantly affect the value of knee energy or uncertainty of the exponent α . However,

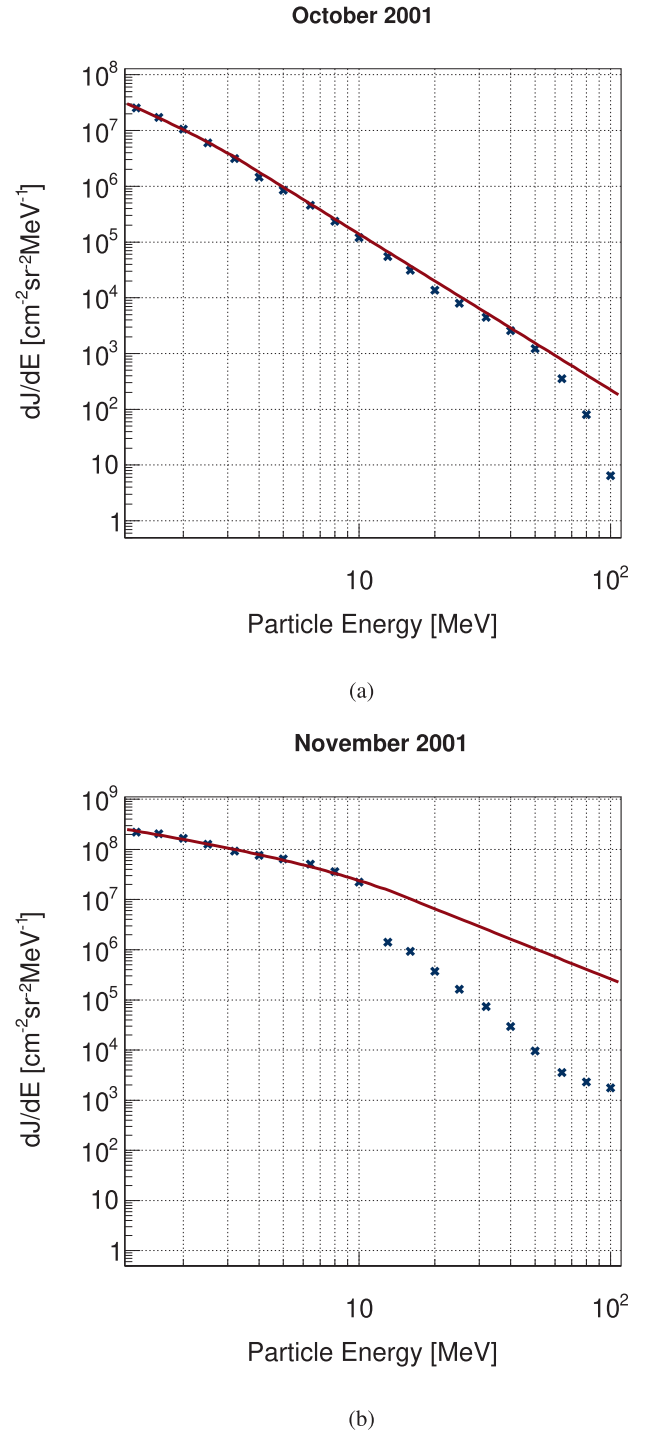


Fig. 4. SEP fluence energy spectra for the: (a) 11 October 2001 event, (b) 24 November 2001 event. Red lines indicate the double power law fit.

the uncertainty of exponent β is more significantly affected and for this reason in further analysis we will rely on exponent α more for the parametrization of fluence spectra.

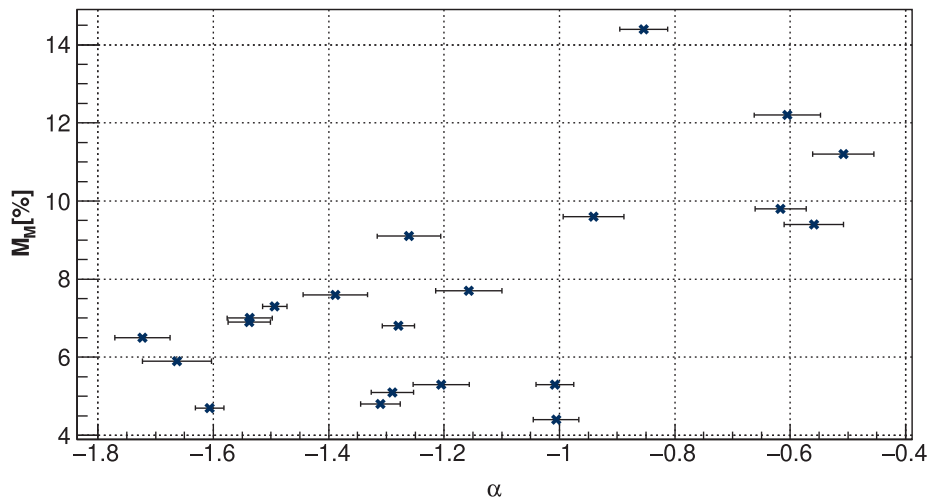
4. Correlative analysis

We have performed correlative analysis between power exponents chosen to parametrize SEP fluence and selected

Table 2

Correlation coefficients (r) between SEP fluence spectra power exponents and selected FD, CME and geomagnetic field indices.

	α	β	M	M_M	V_{meanC}	V_{mean}	V_{max}	Kp_{max}	Ap_{max}	Dst_{min}
α	1.00	0.96	0.67	0.64	0.77	0.75	0.66	0.40	0.53	-0.40
β	0.96	1.00	0.67	0.67	0.72	0.70	0.60	0.44	0.50	-0.38
M	0.67	0.67	1.00	0.84	0.79	0.79	0.79	0.53	0.65	-0.41
M_M	0.64	0.67	0.84	1.00	0.57	0.57	0.53	0.69	0.69	-0.46
V_{meanC}	0.77	0.72	0.79	0.57	1.00	1.00	0.92	0.61	0.77	-0.58
V_{mean}	0.75	0.70	0.79	0.57	1.00	1.00	0.92	0.62	0.78	-0.60
V_{max}	0.66	0.60	0.79	0.53	0.92	0.92	1.00	0.49	0.71	-0.58
Kp_{max}	0.40	0.44	0.53	0.69	0.61	0.62	0.49	1.00	0.94	-0.78
Ap_{max}	0.53	0.50	0.65	0.69	0.77	0.78	0.71	0.94	1.00	-0.87
Dst_{min}	-0.40	-0.38	-0.41	-0.46	-0.58	-0.60	-0.58	-0.78	-0.87	1.00

Fig. 5. Dependence of FD magnitude for particles with 10GV rigidity corrected for magnetospheric effects (M_M) on power exponent α .

parameters from Izmiran database. The results are presented in Table 2. Worth noting is the slightly lower statistics for V_{mean} due to exclusion of two events for which this parameter was not available.

Strong correlation between FD magnitude for particles with 10GV rigidity (M) and mean CME (V_{meanC} , V_{mean}) and maximum SW (V_{max}) velocities illustrates the important role these parameters have in driving FD events, as has been discussed in detail by several authors (i.e. Belov et al. (2014)). On the other hand, correlation between these velocities and parameter M_M is noticeably smaller. M_M is FD magnitude for particles with 10GV rigidity corrected for magnetospheric effect (using Dst index), so we could approximate it as an estimated measure of the FD magnitude in interplanetary magnetic field.

If we now look at how SEP fluence spectra power exponents relate to other parameters in Table 2, we observe the best correlation with mean CME velocities, while it is somewhat smaller with maximum SW velocity. Correlation with FD magnitude (M) is smaller than for CME velocities, however interestingly the correlation with the corrected FD magnitude (M_M) appears larger than in the case of CME velocities. One possible explanation for this could be that the shape of SEP fluence spectrum is more related to CR disturbance induced in interplanetary magnetic and less

to one induced in geomagnetic field. What could support this assumption further is the fact that we observe smaller correlation between α and β exponents and geomagnetic indices Kp_{max} , Ap_{max} and Dst_{min} than between these indices and CME velocities.

It should be said that even though SEP fluence spectra power exponents are not directly measured independent variables, the procedure to calculate them is relatively simple, while procedure used to calculate FD magnitudes (using GSM approach) is somewhat less straightforward and accessible. Hence, these exponents could be used to give a first estimate of Forbush decrease magnitudes outside atmosphere and magnetosphere. Having this in mind, we could conclude that SEP fluence power exponents could be better predictor variables (in the sense described above) of FD magnitude in interplanetary space than CME velocities are, while they are less reliable predictor variables of FD magnitude observed at Earth. If true, this could possibly lead us a small step closer to empirically decoupling the effects of IMF and geomagnetic fields on CR.

To further examine how FD magnitude corrected for magnetospheric effects is related to the shape of SEP fluence spectra, we have analyzed their dependence, which is plotted on Fig. 5. Both power exponents exhibit similar dependence, but only plot for α is shown, as it has consid-

Table 3

Correlation coefficients (r) between FD magnitudes for particles with 10GV rigidity (uncorrected M and corrected for magnetospheric effect M_M) and SEP fluence spectra power exponents, selected FD, CME and geomagnetic field indices for particles with $M_M \geq 6\%$ (left) and particles with $M_M < 6\%$ (right).

	$M_M \geq 6\%$					$M_M < 6\%$				
	α	β	V_{meanC}	V_{mean}	V_{max}	α	β	V_{meanC}	V_{mean}	V_{max}
M	0.82	0.76	0.84	0.85	0.78	-0.55	-0.25	-0.08	-0.10	0.62
M_M	0.77	0.76	0.52	0.49	0.55	-0.38	0.01	0.23	0.19	0.17

erably smaller uncertainty (as mentioned in Section 3.2) and we believe it to be a more reliable parameter. We can see that the graph is fairly linear, as could be expected based on the correlation coefficients, but on closer inspection it appears as if there are two separate classes of events with somewhat different behavior. If we loosely divide all FD events into low-magnitude set (with M_M less than 6%) and high-magnitude set (with M_M greater or equal to 6%), we can observe much weaker dependence of corrected FD magnitude on power exponent α for the first class than for the second one.

To check if this observation is well founded, we look into the correlation coefficients for these two separate classes, which are shown in Table 3.

We can see that correlation coefficients for these two sets are indeed very different. While in case of FDs with M_M equal or greater than 6% we observe an even larger correlation than before between power exponents α and β and both FD magnitude and corrected FD magnitude (approaching the values of correlation coefficients for CME velocities), coefficients for FDs with M_M less than 6% have very different values, correlation even being negative. Although statistics for this second set of events is rather small (and hence the uncertainty for correlation coefficients might be large), it appears that the assumption about two classes of events does stand. What is more, we observe a similarly drastic difference in correlation coefficients between FD magnitudes and mean CME velocities (with little to none correlation for events with $M_M < 6\%$), also pointing to the existence of two separate classes of events. This could need to be further confirmed using larger statistics, i.e. by including FD events with magnitudes smaller than 4%.

5. Conclusions

We analyzed the connection between CME, SEP and FD events, investigating how the shape of SEP fluence spectra during the global disturbance relates to different CME and FD parameters typically used in such analysis. We fitted SEP fluence spectra with double power law and used power exponents (α and β) from these fits to parameterize the shape of SEP fluence spectra.

By the means of correlative analysis we investigated the connection between SEP fluence spectra power exponents and selected CME and SW parameters (mean CME and maximum SW velocities), as well as selected FD parameters (magnitude for 10GV particles and magnitude for

10GV particles corrected for magnetospheric effect) and various parameters of geomagnetic activity (Kp , Ap and Dst indices).

We observed largest correlation between power exponents and CME velocities. The correlation between power exponents and FD magnitude (M) is significant yet smaller than in case of mean CME velocities (V_{meanC} , V_{mean}) and FD magnitude. On the other hand, the correlation between FD magnitude corrected for magnetospheric effects (M_M) and power exponents is larger than between these magnitudes and mean CME velocities.

The dependence of corrected FD magnitude on power exponent α possibly indicates two separate classes of events in terms of corrected magnitude value, rough boundary being corrected FD magnitude value of 6%. Events with corrected FD magnitude larger than 6% show increased correlation with power exponent α , while for the set of events with this magnitude smaller than 6% correlation even has opposite sign. Similarly considerable difference between two classes of events can be observed in correlations of mean CME velocities and corrected FD magnitude. Even taking into account smaller number of events used in the analysis, this could be an indication of these two groups of events exhibiting different behavior.

With everything considered, we believe we have demonstrated an important connection of the shape of SEP fluence spectra with CME and FD events, and that power exponents α and β can be valuable new parameters to be used in the future study of mentioned phenomena. They seem to be better predictor variables of FD magnitude (and hence CR disturbance) in interplanetary magnetic field than CME velocities, especially in the case of events where FD magnitude corrected for magnetospheric effect is larger than 6%.

Declaration of Competing Interest

The authors declare that they have no known competing financial interests or personal relationships that could have appeared to influence the work reported in this paper.

Acknowledgments

The authors acknowledge funding provided by the Institute of Physics Belgrade, through the grant by the Ministry of Education, Science and Technological Development of the Republic of Serbia.

OMNI data was made available by NASA/GSFC's Space Physics Data Facility's OMNIWeb service. Data from the SOHO experiment, an international collaboration between ESA and NASA, was kindly provided by ERNE team from Turku University, Finland. Neutron monitor data is available online through the use of excellent NEST tool, provided by the Neutron Monitor Database. We would also like to express our gratitude to the cosmic ray group at the IZMIRAN Space Weather Prediction Center at Pushkov Institute of Terrestrial Magnetism, Ionosphere and Radio Wave Propagation of the Russian Academy of Sciences for kindly providing catalogue of Forbush-effects and interplanetary disturbances.

Finally, we would like to thank the Reviewers for constructive comments and useful suggestions that significantly contributed to the quality of the manuscript.

References

- Alhassan, J.A., Okike, O., Chukwude, A.E., 2021. Testing the effect of solar wind parameters and geomagnetic storm indices on galactic cosmic ray flux variation with automatically-selected forbush decreases. *Res. Astron. Astrophys.* 21 (9), 234. <https://doi.org/10.1088/1674-4527/21/9/234>.
- Anastasiadis, A., Lario, D., Papaioannou, A., et al., 2019. Solar energetic particles in the inner heliosphere: status and open questions. *Philosoph. Trans. Roy. Soc. A: Mathe. Phys. Eng. Sci.* 377 (2148), 20180100. <https://doi.org/10.1098/rsta.2018.0100>, URL: <https://royalsocietypublishing.org/doi/abs/10.1098/rsta.2018.0100>.
- Badruddin, B., Aslam, O.P. M., Derouich, M. et al., 2019. Forbush decreases and geomagnetic storms during a highly disturbed solar and interplanetary period, 4–10 september 2017. *Space Weather*, 17(3), 487–496. URL: <https://agupubs.onlinelibrary.wiley.com/doi/abs/10.1029/2018SW001941>. <https://doi.org/10.1029/2018SW001941>.
- Band, D., Matteson, J., Ford, L., et al., 1993. BATSE Observations of Gamma-Ray Burst Spectra. I. Spectral Diversity. *Astrophys. J.* 413, 281–292. <https://doi.org/10.1086/172995>.
- Belov, A., 2008. Forbush effects and their connection with solar, interplanetary and geomagnetic phenomena. *Proc. Int. Astron. Union* 4 (S257), 439–450. <https://doi.org/10.1017/S1743921309029676>.
- Belov, A., Abunin, A., Abunina, M., et al., 2014. Coronal mass ejections and non-recurrent forbush decreases. *Sol. Phys.* 289, 3949–3960. <https://doi.org/10.1007/s11207-014-0534-6>.
- Belov, A., Baisultanova, L., Eroshenko, E., et al., 2005. Magnetospheric effects in cosmic rays during the unique magnetic storm on november 2003. *J. Geophys. Res.: Space Phys.* 110 (A09S20). <https://doi.org/10.1029/2005JA011067>.
- Belov, A., Eroshenko, E., Oleneva, V., et al., 2000. What determines the magnitude of forbush decreases? *Adv. Space Res.* 27 (3), 625–630. [https://doi.org/10.1016/S0273-1177\(01\)00095-3](https://doi.org/10.1016/S0273-1177(01)00095-3), URL: <https://www.sciencedirect.com/science/article/pii/S0273117701000953>.
- Belov, A., Eroshenko, E., Yanke, V., et al., 2018. The Global Survey Method Applied to Ground-level Cosmic Ray Measurements. *Sol. Phys.* 293 (4), 68. <https://doi.org/10.1007/s11207-018-1277-6>.
- Belov, A., Papaioannou, A., Abunina, M., et al., 2021. On the rigidity spectrum of cosmic-ray variations within propagating interplanetary disturbances: Neutron monitor and SOHO/EPHIN observations at ~1–10 GV. *Astrophys. J.* 908 (1), 5. <https://doi.org/10.3847/1538-4357/abd724>.
- Bruno, A., Richardson, I.G., 2021. Empirical model of 10–130 mev solar energetic particle spectra at 1 au based on coronal mass ejection speed and direction. *Sol. Phys.* 296 (36). <https://doi.org/10.1007/s11207-021-01779-4>.
- Cane, H., 2000. Coronal mass ejections and forbush decreases. *Space Sci. Rev.* 93 (1), 55–77. <https://doi.org/10.1023/A:1026532125747>.
- Desai, M., Giacalone, J., 2016. Large gradual solar energetic particle events. *Living Rev. Sol. Phys.* 13 (3). <https://doi.org/10.1007/s41116-016-0002-5>.
- Dumbovic, M., Vršnak, B., Calogovic, J., et al., 2012. Cosmic ray modulation by different types of solar wind disturbances. *A&A* 538, A28. <https://doi.org/10.1051/0004-6361/201117710>.
- Dumbovic, M., Vršnak, B., Guo, J., et al., 2020. Evolution of coronal mass ejections and the corresponding forbush decreases: Modeling vs. multi-spacecraft observations. *Sol. Phys.* 295 (104). <https://doi.org/10.1007/s11207-020-01671-7>.
- Ellison, D.C., Ramaty, R., 1985. Shock acceleration of electrons and ions in solar flares. *Astrophys. J.* 298, 400–408. <https://doi.org/10.1086/163623>.
- Freiherr von Forstner, J.L., Guo, J., Wimmer-Schweingruber, R.F., et al., 2020. Comparing the properties of icme-induced forbush decreases at earth and mars. *J. Geophys. Res.: Space Phys.* 125(3), e2019JA027662. URL: <https://agupubs.onlinelibrary.wiley.com/doi/abs/10.1029/2019JA027662>. <https://doi.org/10.1029/2019JA027662>. E2019JA027662 10.1029/2019JA027662.
- Gopalswamy, N., 2016. History and development of coronal mass ejections as a key player in solar terrestrial relationship. *Geosci. Lett.* 3 (8), 18. <https://doi.org/10.1186/s40562-016-0039-2>.
- Heber, B., Fichtner, H., Scherer, K., 2006. Solar and heliospheric modulation of galactic cosmic rays. *Space Sci. Rev.* 125 (1), 81–91. <https://doi.org/10.1007/s11214-006-9048-3>.
- IZMIRAN Space Weather Prediction Center, 2016. Izmiran space weather prediction center. URL: <http://spaceweather.izmiran.ru/eng/about.html> [Online; accessed 29-January-2022].
- Koldobskiy, S.A., Bindi, V., Corti, C., et al., 2019. Validation of the neutron monitor yield function using data from ams-02 experiment, 2011–2017. *J. Geophys. Res.: Space Phys.* 124 (4), 2367–2379. <https://doi.org/10.1029/2018JA026340>, URL: <https://agupubs.onlinelibrary.wiley.com/doi/abs/10.1029/2018JA026340>.
- Koldobskiy, S., Raukunen, O., Vainio, R., et al., 2021. New reconstruction of event-integrated spectra (spectral fluences) for major solar energetic particle events. *Astron. Astrophys.* 647, A132. <https://doi.org/10.1051/0004-6361/202040058>.
- Lingri, D., Mavromichalaki, H., Belov, A., et al., 2016. Solar activity parameters and associated forbush decreases during the minimum between cycles 23 and 24 and the ascending phase of cycle 24. *Sol. Phys.* 291, 1025–1041. <https://doi.org/10.1007/s11207-016-0863-8>.
- Melkumyan, A., Belov, A., Abunina, M., et al., 2019. On recurrent Forbush Decreases. In: Lagutin, A., Moskalenko, I., Panasyuk, M. (Eds.), *Journal of Physics Conference Series*, IOP Publishing, Bristol, United Kingdom volume 1181 of *Journal of Physics Conference Series*. p. 012009, <https://doi.org/10.1088/1742-6596/1181/1/012009>.
- de Mendonça, R.R. S., Braga, C.R., Echer, E., et al., 2016. The temperature effect in secondary cosmic rays (Muons) observed at the ground: analysis of the global muon detector network data. *Astrophys. J.* 830(2), 88. <https://doi.org/10.3847/0004-637x/830/2/88>.
- Miroshnichenko, L., Nymmik, R., 2014. Extreme fluxes in solar energetic particle events: Methodological and physical limitations. *Radiation Measur.* 61, 6–15. <https://doi.org/10.1016/j.radmeas.2013.11.010>, URL: <https://www.sciencedirect.com/science/article/pii/S1350448713003806>.
- Miteva, R., Samwel, S.W., Zabunov, S., et al., 2020. On the flux saturation of SOHO/ERNE proton events. *Bulgarian Astron. J.* 33, 99.
- Mottl, D.A., Nymmik, R. A., Sladkova, A.I., 2001. Energy spectra of high-energy SEP event protons derived from statistical analysis of experimental data on a large set of events. In: El-Genk, M.S., Bragg, M.J. (Eds.), *Space Technology and Applications International Forum - 2001*, AIP Publishing LLC., New York volume 552 of *American Institute of Physics Conference Series*, pp. 1191–1196, <https://doi.org/10.1063/1.1358071>.

- Neutron Monitor Database, 2022. Neutron Monitor Database. URL: <https://www.nmdb.eu/>.
- Nymmik, R., 2013. Charge states of heavy ions, as determined from the parameters of solar energetic particle spectra. *Bull. Russian Acad. Sci.: Phys.* 77, 490–492. <https://doi.org/10.3103/S1062873813050419>.
- Paassilta, Miikka, Raukunen, Osku, Vainio, Rami, et al., 2017. Catalogue of 55–80 mev solar proton events extending through solar cycles 23 and 24. *J. Space Weather Space Clim.* 7, A14. <https://doi.org/10.1051/swsc/2017013>.
- Papaioannou, A., Belov, A., Abunina, M., et al., 2020. Interplanetary coronal mass ejections as the driver of non-recurrent forrush decreases. *Astrophys. J.* 890 (2), 101. <https://doi.org/10.3847/1538-4357/ab6bd1>.
- Reames, D.V., 1999. Particle acceleration at the sun and in the heliosphere. *Space Sci. Rev.* 90 (3), 413–491. <https://doi.org/10.1023/A:1005105831781>.
- Richardson, I.G., Cane, H.V., 2011. Galactic Cosmic Ray Intensity Response to Interplanetary Coronal Mass Ejections/Magnetic Clouds in 1995–2009. *Sol. Phys.* 270 (2), 609–627. <https://doi.org/10.1007/s11207-011-9774-x>.
- Subramanian, P., Antia, H.M., Dugad, S.R., et al., 2009. Forrush decreases and turbulence levels at coronal mass ejection fronts. *A&A* 494 (3), 1107–1118. <https://doi.org/10.1051/0004-6361:200809551>.
- Torsti, J., Valtonen, E., Lumme, M., et al., 1995. Energetic particle experiment erne. *Sol. Phys.* 162 (1–2), 505–531. <https://doi.org/10.1007/BF00733438>.
- Valtonen, E., Lehtinen, I.-V., 2009. Solar energetic particle fluences from soho/erne. *Acta Geophys.* 57, 116–124. <https://doi.org/10.2478/s11600-008-0056-4>.
- Veselinovic, N., Dragic, A., Savić, M., et al., 2017. An underground laboratory as a facility for studies of cosmic-ray solar modulation. *Nucl. Instrum. Methods Phys. Res. Section A: Accelerat. Spectromet. Detectors Assoc. Equip.* 875, 10–15. URL: <https://www.sciencedirect.com/science/article/pii/S0168900217309634>. <https://doi.org/10.1016/j.nima.2017.09.008>.
- Veselinovic, Nikola, Savić, Mihailo, Dragic, Aleksandar, et al., 2021. Correlation analysis of solar energetic particles and secondary cosmic ray flux. *Eur. Phys. J. D* 75 (6), 173. <https://doi.org/10.1140/epjd/s10053-021-00172-x>.
- Veselinović, N., Dragić, A., Maletić, D., et al., 2015. Cosmic rays muon flux measurements at Belgrade shallow underground laboratory. In: Trache, L., Chesneanu, D., Alexandru Ur, C. (Eds.), *Exotic Nuclei and Nuclear/Particle Astrophysics (V) From Nuclei to Stars: Carpathian Summer School of Physics 2014*, AIP Publishing LLC., New York volume 1645 of American Institute of Physics Conference Series, pp. 421–425. <https://doi.org/10.1063/1.4909614>.
- Yashiro, S., Gopalswamy, N., Michalek, G., et al., 2004. A catalog of white light coronal mass ejections observed by the soho spacecraft. *J. Geophys. Res.: Space Phys.* 109 (A7). <https://doi.org/10.1029/2003JA010282>.
- Zhao, L., Zhang, M., Rassoul, H.K., 2016. Double power laws in the event-integrated solar energetic particle spectrum. *Astrophys. J.* 821 (1), 62. <https://doi.org/10.3847/0004-637x/821/1/62>.



Article

Impacts of Extreme Space Weather Events on September 6th, 2017 on Ionosphere and Primary Cosmic Rays

Aleksandra Kolarski, Nikola Veselinović, Vladimir A. Srećković, Zoran Mijić, Mihailo Savić and Aleksandar Dragić

Special Issue

Space Weather: Observations and Modeling of the Near Earth Environment II

Edited by

Dr. Saioa A. Campuzano and Dr. Dario Sabbagh





Article

Impacts of Extreme Space Weather Events on September 6th, 2017 on Ionosphere and Primary Cosmic Rays

Aleksandra Kolarski , Nikola Veselinović , Vladimir A. Srećković , Zoran Mijić * , Mihailo Savić
and Aleksandar Dragić

Institute of Physics Belgrade, University of Belgrade, Pregrevica 118, 11080 Belgrade, Serbia

* Correspondence: zoran.mijic@ipb.ac.rs; Tel.: +381-11-3713134

Abstract: The strongest X-class solar flare (SF) event in 24th solar cycle, X9.3, occurred on 6 September 2017, accompanied by earthward-directed coronal mass ejections (CMEs). Such space weather episodes are known to cause various threats to human activities ranging from radio communication and navigation disturbances including wave blackout to producing geomagnetic storms of different intensities. In this study, SFs' ionospheric impacts and effects of accompanied heliospheric disturbances on primary cosmic rays (CR) are investigated. This work offers the first detailed investigation of characteristics of these extreme events since they were inspected both from the perspective of their electromagnetic nature, through very low frequency (VLF) radio waves, and their corpuscular nature of CR by multi-instrumental approach. Aside data recorded by Belgrade VLF and CR stations, data from GOES and SOHO space probes were used for modeling and analysis. Conducted numerical simulations revealed a significant change of ionospheric parameters (sharpness and effective reflection height) and few orders of magnitude increase of electron density. We compared our findings with those existing in the literature regarding the ionospheric response and corresponding parameters. In addition, Forbush decrease (FD) magnitude, corrected for magnetospheric effect, derived from measurements, and one predicted from power exponents used to parametrize the shape of energetic proton fluence spectra at L1 were compared and found to be in good agreement. Presented findings could be useful for investigation of atmospheric plasma properties, particles' modeling, and prediction of extreme weather impacts on human activities.

Keywords: solar flares; coronal mass ejections; atmospheric ionization; sudden ionospheric disturbances; ionospheric parameters; solar energetic particles; secondary cosmic ray flux; Forbush decreases



Citation: Kolarski, A.; Veselinović, N.; Srećković, V.A.; Mijić, Z.; Savić, M.; Dragić, A. Impacts of Extreme Space Weather Events on September 6th, 2017 on Ionosphere and Primary Cosmic Rays. *Remote Sens.* **2023**, *15*, 1403. <https://doi.org/10.3390/rs15051403>

Academic Editors: Dario Sabbagh and Saioa A. Campuzano

Received: 17 January 2023

Revised: 23 February 2023

Accepted: 28 February 2023

Published: 2 March 2023



Copyright: © 2023 by the authors. Licensee MDPI, Basel, Switzerland. This article is an open access article distributed under the terms and conditions of the Creative Commons Attribution (CC BY) license (<https://creativecommons.org/licenses/by/4.0/>).

1. Introduction

As an important aspect of space weather applications, ionospheric responses to intense solar flares (SFs) and coronal mass ejections (CMEs) have been investigated for several decades [1–3]. Short in duration but huge explosive events on the Sun release high-energy particles and intense broad range radiation influencing the state of the Earth's upper atmosphere. While enhanced EUV radiation disturbs E and F regions of the ionosphere, during solar flares, X-ray radiation can increase by several orders of magnitude and cause an extra ionization within the ionospheric D-layer [4,5]. The increase in the rate of change of atmospheric ionization depends on both the flare class and the rate of change in flare radiations [6]. For the investigation of D-region behavior, radio wave measurements at very low and low frequencies (VLF-LF) are widely used [7–9]. SFs have a direct radio wave interference effect on Global Navigation Satellite System (GNSS) transmission and other radio systems [10–12]. High-frequency (HF) radio wave blackout and magnetic field variation have also been documented and studied [11,13].

Solar activity can produce extreme phenomena which are more likely around the maximum of the 11-year cycle. One such type of events are SFs that are, in most cases, followed by CMEs [14]. CME releases a large-scale flux of charged particles from solar

corona with an accompanying embedded magnetic field. This additional flux of charged particles emerging in interplanetary space is defined as interplanetary coronal mass ejection (ICME). When propagating with speed greater than magnetosonic wave speed (in solar wind reference frame), ICME can form a shock due to interaction with ambient solar wind. In situ measurements of the environment performed by space probes at different locations in the heliosphere can provide information about various solar weather parameters. They also include direct measurements of fast-moving energetic particles that can be in temporal correlation with CMEs and SFs [15]. These particles can originate from the Sun, in which case they are called solar energetic particles (SEPs) or can be accelerated locally by an ICME related shock when they are referred to as energetic storm particles (ESPs). Several space probes placed at Lagrange point 1 (L1) between the Sun and the Earth constantly monitor this flux, in addition to a number of probes at Earth's vicinity and elsewhere throughout the heliosphere [16]. Enhancement of interplanetary magnetic field (IMF) creates additional modulation of cosmic ray (CR) and can lead to one of the transient phenomena, Forbush decrease (FD). FD is a rapid depression of measured CR flux (typically occurring within a day), followed by a gradual recovery that can last for several days [17]. Correlation between FD parameters (magnitude of decrease, duration, time evolution) and various parameters of solar wind plasma have been studied in the past [18–20].

Extreme space weather events can have severe impacts on wide areas of human activities. Historically, such events are not very frequent, but the probability of their occurrence over the next decade is not negligible (i.e., for geomagnetic storms, it has been estimated to be about 12% [21]). Extreme events can cause significant damage to sensitive satellite components and increase absorbed radiation dose in space, which can pose a serious health hazard to astronauts. Energetic particle flux during extreme solar activity events is studied and different models of the space environment are proposed for forecasting schemes. Even though many studies have been carried out, still, only limited information is available on an approximate assessment of the direct impact such events can have on technological infrastructure and what the indirect associated expenses would be [22].

Study of ionospheric reaction to SFs is currently very relevant research, given the prospect of improving the capacity and reliability of anticipating space weather disturbances, which might affect the performance of a wide range of space-borne and ground-based technological systems and pose a danger to human health and safety [23,24].

The 24th solar cycle began in December 2008 and although approaching the solar minimum and the low solar activity, several strong SFs occurred in September 2017, including the X9.3 class flare, the strongest one in that cycle [25,26]. A lot of studies have been published analyzing different aspects of these extreme weather events. The SF effect on the chemical structure of the upper and middle atmosphere is reported in [27]. In the study presented in [28], the analysis of total electron content (TEC) and rate of change of TEC index to probe the storm-time ionospheric TEC irregularities in the Indian longitude sector during the space weather events of 6–10 September 2017 was presented. During the flares, the total radio fade-out in the range of 30 to 90 min at the Hermanus and Sao Luis ionosondes is reported [29]. It is also observed that SFs' effects on the ionosphere last longer than the effects on the Earth's magnetic field [30]. The effects of the strong X9.3 flare of 6 September 2017, following its impact on the ionosphere and the resulting difficulties for existing (e.g., precise positioning and GNSS navigation support services) and future technologies (e.g., autonomous car navigation) have been analyzed [10].

In this paper, X-class SFs of 6 September 2017 ionospheric impacts and the effects of accompanied heliospheric disturbances on primary cosmic rays are investigated. The atmospheric D-region parameters and electron density are obtained and analyzed along with various heliospheric parameters (associated with the accompanying ICME) measured in-situ at L1, as well as flux of secondary cosmic ray muons measured on the ground and shallow-underground levels. Since all empirical models are based upon data obtained through numerous studies, such as International Reference Ionosphere model [31], each

case study of extreme weather events is of great significance, not only for the atmospheric plasma properties investigations, but also for the particles' modeling procedures. With that goal, modulation of ionosphere and CR flux by intense X-class SF events was investigated through a multi-instrumental approach, by employing space- and ground-based observations on one hand, and by conducting proposed numerical simulations on the other hand, using both original VLF and CR measurements (from the same location in Belgrade) as well as data and results from other observing stations worldwide. Through extensive comparison, noticed agreements and disagreements between results are highlighted as well.

2. Materials and Methods

Galactic cosmic rays interact with interplanetary magnetic fields as they traverse our solar system. IMF is a solar magnetic field carried by the solar wind, a stream of charged particles propagating outward from the Sun. Interaction of CRs with IMF modulates CR flux as is also evident from measurements of CR flux intensity with Earth-based CR detectors [32]. Galactic cosmic rays, upon reaching Earth, interact with atmospheric atoms and molecule nuclei, generating a shower of secondary particles. Secondary CRs vertical flux, at the bottom of the atmosphere (at atmospheric depth 1000 g cm^{-2}), for particles' energies larger than 1 GeV, is composed mainly of muons ($\approx 90 \text{ m}^{-2} \text{ s}^{-1} \text{ sr}^{-1}$), protons and neutrons ($\approx 2 \text{ m}^{-2} \text{ s}^{-1} \text{ sr}^{-1}$), electrons and positrons ($\approx 0.2 \text{ m}^{-2} \text{ s}^{-1} \text{ sr}^{-1}$), and charged pions ($\approx 0.04 \text{ m}^{-2} \text{ s}^{-1} \text{ sr}^{-1}$) as well as neutrinos [33]. Observation of these secondary CRs can be conducted in the atmosphere, on the ground or even underground, detecting one or several different types of produced particles. A worldwide network of neutron monitors (NM) and ground detectors that detect hadronic components of secondary CRs have been in use for decades. NMs are sensitive to primary CRs with energies of about 0.5–20 GeV. Another type of widely used Earth-based CR detectors are muon monitors, focused on detecting the muon component of secondary CRs. Muon monitors are sensitive to higher energies of primary CRs, thus complementing NMs measurements [34].

Belgrade CRs station is a part of the Low-background Laboratory for Nuclear Physics (LBLNP) at the Institute of Physics Belgrade (IPB), Serbia. It has two identical detector set-ups placed on two different levels, one on ground level (GLL) and the other in shallow-underground (UL). Underground level is situated below 12 m of loess overburden (25-m water equivalent). This setup allows for monitoring of secondary CR's muons flux that originates from two different energy ranges under the same environmental conditions (such as geomagnetic location, atmospheric parameters, experimental setup). Altitude of the station is 78 m above sea level, with a geomagnetic latitude of $39^{\circ}32' \text{ N}$. Relation between the measured count rate of these energy-integrating detectors with flux of primary CRs at the top of the atmosphere was found using a calculated detector yield function. Additionally, due to the sensitivity of secondary muons to varying properties of the atmosphere, which acts as a moderator, correction of measured flux for atmospheric pressure and variation of temperature throughout the whole atmospheric column from the top of the atmosphere to the ground is needed. Details of the detector systems and response function of Belgrade CR station acquired using Monte Carlo simulation of CR transport, along with the description and results of atmospheric and efficiency corrections are presented in [35,36].

For inspection of the Earth's lower ionospheric response to intense solar activity during events of energetic solar outbursts (such as SFs and CMEs) during the descending branch of the 24th solar cycle, as in September 2017, VLF radio signal registrations from Belgrade's (BEL; 44.85° N , 20.38° E) Absolute Phase and Amplitude Logger (AbsPAL) station database were used. This system is a part of the Laboratory for Astrophysics and Physics of Ionosphere at the IPB, Serbia. Numerical simulations conducted in this paper rely on application of the well known and widely exploited technique of Long Wavelength Propagation Capability (LWPC) software [37] utilization on one hand, based on hop wave theory and the ionospheric exponential model [38,39], and on the FlarED' Method and Approximate Analytic Expression application [5,40] on the other hand: the novel approach based on retrieving ionospheric parameters directly from solar X-ray radiation spectral

components of soft range. Here, novel approach is applied on two cases of SF events within the strongest X-class (the weaker X2.2 and stronger X9.3), making the validation of the proposed approximate method firmly applicable and reliable across the entire X-class range, in addition to some previous recent research all regarding cases of weaker X-class SFs from the lower section of X-class range [5,8,40]. The methodology used relies on simultaneous monitoring of several VLF signals during regular and irregular ionospheric conditions, both for amplitude and phase, and obtaining properties of perturbations directly from observed recorded VLF data, by signal values' comparison between unperturbed and perturbed states. The details are presented in Section 3.2 and Supplementary Material.

3. Results

3.1. Solar Energetic Particles and Secondary Cosmic Ray Flux during and after Intense SF Events

The strongest flare of solar cycle 24 (classified as X9.3) happened in early September 2017 during the declining phase of this solar cycle. Active region AR12673 [41] was the cause of unusual and intensive solar activity. This region produced several more SFs around that time with the most intense one occurring on 6 September 2017. The flare was closely followed by a severe geomagnetic storm that began on 7 September. In total, four different possibly related CMEs erupted within several days. The first of these was a halo CME that happened on 4 September which, together with the second one, affected CR flux and produced an intense Forbush decrease on 7 September. Magnitude of FD for 10 GV rigidity primary CR corrected for magnetospheric effect (M_M) [18] was -7.7% (quoted from IZMIRAN database of FD parameters [42]).

Solar activity and the accompanying heliospheric disturbance during early September 2017 have been studied in detail in a number of published articles that indicate that successive CMEs between 4–6 September produced complex transients. Complex interactions caused by the passage of ICME are not so simple to model, one consequence being that it is not so straightforward to predict time of arrival of the disturbance on Earth [43]. However, in-situ measurements by space probes at L1 can help in this regard. Based on data from Solar and Heliospheric Observatory (SOHO)/Large Angle and Spectrometric Corona-graph (LASCO)/C2 [44] and analysis given in [45], the first CME from AR12673 with a moderate speed of approximately 710 km s^{-1} appeared on 4 September followed by a much faster (approx. 1350 km s^{-1}) second CME. These two CMEs merged in lower solar corona into a single structure producing single shock followed by a prolonged sheath region which was detected at L1 on 6 September. The second shock arrived at L1 on 7 September as a result of CME that occurred on 6 September. This CME had a high velocity of 1480 km s^{-1} and its eruption coincides with the X9.3 SF. This shock was followed by a turbulent sheath region and a magnetic cloud. One repository where such measurements can be found compiled in the form of low- and high-resolution OMNI data can be found at GSFC/Space Physics Data Facility [46]. Low-resolution OMNI data (used in this study) contains hourly values for various heliospheric and geomagnetic indices. One of the probes that monitors variation of energetic proton flux at L1 is the ERNE instrument onboard SOHO probe [47]. It consists of two separate particle detectors with complementing detector energy ranges (for lower and higher particle energies) and provides energetic particle flux measurements in 20 energy bins (ranging from 1.3 up to 130 MeV per nucleon) with a time resolution of one hour (data are available at [48]). Apart from providing insight into SF/CME/ICME induced disturbance in the heliosphere, measurements done by this instrument could be useful for predicting the effects that these phenomena have on cosmic rays, as some studies have shown [49]. Proton flux recorded during early September 2017 is showed in Figure 1 and Figures S1 and S2 in Supplementary Material. As it is often difficult to determine the acceleration mechanism related to violent events on the Sun (especially when accelerated particles are detected near Earth), for the sake of simplicity, going forward, we will refer to both solar energetic particles (accelerated near the Sun) and energetic storm particles (accelerated in interplanetary space) as SEP.

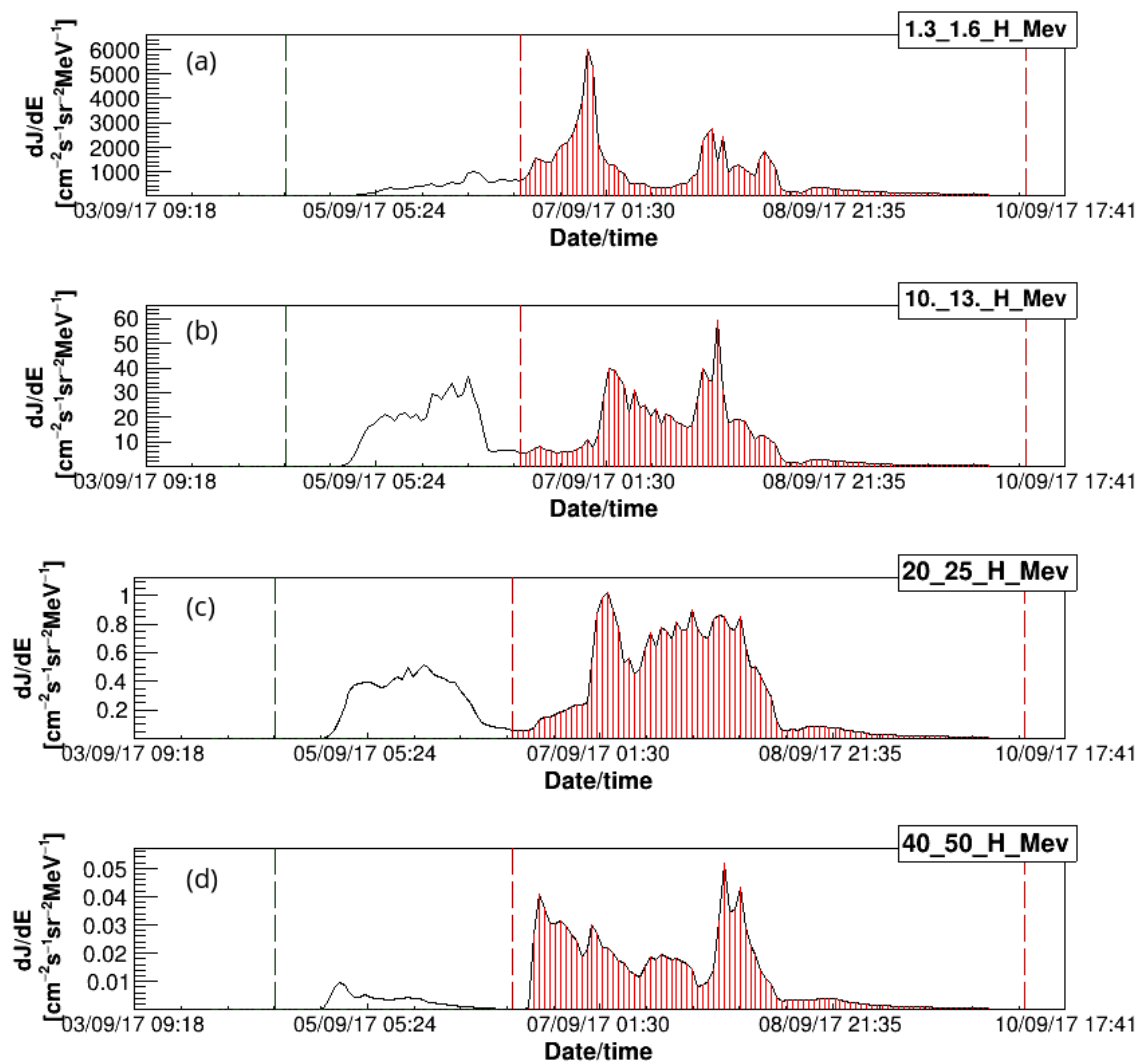


Figure 1. Hourly time series (UT) for several different proton channels from SOHO/ERNE ((a) 1.3–1.6 MeV, (b) 10–13 MeV, (c) 20–25 MeV, (d) 40–50 MeV channels' energy bands) for September 2017. Integration interval for spectral fluence is indicated with red vertical dashed lines.

In order to determine SEP fluence related to heliospheric disturbances and FD events during early September 2017, integration of SOHO/ERNE proton flux time series in separate energy channels is needed over the time period associated with a given FD event. Determination of this time period during complex solar activity in September 2017 is not simple or straightforward. Using procedures described in [36] that rely on the IZMIRAN database, as well as neutron monitor data and data measured at Belgrade muon station, we can determine optimal integration intervals more reliably.

Generally, SEP fluence spectrum exhibits a change of slope (sometimes referred to as a “knee”). Several different models are proposed to describe this characteristic shape [50–52]. We chose to use the double power law proposed in [53] given by Equation (1):

$$f(E) = \begin{cases} E^{-a} \exp\left(-\frac{E}{E_k}\right), & E < (b-a)E_k \\ E^{-b} [(b-a)E_k]^{b-a} \exp(a-b), & E > (b-a)E_k \end{cases} \quad (1)$$

where E is the particle energy, E_k is the “knee” energy (at which the break in the spectrum occurs), a and b are power exponents related to energy ranges below and above E_k , respectively. Exponents a and b are determined by fitting the proton fluence spectrum using Equation 1 and are used to parameterize its shape. E_k is set as a fixed parameter and

is determined from the known dependence of “knee” energy on integral fluence. More detailed description of the procedure can be found in [49]. The shape of fluence spectrum and fitted double power law for the September event are shown in Figure 2. Obtained values were -1.16 for exponent a and -2.5 for exponent b (taking 6.8 MeV as value for “knee” energy).

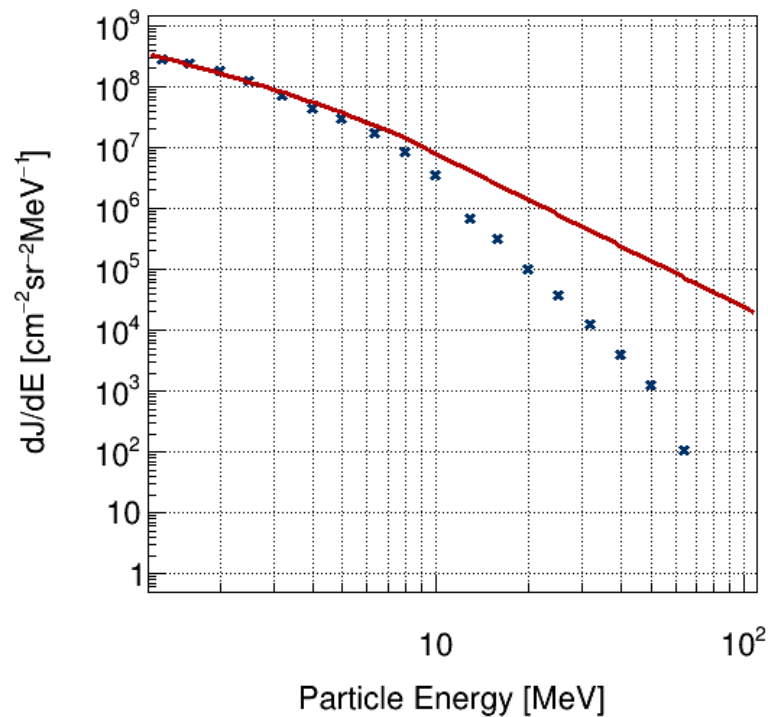


Figure 2. Fluence spectrum for energetic protons measured by SOHO/ERNE at L1 during FD in September 2017. Data points represent fluence integrated in different energy channels over time of duration of the event, while red line represents the fitted double power law.

Observed underestimate of fluence in higher energy channels can be explained by the assumption that there are contributions of low energy CR in these energy ranges that are suppressed with additional heliospheric disturbance and can be more pronounced for more extreme solar activity events. Additionally, this discrepancy between model and measured fluence can be due to saturation of high energy channels during events with greater SEP flux [54].

Contribution of these higher energy channels to integral flux is rather small and it does not significantly affect total flux, however, it does add to higher uncertainty of b , which is why this exponent is seldom used in analysis. Based on the established correlation between a exponent and FD magnitude corrected for magnetospheric effect [49], an estimated value of 8.3% was obtained for M_M , which is in reasonably good agreement with the value found in the IZMIRAN database. Large disturbances in the heliosphere in early September 2017 that cause large FD are part of a complex event that can lead to disturbance in the magnetosphere and primary CR flux variability, but also influence dynamic processes in the ionosphere.

3.2. Monitoring Low Altitude Mid-Latitude Ionosphere during intense SF events

Monitoring of the mid-latitude ionospheric D-region (50–90 km) from BEL station during September 2017 were simultaneously conducted for all VLF signals recorded by the AbsPAL system. Geographical position of BEL VLF system and the VLF transmitters (GQD/22.10 kHz, Anthorn UK and TBB/26.70 kHz, Bafa Turkey) are given in Figure S3. Both shown signals are of short great circle paths (GCPs) propagating mostly over land. In general, the GQD signal arrives to Belgrade from the north, in NW-SE direction, with

GCPGQD = 1982 km covering almost two time zones, while TBB signal arrives from the south, in SE-NW direction, with GCPTBB = 1020 km covering one time zone (Table 1). Corresponding incident solar X-ray flux data were obtained from the Geostationary Operational Environmental Satellite (GOES) database [55].

Table 1. VLF transmitting sites.

	Freq. (kHz)	Country	Latitude (°)	Longitude (°)	GCP (km)	Prop. Path Direction
Transmitter:						
GQD	22.10	UK	54.73 N	2.88 W	1982	NW to SE
TBB	26.70	Turkey	37.43 N	27.55 E	1020	SE to NW

We studied data from 6 September 2017 belonging to the descending branch of the 24th solar cycle, with the strongest SF event X9.3 reported during the last solar cycle and the earth-directed CME which produced FD. September 2017 was the most active month during 2017, with a total of 99 SFs reported, of which there were 68 C, 27 M, and four X class events. During 6 September 2017, there were seven SFs reported in total, of which there were two C, three M, and two X-class SFs. Such intense solar activity significantly affected Earth's lower ionosphere, which can be clearly observed both as amplitude and phase perturbations on sub-ionospheric propagating VLF signals and was documented on BEL AbsPAL recordings. The two strongest SFs reported on 6 September 2017, i.e., X2.2 and X9.3—overall the strongest SF from the last solar cycle, as observed on GQD and TBB signal traces, practically occurred during the established stable daytime ionospheric conditions, when both traces were entirely sunlit. BEL GQD data during the entire day of 6 September 2017, with the accompanying incident solar X-ray flux from soft spectral range (0.1–0.8 nm) are given in Figure S4. As the best representative quiet day, 3 September 2017 was chosen. As observed on GQD signal, solar-induced sudden ionospheric disturbances (SIDs) are denoted by black arrows accompanied with the time of each SF event's occurrence in UT. Both amplitude and phase perturbation follow the SF events' evolution, with time delays corresponding to the sluggishness of the ionosphere [56]. Oscillatory character of the perturbations characteristic for GQD signal registered by BEL station, can still be recognized on the signal's phase, especially in the case of the weaker SF, while in the case of the amplitude, this feature is no longer observable mostly due to inducing SF's intensity [5,7,57–59]. Although these two SF occurred back-to-back, it is possible to determine individual contributions of each SF on signal recordings. It can be stated that, although these SFs strongly impacted the Earth-ionosphere waveguide for several hours, as observed from BEL station, the mid-latitude lower ionosphere fully recovered and went back to its regular conditions. Preflare ionospheric state can be treated as quiet.

Comparison between GQD and TBB signal recordings, arriving from opposite directions to the BEL station, but both of short GCPs, is given in Figure 3, as an enlarged section related to time evolution of X2.2 and X9.3 SFs.

Amplitude change in both signals is of similar behavior, simply following the incident solar X-ray radiation, with similar relative change in the amplitude amount compared to unperturbed conditions $\Delta A \approx 7$ dB. However, in the case of the TBB signal, there is a more rapid decreasing trend after the peak value corresponding to the maximal amplitude change in both SF cases. In the case of the GQD signal, relative change in the phase amount compared to unperturbed conditions ΔPh (°) is several tens of degrees, with still recognizable oscillatory behavior characteristic for BELGQD. Unfortunately, in the case of the TBB signal, phase data were unusable so that further analysis, neither qualitative nor quantitative and neither any of the numerical simulations, were not possible to conduct. The TBB signal recordings given are purely interesting from the point of view of amplitude comparison with the GQD signal, with total opposite GCPs as recorded in Belgrade.

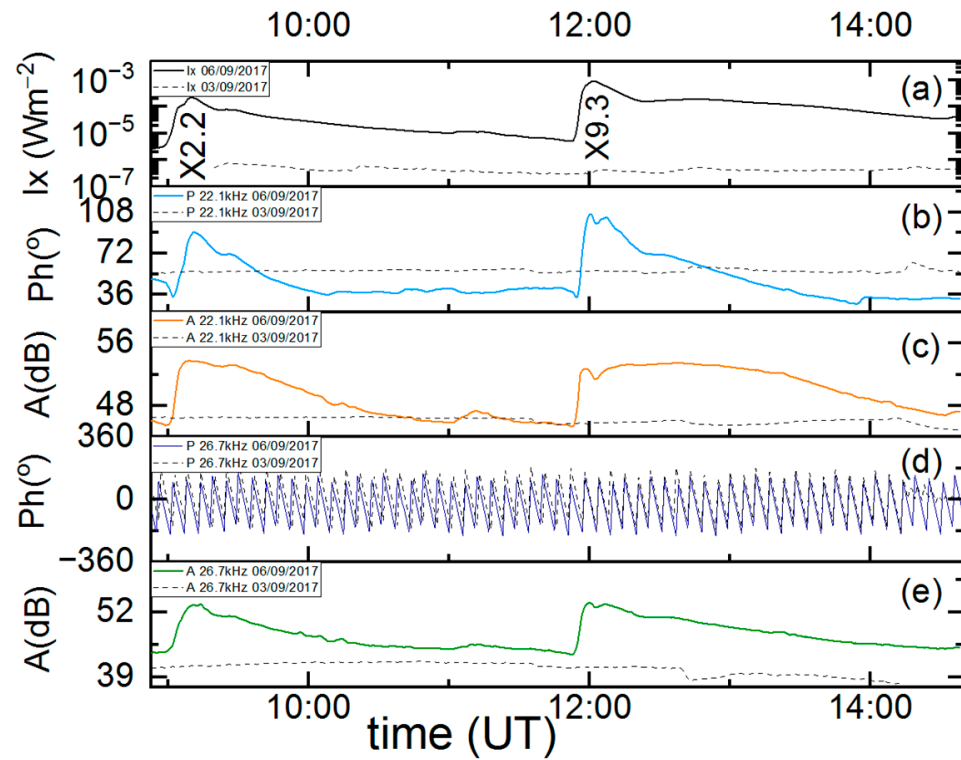


Figure 3. Simultaneous variations of X-ray flux (a) with phase delay, (b) amplitude delay, (c) variations of GQD/22.10 kHz and phase delay, (d) amplitude delay, (e) variations of TBB/26.70 kHz signals versus universal time UT during occurrence of X2.2 and X9.3 class SFs of 6 September 2017. Observed amplitude and phase perturbations with the quiet signal of 3 September 2017 (dashed black) are measured at Belgrade station. Time variation of soft X-ray irradiance is measured by GOES-15 satellite.

3.3. Analysis of Signal Propagation Parameters during Intense SF Events

SFs' occurrence time and evolution were both favorable regarding applied modeling procedures, due to stable daytime GQD waveguide conditions. This was particularly significant for application of the first of previously mentioned numerical procedures in the Methods section, i.e., application of Wait's theory through LWPC software utilization, based upon the two-component exponential model. VLF sub-ionospheric propagation simulations, depending on pair of so-called Wait's parameters β (km^{-1}) and H' (km) (representing time-dependent parameter of lower ionospheric boundary sharpness and VLF signal's reflection height), are conducted using Equation (2) valid for daytime ionosphere [39]:

$$N_e(h, H', \beta) = 1.43 \cdot 10^{13} \cdot e^{(-0.15 \cdot H')} \cdot e^{[(\beta - 0.15) \cdot (h - H')]} \text{, (m}^{-3}\text{)} \quad (2)$$

Parameters β and H' for unperturbed daytime ionospheric conditions are within software predefined as 0.3 km^{-1} and 74 km , respectively, while for each case of perturbed conditions, they must be individually modeled as input parameter pairs along GCP, depending on determined measured amplitude and phase perturbations. Modeling procedure is based on trial-and-error technique, with the goal of achieving the best fit between measured and simulated values of amplitude and phase perturbations obtained through modeling. Results from this numerical procedure in the case of X2.2 and X9.3 SFs of 6 September 2017, for their entire time evolution, are given in Figure 4. Both sharpness (Figure 4b) and effective reflection height (Figure 4a) are in correlation with incident soft X-ray flux (Figure 4c).

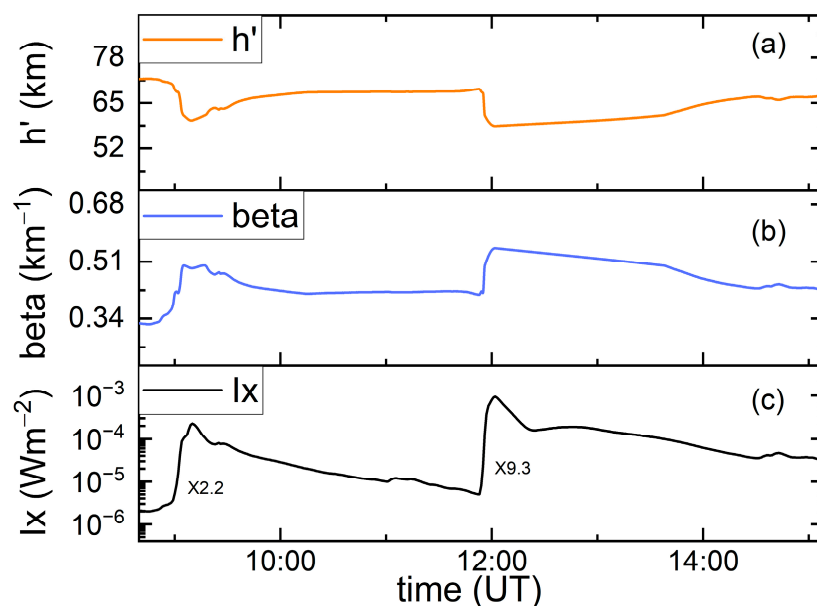


Figure 4. Simultaneous variations of the effective reflection height h' , (a) sharpness β , (b) and X-ray flux (c) during the occurrence of two successive X-ray flares of 6 September 2017.

Obtained modeled values of sharpness and reflection heights corresponding to X-ray flux peaks revealed: in the case of X2.2 SF at 09:10 UT with $I_{x_{\max}} = 2.2658 \cdot 10^{-4} \text{ Wm}^{-2}$, sharpness increased for amount of 0.13 km^{-1} and reflection height was lowered for 14 km, while in the case of X9.3 SF at 12:02 UT with $I_{x_{\max}} = 9.3293 \cdot 10^{-4} \text{ Wm}^{-2}$, sharpness increased for the amount of 0.25 km^{-1} and reflection height was lowered for 15.6 km, compared with their predefined unperturbed values.

Electron density was calculated at the reflection height, when $h = H'$ throughout altitude range corresponding to lower ionosphere (50–90 km), but it must be noted that at the range boundaries, results obtained from calculations should be taken with caution due to possible model failure. Electron density profiles corresponding to the influence of two X-class SFs from 6 September 2017, as observed on the GQD signal at BEL station, are given in Figure 5, in black and red for X2.2 and X9.3 SFs respectively, while quiet ionospheric conditions are given in blue. Conducted calculations indicate that N_e for these two SFs differ within one order of magnitude throughout the entire altitude range. Looking separately, at a height of 74 km, compared to unperturbed ionospheric state, N_e increased by almost three and about 3.5 orders of magnitude during the cases of weaker and stronger SF events respectively.

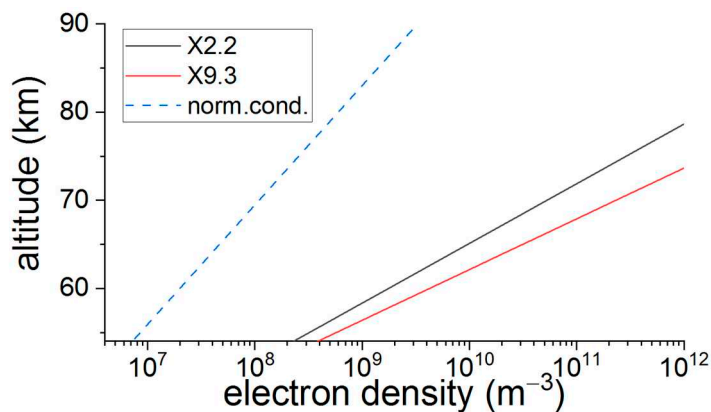


Figure 5. The height profile of electron density at peak time for two successive X-class SFs of 6 September 2017.

For time evolution of X2.2 and X9.3 SFs of 6 September 2017, during about 12 h, a novel approach for obtaining GQD signal propagation parameters, sharpness β and reflection height H' from incident solar X-ray irradiance, was applied by employing the FlarED' Method and Approximate Analytic Expression application, where electron density is calculated with simple logarithmic second-degree polynomial Equation (3) specially designed to take ionospheric response time delay through height-dependent coefficients into calculations (for more details see [5,40]):

$$\log Ne(h, Ix) = a_1(h) + a_2(h) \cdot \log Ix + a_3(h) \cdot (\log Ix)^2 \quad (3)$$

where $a_1(h)$, $a_2(h)$, and $a_3(h)$ are height-dependent coefficients, Ix is solar X-ray flux (Wm^{-2}), and h is height (km). Such calculated Ne values are in good agreement with those obtained using other simulation methods related to the two-component exponential model and VLF sub-ionospheric propagation simulations conducted through the use of LWPC software [40]. Figure 6 presents a 12-h variation of solar X-ray flux within two spectral bands provided by GOES-15 and -13 satellites (Figure 6a) and the corresponding Ne (m^{-3}) during these two X-class SFs (Figure 6b).

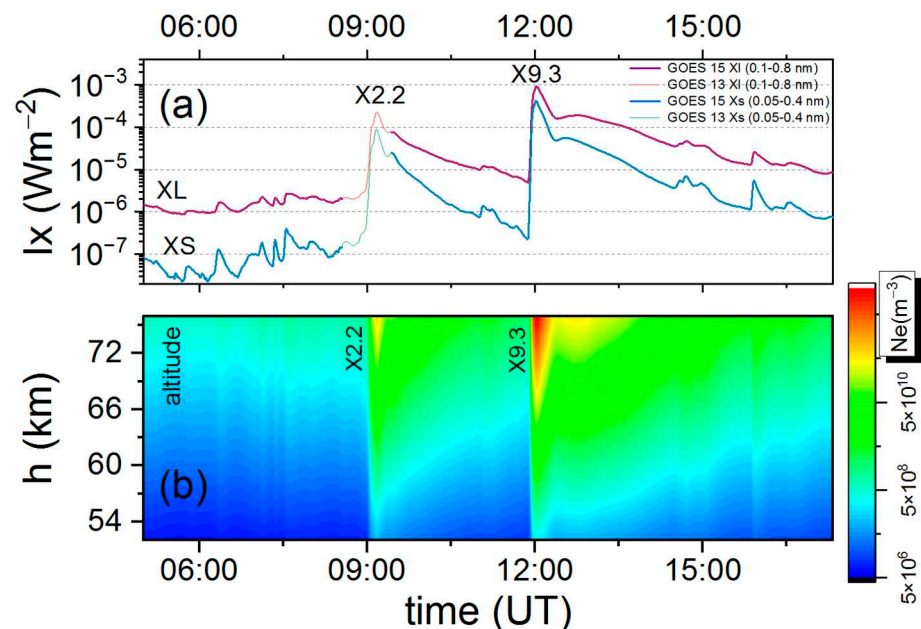


Figure 6. Variation of X-ray flux (a) as measured by GOES-15 and -13 satellites and the surface plot of corresponding electron density profile (b) versus universal time UT during two successive X-class SFs of 6 September 2017. The results are obtained using simple approximative Equation (3).

3.4. Analysis of Cosmic Ray Flux Registered by Belgrade Station during Early September 2017

As a result of solar activity at the beginning of September 2017, a strong FD was detected, resulting in a decrease of CR flux of close to 15% (as observed on the South Pole [60]). The effect was also detected on lower latitudes, being intense enough to be detected by underground muon monitors that are generally sensitive to higher energies of galactic CRs. To get a better perspective of data recorded by Belgrade muon station during this period (both by GLL and UL), we compared it against selected neutron monitor measurements (provided by the Neutron Monitor Database [61]). For this purpose, we chose three NMs: one on the opposite hemisphere with low effective vertical geomagnetic cutoff rigidity R_c , one near the North Pole, and one relatively close to Belgrade muon station with a comparable R_c . All selected stations have different asymptotic directions, R_c , and altitude and are generally sensitive to primary CR with lower median rigidity than CR detected by Belgrade muon station. Median rigidity (R_m) is the rigidity of primary CR where half of all contributions to detector count rate originates from primary CR with

rigidity lower than that specific value. Basic characteristics for NM stations are as follows: South Pole (SOPO, 90.00°S, altitude 2820 m, $R_c = 0.1$ GV, median rigidity $R_m = 10$ GV), Thule (THUL, 76.5°N, 68.7°W, 26 m, $R_c = 0.3$ GV, $R_m = 12.6$ GV), and Athens (ATHN, 37.97°N, 23.78°E, 260 m, $R_c = 8.53$ GV, $R_m = 25.1$ GV). Belgrade muon station, as mentioned before, measures muon flux on ground level (GLL, 44.85°N, 20.38°E, 75 m, $R_c = 5.3$ GV, $R_m = 63$ GV) and underground level (UL, 44.85°N, 20.38°E, 75 m, $R_c = 12$ GV, $R_m = 122$ GV). Median rigidity for NM stations is retrieved from [62]. For Belgrade muon station, R_m values for GLL and UL were determined using the response function obtained by means of Monte Carlo simulation for CR transport. Time series of detected flux for all stations during early September 2017 are given in Figure 7. Flux is normalized using a ten-day average before the FD. This longer interval was chosen due to unusually high solar activity during the period of interest.

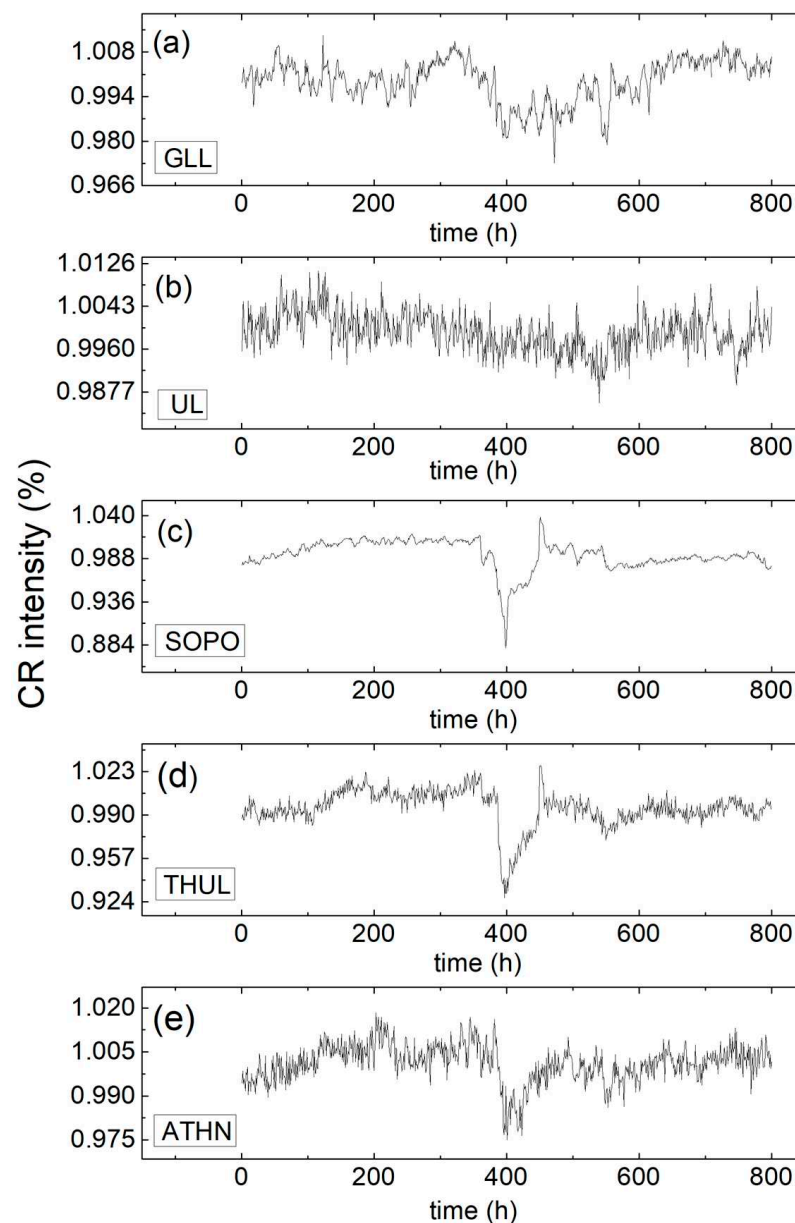


Figure 7. Normalized time series of secondary CR flux detected at several ground and one shallow-underground monitors: (a) ground (GLL) and (b) underground (UL) detector at Belgrade muon station, (c) South pole NM (SOPO), (d) Thule NM (THUL), and (e) Athens NM (ATHN).

Hourly time series show that all stations detected FD around the same time, however, time profiles are not the same. This is due to the specific sensitivity of selected CR stations to primary CR with different rigidities. Additionally, the measured magnitude of the FD is not the same for all detector stations. As expected, UL, GLL, and Athens, with higher cutoff and median rigidity, recovered from sharp depression sooner than stations at higher latitudes (with lower R_c). For a more quantitative description of the relationship between observations from selected monitors, cross-correlation analysis of hourly time series for different stations can be applied using Pearson coefficient with a 2-tail test for significance. Correlation coefficients between data recorded by these ground stations during September 2017 are given in Table 2.

Table 2. Statistical correlation between ground stations during September 2017.

Pearson Corr.	ATHN	SOPO	GLL	UL	THUL
ATHN	1	0.55084	0.43443	0.5056	0.61535
SOPO		1	0.18941	0.45194	0.81747
GLL			1	0.69325	0.36496
UL				1	0.51526
THUL					1

These ground (and one shallow-underground) stations have different locations, different cut-off rigidities, and different energy-dependent detection efficiency of the detectors. All these differences can lead to better understanding of these different correlation coefficients.

Further insight can be gathered by comparing variability of CR flux measured by different stations, as well as geomagnetic activity and selected space weather parameters for the early part of September, which are presented in Figure 8. One-hour time resolution was used for all data. The ICME list compiled by Richardson and Cane [63] and the CME list provided by SOHO/LASCO [64] were used to precisely time the near Earth passage of two ICMEs observed during this period (respective time intervals indicated in Figure 8 by dashed blue lines).

In the days following early September X-flares, two sudden storm commencements (SSCs), or two shocks, arrived during the last hours of 6–7 September (indicated by solid blue lines in Figure 8). They were followed by a sheath region and ICME ejecta. Interaction of shock and sheath region of ICME2 with ICME1 ejecta, visible in the sudden change of solar wind parameters, led to the observed intense geomagnetic activity and consequent FD. This CME-CME interaction with its complex structure was the main reason for the extensive geomagnetic storm [65] and a strong detected FD. With arrival of the first ICME, CR flux showed a small decrease detected as a low-magnitude FD by NM stations [66] (at 23:43:00 UT on 6 September, with magnitude of 1.8% according to IZMIRAN database).

When the second fast interplanetary shock arrived and interacted with ejecta from the previous ICME, a sharp decrease in CR flux and one of the largest FDs in solar cycle 24 was detected (at 23:00:00 UT on 7 September, with magnitude of 7.7% according to IZMIRAN database). Main FD was clearly visible even with muon detectors, which leads to the conclusion that inhomogeneities in the heliosphere created by interaction of these two ICMEs modulated CR extensively. The recovery phase of this FD was influenced by disturbed interplanetary condition, the effect being dependent on particle energy as was evident by comparing profiles of CR time series recorded by different stations. Before the end of the recovery phase, another flare (X8.2 of 10 September) led to a small ground level enhancement (GLE), the last one of solar cycle 24 (GLE #72). Recovery time of the main FD was approximately three days in total, which is a relatively short period for such a large CR modulation. Cross-correlation coefficients between CR time series measured by Belgrade muon station and selected space weather parameters for the period of six days (during 5–10 September) are given in Table 3.

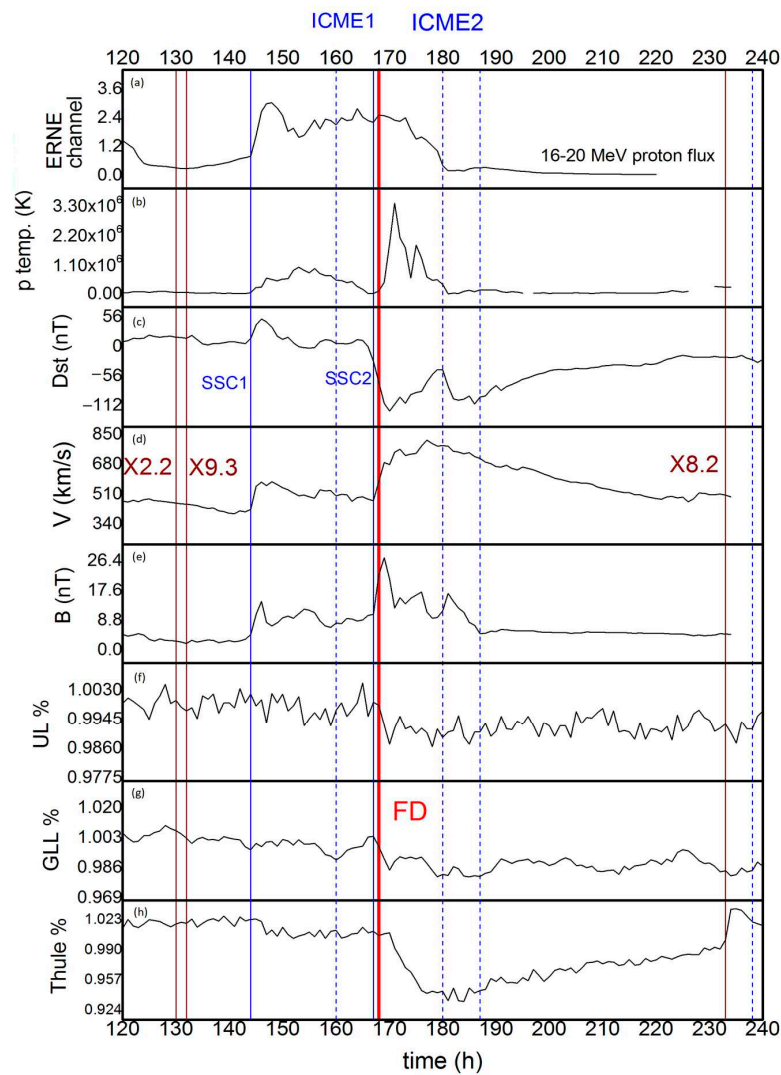


Figure 8. Hourly variation in CR intensity measured at ground station ((f) UL, (g) GLL, (h) Thule), (e) magnitude of interplanetary magnetic field B, (d) velocity of solar wind V, (c) Dst index, (b) proton temperature, and (a) one of the proton channels measured by ERNE/SOHO during early September 2017 (period 4th–10th).

Table 3. Statistical correlation (with significance) between time series of CR flux measured at ground stations and selected space weather parameters during 5–10 September 2017.

Pearson Corr.	Thule		GLL		UL	
Thule	1					
GLL	0.67213	(<10 ⁻⁶)	1			
UL	0.62741	(<10 ⁻⁶)	0.75552	(<10 ⁻⁶)	1	
Average B	-0.238	(<0.008)	-0.242	0.007	-0.243	<0.007
SW speed	-0.80562	(<10 ⁻⁶)	-0.62829	(<10 ⁻⁶)	-0.58503	(<10 ⁻⁶)
Dst Index	0.77923	(<10 ⁻⁶)	0.6979	(<10 ⁻⁶)	0.65494	(<10 ⁻⁶)
Proton Channel 16–20 MeV	0.43083	<10 ⁻⁵	0.38276	<10 ⁻⁴	0.31715	<10 ⁻³

During this period, apparent correlation can be established between selected parameters. This correlation is larger for Thule NM than in the case of Belgrade Muon monitor. Due to the short period, correlation between proton flux at L1 and detected CR flux on all stations is exaggerated.

4. Discussion

The cascade of strong solar activity from AR12673 that occurred in early September 2017 was among others characterized by a number of SFs. Several concurrent interconnecting CMEs/ICMEs emerged in a relatively short period, inducing a disturbance in the heliosphere. The complex structure of interacting CMEs/ICMEs produced an extensive geomagnetic storm and ionospheric disturbance and affected the flux of primary CR (visible as a FD). Additionally, the mentioned phenomena were responsible for the increased flux of energetic particles in interplanetary space. The origin and acceleration mechanism for energetic protons measured at L1 is not so straightforward to determine due to complicated interactions of all effects potentially involved. In case these particles originate from the Sun, correlation between SF properties and SEP fluence is supposed to be rather poor, although it is suggested that primary acceleration of SEP to higher energies occur in close proximity to the flare site [67,68]. If, on the other hand, these particles are accelerated in interplanetary space due to the passage of ICME shock, some correlation can be established (i.e., between measured proton fluence and CME/ICME velocity). However, regardless of their origin, the shape of energetic proton fluence spectrum can hold useful information about heliospheric disturbance and can even provide insight into the effect that this disturbance has on the flux of primary CR in interplanetary space (especially when more intense events are concerned). That was also demonstrated in this case, where the magnitude of the corresponding FD corrected for magnetospheric effect estimated from proton fluence spectra was in good agreement with the value for M_M calculated based on NM measurements.

Impacts of the soft range X-ray solar electromagnetic radiation released from two powerful SF events from 6 September 2017 onto the European mid-latitude ionospheric D-region were monitored and inspected based on recordings from BEL narrowband VLF receiving station, belonging to a global ground-based VLF network system. Lower ionospheric disturbances induced by incident soft range X-ray radiation were indirectly examined regarding simultaneous perturbations of VLF radio signals' propagation parameters within the Earth-ionosphere waveguide, with analysis conducted for signals with short GCPs (Table 1; Figure S3).

Aside from quiet ionospheric preflare conditions, SFs' occurrence times were also favorable in terms of applied modeling procedure using the LWPC software package, since analyzed signals on their GCPs towards BEL station were transmitted through waveguides under already established stable daytime ionospheric conditions. Since this procedure relies on trial-and-error technique in acquiring the best fitting pair of Wait's parameters for depicting real measured data with the modeled data, and from that, by obtaining information regarding lower ionospheric conditions based on modeled ones, both of these prerequisites significantly eased an already highly challenging task of modeling X-class SFs and especially those most energetic among them. In such disturbed conditions, both ionospheric plasma properties and related corresponding VLF signal propagation parameters are drastically changed compared with the regular state. Accordingly, electron density height profiles are also changed in regard to both time and space distributions. As expected, the evolution of observed VLF signals' perturbations was with similar characteristics, following a lower ionospheric response to incident solar X-ray flux with delay times corresponding to the sluggishness of the ionosphere and were of amounts expected for cases of such powerful events (Figure 3). Their back-to-back occurrence did not allow for individual duration specification of each SF's impact on analyzed VLF signals, however, their individual contribution was possible to determine. According to registered VLF BEL data, after a several-hour lasting disturbance, the lower ionosphere fully recovered (Figure S4).

For the state of maximal perturbation that corresponds to SFs' X-ray flux peaks, perturbed GQD signal's amplitudes are 118% and 117% of unperturbed, while phases are 165% and 192% of unperturbed. Wait's parameters are in correlation with incident soft X-ray flux and modeling results based upon exponential conductivity increase with height within the ionosphere suggesting that perturbed sharpnesses are 143.3% and 183.3% of unperturbed, while perturbed reflection heights are 81% and 78.9% of unperturbed,

respectively to SFs (Figure 4). As expected, in the case of the stronger SF event, propagation was more affected by the induced disturbance, causing the reflecting edge boundary to become significantly sharper, while reflecting edge height descended for 1.6 km^{-1} more than in case of the weaker one. Numerically, simulated ionospheric conditions fit well with observed ones, as indirectly obtained through GQD signal's amplitude and phase measurements. Due to its short GCP and stable daytime ionospheric conditions, averaged conditions that were held within the waveguide during the modeling procedure can be considered reliable. Electron densities calculated using Equation (2) for the D-region altitude range show about one order of magnitude difference between analyzed SFs at their peak, giving a reflection height of 74 km an increase in electron density of 82.1% compared between stronger and weaker events (Figure 5).

The effects on the ionosphere of the largest SF event of the last decade, X9.3 together with X2.2, occurred on 6 September 2017, observed through GQD VLF signal response in relation to the SF class, were compared with some other cases of strong SF events, including several major SFs (2003–2011 of class X28+–X6.9) and other SFs (from 2006–2017 of class X1–X9.3 and from period 1994–1998 in range X1–X5). Figure S5 provides a comparison of the results obtained in this study (black stars) and those available in the literature [5,7,8,69–77]. Presented ionospheric parameters (β and H') and corresponding electron densities are related to results from two hundred cases of SF events recorded in Belgrade on GQD trace in the period of 2003–2017 in other mid-latitudinal ionospheric sectors and the low-latitudinal ionospheric sector. In order to ensure better insight into the tendency of parameters with the SF events' strength, smaller diagrams containing the entire C–X-class range are embedded in Figure S5. It can be seen that values of signal parameters for some X-class events are quite scattered.

Our results fit well with the general trend (linear fit), considering that most of the available cases taken into consideration are from the mid-latitudinal sector. A significant discrepancy notable in the enlarged X-class section, related to results from [69] and [70], is probably caused by latitudinal factor (due to low-latitudinal observations likewise as suggested in [71] and similarly due to observations obtained more towards higher-latitude compared with Belgrade receiver site, respectively). A novel proposed approximate method that employs approximative Equation (3) for obtaining ionospheric parameters was validated both for cases of weaker and stronger SFs and expanded further towards the upper boundary of X-class range, as compared to recent previous studies employing this technique. Applied novel approach provides mapping of the entire ionospheric altitude range (Figure 6) in a simpler and easier to conduct manner. Results obtained in this study using this novel approach applied to X-class SFs could be useful for validation of the available ionospheric models and as input data for other climate models.

Furthermore, increased solar activity at the beginning of September 2017 had a significant effect on cosmic rays observed as a decrease in measured flux by all relevant CR stations. Intensity of the event was such that the energy range of affected primary CR was wide enough for the effect to be detected both by neutron monitors and muon detectors. The decrease was even observable in shallow-underground muon measurements, although to a much lesser extent. Temporal agreement between measurements taken by different detectors was good, while the shape of detected FD varied, as would be expected due to difference in location, instrument design, and sensitivity. Cross-correlation analysis of hourly time series for different stations (presented in Table 2) shows expected positive correlation, where obtained coefficients are consistent with values expected based on differences in detector location, particular setups, station specific environmental conditions, and most importantly, the energy (rigidity) range of primary CR they are sensitive to. GLL and UL have the same position, however, correlation is not so high (≈ 0.7) due to different R_c and R_m . Nevertheless, this correlation is higher than that between either of the detectors and any of the neutron monitor stations. NMs have more similar R_c and R_m values, so this correlation is greater despite their different location. As far as correlation between measured CR flux and selected space weather and geomagnetic parameters is concerned,

a larger correlation observed for NM (Table 3) can almost certainly be attributed to the fact that muon detectors are sensitive to higher energy CR (which are less modulated by disturbances in the heliosphere). Correlation between selected proton channel (particles with energy between 16 and 20 MeV) and CR flux is exaggerated as it is a consequence of a relatively short time interval taken for analysis. This value is greatly reduced if a longer interval is taken into consideration, even appearing as a small anticorrelation. This is expected as proton flux with its turbulent magnetic field scatters CR and thus can produce a decrease in detected CR flux. Inverse correlation of magnetic field and solar wind speed with CR flux is anticipated due to the same reason.

Forbush decrease in early September 2017 was caused by compound solar wind disturbance formed due to the interaction of several ICMEs. This time interval is particularly interesting because it happens in a descending-to-minimum phase of a solar cycle. The apparent multitude of solar activity is more characteristic to other phases. For example, similar series of successive CMEs led to FD in March 2012 [78] during the ascending phase of the solar cycle, but this heightened activity of the Sun, isolated between relatively quiet periods, allows for better study of the phenomena. Forecasting these multiple CME interaction events and predicting time of arrival is very difficult [45] but needed, so this series of events can be a good case study.

Although no apparent correlation between SF intensity and solar wind and FD parameters is clearly demonstrable, the majority of more intense FDs are caused by a CME/ICME following a significant SF, thus indicating a likely connection. For one such complex event, accompanying disturbances induced in the heliosphere, magnetosphere, and ionosphere are generally directly attributed to different sources and establishing clear relationships between various parameters used to describe them is far from straightforward. Yet, based on some general features, it is possible to make rudimentary event classification, where within certain classes, some of these relationships may be more pronounced. Strong flares do not necessarily produce a significant FD (although can have an associated GLE, as is the case for X14.4 flare that occurred on 15 April 2001), can produce both strong FDs and GLEs (e.g., GLE #69 on 20 January 2005, GLE #66 on 28 October and GLE #67 on 2 November 2003), or can produce strong FD but without associated GLE (e.g., 7 March 2012, related to X5.4 flare and September 2017 event studied here). It has been shown [49,79] that events that fall in this last category exhibit stronger correlations between FD magnitude and some space weather parameters, specifically average CME speed. More recently, a correlation between FD magnitude (especially in the case of more intense FDs) and shape of energetic proton spectra measured at L1 has been reported for this class of events. As the number of such events is relatively low, it is of significance that results presented in this work are consistent with the indicated relationship. For reference, dependence of FD magnitude on selected SF, CME, and geomagnetic parameters for some of the mentioned events is given in Figure S6.

5. Conclusions

The influence of severely disturbed space weather conditions of 6 September 2017 on parameters of the Earth's atmosphere was studied, in relation to the relatively close and far surroundings of the Earth. The influence of strong X-class SFs on the ionosphere and primary cosmic rays, based on space- and ground-based observations on one hand and simulations on the other hand, are presented. It contributes to better understanding of solar-terrestrial coupling processes and how primary cosmic rays and the ionosphere respond under conditions during the X-class SF events. Based on the results presented, the following conclusions can be drawn:

- SEP fluence during strongly disturbed conditions of the heliosphere in early September 2017 was calculated from SOHO/ERNE data and modeled using double power law. Relationships between power exponents used to parameterize the shape of fluence spectrum and FD magnitude corrected for magnetospheric effect are consistent with ones expected for this type of event. Hourly time series of secondary CR flux, detected by several ground-based monitors and one shallow-underground monitor, show that

- all stations detected FD at the same time. Cross-correlation between these time series, and between CR time series and some geomagnetic activity indices, as well as selected IMF and solar wind parameters, are presented. Sensitivity of different stations to primary CR with different rigidity results in different time profiles, maximal decreases, and duration of recovery phase of FD;
- We observed that a correlation between heliospheric and geomagnetic parameters decreases with increase of median energy of the CR detected by different stations and that shows an extension of CR modulation of complex CME-CME interaction structure initiated with strong SFs;
 - Impact of intense solar activity onto the Earth's lower ionosphere, through analyzed X-class SFs, was clearly observed (perturbed amplitudes are 118% and 117% of unperturbed, while perturbed phases are 165% and 192% of unperturbed, for X2.2 and X9.3, respectively). BEL AbsPAL recordings of registered VLF signals during SF events are in correlation with X-ray flux (with time delays corresponding to the sluggishness of the ionosphere). Although X2.2 and X9.3 occurred back-to-back, it was possible to determine individual contributions of each SF based upon registered VLF signals;
 - Numerical simulations were conducted through the application of the LWPC software package and the FlarED' Method and Approximate Analytic Expression application's novel approach. The ionospheric parameters (sharpness and effective reflection height) and electron density are in correlation with incident X-ray flux of soft range. N_e for these two SFs revealed the difference within one order of magnitude throughout the entire altitude range considered. Compared to quiet ionospheric conditions, N_e at the reference height increased by several orders of magnitude during both SF events. As monitored by BEL VLF station in the mid-latitudinal sector, both presented X-class SFs are common in properties and behavior, as could be expected for intense SF events, according to their strength. However, there is a significant difference in estimations of ionospheric parameters related to some other cases of reported X-class SFs from different sectors.

Although there are numerous papers related to the influence of SF events on Earth's ionosphere, the vast majority of present case studies of selected SF events, more or less are extensively related to numbers of examined cases. X-class SF events have never been systematically studied in terms of lower ionospheric response. Coupling processes between such extreme space weather events and the lower ionosphere are not well understood. In addition, many intense SF events are related to other energetic solar events like CMEs and SEPs. Comprehensive research is needed especially in terms of retrieving a global (worldwide) lower ionospheric response to such strong events from propagation parameters of radio signals as a remote sensing technique. Case studies, although restricted to some selected events and with great contribution of "local" components contained within obtained and presented results, would provide substantial contributions.

This study emphasized the relevance of the ionospheric response, which was analyzed using a multi-instrument method, and gave a comprehensive examination of the events from the Sun to the Earth. It gave an insight into the sudden increase in ionization during the storm and strong SFs from the beginning of September 2017 and the potential effects on radio communication. Since conditions in the D-region of the ionosphere have a dramatic effect on high frequency communications and low frequency navigation systems, the ionospheric responses (and its parameters like β , H' and N_e) to severe SFs are a key topic of study in ionospheric physics and are considered to be an important factor for space weather predictions, improvement of empirical models, and applications of machine learning techniques in atmospheric sciences.

Supplementary Materials: The following supporting information can be downloaded at: <https://www.mdpi.com/article/10.3390/rs15051403/s1>, Figure S1: Differential SEP fluxes during extreme solar event in September 2017, measured by SOHO/ERNE energetic particle sensors LET (Low Energy Detector) proton channels. Red vertical dashed lines indicate the time for the start and the end

of interval used to calculate the integral flux.; Figure S2: Differential SEP fluxes during extreme solar event in September 2017, measured by SOHO/ERNE energetic particle sensors HET (High Energy Detector) proton channels. Red vertical dashed lines indicate the time for the start and the end of interval used to calculate the integral flux.; Figure S3: The geographic position of Belgrade (BEL) VLF receiver and the GQD transmitter (54.73°N, 2.88°W), Anthorn UK and TBB transmitter (37.43°N, 27.55°E) Bafa Turkey with GCP of sub-ionospheric propagating VLF signals.; Figure S4: Simultaneous variations of X-ray flux (red), phase (blue), and amplitude (orange) of GQD/22.10 kHz signal versus universal time UT during occurrence of X2.2 and X9.3 class solar flares of 6 September 2017 (from upper to lower panel). Observed amplitude and phase perturbations on GQD radio signal, as well as quiet signal (dashed black), are measured at Belgrade station. Time variation of soft X-ray irradiance is measured by GOES-15 satellite.; Figure S5: Lower ionospheric response to SF events of different strength across X-class (shaded gray area), obtained indirect modeling of VLF signals' propagation parameters: (a) sharpness β (km^{-1}), and (b) effective reflection height H' , (km) and (c) estimated corresponding electron densities N_e (m^{-3}), in function of X-ray flux; results from our research are presented by black stars.; Figure S6: Magnitude of the FD versus the average CME velocity between the Sun and the Earth, calculated using the time of the beginning of the associated CME observations (a) Minimal Dst-index in the event, (b) maximal X-ray flare power (c) with associated flare indicated in red.

Author Contributions: Conceptualization, V.A.S.; writing—original draft preparation, V.A.S., A.K. and N.V.; writing—review and editing A.K., N.V., V.A.S., Z.M., M.S. and A.D. The authors had full access to the data and took responsibility for their integrity. All authors have read and agreed to the published version of the manuscript.

Funding: This work was funded by the Institute of Physics Belgrade, University of Belgrade, through a grant by the Ministry of Science, Technological Development and Innovations of the Republic of Serbia.

Data Availability Statement: VLF data were recorded at the Institute of Physics Belgrade, University of Belgrade and can be obtained upon request. Please contact V.A.S.

Acknowledgments: The article is based upon work from COST Action CA18212—Molecular Dynamics in the GAS phase (MD-GAS), supported by COST (European Cooperation in Science and Technology). Authors thank D. Šulić for instrumental set-up and useful discussions. OMNI data was made available by NASA/GSFC's Space Physics Data Facility's OMNIWeb service. This CME catalog is generated and maintained at the CDAW Data Center by NASA and The Catholic University of America in cooperation with the Naval Research Laboratory. SOHO is a project of international cooperation between ESA and NASA. We acknowledge the NMDB database, founded under the European Union's FP7 program (contract no.213007) for providing data. We also gratefully acknowledge using data from the catalogue of Forbush effects and interplanetary disturbances provided by Cosmic Ray Group at the IZMIRAN Space Weather Prediction Center at Pushkov Institute of Terrestrial Magnetism, Ionosphere, and Radio Wave Propagation of the Russian Academy of Sciences.

Conflicts of Interest: The authors declare no conflict of interest. The funders had no role in the design of the study; in the collection, analyses, or interpretation of data; in the writing of the manuscript, or in the decision to publish the results.

References

1. Manju, G.; Pant, T.K.; Devasia, C.V.; Ravindran, S.; Sridharan, R. Electrodynamical response of the Indian low-mid latitude ionosphere to the very large solar flare of 28 October 2003—A case study. *Ann. Geophys.* **2009**, *27*, 3853–3860. [[CrossRef](#)]
2. Fu, H.; Zheng, Y.; Ye, Y.; Feng, X.; Liu, C.; Ma, H. Joint Geoeffectiveness and Arrival Time Prediction of CMEs by a Unified Deep Learning Framework. *Remote Sens.* **2021**, *13*, 1738. [[CrossRef](#)]
3. Sahai, Y.; Becker-Guedes, F.; Fagundes, P.R.; Lima, W.L.C.; de Abreu, A.J.; Guarnieri, F.L.; Candido, C.M.N.; Pillat, V.G. Unusual ionospheric effects observed during the intense 28 October 2003 solar flare in the Brazilian sector. *Ann. Geophys.* **2007**, *25*, 2497–2502. [[CrossRef](#)]
4. Le, H.; Liu, L.; Chen, Y.; Wan, W. Statistical analysis of ionospheric responses to solar flares in the solar cycle 23. *J. Geophys. Res. Space Phys.* **2013**, *118*, 576–582. [[CrossRef](#)]
5. Srećković, V.A.; Šulić, D.M.; Ignjatović, L.; Vujčić, V. Low Ionosphere under Influence of Strong Solar Radiation: Diagnostics and Modeling. *Appl. Sci.* **2021**, *11*, 7194. [[CrossRef](#)]
6. Kelley, M.C. *The Earth's Ionosphere: Plasma Physics and Electrodynamics*; Academic Press: Cambridge, MA, USA, 2009.

7. Barta, V.; Natras, R.; Srećković, V.; Koroncay, D.; Schmidt, M.; Šulic, D. Multi-instrumental investigation of the solar flares impact on the ionosphere on 05–06 December 2006. *Front. Environ. Sci.* **2022**, *10*, 904335. [[CrossRef](#)]
8. Kolarski, A.; Srećković, V.A.; Mijić, Z.R. Response of the Earth's Lower Ionosphere to Solar Flares and Lightning-Induced Electron Precipitation Events by Analysis of VLF Signals: Similarities and Differences. *Appl. Sci.* **2022**, *12*, 582. [[CrossRef](#)]
9. Nina, A. Modelling of the Electron Density and Total Electron Content in the Quiet and Solar X-ray Flare Perturbed Ionospheric D-Region Based on Remote Sensing by VLF/LF Signals. *Remote Sens.* **2022**, *14*, 54. [[CrossRef](#)]
10. Berdermann, J.; Kriegel, M.; Banyś, D.; Heymann, F.; Hoque, M.M.; Wilken, V.; Borries, C.; Heßelbarth, A.; Jakowski, N. Ionospheric Response to the X9.3 Flare on 6 September 2017 and Its Implication for Navigation Services Over Europe. *Space Weather* **2018**, *16*, 1604–1615. [[CrossRef](#)]
11. Yasyukevich, Y.; Astafyeva, E.; Padokhin, A.; Ivanova, V.; Syrovatskii, S.; Podlesnyi, A. The 6 September 2017 X-Class Solar Flares and Their Impacts on the Ionosphere, GNSS, and HF Radio Wave Propagation. *Space Weather* **2018**, *16*, 1013–1027. [[CrossRef](#)]
12. De Paula, V.; Segarra, A.; Altadill, D.; Curto, J.J.; Blanch, E. Detection of Solar Flares from the Analysis of Signal-to-Noise Ratio Recorded by Digisonde at Mid-Latitudes. *Remote Sens.* **2022**, *14*, 1898. [[CrossRef](#)]
13. Demyanov, V.V.; Yasyukevich, Y.V.; Ishin, A.B.; Astafyeva, E.I. Ionospheric super-bubble effects on the GPS positioning relative to the orientation of signal path and geomagnetic field direction. *GPS Solut.* **2012**, *16*, 181–189. [[CrossRef](#)]
14. Yashiro, S.; Gopalswamy, N. Statistical relationship between solar flares and coronal mass ejections. *Proc. Int. Astron. Union* **2008**, *4*, 233–243. [[CrossRef](#)]
15. Desai, M.; Giacalone, J. Large gradual solar energetic particle events. *Living Rev. Sol. Phys.* **2016**, *13*, 3. [[CrossRef](#)]
16. Freiherr von Forstner, J.L.; Guo, J.; Wimmer-Schweingruber, R.F.; Dumbović, M.; Janvier, M.; Démoulin, P.; Veronig, A.; Temmer, M.; Papaioannou, A.; Dasso, S.; et al. Comparing the Properties of ICME-Induced Forbush Decreases at Earth and Mars. *J. Geophys. Res. Space Phys.* **2020**, *125*, e2019JA027662. [[CrossRef](#)]
17. Cane, H.V. Coronal Mass Ejections and Forbush Decreases. *Space Sci. Rev.* **2000**, *93*, 55–77. [[CrossRef](#)]
18. Belov, A.V.; Eroshenko, E.A.; Oleneva, V.A.; Struminsky, A.B.; Yanke, V.G. What determines the magnitude of forbush decreases? *Adv. Space Res.* **2001**, *27*, 625–630. [[CrossRef](#)]
19. Papaioannou, A.; Belov, A.; Abunina, M.; Eroshenko, E.; Abunin, A.; Anastasiadis, A.; Patsourakos, S.; Mavromichalaki, H. Interplanetary Coronal Mass Ejections as the Driver of Non-recurrent Forbush Decreases. *Astrophys. J.* **2020**, *890*, 101. [[CrossRef](#)]
20. Belov, A.; Shlyk, N.; Abunina, M.; Belova, E.; Abunin, A.; Papaioannou, A. Solar Energetic Particle Events and Forbush Decreases Driven by the Same Solar Sources. *Universe* **2022**, *8*, 403. [[CrossRef](#)]
21. Riley, P.; Love, J.J. Extreme geomagnetic storms: Probabilistic forecasts and their uncertainties. *Space Weather* **2017**, *15*, 53–64. [[CrossRef](#)]
22. Eastwood, J.P.; Biffis, E.; Hapgood, M.A.; Green, L.; Bisi, M.M.; Bentley, R.D.; Wicks, R.; McKinnell, L.A.; Gibbs, M.; Burnett, C. The Economic Impact of Space Weather: Where Do We Stand? *Risk Anal.* **2017**, *37*, 206–218. [[CrossRef](#)] [[PubMed](#)]
23. Kumar, A.; Kashyap, Y.; Kosmopoulos, P. Enhancing Solar Energy Forecast Using Multi-Column Convolutional Neural Network and Multipoint Time Series Approach. *Remote Sens.* **2023**, *15*, 107. [[CrossRef](#)]
24. Alabdulgader, A.; McCraty, R.; Atkinson, M.; Dobyns, Y.; Vainoras, A.; Ragulskis, M.; Stolc, V. Long-Term Study of Heart Rate Variability Responses to Changes in the Solar and Geomagnetic Environment. *Sci. Rep.* **2018**, *8*, 2663. [[CrossRef](#)] [[PubMed](#)]
25. Bruno, A.; Christian, E.R.; de Nolfo, G.A.; Richardson, I.G.; Ryan, J.M. Spectral Analysis of the September 2017 Solar Energetic Particle Events. *Space Weather* **2019**, *17*, 419–437. [[CrossRef](#)]
26. Chamberlin, P.C.; Woods, T.N.; Didkovsky, L.; Eparvier, F.G.; Jones, A.R.; Machol, J.L.; Mason, J.P.; Snow, M.; Thiemann, E.M.B.; Viereck, R.A.; et al. Solar Ultraviolet Irradiance Observations of the Solar Flares During the Intense September 2017 Storm Period. *Space Weather* **2018**, *16*, 1470–1487. [[CrossRef](#)]
27. Pikulina, P.; Mironova, I.; Rozanov, E.; Karagodin, A. September 2017 Solar Flares Effect on the Middle Atmosphere. *Remote Sens.* **2022**, *14*, 2560. [[CrossRef](#)]
28. Vankadara, R.K.; Panda, S.K.; Amory-Mazaudier, C.; Fleury, R.; Devanaboyina, V.R.; Pant, T.K.; Jamjareegulgarn, P.; Haq, M.A.; Okoh, D.; Seemala, G.K. Signatures of Equatorial Plasma Bubbles and Ionospheric Scintillations from Magnetometer and GNSS Observations in the Indian Longitudes during the Space Weather Events of Early September 2017. *Remote Sens.* **2022**, *14*, 652. [[CrossRef](#)]
29. Amaechi, P.O.; Akala, A.O.; Oyedokun, J.O.; Simi, K.G.; Aghogho, O.; Oyeyemi, E.O. Multi-Instrument Investigation of the Impact of the Space Weather Events of 6–10 September 2017. *Space Weather* **2021**, *19*, e2021SW002806. [[CrossRef](#)]
30. Curto, J.J.; Marsal, S.; Blanch, E.; Altadill, D. Analysis of the Solar Flare Effects of 6 September 2017 in the Ionosphere and in the Earth's Magnetic Field Using Spherical Elementary Current Systems. *Space Weather* **2018**, *16*, 1709–1720. [[CrossRef](#)]
31. Bilitza, D. IRI the International Standard for the Ionosphere. *Adv. Radio Sci.* **2018**, *16*, 1–11. [[CrossRef](#)]
32. Moraal, H. Cosmic-Ray Modulation Equations. *Space Sci. Rev.* **2013**, *176*, 299–319. [[CrossRef](#)]
33. Dorman, L.I. *Cosmic Rays in the Earth's Atmosphere and Underground*; Springer: Dordrecht, The Netherlands, 2004; Volume 303, p. 862.
34. Zhang, J.L.; Tan, Y.H.; Wang, H.; Lu, H.; Meng, X.C.; Muraki, Y. The Yangbajing Muon–Neutron Telescope. In *Nuclear Instruments and Methods in Physics Research Section A: Accelerators, Spectrometers, Detectors and Associated Equipment*; Elsevier: Amsterdam, The Netherlands, 2010; Volume 623, pp. 1030–1034. [[CrossRef](#)]

35. Veselinović, N.; Dragić, A.; Savić, M.; Maletić, D.; Joković, D.; Banjanac, R.; Udovičić, V. An underground laboratory as a facility for studies of cosmic-ray solar modulation. In *Nuclear Instruments and Methods in Physics Research Section A: Accelerators, Spectrometers, Detectors and Associated Equipment*; Elsevier: Amsterdam, The Netherlands, 2017; Volume 875, pp. 10–15.
36. Savić, M.; Maletić, D.; Dragić, A.; Veselinović, N.; Joković, D.; Banjanac, R.; Udovičić, V.; Knežević, D. Modeling Meteorological Effects on Cosmic Ray Muons Utilizing Multivariate Analysis. *Space Weather* **2021**, *19*, e2020SW002712. [[CrossRef](#)]
37. Ferguson, J. *Computer Programs for Assessment of Long-Wavelength Radio Communications, Version 2.0: User's Guide and Source Files*; Space and Naval Warfare Systems Center: San Diego, CA, USA, 1998.
38. Mitra, A.P. *Ionospheric Effects of Solar Flares*; Springer: Berlin/Heidelberg, The Netherlands, 1974; Volume 46.
39. Wait, J.R.; Spies, K.P. *Characteristics of the Earth-Ionosphere Waveguide for VLF Radio Waves*; US Department of Commerce, National Bureau of Standards: Gaithersburg, MD, USA, 1964; Volume 13.
40. Srećković, V.A.; Šulić, D.M.; Vujčić, V.; Mijić, Z.R.; Ignjatović, L.M. Novel Modelling Approach for Obtaining the Parameters of Low Ionosphere under Extreme Radiation in X-Spectral Range. *Appl. Sci.* **2021**, *11*, 11574. [[CrossRef](#)]
41. AR12673 History. Available online: http://helio.mssl.ucl.ac.uk/helio-vo/solar_activity/arstats/arstats_page4.php?region=12673 (accessed on 14 December 2022).
42. Space Weather Prediction Center (IZMIRAN). Available online: <http://spaceweather.izmiran.ru/eng/dbs.html> (accessed on 22 January 2022).
43. Wold, A.M.; Mays, M.L.; Taktakishvili, A.; Jian, L.K.; Odstrcil, D.; MacNeice, P. Verification of real-time WSA–ENLIL+Cone simulations of CME arrival-time at the CCMC from 2010 to 2016. *J. Space Weather Space Clim.* **2018**, *8*, A17. [[CrossRef](#)]
44. Gopalswamy, N.; Yashiro, S.; Michalek, G.; Stenborg, G.; Vourlidas, A.; Freeland, S.; Howard, R. The SOHO/LASCO CME Catalog. *Earth Moon Planets* **2009**, *104*, 295–313. [[CrossRef](#)]
45. Werner, A.L.E.; Yordanova, E.; Dimmock, A.P.; Temmer, M. Modeling the Multiple CME Interaction Event on 6–9 September 2017 with WSA-ENLIL+Cone. *Space Weather* **2019**, *17*, 357–369. [[CrossRef](#)]
46. SPDF - OMNIWeb Service. Available online: https://spdf.gsfc.nasa.gov/pub/data/omni/low_res_omni/ (accessed on 10 November 2022).
47. Torsti, J.; Valtonen, E.; Lumme, M.; Peltonen, P.; Eronen, T.; Louhola, M.; Riihonen, E.; Schultz, G.; Teittinen, M.; Ahola, K.; et al. Energetic particle experiment ERNE. *Sol. Phys.* **1995**, *162*, 505–531. [[CrossRef](#)]
48. Multi-Source Spectral Plots (MSSP) of Energetic Particle. Available online: https://omniweb.gsfc.nasa.gov/ftpbrowser/flux_spectr_m.html (accessed on 25 October 2022).
49. Savić, M.; Veselinović, N.; Dragić, A.; Maletić, D.; Joković, D.; Udovičić, V.; Banjanac, R.; Knežević, D. New insights from cross-correlation studies between solar activity indices and cosmic-ray flux during Forbush decrease events. *Adv. Space Res.* **2022**, *71*, 2006–2016. [[CrossRef](#)]
50. Band, D.; Matteson, J.; Ford, L.; Schaefer, B.; Palmer, D.; Teegarden, B.; Cline, T.; Briggs, M.; Paciesas, W.; Pendleton, G.; et al. BATSE Observations of Gamma-Ray Burst Spectra. I. Spectral Diversity. *Astrophys. J.* **1993**, *413*, 281. [[CrossRef](#)]
51. Ellison, D.C.; Ramaty, R. Shock acceleration of electrons and ions in solar flares. *Astrophys. J.* **1985**, *298*, 400–408. [[CrossRef](#)]
52. Mottl, D.A.; Nymmik, R.A.; Sladkova, A.I. Energy spectra of high-energy SEP event protons derived from statistical analysis of experimental data on a large set of events. *AIP Conf. Proc.* **2001**, *552*, 1191–1196. [[CrossRef](#)]
53. Zhao, L.; Zhang, M.; Rassoul, H.K. Double power laws in the event-integrated solar energetic particle spectrum. *Astrophys. J.* **2016**, *821*, 62. [[CrossRef](#)]
54. Miteva, R.; Samwel, S.W.; Zabunov, S.; Dechev, M. On the flux saturation of SOHO/ERNE proton events. *Bulg. Astron. J.* **2020**, *33*, 99.
55. NOAA National Centers for Environmental Information. Available online: <https://satdat.ngdc.noaa.gov/sem/goes/data/avg/> (accessed on 10 October 2022).
56. Žigman, V.; Grubor, D.; Šulić, D. D-region electron density evaluated from VLF amplitude time delay during X-ray solar flares. *J. Atmos. Sol.-Terr. Phys.* **2007**, *69*, 775–792. [[CrossRef](#)]
57. Kolarski, A.; Grubor, D. Sensing the Earth's low ionosphere during solar flares using VLF signals and goes solar X-ray data. *Adv. Space Res.* **2014**, *53*, 1595–1602. [[CrossRef](#)]
58. Kolarski, A.; Srećković, V.A.; Mijić, Z.R. Monitoring solar activity during 23/24 solar cycle minimum through VLF radio signals. *Contrib. Astron. Obs. Skaln. Pleso* **2022**, *52*, 105. [[CrossRef](#)]
59. Šulić, D.; Srećković, V.A.; Mihajlov, A.A. A study of VLF signals variations associated with the changes of ionization level in the D-region in consequence of solar conditions. *Adv. Space Res.* **2016**, *57*, 1029–1043. [[CrossRef](#)]
60. Dorman, L.; Tassev, Y.; Velinov, P.I.Y.; Mishev, A.; Tomova, D.; Mateev, L. Investigation of exceptional solar activity in September 2017: GLE 72 and unusual Forbush decrease in GCR. *J. Phys. Conf. Ser.* **2019**, *1181*, 012070. [[CrossRef](#)]
61. Neutron Monitor Database. Available online: <https://www.nmdb.eu/> (accessed on 20 October 2022).
62. Kojima, H.; Shibata, S.; Oshima, A.; Hayashi, Y.; Antia, H.; Dugad, S.; Fujii, T.; Gupta, S.K.; Kawakami, S.; Minamino, M.; et al. Rigidity Dependence of Forbush Decreases. In *Proceedings of the 33rd International Cosmic Ray Conference, Rio de Janeiro, Brazil, 2–9 July 2013*.
63. Near-Earth Interplanetary Coronal Mass Ejections Since January 1996. Available online: <https://izw1.caltech.edu/ACE/ASC/DATA/level3/icmetable2.htm> (accessed on 15 October 2022).

64. Soho Lasco Cme Catalog Cdaw Data Center. Available online: https://cdaw.gsfc.nasa.gov/CME_list/ (accessed on 10 November 2022).
65. Scolini, C.; Chané, E.; Temmer, M.; Kilpua, E.K.J.; Dissauer, K.; Veronig, A.M.; Palmerio, E.; Pomoell, J.; Dumbović, M.; Guo, J.; et al. CME–CME Interactions as Sources of CME Geoeffectiveness: The Formation of the Complex Ejecta and Intense Geomagnetic Storm in 2017 Early September. *Astrophys. J. Suppl. Ser.* **2020**, *247*, 21. [[CrossRef](#)]
66. Badruddin, B.; Aslam, O.P.M.; Derouich, M.; Asiri, H.; Kudela, K. Forbush Decreases and Geomagnetic Storms During a Highly Disturbed Solar and Interplanetary Period, 4–10 September 2017. *Space Weather* **2019**, *17*, 487–496. [[CrossRef](#)]
67. Miteva, R.; Klein, K.L.; Malandraki, O.; Dorrian, G. Solar Energetic Particle Events in the 23rd Solar Cycle: Interplanetary Magnetic Field Configuration and Statistical Relationship with Flares and CMEs. *Sol. Phys.* **2013**, *282*, 579–613. [[CrossRef](#)]
68. Ravishankar, A.; Michałek, G. Non-interacting coronal mass ejections and solar energetic particles near the quadrature configuration of Solar TERrestrial RELations Observatory. *Astron. Astrophys.* **2020**, *638*, A42. [[CrossRef](#)]
69. Pandey, U.; Singh, B.; Singh, O.P.; Saraswat, V.K. Solar flare induced ionospheric D-region perturbation as observed at a low latitude station Agra, India. *Astrophys. Space Sci.* **2015**, *357*, 35. [[CrossRef](#)]
70. Gavrilov, B.G.; Ermak, V.M.; Lyakhov, A.N.; Poklad, Y.V.; Rybakov, V.A.; Ryakhovsky, I.A. Reconstruction of the Parameters of the Lower Midlatitude Ionosphere in M- and X-Class Solar Flares. *Geomagn. Aeron.* **2020**, *60*, 747–753. [[CrossRef](#)]
71. Venkatesham, K.; Singh, R. Extreme space-weather effect on D-region ionosphere in Indian low latitude region. *Curr. Sci.* **2018**, *114*, 1923–1926. [[CrossRef](#)]
72. Thomson, N.R.; Rodger, C.J.; Clilverd, M.A. Large solar flares and their ionospheric D region enhancements. *J. Geophys. Res. Space Phys.* **2005**, *110*. [[CrossRef](#)]
73. Grubor, D.; Šulić, D.; Žigman, V. The response of the Earth-ionosphere VLF waveguide to the January 15–22 2005 solar events. In Proceedings of the IUGG XXIV General Assembly, Perugia, Italy, 2–13 July 2007.
74. Kolarski, A.; Grubor, D. Monitoring VLF signal perturbations induced by solar activity during January 2005. In Proceedings of the The XIX Serbian Astronomical Conference, Belgrade, Serbia, 13–17 October 2020; pp. 387–390.
75. Kumar, S.; Kumar, A.; Menk, F.; Maurya, A.K.; Singh, R.; Veenadhari, B. Response of the low-latitude D region ionosphere to extreme space weather event of 14–16 December 2006. *J. Geophys. Res. Space Phys.* **2015**, *120*, 788–799. [[CrossRef](#)]
76. Tan, L.M.; Thu, N.N.; Ha, T.Q.; Marbouti, M. Study of solar flare induced D-region ionosphere changes using VLF amplitude observations at a low latitude site. *Indian J. Radio Space Phys.* **2014**, *43*, 197–246.
77. McRae, W.M.; Thomson, N.R. Solar flare induced ionospheric D-region enhancements from VLF phase and amplitude observations. *J. Atmos. Sol.-Terr. Phys.* **2004**, *66*, 77–87. [[CrossRef](#)]
78. Zhao, L.L.; Zhang, H. Transient galactic cosmic-ray modulation during solar cycle 24: A comparative study of two prominent forbush decrease events. *Astrophys. J.* **2016**, *827*, 13. [[CrossRef](#)]
79. Lingri, D.; Mavromichalaki, H.; Belov, A.; Eroshenko, E.; Yanke, V.; Abunin, A.; Abunina, M. Solar Activity Parameters and Associated Forbush Decreases During the Minimum between Cycles 23 and 24 and the Ascending Phase of Cycle 24. *Sol. Phys.* **2016**, *291*, 1025–1041. [[CrossRef](#)]

Disclaimer/Publisher’s Note: The statements, opinions and data contained in all publications are solely those of the individual author(s) and contributor(s) and not of MDPI and/or the editor(s). MDPI and/or the editor(s) disclaim responsibility for any injury to people or property resulting from any ideas, methods, instructions or products referred to in the content.

Manuscript Details

Manuscript number	ASTROPARTPHYS_2018_197
Title	A novel method for atmospheric correction of cosmic-ray data based on principal component analysis
Article type	Full Length Article

Abstract

A new method for atmospheric correction of cosmic ray data is designed. It's fully empirical, based on the principal component analysis. The method requires knowledge of the pressure and the temperature profile of the atmosphere. It's applicable to all muon detectors. The method is tested on muon data from two detectors in Belgrade cosmic ray station, one located on the ground level and the other at the depth of 25 mwe. Correction reduces variance by 64.5% in ground level detector data and 38.1% in underground data. At the same time, the amplitude of the annual variation is reduced by 86.0% at ground level and 54.9% underground. With the same data sets the presented method performs better than the integral correction method.

Keywords cosmic-ray muons; atmospheric correction; temperature effect; principal component analysis

Corresponding Author Aleksandar Dragic

Corresponding Author's Institution Institute of Physics

Order of Authors Mihailo Savic, Aleksandar Dragic, Dimitrije Maletic, Nikola Veselinovic, Radomir Banjanac, Dejan Joković, Vladimir Udovičić

Submission Files Included in this PDF

File Name [File Type]

TCORRPCA.pdf [Manuscript File]

Submission Files Not Included in this PDF

File Name [File Type]

TCorrPCA.zip [LaTeX Source File]

To view all the submission files, including those not included in the PDF, click on the manuscript title on your EVISE Homepage, then click 'Download zip file'.

1
2
3
4
5
6
7
8
9
10
11
12
13
14
15
16
17

A novel method for atmospheric correction of cosmic-ray data based on principal component analysis

M. Savić^a, A. Dragić^{a,*}, D. Maletić^a, N. Veselinović^a, R. Banjanac^a, D.
Joković^a, and V. Udovičić^a

^a*Institute of Physics, University of Belgrade, Pregrevica 118, 11080 Zemun, Serbia*

Abstract

19
20
21
22
23
24
25
26
27
28
29
30
31
32
33
34

A new method for atmospheric correction of cosmic ray data is designed. It's fully empirical, based on the principal component analysis. The method requires knowledge of the pressure and the temperature profile of the atmosphere. It's applicable to all muon detectors. The method is tested on muon data from two detectors in Belgrade cosmic ray station, one located on the ground level and the other at the depth of 25 mwe. Correction reduces variance by 64.5% in ground level detector data and 38.1% in underground data. At the same time, the amplitude of the annual variation is reduced by 86.0% at ground level and 54.9% underground. With the same data sets the presented method performs better than the integral correction method.

1. Introduction

37
38
39
40
41
42
43
44
45
46
47

Count rates of ground based or underground cosmic-ray (CR) muon detectors are affected by atmospheric parameters (air pressure and temperature at different heights). The proper description of atmospheric effects is necessary for understanding primary CR variations, originating outside of the atmosphere.

5
42
43
44
45
46
47

Early studies in CR temporal variations [1, 2] revealed the existence of a variation caused by the change of air pressure, the so called "barometric effect". With the increase in pressure the atmosphere represents thicker absorber, re-

*Corresponding author
Email address: dragic@ipb.ac.rs (A. Dragić)

57
58
59
60
61
62
63
64
65
66
67
68
69
70
71
72
73
74
75
76
77
78
79
80
81
82
83
84
85
86
87
88
89
90
91
92
93
94
95
96
97
98
99
100
101
102
103
104
105
106
107
108
109
110
111
112

sulting in reduced number of muons reaching the ground level. Therefore, muon
10 flux is expected to be anti-correlated with atmospheric pressure.

Observed negative correlation between muon flux and atmospheric tempera-
ture, the so called "negative temperature effect", has been explained by Blackett
[3] to be a consequence of muon decay. During warm periods the atmosphere is
expanded and the main layer of muon production ($\sim 100\text{mb}$) is higher, resulting
15 in longer muon path and lower surviving probability to the ground level. Low
energy muons are more affected, while the flux of high energy muons, capable
of penetrating great depth, does not suffer. At deep underground experiments
another type of temperature effect, "positive temperature effect" is pronounced
[4]. Development of nuclear emulsions capable of detecting energetic charged
20 particles lead to discovery of charged pions in CRs and $\pi - \mu$ decay [5, 6, 7]. The
positive temperature effect is interpreted as a consequence of later process [8, 9].
Pions created in the interactions of primary CR particles with the atmospheric
nuclei can decay into muons or interact with air nuclei. Higher temperature in
the production layer means lower air density and consequently, lower interaction
25 probability and higher muon production.

In most cases linear regression is sufficient to account for the barometric effect.
The temperature effects are treated by empirical and theoretical methods. In
addition to the barometric coefficient β , **the method of effective level of
generation** [8] introduces two empirical parameters: α_H to encounter for muon
30 intensity variations δI_μ correlated with the change of the height of generation
level δH (negative effect) and α_T for the changes of the temperature of this
level (positive temperature effect).

$$\delta I_\mu = \beta \delta p + \alpha_H \delta H + \alpha_T \delta T \quad (1)$$

Duperier method has been successfully used in many studies for the atmospheric
corrections of muon data ([10, 11, 12, 13, 14, 15] etc.).

35 It's been argued [16, 17] that for correct temperature correction of muon
detectors count rate the vertical temperature profile of the entire atmosphere
needs to be known. In the so called **integral method** the muon intensity

variations caused by the temperature are described by the equation:

$$\frac{\delta I_\mu}{I_\mu} = \int_0^{h_0} W_T(h) \delta T(h) dh \quad (2)$$

where $\delta T(h)$ is the variation of temperature at isobaric level h with respect to the referent value and $W_T(h)$ is the temperature coefficient density. The coefficients are calculated theoretically and the best known calculations are given in references [18] and [19].

The **mass-average temperature method** [20] is a variant of the integral method, based on the assumption of small changes of the temperature coefficient density $W_T(h)$ with the atmospheric depth h allowing its average value \overline{W}_T to be put in front of the integral in the equation (2) and on determination of the mass-averaged temperature T_m :

$$\frac{\delta I_\mu}{I_\mu} = \overline{W}_T(h) \int_0^{h_0} \delta T(h) dh = \overline{W}_T(h) \cdot \delta T_m \quad (3)$$

The method was used in numerous studies ([21], [22], [23] to name a few).

Another form of the integral method is **the effective temperature method** [24]. By introducing the temperature coefficient α_T :

$$\alpha_T = \int_0^{h_0} W_T(h) dh$$

the equation (2) can be normalized as:

$$\frac{\delta I_\mu}{I_\mu} = \int_0^{h_0} W_T(h) dh \cdot \frac{\int_0^{h_0} W_T(h) \delta T(h) dh}{\int_0^{h_0} W_T(h) dh} = \alpha_T \cdot \delta T_{eff} \quad (4)$$

where the effective temperature T_{eff} is defined as:

$$T_{eff} = \frac{\int_0^{h_0} W_T(h) T(h) dh}{\int_0^{h_0} W_T(h) dh}$$

The later method is popular with the underground muon telescopes [25, 26].

Different methods of atmospheric correction might be compared on the basis of several criteria. One is requirement of the lowest variance of corrected data. Since the most prominent temperature effect on CR time series is seasonal variation, another criterion is the smallest residual amplitude of seasonal variation

169
170
171
172
173
174
175 after correction is applied. The later does not take into account possible genuine
176 seasonal variation of non-atmospheric origin.
177

178 Early studies comparing Dupierier's empirical and Dorman's theoretical meth-
179 ods ([27] and references therein) found similar accuracy of two methods, with
180 essentially the same corrections at sea level, but with the integral method over-
181 estimating the temperature effect.
182
183

184 A more recent study [28] compared different methods of atmospheric cor-
185 rection for data from Nagoya and Tibet supertelescopes, as well as Yakutsk,
186 Moscow and Novosibirsk telescopes. They found the mass-averaged tempera-
187 ture method to practically coincide with the integral method. On the other
188 hand, the effective level of generation method for Nagoya shows discrepancy
189 from the integral method in wintertime, being able to eliminate only 50% of the
190 temperature effect. Even with the integral method in the case of Tibet muon
191 telescope the removal of temperature effect is achieved with the density of tem-
192 perature coefficients 3 times higher than calculated ones. The precise origin of
193 disagreement is unknown.
194
195
196
197

198 The method of the effective level of generation takes care of key physical
199 causes of the temperature effect. However, it does not make optimal use of
200 the temperature data. Also, the assumption of a single level of main muon
201 production is a simplification. Detailed CORSIKA simulation of the shower
202 development in the atmosphere reveals the actual distribution of the muon gener-
203 ation heights (see Figure 1).
204
205

206 Different implementations of the integral method exist, employing different
207 approximations, choice of parameters, models of the atmosphere, whether kaon
208 contribution is taken into account, leading to differences in calculated density
209 temperature coefficients (see for instance discussion in [29]). As already men-
210 tioned, on the case of Tibet telescope [28] theoretical calculations do not fully
211 correspond to the local experimental conditions and the origin of disagreement
212 is difficult to trace.
213
214

215 The effective temperature method lacks universality, since it works best with
216 the data from deep underground detectors.
217
218

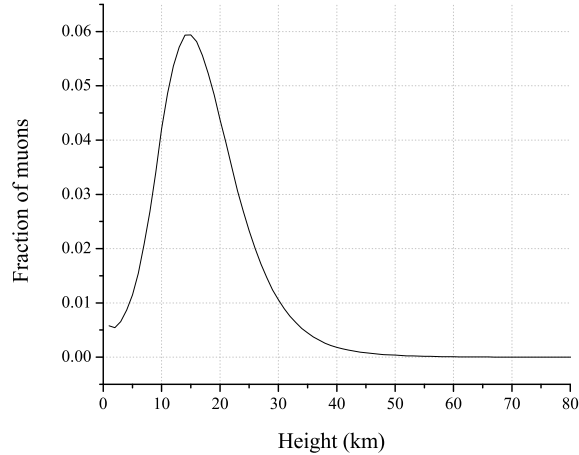


Figure 1: Distribution of muon generation at different heights in the atmosphere, according to CORSIKA simulation.

Here we propose a new method for atmospheric corrections. It's fully empirical, makes use of the available temperature data through entire atmosphere and it's applicable to arbitrary detector irrespective to energy sensitivity and is simple to implement. The method is based on the principal component analysis, thus reducing dimensionality of the problem, exploiting correlations between atmospheric variables and ensuring mutual independence of correction parameters. The price is loss of clear physical interpretation of these parameters, since the pressure and the temperature at different levels are treated on equal footing.

2. Method Description

2.1. Meteorological data

Set of variables that enter principal component decomposition consists of atmospheric temperature profile for the given location as well as locally measured atmospheric pressure. Meteorological balloon soundings for Belgrade are not done frequently enough to be used for suggested analysis. As a consequence,

281
282
283
284
285
286
287
288 100 modeled temperatures were used instead. However, there were enough balloon
289 sounding data for testing consistency of the modeled temperatures.

290 There are several weather and global climate numerical models available
291 today. Here, Global Forecast System [30] data was used. GFS is a weather fore-
292 cast model, developed by National Centers for Environmental Prediction [31],
293 which is able to predict large number of atmospheric and land-soil parameters.
294 105 Apart from forecast data, GFS also provides retrospective data produced taking
295 into account most recent measurements by a world wide array of meteorologi-
296 cal stations. Retrospective data are produced four times a day at 00:00, 06:00,
297 12:00 and 18:00 UTC. Data with finer temporal resolution are obtained by cubic
298 spline interpolation. Temperatures for the following 25 isobaric levels (in mb)
299 110 were used for initial analysis: 10, 20, 30, 50, 70, 100, 150, 200, 250, 300, 350,
300 400, 450, 500, 550, 600, 650, 700, 750, 800, 850, 900, 925, 975, 1000. Hori-
301 zontal spatial resolution for modeled data is 0.5 degrees, so coordinates closest
302 to the experiment location (latitude 44.86, longitude 20.39), were selected with
303 this precision. Before any further analysis was done, GFS modeled temperature
304 115 profiles were compared to local meteorological balloon soundings for Belgrade,
305 where balloon data was available. Figure 1 shows profile of differences between
306 modeled and measured values for different isobaric levels. Disagreement was
307 found between measured and modeled temperature at the lowest level. As a
308 result, it was decided not to use temperature data for isobaric level of 1000 mb
309 120 in further analysis. Ground temperature data measured by local meteorological
310 stations was used for lowest layer instead. Similar problem with the GFS data
311 was reported before by [28] who found $5^{\circ}C$ deviation in the summertime near
312 ground level at Yakutsk location.

313
314
315
316
317
318
319
320
321
322 125 Atmospheric pressure and ground level temperature from the Republic Hydro-
323 meteorological Service of Serbia was used to compose unique local pressure and
324 temperature time series.
325
326
327
328
329
330

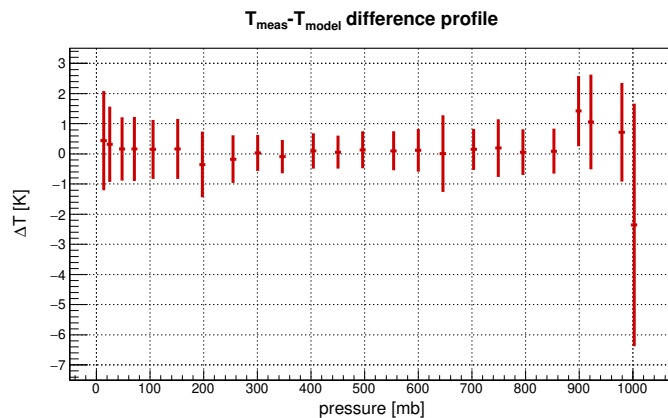


Figure 2: Distribution of differences between measured temperatures and modeled by GFS.

2.2. Cosmic-ray data

The analysis is performed on data from Belgrade muon detectors. The Belgrade cosmic-ray station, together with the present detector arrangement is described in details elsewhere [32]. Two muon detectors are located in the laboratory, one at the ground level and the other at the depth of 25 mwe. Data are recorded on the event-by event basis and can be integrated into the time series with the arbitrary time resolution. For most purposes hourly data are used. Muon detectors are sensitive to primary cosmic rays of 59 GeV median energy in the case of ground level detector and 137 GeV for underground detector.

2.3. Principal component decomposition

Principal component analysis is a convenient and widely used data reduction method when dealing with strongly correlated data. It transforms the original set of variables into a set of uncorrelated variables (called principal components (PC)). The principal components are ordered according to decreasing variance. In our case, there are 26 input variables: 24 modeled temperatures (isobaric level 1000 mb temperature excluded), locally measured ground level temperature and local atmospheric pressure. Initial variables were centered and normalized before decomposition. After decomposition, a new set of 26 principal components was

393
394
395
396
397
398
399 obtained. Decomposition should not be regarded as universal, but it should be
400 redone for every location and period under study.
401

402 One year was selected as a suitable time period for the analysis, in order to
403 reduce possible seasonal bias, due to atmospheric temperature annual variation.
404
405 Additional criteria were quality and consistency of muon data. Taking this
150 406 into account, final time interval selected for analysis was from 01.06.2010 to
407 31.05.2011.
408

409 Figure 3 shows composition plots for the first nine principal components,
410 that account for 98% of total variance. X-axis represents input atmospheric
411 variables, first being atmospheric pressure, followed by 10 mb layer tempera-
155 412 ture, last being ground level local temperature. Y-axis represents decomposi-
413 tion rotations for a given principal component. Interesting features observed on
414 these plots are that first two principal components depend almost exclusively
415 on temperature. The first one is mostly combination of temperatures in the
416 troposphere (isobaric levels 250 - 1000 mb) with almost equal weights. The
417 second eigenvector accounts for significant variance of temperatures in higher
418 atmospheric levels (10 - 250 mb), with the strongest contribution centered in the
160 419 tropopause. Components 3 to 6 have mixed p-T composition. The correlation of
420 atmospheric pressure and temperature at different heights is not surprising. The
421 diurnal and semi-diurnal oscillations of pressure are attributed to the warming
422 of the upper atmosphere by the Sun 33. This correlation makes it impossible
423 to define a single barometric parameter in PCA based method of atmospheric
424 corrections. It's worth mentioning that Dorman 34 recognizes three different
425 barometric effects: absorption, decay and generation effect. It also indicates
165 426 that empirical methods with separated pressure and temperature corrections
427 might lead to overcorrection.
428
429
430
431
432
170 433
434

435 The values of the eigenvectors for these first nine components are also given
436 in Table 1.
437

438 Figure 4 shows plot of proportion of variance as well as plot of cumulative
439 variance for obtained principal components. Corresponding numerical values
440 are given in Table 2.
175 441
442
443
444
445
446
447
448

449
 450
 451
 452
 453
 454
 455
 456
 457
 458
 459
 460
 461
 462
 463
 464
 465
 466
 467
 468
 469
 470
 471
 472
 473
 474
 475
 476
 477
 478
 479
 480
 481
 482
 483
 484
 485
 486
 487
 488
 489
 490
 491
 492
 493
 494
 495
 496
 497
 498
 499
 500
 501
 502
 503
 504

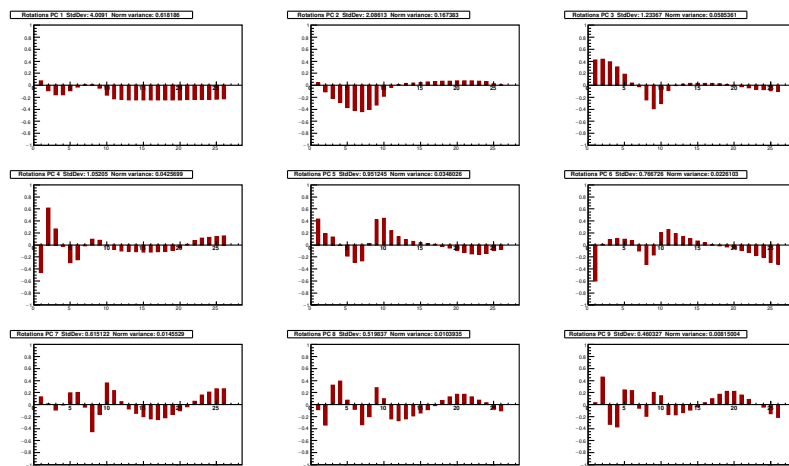


Figure 3: Composition of nine principal components with largest variance (in decreasing order). Input variables are displayed on x-axis: 1 being pressure, 2 temperature of 10mb isobaric level, 26 being local ground level temperature. Y-axis represents rotations.

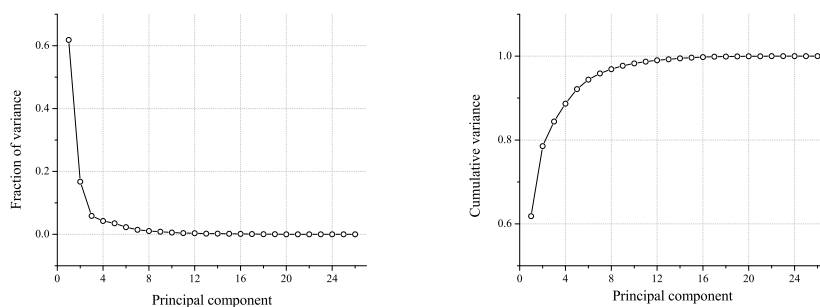


Figure 4: Proportion of variance (left) and cumulative proportion of variance (right) for all 26 principal components

Usually, only a first few principal components (containing high fraction of total variance) are of practical interest. There are various different methods and rules for choosing how many PCs to retain in the analysis, none completely free of subjectivity (see for example a thorough discussion in [35]). A rule based on cumulative percentage of total variation usually recommends to retain PCs responsible for 70-90% of total variation. When one or two components are

505
506
507
508
509
510
511
512
513
514
515
516
517
518
519
520
521
522
523
524
525
526
527
528
529
530
531
532
533
534
535
536
537
538
539
540
541
542
543
544
545
546
547
548
549
550
551
552
553
554
555
556
557
558
559
560

Table 1: Definition of first nine principal components.

Variables	Principal components								
	PC1	PC2	PC3	PC4	PC5	PC6	PC7	PC8	PC9
T(10)	0.07699	0.04117	0.44694	-0.61285	0.16301	-0.57121	0.14028	-0.08106	0.03443
T(20)	-0.0947	-0.11603	0.43488	0.5344	0.43741	-0.11036	-0.04499	-0.15825	0.46469
T(30)	-0.16947	-0.21766	0.35754	0.18029	0.20527	0.08546	-0.07719	0.20635	-0.40309
T(50)	-0.16476	-0.27825	0.29593	-0.02505	-0.02204	0.14134	0.00634	0.28574	-0.47812
T(70)	-0.09124	-0.37682	0.20969	-0.17322	-0.25798	0.12084	0.19349	0.14645	0.18493
T(100)	-0.01483	-0.42304	0.04507	-0.08651	-0.3472	0.09965	0.18155	0.01024	0.31886
T(150)	0.02192	-0.43132	-0.02451	0.08228	-0.25692	-0.04937	-0.06464	-0.3103	0.1183
T(200)	0.01487	-0.40127	-0.24673	0.03037	0.012	-0.32566	-0.43658	-0.28393	-0.23316
T(10)	-0.04737	-0.33404	-0.38636	-0.13563	0.40141	-0.2069	-0.16852	0.31181	0.07995
T(250)	-0.16218	-0.17984	-0.29739	-0.18123	0.43708	0.18013	0.32866	0.13662	0.17389
T(300)	-0.22473	-0.03266	-0.07561	-0.14073	0.21179	0.26504	0.23807	-0.27931	-0.06785
T(350)	-0.2369	0.01439	0.00488	-0.12991	0.0998	0.1988	0.05306	-0.31612	-0.0771
T(400)	-0.23956	0.03362	0.02958	-0.12159	0.04075	0.14932	-0.06959	-0.27189	-0.04852
T(450)	-0.24028	0.04271	0.0402	-0.11503	0.00384	0.10744	-0.14772	-0.21165	-0.01823
T(500)	-0.24005	0.04935	0.0428	-0.11304	-0.02187	0.07218	-0.19893	-0.14512	0.03068
T(550)	-0.23958	0.05695	0.03965	-0.11295	-0.03254	0.0388	-0.23263	-0.06843	0.08056
T(600)	-0.23881	0.06549	0.03681	-0.10649	-0.04369	0.01102	-0.24562	0.02401	0.12499
T(650)	-0.23854	0.07279	0.0236	-0.09184	-0.06132	-0.01542	-0.21788	0.12597	0.15977
T(700)	-0.23835	0.0801	0.00429	-0.06052	-0.07601	-0.04668	-0.16785	0.19559	0.14932
T(750)	-0.23842	0.08071	-0.01837	-0.01332	-0.09245	-0.07308	-0.11295	0.22563	0.12401
T(800)	-0.23814	0.07557	-0.03907	0.05036	-0.10989	-0.09943	-0.04696	0.19596	0.07735
T(850)	-0.23701	0.0675	-0.06202	0.1081	-0.11988	-0.12745	0.04989	0.13672	0.0304
T(900)	-0.23535	0.05462	-0.07977	0.14776	-0.11454	-0.16955	0.16551	0.06204	-0.02952
T(925)	-0.23414	0.04606	-0.08313	0.15641	-0.10257	-0.19925	0.21877	0.01715	-0.05804
T(975)	-0.23108	0.00789	-0.08827	0.13022	-0.05888	-0.28046	0.284	-0.11523	-0.12249
T(1000)	-0.22494	-0.01582	-0.10092	0.13401	-0.04977	-0.30749	0.28553	-0.16516	-0.15908

561
562
563
564
565
566
567
568
569
570
571
572
573
574
575
576
577
578
579
580
581
582
583
584
585
586
587
588
589
590
591
592
593
594
595
596
597
598
599
600
601
602
603
604
605
606
607
608
609
610
611
612
613
614
615
616

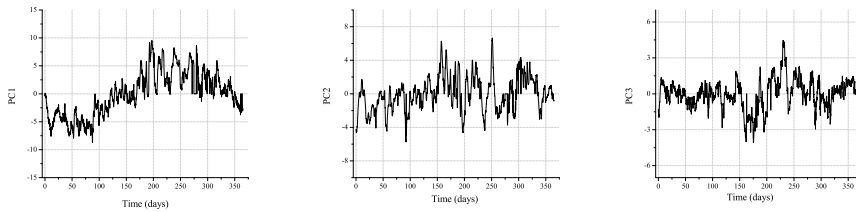
Table 2: Variance (individual and cumulative) for all 26 PCs.

Principal component	Eigenvalue	Percentage of variance	Cumulative variance (%)
1	4.0091	0.618186	0.618186
2	2.08613	0.167383	0.785569
3	1.23367	0.0585361	0.844105
4	1.05205	0.0425699	0.886675
5	0.951245	0.0348026	0.921478
6	0.766726	0.0226103	0.944088
7	0.615122	0.0145529	0.958641
8	0.519837	0.0103935	0.969034
9	0.460327	0.00815004	0.977184
10	0.382006	0.00561263	0.982797
11	0.32832	0.00414592	0.986943
12	0.294489	0.00333553	0.990278
13	0.247876	0.00236317	0.992642
14	0.239462	0.00220546	0.994847
15	0.206157	0.00163465	0.996482
16	0.184453	0.00130857	0.99779
17	0.144657	8.04834E-4	0.998595
18	0.119676	5.5086E-4	0.999146
19	0.0938189	3.38538E-4	0.999485
20	0.0739496	2.10328E-4	0.999695
21	0.0586253	1.32189E-4	0.999827
22	0.0414996	6.62391E-5	0.999893
23	0.0338811	4.41511E-5	0.999937
24	0.0281359	3.04472E-5	0.999968
25	0.0219102	1.84637E-5	0.999986
26	0.0188263	1.36319E-5	1

dominant, higher value (95%) is appropriate. In our case it would mean keeping first 6 PCs. According to Kaiser's rule only PCs with the eigenvalue $\lambda > 1$

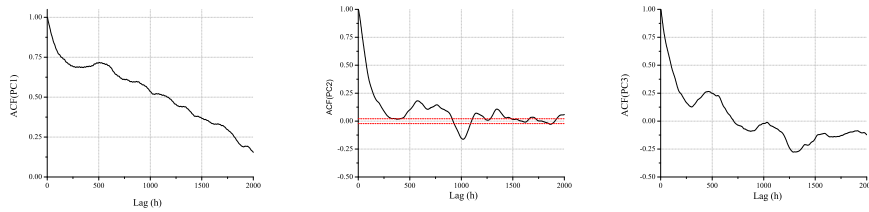
617
 618
 619
 620
 621
 622
 623 should be retained. Jolliffe [35] suggested 0.7 as correct level, exceeded by six of
 624 our PCs. Another rule proposes to retain components with the eigenvalue above
 625 mean, a condition satisfied by first seven of our PCs. Another popular model
 626 is broken stick, but in application to our problem is too restrictive, leading to
 627 only two relevant PCs. The scree graph or log-eigenvalue diagram don't provide
 628 clean cut with our set of PCs.
 629
 630
 631

632 To test the meaningfulness of potentially relevant PCs, the time series from
 633 PC data are constructed and tested whether they are distinguishable from white
 634 noise. The procedure is often done when principal component analysis is applied
 635 to atmospheric physics problems [36]. The time series with hourly resolution
 636 for the first three PCs are plotted on Figure 5.
 637
 638



639
 640
 641
 642
 643
 644
 645
 646
 647
 648 Figure 5: Time series of the first 3 PCs.

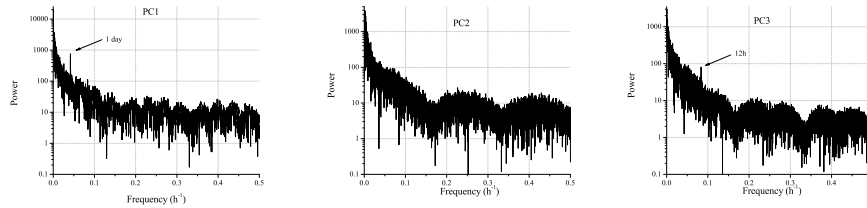
649 The subsequent temperature and pressure measurements are highly corre-
 650 lated, as evident from autocorrelation function plot for selected PCs (Figure
 651 6).
 652
 653



654
 655
 656
 657
 658
 659
 660
 661
 662
 663 Figure 6: Autocorrelation function of the first 3 PCs.

664 The spectral analysis of the PC time series reveals, for PCs with the strong

673
674
675
676
677
678
679
680 pressure component, semi-diurnal periodicity in addition to diurnal (Figure 7).
681



690 Figure 7: Spectral analysis of time series of the first 3 PCs.

691
692 Since our purpose is the regression of muon data with principal components,
693 selecting the components with significantly high variance is not the main is-
694 sue. It is more important to identify PCs with high correlation with CR data.
695 Components with relatively low variance, can have high predictive power.
696
697

698 *2.4. Correlation of principal components with CR muon count rate and correc-*
699 *tion of muon data*
700

701 Scatter plot of muon count rate vs. PCs, together with the linear fit for
702 the first nine principal components are shown on Figure 8 (GLL) and Figure
703 9 (UL). In the analysis hourly summed muon counts and principal component
704 values for the respective hour were used. To minimize the effect of geomagnetic
705 values for the respective hour were used. To minimize the effect of geomagnetic
706 disturbances, only data for international quiet days were taken into account.
707 The values of correlation coefficients are listed in Table 3.
708
709

710 Table 3: Correlation coefficients between principal components and muon count rate in the
711 ground level laboratory (GLL) and underground laboratory (UL).
712
713

PC	1	2	3	4	5	6	7	8	9	10	11	12	13	14	15	16	17	18	19	20	21	22	23	24	25	26
GLL	0.43	0.01	-0.37	0.48	-0.55	0.30	-0.01	0.03	-0.01	0.06	0.00	-0.04	0.00	0.01	0.02	-0.01	0.00	-0.01	-0.01	0.03	-0.03	0.00	0.02	-0.01	0.04	0.02
UL	0.26	0.02	-0.48	0.21	-0.19	0.52	0.02	0.04	0.07	0.04	0.01	-0.04	-0.07	0.06	-0.02	-0.05	0.04	0.04	-0.02	0.00	0.00	0.01	0.00	-0.03	0.01	0.01

714
715
716
717
718 Principal components PC1, PC3, PC4, PC5 and PC6 have been identified
719 as ones with significant contribution to the muon flux variation. Interestingly
720 enough, the PC2, responsible for 16.7% variance of the meteorological data has
721
722
723
724
725
726
727
728

729
730
731
732
733
734
735
736
737
738
739
740
741
742
743
744
745
746
747
748
225
749
750
751
752
753
754
755
756
757
758
759
760
761
762
763
764
765
766
767
768
769
770
771
772
773
774
775
776
777
778
779
780
781
782
783
784

very little effect on muon flux, at neither ground nor underground level. Ground level muon flux variation is more affected by the first principal component, depending chiefly on the temperature in the troposphere. The finding agrees with usual negative temperature effect. The other PCs are difficult to compare with traditional correction parameters. Yet, the effect of PC3, that is composed more from upper atmosphere temperatures and hence could be loosely associated with positive temperature effect, is more pronounced for the underground muon flux. Fourth and fifth principal components with strong pressure contribution affect more ground level muon flux. On the other hand, PC6, also the one with high pressure component, has more pronounced influence on underground muon flux.

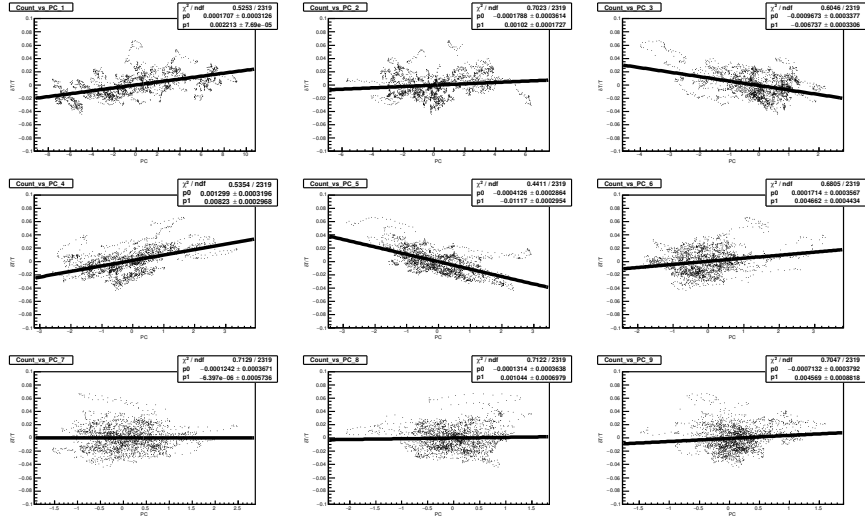


Figure 8: Muon count dependence on principal components for the first nine principal components (GLL).

Gradients obtained from the fits for the significant principal components 1, 3, 4, 5 and 6 were then used to calculate the PCA corrected muon count according to the formula:

$$N_{\mu}^{(corr)} = N_{\mu} - \langle N_{\mu} \rangle \sum_i k_i PC_i, \quad i = 1, 3, 4, 5, 6 \quad (5)$$

where $N_{\mu}^{(corr)}$ corr is the corrected muon count, N_{μ} is the raw muon count,

785
786
787
788
789
790
791
792
793
794
795
796
797
798
799
800
801
802
803
804
805
806
807
808
809
810
811
812
813
814
815
816
817
818
819
820
821
822
823
824
825
826
827
828
829
830
831
832
833
834
835
836
837
838
839
840

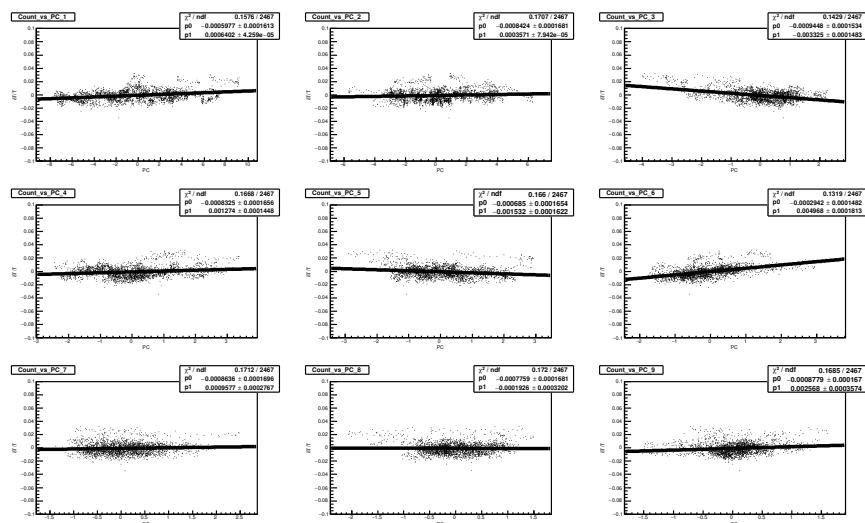


Figure 9: Muon count dependence on principal components for the first nine principal components (UL).

230 $\langle N_\mu \rangle$ is the mean count for the whole period, k_i are the gradients and PC_i
 are the corresponding principal components. Resulting corrected muon count
 time series are plotted on figures 8 (GLL) and 9 (UL) along with raw and pres-
 814 sure only corrected time series. Pressure corrected time series are produced for
 815 reference. Barometric coefficient was determined by applying linear regression
 816 to the same data set used for PCA. Data was previously corrected for tempera-
 817 ture effect using integral method, as in Ref. [37]. Pressure corrected and PCA
 818 corrected time series are fitted with sine function with annual period in order to
 819 illustrate how PCA correction affects yearly variation induced by temperature
 820 effect.

240 PCA based atmospheric corrections remove 64.5% of total variance in GLL
 826 time series and 38.1% in UL time series. Pressure corrected CR time series
 827 exhibit annual variation, a consequence of the temperature effect. The perfor-
 828 mance of the temperature correction may be tested by comparing the amplitude
 829 of the annual variation before and after correction. With presented method the
 830 amplitude of the annual variation is reduced by 86% (54.9%) in the case of GLL
 832
 245

841
842
843
844
845
846
847
848
849
850
851
852
853
854
855
856
857
858
859
860
861
862
863
864
865
866
867
868
869
870
871
872
873
874
875
876
877
878
879
880
881
882
883
884
885
886
887
888
889
890
891
892
893
894
895
896

(UL) with respect to the pressure only corrected time series.

To further test the new method, the atmospheric correction of GLL data are performed by the integral method. The correction resulted in 56.25% of variance reduction and 68.1% of reduction of the amplitude of the annual wave. At least in the case of our CR data set the new method performs somewhat better than the integral method.

250

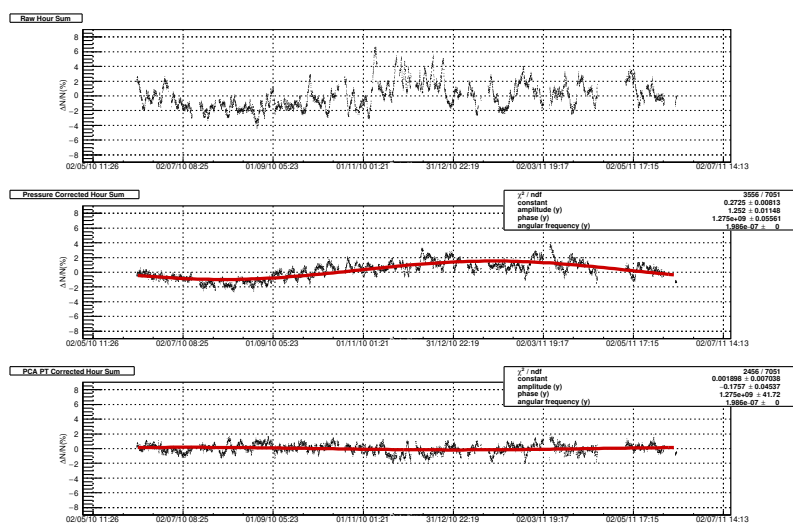


Figure 10: Raw (upper panel), pressure corrected (middle panel) and pressure+temperature (PCA method) corrected (lower panel) muon count for GLL.

897
898
899
900
901
902
903
904
905
906
907
908
909
910
911
912
913
914
915
916
917
918
919
920
921
922
923
924
925
926
927
928
929
930
931
932
933
934
935
936
937
938
939
940
941
942
943
944
945
946
947
948
949
950
951
952

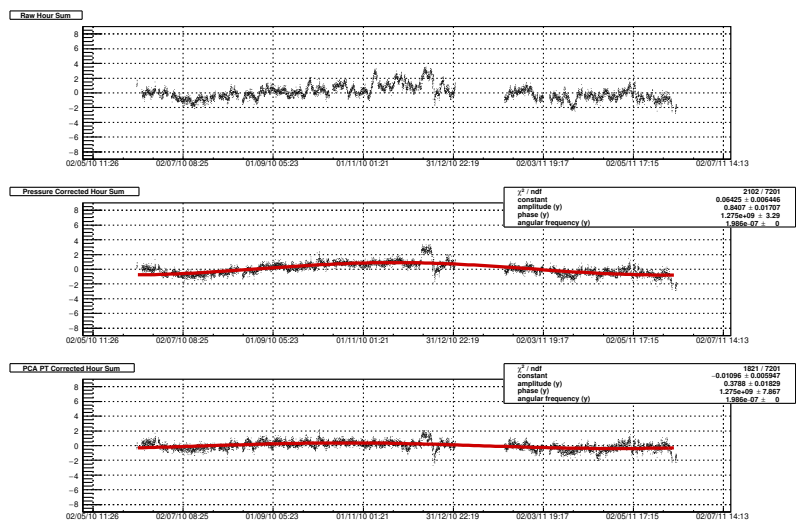


Figure 11: Raw, pressure corrected and pressure+temperature (PC method) corrected muon count for UL.

953
954
955
956
957
958
959
960

3. Conclusion

961 The principal component analysis is successfully used to construct a new
962 empirical method for the atmospheric corrections of CR muon data. The method
963 is equally applicable to all muon detectors, irrespective to location: ground level,
255 964 shallow or deep underground. It requires knowledge of the atmospheric pressure
965 and temperatures along the entire atmosphere, which is nowadays available in
966 databases such as GFS. The method is suitable for the near real-time correction,
967 with the delay defined by the availability of the atmospheric data (one day in
968 the case of present GFS data). When applied to Belgrade muon data from
969 two detectors (ground level and at 25 mwe), the method requires correction to
970 five parameters, determined from linear regression. With the same CR dataset,
971 the present method yields results superior to the integral method in terms of
972 variance reduction and reduction of the annual variation. The new method is
973 also suitable for temperature corrections of the neutron monitor data, which is
974 seldom done in practice.
265 975
976
977
978
979
980

981 **Acknowledgments** The authors are deeply grateful to Dr. Viktor Yanke
982 for the encouragement and useful advice.

983 The present work was funded by the Ministry of Education, Science and
984 Technological Development of the Republic of Serbia, under the Project No.
270 985 171002.
986
987
988

References

- 989
990
991 [1] L. Myssowsky, L. Tuwim, Unregelmäßige intensitätsschwankungen der
992 höhenstrahlung in geringer seehöhe, Zeitschrift für Physik 39 (2-3) (1926)
993 146–150.
275 994
995
996 [2] E. Steinke, Über schwankungen und barometereffekt der kosmischen ultra-
997 strahlung im meeresniveau, Zeitschrift für Physik 64 (1-2) (1930) 48–63.
998
999 [3] P. M. Blackett, On the instability of the barytron and the temperature
1000 effect of cosmic rays, Physical Review 54 (11) (1938) 973.
1001
1002
1003
1004
1005
1006
1007
1008

- 1009
1010
1011
1012
1013
1014
1015
1016
1017
1018
1019
1020
1021
1022
1023
1024
1025
1026
1027
1028
1029
1030
1031
1032
1033
1034
1035
1036
1037
1038
1039
1040
1041
1042
1043
1044
1045
1046
1047
1048
1049
1050
1051
1052
1053
1054
1055
1056
1057
1058
1059
1060
1061
1062
1063
1064
- 280 [4] M. Forro, Temperature effect of cosmic radiation at 1000-m water equivalent depth, *Physical Review* 72 (9) (1947) 868.
- [5] C. M. G. Lattes, G. P. Occhialini, C. F. Powell, Observations on the tracks of slow mesons in photographic emulsions, *Nature* 160 (4067) (1947) 486.
- 285 [6] C. M. G. Lattes, H. Muirhead, G. P. Occhialini, C. F. Powell, Processes involving charged mesons, *Nature* 159 (4047) (1947) 694.
- [7] G. Occhialini, C. Powell, Nuclear disintegrations produced by slow charged particles of small mass, *Nature* 159 (4032) (1947) 186.
- [8] A. Duperier, The meson intensity at the surface of the earth and the temperature at the production level, *Proceedings of the Physical Society. Section A* 62 (11) (1949) 684.
- 290 [9] A. Duperier, Temperature of the upper atmosphere and meson production, *Nature* 167 (4243) (1951) 312.
- [10] C. Baker, D. Hall, J. Humble, M. Duldig, Atmospheric correction analysis for the mawson muon telescopes, in: *International Cosmic Ray Conference*, Vol. 3, 1993, p. 753.
- 295 [11] A. Maghrabi, M. Almutayri, Atmospheric effect on cosmic ray muons at high cut-off rigidity station, *Advances in Astronomy* 2016.
- [12] C. R. Braga, A. Dal Lago, T. Kuwabara, N. J. Schuch, K. Munakata, Temperature effect correction for the cosmic ray muon data observed at the brazilian southern space observatory in são martinho da serra, in: *Journal of Physics: Conference Series*, Vol. 409, IOP Publishing, 2013, p. 012138.
- 300 [13] G. C. Castagnoli, M. Doderò, Temperature effect of the muon component underground and pion attenuation length, *Il Nuovo Cimento B* (1965-1970) 51 (2) (1967) 525–534.

- 1065
1066
1067
1068
1069
1070
1071
1072
1073
1074
1075
1076
1077
1078
1079
1080
1081
1082
1083
1084
1085
1086
1087
1088
1089
1090
1091
1092
1093
1094
1095
1096
1097
1098
1099
1100
1101
1102
1103
1104
1105
1106
1107
1108
1109
1110
1111
1112
1113
1114
1115
1116
1117
1118
1119
1120
- 305 [14] A. Fenton, R. Jacklyn, R. Taylor, Cosmic ray observations at 42 m we
underground at hobart, tasmania, *Il Nuovo Cimento* (1955-1965) 22 (2)
(1961) 285–295.
- [15] M. Zazyan, M. Ganeva, M. Berkova, V. Yanke, R. Hippler, Atmospheric
effect corrections of mustang data, *Journal of space weather and space*
310 *climate* 5 (2015) A6.
- [16] L. Dorman, The temperature effect of the hard component of cosmic rays,
in: *Doklady Akad. Nauk SSSR*, Vol. 95, 1954.
- [17] E. Feinberg, On the nature of cosmic ray barometric and temperature ef-
fects, *DAN SSSR* 53 (5) (1946) 421–424.
- 315 [18] L. I. Dorman, Cosmic ray variations, Tech. rep., FOREIGN TECHNOL-
OGY DIV WRIGHT-PATTERSON AFB OHIO (1957).
- [19] K. Maeda, M. Wada, Atmospheric temperature effect upon the cosmic-ray
intensity at sea level, *J. Sci. Research Inst.(Tokyo)* 48.
- [20] V. Dvornikov, Y. Y. Krest'yannikov, A. Sergeev, Determination of the
320 variation of average-mass temperature of the atmosphere by data of cosmic
ray intensity., *Geomagnetism and aeronomy* 16 (1976) 923–925.
- [21] V. Yanchukovsky, G. Y. Filimonov, R. Hisamov, Atmospheric variations in
muon intensity for different zenith angles, *Bulletin of the Russian Academy*
of Sciences: Physics 71 (7) (2007) 1038–1040.
- 325 [22] R. De Mendonça, C. Braga, E. Echer, A. Dal Lago, K. Munakata,
T. Kuwabara, M. Kozai, C. Kato, M. Rockenbach, N. Schuch, et al.,
The temperature effect in secondary cosmic rays (muons) observed at the
ground: analysis of the global muon detector network data, *The Astro-*
physical Journal 830 (2) (2016) 88.
- 330 [23] A. Dmitrieva, I. Astapov, A. Kovylyaeva, D. Pankova, Temperature effect
correction for muon flux at the earth surface: estimation of the accuracy

1121
1122
1123
1124
1125
1126
1127 of different methods, in: Journal of Physics: Conference Series, Vol. 409,
1128 IOP Publishing, 2013, p. 012130.
1129

1130 [24] P. H. Barrett, L. M. Bollinger, G. Cocconi, Y. Eisenberg, K. Greisen, Inter-
1132 pretation of cosmic-ray measurements far underground, Reviews of Modern
335 Physics 24 (3) (1952) 133.
1134

1135 [25] S. Tilav, P. Desiati, T. Kuwabara, D. Rocco, F. Rothmaier, M. Simmons,
1136 H. Wissing, et al., Atmospheric variations as observed by icecube, arXiv
1137 preprint arXiv:1001.0776.
1138
1139

1140 [26] P. Adamson, C. Andreopoulos, K. Arms, R. Armstrong, D. Auty, D. Ayres,
1141 C. Backhouse, J. Barnett, G. Barr, W. Barrett, et al., Observation of muon
1142 intensity variations by season with the minos far detector, Physical Review
1143 D 81 (1) (2010) 012001.
1144
1145

1146 [27] C. H., B. M., S. J. F., Introduction of meteorological correc-
1147 tions into meson monitor data, Tellus 19 (1) (1967) 143–160.
345

1148 [arXiv:https://www.onlinelibrary.wiley.com/doi/pdf/10.1111/j.2153-3490.1967.tb01468.x](https://www.onlinelibrary.wiley.com/doi/pdf/10.1111/j.2153-3490.1967.tb01468.x),
1149 [doi:10.1111/j.2153-3490.1967.tb01468.x](https://doi.org/10.1111/j.2153-3490.1967.tb01468.x).
1150

1151 [28] M. D. Berkova, A. V. Belov, E. A. Eroshenko, V. G. Yanke, Temperature
1152 effect of the muon component and practical questions for considering it
1153 in real time, Bulletin of the Russian Academy of Sciences: Physics 75 (6)
1154
350 (2011) 820–824. [doi:10.3103/S1062873811060086](https://doi.org/10.3103/S1062873811060086).
1155
1156

1157 [29] A. Dmitrieva, R. Kokoulin, A. Petrukhin, D. Timashkov, Cor-
1158 rections for temperature effect for ground-based muon ho-
1159 doscopes, Astroparticle Physics 34 (6) (2011) 401 – 411.
1160
1161
355 [doi:https://doi.org/10.1016/j.astropartphys.2010.10.013](https://doi.org/10.1016/j.astropartphys.2010.10.013).
1162
1163

1164 [30] Global forecast system (gfs).

1165 URL <https://www.ncdc.noaa.gov/data-access/modeldata/model-datasets/global-forecast-system>


1166 [31] National centers for environmental prediction (ncep).

1167 URL <http://www.ncep.noaa.gov/>
1168
1169
1170

- 1177
1178
1179
1180
1181
1182
1183
1184
1185
1186
1187
1188
1189
1190
1191
1192
1193
1194
1195
1196
1197
1198
1199
1200
1201
1202
1203
1204
1205
1206
1207
1208
1209
1210
1211
1212
1213
1214
1215
1216
1217
1218
1219
1220
1221
1222
1223
1224
1225
1226
1227
1228
1229
1230
1231
1232
- 360 [32] A. Dragic, V. Udovicic, R. Banjanac, D. Jokovic, D. Maletic, N. Veselinovic, M. Savic, J. Puzovic, I. V. Anicin, The New Setup in the Belgrade Low-Level and Cosmic-Ray Laboratory, Nuclear Technology & Radiation Protection 26 (3) (2011) 181–192.
- [33] B. Haurwitz, The diurnal surface-pressure oscillation, Archiv für Meteorologie, Geophysik und Bioklimatologie, Serie A 14 (4) (1965) 361–379.
365 [doi:10.1007/BF02253483](https://doi.org/10.1007/BF02253483).
- [34] L. I. Dorman, Cosmic Rays in the Earth's Atmosphere and Underground, Springer Netherlands, 2004. [doi:10.1007/978-1-4020-2113-8](https://doi.org/10.1007/978-1-4020-2113-8).
- [35] I. Jolliffe, Principal Component Analysis, Springer-Verlag, 2002.
370 [doi:10.1007/b98835](https://doi.org/10.1007/b98835).
- [36] P. R. W., C. D. Mobley, Principal component analysis in meteorology and oceanography, Amsterdam: Elsevier, 1988.
- [37] M. Savić, D. Maletić, D. Joković, N. Veselinović, R. Banjanac, V. Udovičić, A. Dragić, Pressure and temperature effect corrections of atmospheric muon data in the belgrade cosmic-ray station, Journal of Physics: Conference Series 632 (1) (2015) 012059.



Application of Geant4 simulation in measurement of cosmic-ray muon flux and studies of muon-induced background

Dejan Joković^a , Dimitrije Maletić, Aleksandar Dragić, Nikola Veselinović, Mihailo Savić, Vladimir Udovičić, Radomir Banjanac, David Knežević

Institute of Physics, University of Belgrade, Pregrevica 118, Belgrade 11080, Serbia

Received: 3 May 2023 / Accepted: 28 October 2023

© The Author(s), under exclusive licence to Società Italiana di Fisica and Springer-Verlag GmbH Germany, part of Springer Nature 2023

Abstract The low-level underground laboratory at the Institute of Physics Belgrade is a facility for gamma-ray spectroscopy measurements and for measurements of cosmic-ray muon intensity. Related to the two research subjects, studies of cosmic-ray muon-induced background in gamma spectroscopy are of particular interest. Continuous measurements of cosmic muon intensity at the ground level and underground sites have been carried out by means of plastic scintillation detectors. The detector response, interpretation of the experimental spectra and their calibration were obtained and verified using a Geant4-based simulation. The results of the simulation were used in measurement of muon flux at the surface and shallow underground (25 m w e)—the measured fluxes are $(170 \pm 6) \text{ m}^{-2} \text{ s}^{-1}$ and $(44 \pm 1) \text{ m}^{-2} \text{ s}^{-1}$, respectively. An underground muon detector can operate in coincidence with a high-purity germanium gamma-ray detector, which allows investigations of muon-induced processes in germanium spectrometers. In low-level gamma spectroscopy, neutrons produced by muons in the lead shielding of a germanium detector contribute to the detector background. Simulation of prompt muon-induced background as well as simulation of neutron production by cosmic muons in lead were carried out. Estimated neutron yield in lead is $(3.1 \pm 0.4) \times 10^{-5}$ neutrons per g/cm^2 , per tagged muon. Also the average neutron multiplicity is calculated.

1 Introduction

The low-background underground laboratory at the Institute of Physics Belgrade has been designed as a multi-purpose facility for gamma-ray spectroscopy measurements of low activities, as well as for measurements of cosmic-ray intensity. The two main research objectives intersect in studies of cosmic-ray muon-induced background in gamma spectroscopy measurements. The laboratory is located at near-sea level, at the altitude of 78 m. It consists of two separate parts—the ground level and the underground; the shallow underground part is dug at the depth of about 12 m beneath the surface. The earth above the underground site consists of four layers of loess with average density of $(2.0 \pm 0.1) \text{ g}/\text{cm}^3$. With the 30 cm thick concrete ceiling, the overburden is approximately equal to 25 m of water equivalent (m w e; 1 m w e gives an interaction depth of $1 \text{ hg}/\text{cm}^2$). It provides a good environment for gamma spectroscopy—the overburden soil layer absorbs almost all nucleonic component of cosmic rays and reduces muon flux by about four times. Radon concentration is kept low by preventing diffusion from the soil and by maintaining constant overpressure in the room. One shielded high-purity germanium (HPGe) spectrometer is dedicated for low-level gamma measurements in the underground laboratory. It can operate in coincidence with a muon scintillation detector, which enables investigations of muon-induced events in the germanium detector. More details on the laboratory can be found in [1].

Cosmic-ray muon intensity has been continuously measured at both the ground level and underground sites since 2002. The current experimental set-up, described in the next section, was upgraded and commissioned in 2008. Measurements of muon intensity and its temporal variations can give some information on primary cosmic radiation, interaction processes in the atmosphere and solar modulation. Low-energy primary cosmic rays are under large influence of interplanetary magnetic field, whose structure varies because of solar activity, which has various periodic and aperiodic features. Therefore, temporal variations of cosmic muon flux are expected to be a good indicator of solar activity. These measurements yielded some results on muon flux and its variations [2–5]. In shallow and deep underground laboratories cosmic muons represent an important source of background, either directly or by generating high-energy neutrons in interactions in rock or detector and its surroundings [6–8]. Results of a preliminary study on muon-induced neutron production rate were published in [9].

Today applications of various Monte Carlo simulation methods make an essential part of experimental research. These simulation methods are found to be very useful for modeling detector response, accurate interpretation of experimental data, particularly

^a e-mail: yokovic@ipb.ac.rs (corresponding author)

experimental spectra and their features, as well as for detector calibration. There is a handful of Monte Carlo toolkits used in nuclear and particle physics studies, one of the most commonly used is Geant4 (Geometry aNd Tracking), which has been developed and maintained at CERN [10–12]. Geant4 is a framework for accurate Monte Carlo simulations of particle transport through matter. It contains a complete set of routines for modeling particle trajectories and interactions: detector geometry and materials, physics processes, event generation, detector response and analysis and visualization. Versatility and flexibility of Geant4 allow users to build customized simulation programmes that fit their specific needs. Another advantage of the toolkit is that a built simulation can be easily modified, so as to be suitable for different detector configurations. Increase in computational power enabled Geant4 simulations to be no longer time demanding in order to achieve good statistical uncertainties, due to use of parallel computing, multithreading, etc. Uses of Geant4 span from high energy, nuclear and accelerator physics to medical and space science.

In experiments carried out in the Belgrade underground laboratory, Geant4-based simulations have been developed in order to obtain detector response for various detector configurations, as well as for interpretation of the experimental spectra and their calibration. They include simulations of response of the plastic scintillation detectors for cosmic-ray muon studies and simulations of the germanium detector for gamma spectroscopy. Here we present an overview of applications of Geant4 simulations in measurement of cosmic-ray muon fluxes at the ground level and underground sites and for estimation of muon-induced background in the lead shield of the HPGe detector.

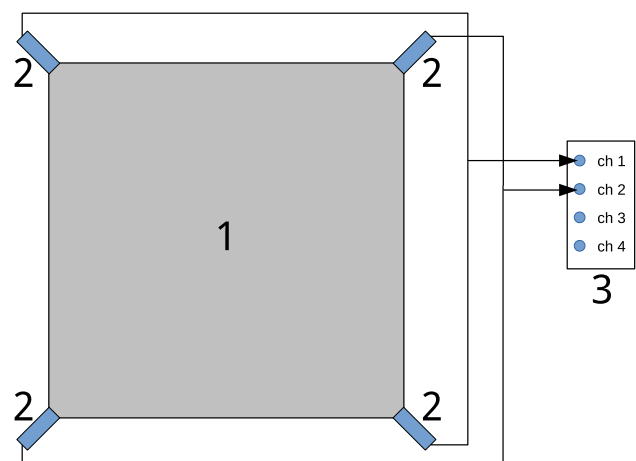
2 Experimental set-up

Measurements of cosmic-ray muon intensity have been performed by means of plastic scintillation detectors, situated in both the ground level and underground parts of the laboratory. Each detector configuration consists of one large scintillator with an accompanying data acquisition system. The two experimental set-ups are identical but they operate independently, each detector has its dedicated data acquisition module. A sketch of the detector set-up is displayed in Fig. 1.

The polystyrene-based scintillator (similar to NE102) has a rectangular shape with base area $100\text{ cm} \times 100\text{ cm}$ and thickness 5 cm, housed in 1 mm thick aluminum. It lies horizontally on its largest side. At each corner of the scintillator a 2-inch photomultiplier tube (PMT) is attached, pointing at the detector's diagonal. Individual signals from the photomultiplier tubes looking at the same diagonal, i.e., two opposite photomultipliers, are summed in one output signal. Hence two output signals from the two detector's diagonals are recorded and stored on tape. The data acquisition system is based on a fast 4-channel analog-to-digital converter (ADC), model CAEN N1728B, which has 100 MHz sampling frequency (time resolution 10 ns). Two input ADC channels are used for the summed signals from the two diagonals of the scintillator, respectively, there are two signals per scintillator, each feeding one ADC channel. The third and/or fourth ADC channels are reserved for other detectors, such as germanium detector. Information about each event (input channel, time tag, amplitude) whose amplitude is above threshold is stored in an event list, which allows offline analyses of single and coincidence events between different channels within a chosen time window. Time and amplitude spectra are formed by histogramming data from the event list, for single ADC channels or for two or more coinciding channels.

Single spectra of the plastic scintillators result from the summed signals from the PMTs on the same diagonal, which are fed to two ADC channels separately; hence two single spectra are produced for each detector. The typical experimental spectra, for both the surface and underground detectors, are presented in Fig. 2. They are mainly composed of energy deposit spectra of cosmic rays that pass through the scintillator and of Compton scattered environmental gamma radiation, as a dominant source of background. The main feature in the spectra is a peak that should correspond to muon and electron energy loss in the 5 cm thick scintillator. However, this energy loss peak, and subsequently cosmic events, cannot be separated from the background, which is quite significant because of the detector's large size and its four PMTs (Fig. 2).

Fig. 1 Experimental set-up for cosmic-ray intensity measurements: plastic scintillation detector (1), photomultiplier tubes (2), analog-to-digital converter (3)



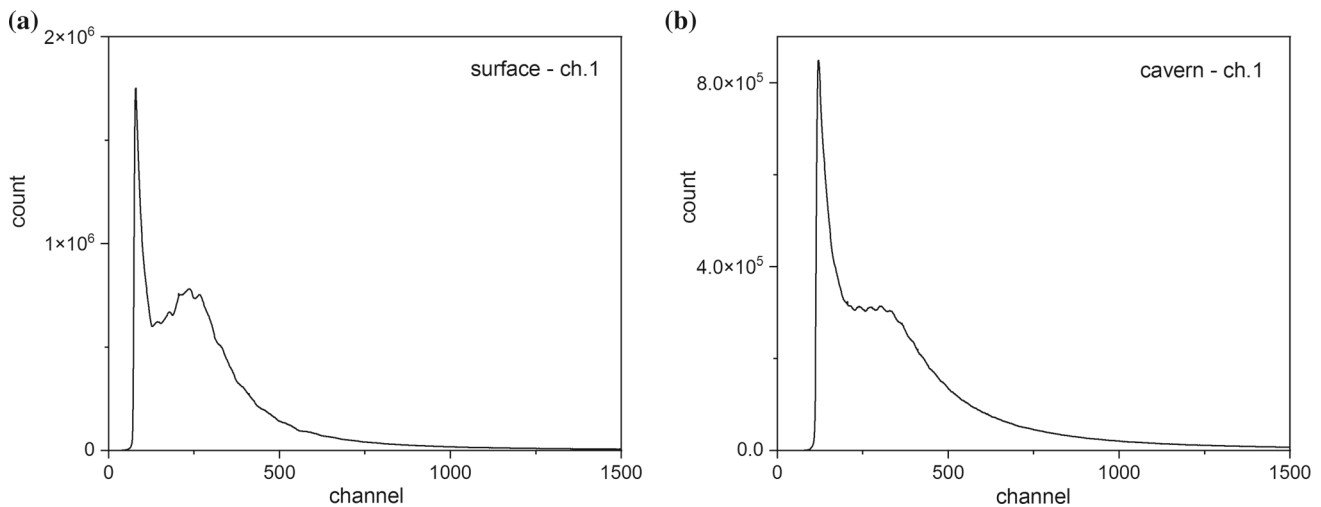
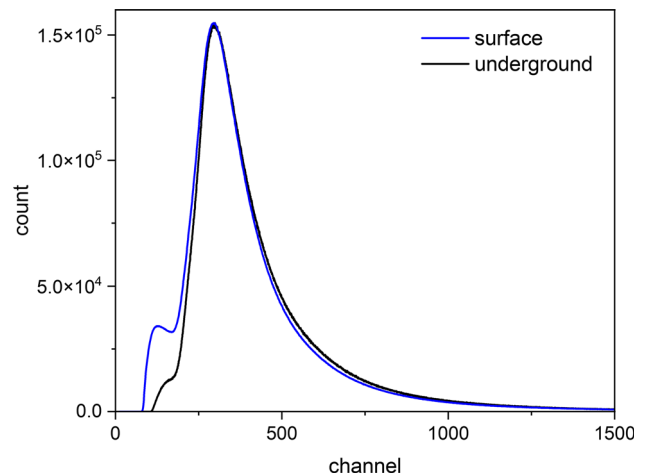


Fig. 2 Typical single spectra of the surface (left) and underground (right) scintillation detectors, produced by the summed signals from the PMTs looking at the same detector's diagonal. They are composed of energy deposit spectra of cosmic rays and of environmental gamma radiation

Fig. 3 Normalized coincidence spectra of the surface and underground detectors. The spectra are considered as solely energy deposit spectra of cosmic-ray charged particles. Both spectra exhibit a peak that corresponds to charged particle energy loss in the 5 cm thick plastic scintillator



Investigation of responses of the single PMTs have shown that cosmic events can be selected by coinciding events that promptly trigger all four PMTs, i.e., both detector's diagonals. Time interval spectra of coincidences between the ADC channels that are fed by the two diagonals, have a sharp peaked distribution that is 40 ns wide and stretches up to ± 50 ns upon the peak (given the 10 ns time resolution of the ADCs). Prompt coincidences selected within a time window of 100 ns are associated to cosmic rays. This procedure virtually removes background, as environmental gamma rays cannot trigger both diagonals. The coincidence spectra are considered as solely due to energy losses by charged particles in the scintillator. These interpretations of the experimental spectra have been supported by Geant4 simulations. The individual coincidence spectra per the diagonal are then summed into one energy deposit spectrum, per the detector; the coincidence spectra for both the surface and underground detectors are presented in Fig. 3.

The coincidence spectra of the scintillators show a well-defined peak of the charged particle energy losses, while the low-energy background present in the single spectra vanishes (Figs. 2, 3). Since the specific energy loss for muons is ~ 2 MeV per g/cm^2 , the spectral peak should be at the energy ~ 11 MeV, for the 5 cm thick plastic scintillator. Comparing the spectra of the detectors at the surface and in the underground laboratory one can notice the difference in their shape at lower energies. This difference points to the contribution of electromagnetic component of cosmic rays (electrons, positrons and photons), whose flux is significant at the surface. It is absent underground, where practically only muon component is present. Hence, it is plausible to assume that events recorded by the underground detector are only muon events, while for the surface detector they include electromagnetic component. Moreover, due to edge effects there are some cosmic events that fall below the instrumental cuts. The amount of these lost events can be found by comparing experimental results with simulations (Sect. 3).

3 Measurement of cosmic-ray muon flux

3.1 Simulation

With the aim of corroborating the aforementioned statements and interpretations, a Geant4-based application for modeling detector response of the scintillation detectors has been developed. It can be also used for calibration of spectra. The simulation has been done along the same lines as in the previous works [2, 13]. Latest Geant4 version used for this work is 11.0. In Geant4, an event is generated by defining primary particle, its initial position, momentum direction and energy. In the simulation of the underground detector, primary particles were muons, since it can be assumed that only muons are present at the depth of 25 m w e. Muons were gunned from the horizontal and vertical sides of the detector. Particle positions and momentum directions were generated in accordance with the muon directional intensity, which depends on zenith angle: $I(\theta) = I(0) \cos^n \theta$, where n has a value 1.85 at sea level and 1.55 at the 25 m w e depth [14, 15]. Integrated intensity of muons that pass through the horizontal surface is

$$J_h = \int_{\Omega} I(\theta) \cos \theta \sin \theta d\theta d\phi = 2\pi I(0) \int_0^{\pi/2} \cos^{(n+1)} \theta \sin \theta d\theta = 2\pi I(0) \frac{1}{n+2}, \quad (1)$$

while integrated intensity of muons that pass through the vertical surface is

$$J_v = \int_{\Omega} I(\theta) \sin^2 \theta \cos \phi d\theta d\phi = I(0) \int_{\Omega} \cos^n \theta \sin^2 \theta \cos \phi d\theta d\phi, \quad (2)$$

latter integrated over a quarter of the sphere. From the ratio J_h/J_v it follows that muons have higher probability to hit the horizontal than the vertical surface—for $n = 1.55$, $J_h/J_v = 3.64$ per unit area, and for $n = 1.85$, $J_h/J_v = 3.88$. These probabilities were taken into account when primary positions on the horizontal and vertical detector's sides were generated.

The particle energy was calculated in two steps. First, energy at the surface was sampled from the Gaisser's formula for muon energy spectrum at sea level [16]:

$$\frac{dJ_{\mu}(E)}{dE} = 0.14E^{-2.7} \left(\frac{1}{1 + 1.1 \frac{E \cos \theta}{115 \text{ GeV}}} + \frac{0.054}{1 + 1.1 \frac{E \cos \theta}{850 \text{ GeV}}} \right), \quad (3)$$

where E is the muon energy in GeV, and $\cos \theta$ is sampled from the $\cos^{1.85} \theta$ distribution. The formula does not describe well experimental data at lower energies and larger zenith angles, so it was modified according to [17]. Muon energy loss in the earth layer was calculated from the practical equation for total energy loss of muons in standard rock, in units of MeV [18]:

$$-\left(\frac{dE}{dx}\right) = 1.84 + 4.65 \cdot 10^{-6} E + 0.076 \ln \left(\frac{E'}{m_{\mu} c^2} \right) [\text{MeV}/(\text{g}/\text{cm}^2)], \quad (4)$$

where E' is the maximum transferable energy $E' = E^2 / (E + m_{\mu}^2 c^2 / 2m_e)$, m_{μ} is the mass of the muon, and m_e is the mass of the electron. The muon path length, i.e., layer thickness, dx was calculated as $25/\cos \theta$ hg/cm². The energy loss was then subtracted from the value sampled from Eq. 3, and the deducted value was taken for the initial muon energy in the simulation. The muon energy spectrum underground is thus hardened because low-energy muons are removed.

Muons were tracked through the scintillator as a sensitive detector. When a muon passes through a material, it interacts with matter—in these interactions it deposits a portion of its energy, which adds to the overall energy deposit spectrum. Physics processes were applied through the Geant4 physics list QGSP_BERT_HP, which include all interactions leading to production of secondaries, as well as for calculation of energy losses in the detector. For the purpose of simulation of the plastic scintillators electromagnetic interactions of muons, electrons and gammas are relevant (constructor G4EmStandardPhysics_option4 was activated).

The normalized simulated and experimental spectra agree very well, thus verifying interpretation of the detector response and the experimental results (Fig. 4). Furthermore, by comparing the two spectra one can find the percentage of muon events that are not recorded due to instrumental cuts. It is equal to the ratio of counts in the two spectra, here it is approx. 6%. This correction was applied in calculation of the muon flux underground. Relative arbitrariness in estimation of the fraction of lost events contributes to the uncertainty of the measured muon flux to a large degree.

When the same simulation was applied for the surface detector, there was a large discrepancy between the simulation and experimental results. This led to a conclusion that besides muonic, electromagnetic component of cosmic rays also had to be taken into account. Therefore, the model was further extended, so as to include all secondary cosmic-ray particles at the surface. Particle fluxes at the surface were obtained using CORSIKA (COsmic Ray SIMulations for KAscade) programme [19, 20]. It is a Monte Carlo code for simulation of extensive air showers generated by primary cosmic rays in their interactions with air nuclei at the top of the atmosphere. It produces spectra of secondary cosmic rays at a chosen observation level (altitude) above the surface. The output is in a form of a list that keeps information about each particle—its type, momentum, energy and time of arrival. Geant4 provides an interface that can read output files from external event generators and use information to generate primary particles (type, momentum and energy). Hence, CORSIKA served as a primary event generator, while the detector response was modeled by the Geant4 simulation. Details on the CORSIKA simulation—primary cosmic-ray spectrum, hadron interaction models, geomagnetic field, atmospheric model, observation level—can be found in [3].

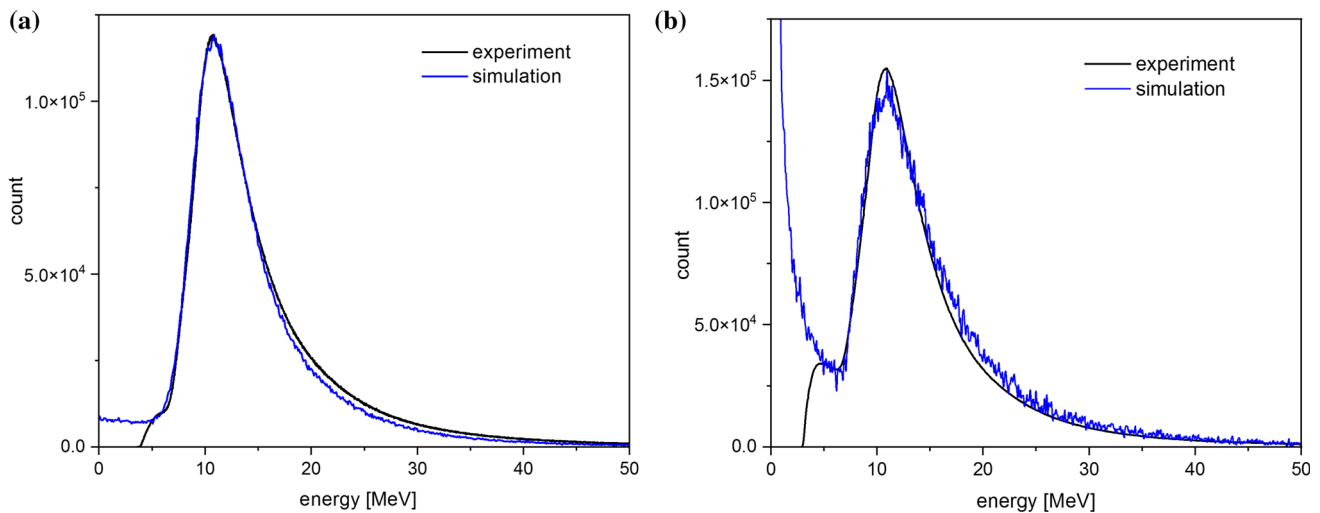


Fig. 4 Normalized experimental (black line) and simulated (blue line) energy deposit spectra of the scintillation detectors in the underground laboratory (left) and at the surface (right). Peak of charged particle energy losses in the spectra is at energy about 11 MeV, approx. equal to muon energy loss in the 5 cm thick plastic scintillator

Primary particles for the simulation of the surface detector, muons, electrons and gammas were, respectively, selected from the CORSIKA output. The energy deposit spectra were then obtained separately for the three types of particles. These individual spectra exhibit some different features, the main difference is that the muon spectrum is virtually the same as for the underground detector, while the gamma ray spectrum is mostly at lower energies [3]. The sum of the individual energy deposit spectra gives the resultant simulated spectrum, which is in good agreement with the experimental one (Fig. 4). It is clearly separated into two parts at ~ 6 MeV, which nearly corresponds to the threshold set by instrumental cuts. At energies exceeding the threshold muon events are dominant, however there is a small but non-negligible contribution of electrons and gammas. The fraction of muons in the simulated spectrum above the instrumental cut is equal to the ratio of muon counts to the total counts—muons make about 87% of the total number of events above the 6 MeV threshold.

3.2 Results

The cosmic muon flux is calculated from the equation $\Phi = N_{\mu}/(St)$, where N_{μ} is number of muons, S surface area and t measurement time. The average muon flux underground was calculated from data recorded during 289 days of measurement ($t = 2.497 \times 10^7$ s). The detection efficiency to muons for this type of detector is close to 100% [21]; the simulation confirms this assumption, but it contributes to uncertainty of the measured flux to a smaller extent. The number of muon events was corrected for events below the instrumental cuts, which was equal to the ratio of normalized counts in the simulated and experimental spectra. About 6% of muon events falls below the cuts. After correction for lost events, the total number of muons is 1.149×10^9 . The horizontal area of the detector is 1 m^2 , however muons also hit vertical sides. On the other hand, muons have higher probability to hit the horizontal than the vertical surface, due to $\cos^2\theta$ directional distribution – 3.64 times higher for the underground detector. The effective detector area is thus 1.055 m^2 . Finally, the muon flux underground, at the 25 m w e depth, is $\Phi = (44 \pm 1) \text{ m}^{-2} \text{ s}^{-1}$. Statistical uncertainties are much smaller than systematic ones, which are partially associated to experimental data treatment, such as the selection of time window for coinciding the single detector spectra and estimation of the fraction of lost muon events below instrumental cuts. Uncertainty of the simulation is roughly estimated by varying parameters of simulation, particularly angular distribution of muons (exponent n in $\cos^n\theta$), thickness of the overburden and calculation of muon energy loss (Eq. 4).

At the surface, the total cosmic-ray flux is the sum of muon and electromagnetic fluxes. First the total flux above the instrumental cut was calculated from the experimental data. Then the percentage of muons above the cut was found from the simulated data—approx. 87% of the total number of events. The flux was also corrected for muon events below the cuts (+ 6%). The effects of seasonal variations are mostly removed due to long measurement time. The total number of cosmic events is 4.079×10^9 . After all corrections applied ($N_{\mu} = N_{\text{tot}} \times 0.87 \times 1.06$), the number of muon events is 3.762×10^9 . The time of measurement is 244 days (2.108×10^7 s), and the effective detector area is 1.0515 m^2 . Finally, muon flux at the surface is $\Phi = (170 \pm 6) \text{ m}^{-2} \text{ s}^{-1}$. The uncertainty was evaluated in a similar way as for the calculation of the muon flux underground. There is also a contribution to the uncertainty that comes from the correction for the fraction of muons in the total flux, which was calculated from the simulation data.

The measured fluxes underground and at the surface are consistent with the previous work, though the muon flux at the surface gives 24% higher value [2]. Integrated muon intensity at sea level is often referred as about $1 \text{ cm}^{-2} \text{ min}^{-1}$ [22], the calculated flux at the surface is in accord with this value. The underground flux adds to the list of muon data in underground laboratories [23]. The integral flux of electromagnetic component at the surface is very approximately estimated to 30% of the total flux.

4 Simulation of muon-induced background

4.1 Muon-induced background in the germanium detector

The muon detector in the underground laboratory can operate in coincidence with a coaxial high-purity germanium detector (ORTEC GEM30). The detector is based on a cylindrical p-type crystal, with the diameter 58.5 mm and the length 56.4 mm, and the active volume 149 cm³. The relative efficiency is 35%, with respect to the efficiency of a 3 × 3 inch NaI detector. The detector is placed inside a 12 cm thick lead castle made of lead with low content of ²¹⁰Pb (specific activity 25 Bq/kg). Due to the 12 m overburden and thick lead shielding, it is suitable for gamma spectroscopy of low-activities. The muon detector is placed directly above the lead castle at the distance 44 cm, and can serve as a veto for additional background suppression. Signals from the HPGe detector are fed into an input channel of the same ADC that is used by the muon detector. The acquisition system allows up to four different inputs; here two inputs are used for signals from the muon detector and one for the HPGe detector. Events recorded by both detectors are stored in one list with information about each event (input channel, trigger time and amplitude). This allows analyses of coincidence or anticoincidence between different channels, by selecting proper time window. In the coincidence mode muon-induced events in the germanium detector can be studied. In the anticoincidence mode the scintillator can serve as an anti-cosmic veto detector.

Geant4 simulations have found wide-ranging applications in gamma spectroscopy with germanium detectors. One of the main subjects that have been studied is evaluation of muon-induced background in germanium detectors, operating at the surface and underground [24–28]. The simulation that combines the underground scintillator and the HPGe detector was performed with a goal to obtain coincidence response of the two-detector system to cosmic muons. It was used to estimate prompt muon-induced background, which originates from direct muon interaction with the germanium crystal or from electrons ionized by muons in the detector and surroundings. It can also give a prediction of background reduction by the anti-cosmic veto [13].

Configuration of an HPGe detector is more complex than a simple scintillator box, which is why the detailed knowledge of the detector geometry is an essential precondition for an accurate modeling. In this simulation the detector was constructed utilizing the detector parameters provided by the manufacturer. The geometry was tested by varying these parameters and looking at how the changes affect the detector response. This method can be also used for uncertainty estimation. Small changes of the parameters may give rise to large deviations between simulated and experimental results. In order to overcome these difficulties an optimization procedure is often performed, by tuning the detector parameters so as to achieve the best possible agreement with experimental values [29]. For use in gamma spectroscopy Geant4 provides low-energy electromagnetic packages that best model interactions of low-energy gamma rays. Here the G4EmStandardPhysics_option4 constructor class, which combines electromagnetic models for simulations with high accuracy, was activated.

First, the simulation of the germanium background generated by prompt muon interactions in the lead shield was performed. Primary muons were generated on the surface of the lead castle, the top and side surfaces. Energy and angular distributions of muons are the same as used in the simulation of muons underground, described in Sect. 3.1. Per event, initial position and momentum direction were sampled from $\cos^{\eta}\theta$ distribution ($\eta = 1.55$), while energy was sampled from the modified Gaisser's formula and subtracted for the muon energy loss (Eq. 3, 4). Here the germanium crystal is a sensitive detector for calculation of energy deposit. The energy deposit spectrum is in high-energy part due to muons that traverse through the germanium crystal, which has a broad peak at about 43 MeV [13]. For gamma spectroscopy measurements the range up to 3 MeV is mostly of interest. This part of the spectrum is due to secondary particles produced by muons in the detector's surroundings, mainly in the lead castle. The prominent annihilation peak builds upon the continuous spectrum.

Then the simulation of the scintillator and the HPGe detector working in coincidence was carried out, with primary muons now generated on the scintillator's surface, in the same way as described in Sect. 3.1. A sketch of the visualized Geant4 geometry and a muon event is displayed in Fig. 5. The coincidences were selected with a simple condition that a muon has to deposit energy in both detectors. The simulated coincidence spectrum of the germanium detector up to 3 MeV, together with the background spectrum, is shown in Fig. 6. The prominent annihilation peak builds upon the continuous spectrum. Integral of this spectrum gives the number of vetoed background events in the range of 0–3 MeV.

Relative background reduction by the anti-cosmic veto was found as a ratio of counts in the two spectra. For the given configuration the veto halves the prompt muon background in the lead shield. However, the total background of the HPGe detector would be diminished by only 15%. The new set-up has the muon detector half the distance closer to the lead castle, which should to some extent improve background reduction. A common anti-cosmic veto system consists of detectors that are placed above and to the sides of a lead castle, so that the veto is triggered by any arriving muon. This type of set-up would provide background reduction as good as possible for the HPGe detector. However, at the moment it is not planned to add more veto detectors.

4.2 Neutron production by muons in lead

Neutrons produced in interactions of cosmic-ray muons with the detector and its surroundings contribute to background, especially in sensitive experiments in deep underground laboratories searching for rare events. In interactions with the detector neutrons produce signals that may mimic signals from the events searched for. Therefore investigation of neutron-induced background is of great importance for low-background measurements. For lead-shielded germanium detectors neutrons produced by cosmic muons in lead

Fig. 5 Visualization of the Geant4 geometry of the scintillator and HPGe detector, and a coincidence muon event. Particle tracks are: blue—muon, green—photon, red—electron

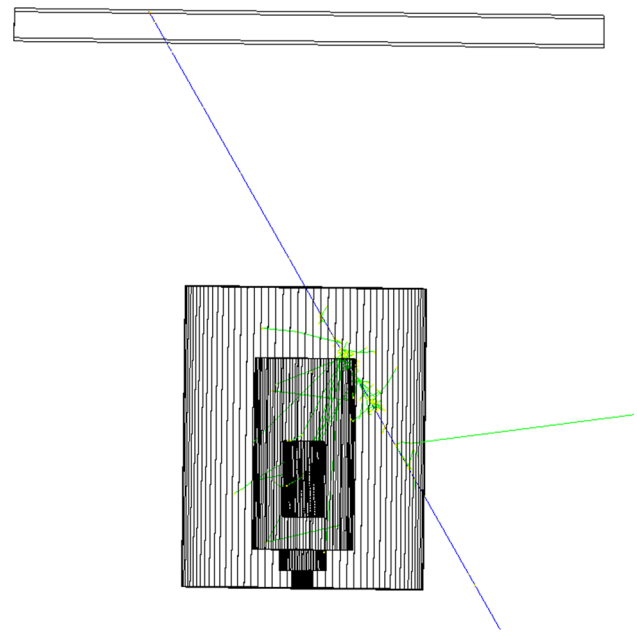
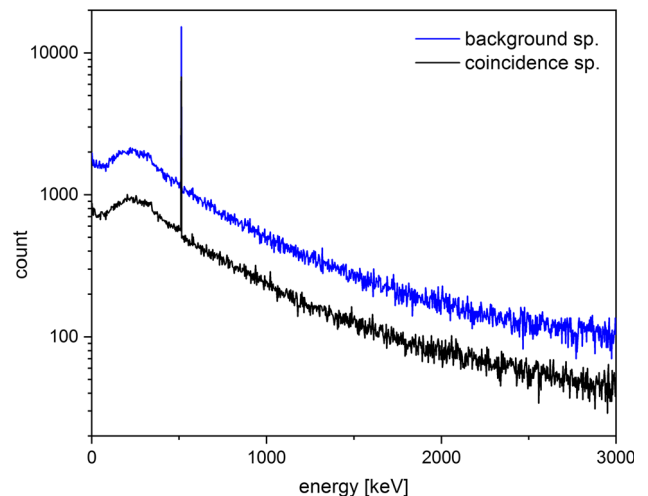


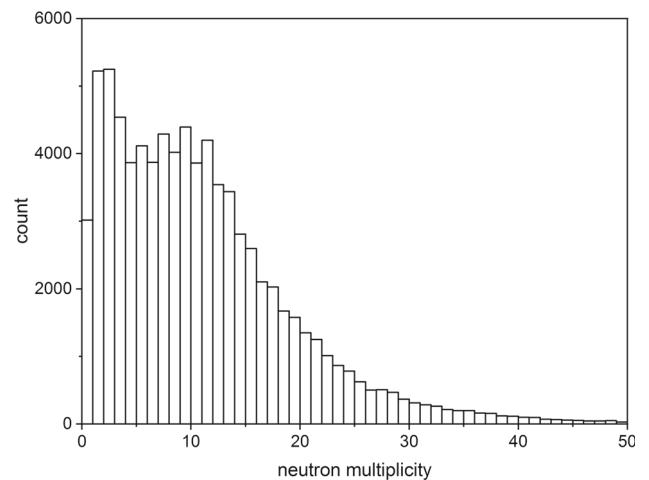
Fig. 6 Normalized background spectrum (blue line) and coincidence spectrum of the HPGe detector (black line) induced by prompt muon interactions in lead, and estimated anti-cosmic veto suppression [13]



are an unavoidable source of background. As it was already pointed out, the experimental set-up in the underground laboratory enables studies of muon-induced events in the HPGe detector, when it works in coincidence with the muon detector. Preliminary results on flux of fast neutrons produced by muons in the lead shielding of the HPGe detector were reported in [9]. Data were collected during over 400 days of measurement. Neutrons were identified from the 692 keV line in the coincidence spectrum, which arises from neutron inelastic scattering on Ge-72 isotope. Neutron production rate can be determined from count rate in the 692 keV line in the spectrum [30]. The muon-induced neutron flux, within the volume of the lead shielding, is $(3.1 \pm 0.5) \times 10^{-4} \text{ cm}^{-2} \text{ s}^{-1}$.

A variety of Geant4 simulation methods have been utilized in studies of production of neutrons by cosmic muons in lead at the surface and underground [31–33]. Here we present the first results of the simulation of muon-induced neutron production in the lead shielding of the HPGe detector. It was done in the same manner as the previous simulations. Primary muons were generated on the top and side surfaces of the lead castle. Muon energy and directional distributions followed the same procedure described in Sect. 3. Hadronic interactions were included through the Geant4 QGSP_BERT_HP physics list. It uses high precision neutron models and cross sections for low-energy neutron interactions. For electromagnetic part the G4EmStandardPhysics_option4 constructor was activated. The simulation was then repeated with the physics lists FTFP_BERT_HP and Shielding, latter is recommended for neutron transport. All three physics models invoke the same classes for neutron interactions. There was no significant difference in the results. Because energy thresholds for production of secondary particles were set at low values, large number of particles was produced. Hence all secondaries but muons and neutrons were killed, and only muons and neutrons were tracked through the lead volume.

Fig. 7 Multiplicity distribution of neutrons produced by muons in lead at the 25 m w e depth



Neutron yield in lead can be determined from the equation $Y_n = N_n / (N_\mu l_\mu \rho)$, where N_n is number of neutrons produced, N_μ is number of muons, l_μ is the mean path length of muons and ρ is density. In total 10^8 muon histories were generated, and 9.34×10^5 neutrons were produced. The mean path length that muons travel through the lead castle, obtained from the simulation, is 26.6 cm. Finally, the neutron yield in the lead volume is $(3.1 \pm 0.4) \times 10^{-5}$ neutrons per gcm^{-2} per muon. It was also looked at how many of these neutrons reach the HPGe detector inside the lead castle—it was approx. 2.4% of all neutrons, though statistics was rather poor for precise studies of neutron-induced processes in the germanium detector. Additionally, neutron multiplicity for each event was found, as number of neutrons per tagged muon. Its distribution is shown in Fig. 7, while the average multiplicity is 11.5.

5 Conclusion

The Geant4-based simulations have been extensively used in experiments carried out in the low-background underground laboratory at the Institute of Physics Belgrade. Here presented overview describes applications of Geant4 simulations in measurements of cosmic-ray muon intensity and in gamma spectroscopy studies of events which have origin in cosmic muons. Detector responses of the plastic scintillation detectors and the germanium detector were obtained in order to evaluate experimental results. In simulations of the surface scintillator primary particles were generated by CORSIKA programme, so as to include electromagnetic component, which is absent underground. Simulated energy deposit spectra showed good agreement with experimental ones. Comparing these spectra precise calculations of muon integral intensity could be calculated. The measured muon fluxes at the surface and underground are $(170 \pm 6) \text{ m}^{-2} \text{ s}^{-1}$ and $(44 \pm 1) \text{ m}^{-2} \text{ s}^{-1}$, respectively. The results are consistent with our previous work and available muon data.

Simulation studies of cosmic muon interactions with lead were performed with a goal to estimate muon-induced background in the germanium detector. Muons can cause two types of background: the first one is due to prompt interactions of muons and secondary particles produced by muons and the second one is due to delayed decays of Ge nuclei produced in neutron inelastic collisions. The prompt muon-induced background was estimated with a simulation of the scintillator and the HPGe detector in coincidence, for the given detector configuration. The two detectors can operate in coincidence or anticoincidence provided the correct selection criteria between recorded events. When they work in anticoincidence the scintillator serves as an anti-cosmic veto. Simulated prompt muon background is also an estimation of the reduction of cosmic background by the veto, which in this case is by one half. The new experimental set-up has the muon detector close to the lead castle, which should improve the background reduction. Another task that was carried out was the simulation of neutron production by cosmic muons in lead. The estimated yield in the lead volume is $(3.1 \pm 0.4) \times 10^{-5}$ neutrons per gcm^{-2} per muon. Also neutron multiplicity per tagged muon is obtained. The results make a good basis for further studies of cosmic muon-induced processes in the vicinity of germanium detectors, including production of neutrons and other particles in the overburden rocks.

Acknowledgements The authors acknowledge funding provided by the Institute of Physics Belgrade, through the grant by the Ministry for Science, Technological Development and Innovation of the Republic of Serbia. The authors thank the reviewers for valuable suggestions that improved quality of the manuscript.

Data Availability Statement This manuscript has associated data in a data repository. [Authors' comment: Data sets generated during the current study are available from the corresponding author. Time series of muon flux data are available at http://cosmic.ipb.ac.rs/muon_station/index.html. The simulation code used in this work is publicly available at the zenodo.org data repository, <https://doi.org/10.5281/zenodo.10005170>.]

Declarations

Conflict of interest The authors have no competing interests to declare that are relevant to the content of this article.

References

1. A. Dragić et al., Nucl. Technol. Radiat. Prot. **26**, 181 (2011)
2. A. Dragić et al., Nucl. Instrum. Methods Phys. Res. A **591**, 470 (2008)
3. N. Veselinović et al., Nucl. Instrum. Methods Phys. Res. A **875**, 10 (2017)
4. M. Savić et al., Astropart. Phys. **109**, 1 (2019)
5. N. Veselinović et al., Eur. Phys. J. D **75**, 173 (2021)
6. V.A. Kudryavtsev, L. Pandola, V. Tomasello, Eur. Phys. J. A **36**, 171 (2008)
7. D. Barker, D.-M. Mei, C. Zhang, Phys. Rev. D **86**, 054001 (2012)
8. H.W. Bae, E.J. Jeon, Y.D. Kim, S.W. Lee, Astropart. Phys. **114**, 60 (2020)
9. A. Dragić et al., J. Phys. Conf. Ser. **409**, 012054 (2013)
10. Geant4, <https://geant4.web.cern.ch/>
11. S. Agostinelli et al., Nucl. Instrum. Methods Phys. Res. A **506**, 250 (2003)
12. J. Allison et al., Nucl. Instrum. Methods Phys. Res. A **835**, 186 (2016)
13. D.R. Joković et al., Appl. Radiat. Isot. **67**, 719 (2009)
14. P.K.F. Grieder, *Cosmic Rays at Earth* (Elsevier, Amsterdam, 2001), p.372
15. P.K.F. Grieder, *Cosmic Rays at Earth* (Elsevier, Amsterdam, 2001), p.498
16. T.K. Gaisser, *Cosmic Rays and Particle Physics* (Cambridge University Press, Cambridge, 1990), p.71
17. M. Guan et al., *Muon Simulation at the Daya Bay Site* (Lawrence Berkeley National Laboratory, 2010)
18. P.K.F. Grieder, *Cosmic Rays at Earth* (Elsevier, Amsterdam, 2001), p.467
19. CORSIKA, <https://www.iap.kit.edu/corsika/>
20. D. Heck et al., CORSIKA: a Monte Carlo code to simulate extensive air showers, Report FZKA 6019. (Forschungszentrum Karlsruhe, 1998)
21. T. Enquist et al., Nucl. Instrum. Methods Phys. Res. A **554**, 286 (2005)
22. P.A. Zyla et al., Prog. Theor. Exp. Phys. **2020**, 083C01 (2020)
23. B. Mitrica et al., Adv. High Energy Phys. **2013**, 256230 (2013)
24. N. Jovančević et al., Nucl. Instrum. Methods Phys. Res. A **612**, 303 (2010)
25. N.Q. Hung, V.H. Hai, M. Nomachi, Appl. Radiat. Isot. **121**, 87 (2017)
26. R. Breier, M. Laubenstein, P.P. Povinec, Appl. Radiat. Isot. **126**, 188 (2017)
27. M. Baginova, P. Vojtyla, P.P. Povinec, Astropart. Phys. **143**, 102756 (2022)
28. J. Knezevic et al., Nucl. Instrum. Methods Phys. Res. A **1032**, 166624 (2022)
29. M. Travar et al., J. Radioanal. Nucl. Chem. **332**, 817 (2023)
30. G. Škoro et al., Nucl. Instrum. Methods Phys. Res. A **316**, 333 (1992)
31. L. Reichhart et al., Astropart. Phys. **47**, 67 (2013)
32. Q. Du et al., Astropart. Phys. **102**, 12 (2018)
33. R. Kneißl et al., Astropart. Phys. **111**, 87 (2019)

Springer Nature or its licensor (e.g. a society or other partner) holds exclusive rights to this article under a publishing agreement with the author(s) or other rightsholder(s); author self-archiving of the accepted manuscript version of this article is solely governed by the terms of such publishing agreement and applicable law.



Radon variability due to floor level in two typical residential buildings in Serbia

Vladimir Udovicic,
Nikola Veselinovic,
Dimitrije Maletic,
Radomir Banjanac,
Aleksandar Dragic,
Dejan Jokovic,
Mihailo Savic,
David Knezevic,
Maja Eremic Savkovic

Abstract. It is well known that one of the factors that influence the indoor radon variability is the floor level of the buildings. Considering the fact that the main source of indoor radon is radon in soil gas, it is expected that the radon concentration decreases at higher floors. Thus at higher floors the dominant source of radon is originating from building materials, and in some cases there may be deviations from the generally established regularity. In such sense, we chose one freestanding single-family house with loft and other 16-floor high-rise residential building for this study. The indoor radon measurements were performed by two methods: passive and active. We used passive devices based on track-etched detectors: Radtrak² Radonova. For the short-term indoor radon measurements, we used two active devices: SN1029 and SN1030 (manufactured by Sun Nuclear Corporation). The first device was fixed in the living room at the ground level and the second was moved through the floors of the residential building. Every measuring cycle at the specified floor lasted seven days with the sampling time of 2 h. The results show two different indoor radon behaviours regarding radon variability due to floor level. In the single-family house with loft we registered intense difference between radon concentration in the ground level and loft, while in the high-rise residential building the radon level was almost the same at all floors, and hence we may conclude that radon originated mainly from building materials.

Keywords: Radon variability • Time series

Introduction

Radon sources in the buildings are primarily from soil, building materials and water. Considering the nature of the occurrence and all the sources, the concentration of radon is higher in the ground-floor rooms compared with that in the higher floors of the dwellings in apartments. In the literature one can find a lot of papers dealing with the influence of various factors, including the floor levels, on the radon concentration and variability. In one group of the articles, investigation of the indoor radon concentration distribution due to floor levels of the buildings is the part of the data analysis which was drawn from the national or regional radon surveys [1–6] and others are dedicated to these specific studies [7–11]. In the case of the big buildings with a several number of floors a deviation from the general regularity can be observed, since the dominant source of indoor radon at higher floors is building materials. On the other hand, the radon variability due to floor level, especially in big cities with a much higher number of high-rise buildings and population density compared with rural environments, may have an impact on the assessments of the effective dose from radon exposure at the national level. Usually, the indoor radon map represents the arithmetic mean value of indoor radon concentration on the ground floor, and thus it is not

V. Udovicic✉, N. Veselinovic, D. Maletic, R. Banjanac,
A. Dragic, D. Jokovic, M. Savic, D. Knezevic
Institute of Physics Belgrade
University of Belgrade
Pregrevica 118 St., 11080 Belgrade, Serbia
E-mail: udovicic@ipb.ac.rs

M. Eremic Savkovic
Serbian Radiation and Nuclear Safety and Security
Directorate
Masarikova 5 St., 11000 Belgrade, Serbia

Received: 30 November 2019
Accepted: 17 January 2020

representative of the radon exposure to all citizens since most people do not live on the ground floor. So, it is necessary to convert indoor radon map to a dose map. One of the examples is presented as a plan to develop models that allow correction from ground-floor dwellings to the real situation, accounting data from the national buildings database [12]. In Serbia, national typology of residential buildings is based on the results from the monography “National typology of residential buildings of Serbia” by a group of authors from the Faculty of Architecture [13]. There are six types of the residential buildings in Serbia: two for family housing – freestanding single-family house and single-family house in a row and four types for multifamily housing – freestanding residential building and residential building (lamella) (apartment block with repeated multiple lamellar cores and separate entrances), residential building in a row, and high-rise residential building. Distribution of buildings by type at the national level shows that 97% of all residential buildings are family housing. Also, for all defined types of buildings, number of floors ranges from one to eight above the ground level. Freestanding family houses are mostly ground floor (37%) or ground floor with loft in use (26%), while there is a very low representation of houses that have more than two floors (5%), with average floor level of family buildings of 1.4 [13]. In such sense, we chose one freestanding single-family house with loft with well-known radon characteristics [14] and one 16-floor high-rise residential building for this study.

Materials and methods

Two housing units were selected, one from the family housing group and one high-rise residential building from the collective housing group. The family house has a characteristic construction style in which the house has been built for several years with constant upgrading, which can potentially be a source of radon entry into such houses. The house has a basement and is made of standard materials (brick block, concrete, plaster). Finally, insulation was made using 5-cm thick styrofoam. Long-term measurements of radon concentrations have been carried out in this house by various methods, and several scientific papers have been published so far [14–16].

From the group of residential buildings for collective housing, we chose high-rise building in New Belgrade. It was built in the 1960s as block type. The soliter has a basement, while on the ground floor there are outlets and business premises. The apartments are located in the first floor upward. The soliter has 16 floors. One of the important parameters in the selection of building in municipality New Belgrade is the fact that this municipality is the most populated in Serbia.

The long-term radon measurements were performed with passive device Radtrak² Radonova based on CR-39 track detector. The detectors were exposed for three months from March to June. In the high-rise building, passive radon detectors were deployed at some of the floors in one or several apartments. Time series of measured radon concentrations in the studied residential buildings were obtained using two active devices: SN1029 with the following characteristics declared by the manufacturer – the measurement ranging from 1 Bq·m⁻³ to 99.99 kBq·m⁻³, accuracy equal to ±25%, sensitivity of 0.16 counts/h/Bq·m⁻³ and SN1030 with the following characteristics – the measurement ranging from 1 Bq·m⁻³ to 99.99 kBq·m⁻³, accuracy equal to ±20%, sensitivity of 0.4 counts/h/Bq·m⁻³. SN1029 device were calibrated at the accredited metrological Lab (SUJCHBO Kamenna, Czech Republic) in 2015 and model SN1030 were calibrated by the manufacturer in 2017. Both instruments were presented with excellent results in 2018 NRPI Intercomparisons of radon gas continuous monitors, and also SN1029 device was presented in 2015 NRPI Intercomparisons of radon gas measurement devices at SURO v.v.i. Institute, Prague, Czech Republic within the IAEA Technical Cooperation Projects RER 9153 and RER 9127. These are measuring devices of simple construction and practical application. It is a counter with the addition of a sensor for measuring meteorological parameters. The operator can adjust the time sequences from 0.5 h to 24 h. One measurement cycle can take 1000 h or a total of 720 time sequences (the number of successive measurements, i.e. points in a time series). The devices were set to operate in a 2-h time sequence. One was fixed in the downstairs living room and the other was fixed in repositioning floors in apartment buildings. Each measurement cycle on a given floor lasted seven days.

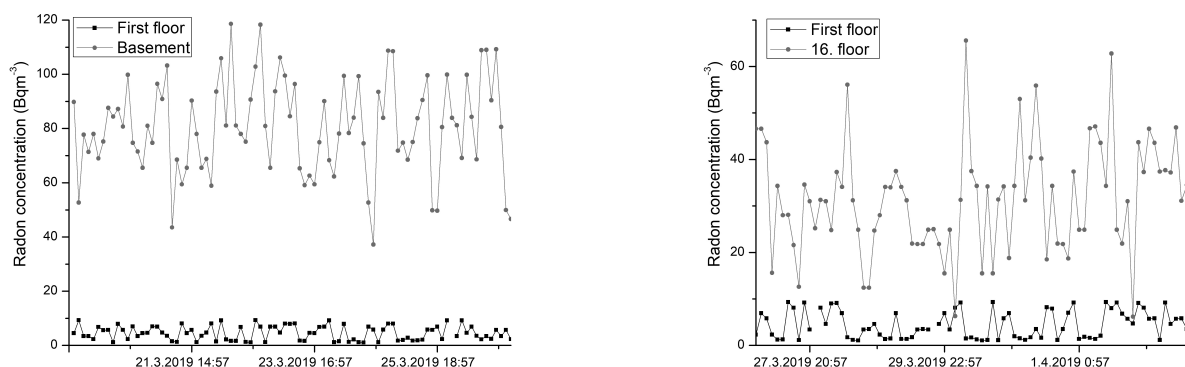


Fig. 1. The time series of the radon concentrations at the first floor vs. basement and 16th floor in the big residential building.

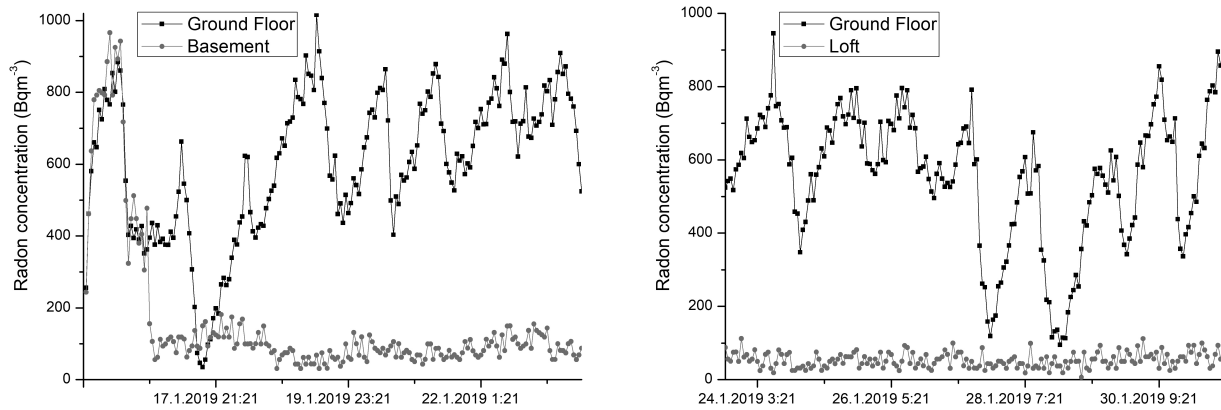


Fig. 2. The time series of the radon concentrations at the first floor vs. basement and loft in the single-family house.

Table 1. Results of indoor radon measurements in the high-rise residential building using passive (Radtrak² Radonova) and active radon devices

Floor level	Radon concentration/ Passive device (Radtrak ²) [Bq·m ⁻³]	Average radon concentration per floor level (Radtrak ²) [Bq·m ⁻³]	Arithmetic mean (standard deviation) radon concentration over measuring cycle [Bq·m ⁻³]
Basement	52 ± 10	53.5	81(17)
	69 ± 12		
	38 ± 10		
	55 ± 10		
1	<10 14 ± 8	14	5(3)
2	17 ± 8	17	24(9)
3			25(10)
4	21 ± 8 20 ± 8	20.5	26(11)
5	11 ± 8 27 ± 10	19	
6	22 ± 8 12 ± 8 17 ± 8	17	
7	23 ± 8	23	25(10)
8	22 ± 8	22	
9	15 ± 8 16 ± 8 22 ± 8	17.7	24(10)
10	20 ± 8 15 ± 8	17.5	
11	16 ± 8	16	
12	<10	<10	
14	20 ± 8 17 ± 8	18.5	29(9)
15	15 ± 8 16 ± 8	15.5	
16	31 ± 8	31	32(12)
Overall mean	24	21.6	30

Results and discussions

Figure 1 shows the illustrative examples that show radon time series from high-rise building, and Fig. 2 originates from the observed single-family house.

The arithmetic mean radon concentrations obtained from long- and short-term measurements are shown in Tables 1 and 2 for high-rise building and single-family house with loft, respectively.

In the family house, it is possible to notice marked variations in radon concentration with 1-day periodicity. Also interesting is the ratio of radon concentration on the ground floor to the basement of the house, which is the opposite of the usual situation in houses with a basement. This inverse behaviour can be explained by the fact that the basement does not cover the whole ground floor but a smaller part of it. The rest of the ground floor is covered by a concrete slab as a substrate, but cracks and poor joint with the walls are potential sources of elevated radon. Also, the differences in the results between two methods, passive and active devices, are due to the fact that presented radon values are measured in different seasons. With high-rise residential building, the situation is the opposite and it can be considered from the first floor that the dominant source of radon is the building material. There may even be a slight increase in the mean radon concentration on the higher floors. Also, the results show very low radon level on the first floor (well below the outdoor values) in the apartment. In such sense, we performed test intercomparison radon measurements for two active devices SN1029 and SN1030 in well-defined and controlled radon atmosphere (radon concentration below 30 Bq·m⁻³) in the **Underground Low-background Laboratory** in the Institute of Physics Belgrade [17, 18]. Additional testing includes the same place and time of the measurements but different sampling time set to 1, 2, 4, 8 and 12 h. The results are shown in Table 3.

In the above performed measurements, both devices show significant differences in the low-level radon range, which may originate from individual instruments characteristics presented in the “Materials and methods” section.

Table 2. Results of indoor radon measurements in the single-family house with loft using passive (Radtrak² Radonova) and active radon devices

Floor level	Radon concentration/Passive device (Radtrak ²) [Bq·m ⁻³]	Arithmetic mean (standard deviation) radon concentration over measuring cycle [Bq·m ⁻³]
Basement		160(202)
Ground level	330 ± 50	579(194)
Loft	18 ± 8	53(21)

Table 3. Test intercomparison indoor radon measurements with active radon devices SN1029 and SN1030

	Arithmetic mean (standard deviation) radon concentration over measuring cycle [Bq·m ⁻³]				
Sampling time [h]	1	2	4	8	12
SN1029	28(12)	28(11)	27(7)	23(6)	32(14)
SN1030	12(6)	14(7)	10(3)	12(5)	14(6)

Conclusions

The results show that the radon behaviour in two different residential buildings is diametrically opposite. In the single-family house with loft we registered intense difference between radon concentration in the ground level and loft, while in the high-rise residential building the radon level was almost the same at all floors and hence we may conclude that radon originated mainly from building materials. However, the results from the high-rise building can be predicted on the basis of work of a group of authors who have determined the internal exposure from construction material used in Serbia which originates from the exhalation of radon and thoron [19] and the study presented in this article [10]. We can expect similar results in any other multistorey buildings in Serbia. In the future work, we will focus on the additional radon measurements in the typical residential buildings from other types of houses.

Acknowledgments. The authors acknowledge funding provided by the Institute of Physics Belgrade through the grant by the Ministry of Education, Science and Technological Development of the Republic of Serbia.

ORCID

References

- Bochicchio, F., Campos-Venuti, G., Piermattei, S., Nucetelli, C., Risica, S., Tommasino, L., Torri, G., Magnoni, M., Agnesod, G., Sgorbati, G., Bonomi, M., Minach, L., Trotti, F., Malisan, M. R., Maggiolo, S., Gaidolfi, L., Giannardi, C., Rongoni, A., Lombardi, M., Cherubini, G., D'Ostilio, S., Cristofaro, C., Pugliese, M., Martucci, V., Crispino, A., Cuzzocrea, P., Sansone Santamaria, A., & Cappai, M. (2005). Annual average and seasonal variations of residential radon concentration for all the Italian Regions. *Radiat. Meas.*, *40*, 686–694.
- Friedmann, H. (2005). Final results of the Austrian Radon Project. *Health Phys.*, *89*(4), 339–348.
- Du, L., Prasauskas, T., Leivo, V., Turunen, M., Pekkonen, M., Kivistie, M., Aaltonen, A., Martuzevicius, D., & Haverinen-Shaughnessy, U. (2015). Assessment of indoor environmental quality in existing multi-family buildings in North-East Europe. *Environ. Int.*, *79*, 74–84.
- Cucoş (Dinu), A., Cosma, C., Dicu, T., Begy, R., Moldovan, M., Papp, B., Niţă, D., Burgehele, B., & Sainz, C. (2012). Thorough investigations on indoor radon in Băiţa radon-prone area (Romania). *Sci. Total Environ.*, *431*, 78–83.
- Yarmoshenko, I., Vasilyev, A., Malinovsky, G., Bossew, P., Žunić, Z. S., Onischenko, A., & Zhukovsky, M. (2016). Variance of indoor radon concentration: Major influencing factors. *Sci. Total Environ.*, *541*, 155–160.
- Kropat, G., Bochud, F., Jaboyedoff, M., Laedermann, J. P., Murith, C., Palacios, M., & Baechler, S. (2014). Major influencing factors of indoor radon concentrations in Switzerland. *J. Environ. Radioact.*, *129*, 7–22.
- Borgoni, R., De Francesco, D., De Bartolo, D., & Tzavidis, N. (2014). Hierarchical modeling of indoor radon concentration: how much do geology and building factors matter? *J. Environ. Radioact.*, *138*, 227–237.
- Xie, D., Liao, M., & Kearfott, K. J. (2015). Influence of environmental factors on indoor radon concentration levels in the basement and ground floor of a building – A case study. *Radiat. Meas.*, *82*, 52–58.
- Man, C. K., & Yeung, H. S. (1999). Modeling and measuring the indoor radon concentrations in high-rise buildings in Hong Kong. *Appl. Radiat. Isot.*, *50*, 1131–1135.
- Vukotić, P., Zekić, R., Antović, N. M., & Andjelić, T. (2019). Radon concentrations in multi-story buildings in Montenegro. *Nucl. Technol. Radiat. Prot.*, *34*, 165–174.
- Lorenzo-González, M., Ruano-Ravina, A., Peón, J., Piñeiro, M., & Barros-Dios, J. M. (2017). Residential radon in Galicia: a cross-sectional study in a radon-prone area. *J. Radiol. Prot.*, *37*(3), 728–741.
- Elío, J., Cinelli, G., Bossew, P., Gutiérrez-Villanueva, J. L., Tollefsen, T., De Cort, M., Nogarotto, A., & Braga, R. (2019). The first version of the Pan-European Indoor Radon Map. *Nat. Hazards Earth Syst. Sci.*, *19*, 2451–2464.
- Jovanović Popović, M., Ignjatović, D., Radivojević, A., Rajčić, A., Čuković Ignjatović, N., Đukanović, Lj., & Nedić, M. (2013). *National typology of residential buildings in Serbia*. Belgrade: Faculty of Architecture University of Belgrade.
- Udovičić, V., Maletić, D., Banjanac, R., Joković, D.,

- Dragić, A., Veselinović, N., Živanović, J., Savić, M., & Forkapić, S. (2018). Multiyear indoor radon variability in a family house—A case study in Serbia. *Nucl. Technol. Radiat. Prot.*, 33(2), 174–179.
15. Maletić, D., Udovičić, V., Banjanac, R., Joković, D., Dragić, A., Veselinović, N., & Filipović, J. (2014). Comparison of multivariate classification and regression methods for indoor radon measurements. *Nucl. Technol. Radiat. Prot.*, 29, 17–23.
16. Filipović, J., Maletić, D., Udovičić, V., Banjanac, R., Joković, D., Savić, M., & Veselinović, N. (2016). The use of multivariate analysis of the radon variability in the underground laboratory and indoor environment. *Nukleonika*, 61(3), 357–360. DOI: 10.1515/nuka-2016-0059.
17. Udovičić, V., Aničin, I., Joković, D., Dragić, A., Banjanac, R., Grabež, B., & Veselinović, N. (2011). Radon time-series analysis in the Underground Low-level Laboratory in Belgrade, Serbia. *Radiat. Prot. Dosim.*, 145(2/3), 155–158.
18. Udovičić, V., Filipović, J., Dragić, A., Banjanac, R., Joković, D., Maletić, D., Grabež, B., & Veselinović, N. (2014). Daily and seasonal radon variability in the underground low-background laboratory in Belgrade, Serbia. *Radiat. Prot. Dosim.*, 160(1/3), 62–64.
19. Ujić, P., Čeliković, I., Kandić, A., Vukanac, I., Đurašević, M., Dragosavac, D., & Žunić, Z. S. (2010). Internal exposure from building materials exhaling ^{222}Rn and ^{220}Rn as compared to external exposure due to their natural radioactivity content. *Appl. Radiat. Isot.*, 68, 201–206.



Correlation analysis of solar energetic particles and secondary cosmic ray flux

Nikola Veselinović^a, Mihailo Savić, Aleksandar Dragić, Dimitrije Maletić, Radomir Banjanac, Dejan Joković, David Knežević, and Vladimir Udovičić

Institute of Physics Belgrade, University of Belgrade, Pregrevica 118, Belgrade 11080, Serbia

Received 31 January 2021 / Accepted 5 May 2021

© The Author(s), under exclusive licence to EDP Sciences, SIF and Springer-Verlag GmbH Germany, part of Springer Nature 2021

Abstract. Galactic cosmic rays entering heliosphere are modulated by interplanetary magnetic field which is carried away from the Sun by the solar wind. Cosmic rays are additionally modulated by coronal mass ejections and shock waves, which can produce Forbush decrease, a transient decrease in the observed galactic cosmic ray intensity. Measurements of magnetic field and plasma parameters in near-Earth space detect regularly coronal mass ejections, so it is important to understand the correlation between near-Earth particles fluxes associated with these coronal mass ejections and Forbush decreases. By combining in situ measurements of solar energetic particles with ground-based observations by the Belgrade muon detector, we analysed the dynamics of the variation of galactic cosmic rays. Correlation between variations of the flux of the cosmic rays and average in situ particle fluxes was investigated during Forbush decreases. Correlation exhibited dependence on the energy of solar wind particles, but also on cut-off rigidities of cosmic rays detected on the ground. The goal of cross-correlation analysis is to help in better understanding of how coronal mass ejections affect space weather as well as the effects they have on primary cosmic ray variations as detected by ground-based cosmic ray detectors.

1 Introduction

Space weather has been widely used as a term to define impact of the Sun, heliosphere and geomagnetic field on our biosphere and our technological systems. Understanding space weather is a matter of both scientific interest and practical importance as its impact could potentially be hazardous to our civilisation. Cosmic ray (CR) observations can also be used to study space weather. Primary (or galactic) CRs are high-energy nuclei (mainly protons) that originate from outside of our solar system. Their flux and energy range is covering several tens of orders of magnitude (flux from 10^{-28} up to 10^4 ($\text{m}^2 \text{sr sec eV/nucleon}$)⁻¹ and energy range up to 10^{21} eV [10]). As charged particles, CRs are sensitive to magnetic field, so often it is more convenient to use geomagnetic rigidity instead of energy to characterise primary CRs. Geomagnetic rigidity is defined as $R = B\rho = pq$, where B is the magnetic field, ρ is the gyroradius of the particle due to this field, p is the particle momentum and q is its charge [14]. As they traverse interplanetary space, galactic CRs interact with helio-

spheric magnetic field. The heliosphere is the region of space around the Sun dominated by the solar wind and the interplanetary magnetic field (IMF). The solar wind is a stream of supersonic plasma blowing outward from the Sun. IMF represents solar magnetic field carried by highly conducting solar wind plasma. Interaction of CRs with this large-scale field modulates CRs flux intensity measured on Earth, which is nested deep inside the heliosphere. Interaction with the heliosphere causes gradient and curvature drift motion of CRs and scattering by the magnetic irregularities embedded in the solar wind [19]. Variations in the solar magnetic field directly affect the heliosphere, most prominent being the solar cycle variation with a period of about 11 years. Solar cycle affects activity of the Sun which is visible in varying number of sunspots, solar flares (SFs) and coronal mass ejections (CMEs). Coronal mass ejection is an extreme solar activity event, followed by significant release of charged particles and accompanying magnetic field from solar corona. Intensity of measured CRs flux anticorrelates with the activity of the Sun, with lower intensity during maximum of the solar cycle and higher intensity during minimum of solar activity.

One of the transient phenomena of this interaction is the Forbush decrease (FD), which represents a rapid depression in CR flux. It is usually characterised by a sudden decrease reaching minimum within one day, followed by a subsequent gradual recovery phase, which

Supplementary information The online version of this article (<https://doi.org/10.1140/epjd/s10053-021-00172-x>) contains supplementary information, which is available to authorized users.

^a e-mail: veselinovic@ipb.ac.rs (corresponding author)

can last for several days. Typical causes of FD are transient interplanetary events related to interplanetary coronal mass ejections (ICMEs). If the speed of the ICME is greater than fast magnetosonic wave speed in the solar wind reference frame, ambient solar wind plasma will be compressed. The shock can be formed, which is driven ahead of ICME and can cause enhancement of IMF. FD can also be formed due to corotating interaction regions between different solar wind streams with different speed [2]. In this paper, we will only focus on ICME induced FDs, of which we will study four cases.

Correlation between parameters characterising FDs (like magnitude of the decrease, duration, one-step or two-step FDs, etc.) and solar wind parameters has been studied for some time. There is reasonable evidence for correlation between FD magnitude and amplitude of magnetic field enhancement B , velocity of CME, maximum solar wind velocities and other parameters as shown in [7, 22]. Also, profile of FDs is modelled and compared with CME magnetic structure, starting from the simple force-free flux rope with circular cross section, but it can deviate from this ideal concept. FD magnitude is explained with cumulative effect of diffusion of CRs through the turbulent sheath region [3, 11]. FD is also energy dependent, where amplitude of decrease is typically around several percent. Higher-rigidity CRs only weakly interact with magnetic disturbances, so no significant change of the flux can be expected for CRs with rigidity of several dozen GV [9]. In order to detect FD at any location, larger statistics are needed for CRs of lower energy. CRs also interact with geomagnetic field which imposes the minimal rigidity CRs must have in order to reach Earth's surface. This geomagnetic cut-off rigidity depends on geomagnetic latitude. It is smaller at the poles and increases with latitude, with some exceptions due to deviation of Earth's magnetic field from the magnetic dipole model (i.e., South Atlantic anomaly [4]).

Primary CRs arriving at Earth interact with atoms and molecules in Earth's atmosphere. CRs with energy above 300–400 MeV/nucleon generate showers of secondary particles. These secondary CRs consist of electrons and photons (electromagnetic component) and harder, in terms of energy, nuclear component of the cascade. Nuclear component, at the bottom of the atmosphere, is composed mainly of muons, protons, neutrons and neutrinos. Secondary CRs can be observed with detectors in the atmosphere (balloon probes), on the ground or even underground. High-energy muons can penetrate deep underground and can be an important component of the background in experiments requiring high sensitivity (dark matter search, proton decay, etc.).

There is a well-known correlation between parameters of solar wind plasma and CR flux, and the goal of this paper is to extend the study of FDs, specifically its magnitude and time evolution, to wider range of parameters of the heliosphere measured routinely with satellites. We concentrate our study on previously scarcely used parameters of the solar wind, particularly flux of

charged particles of different energies. These particles are the source of inhomogeneity in the IMF, so the goal is to try and find distinguishing characteristics of FDs, like magnitude of decrease and FD profile that can be related to the satellite proton flux data, and examine their potential correlation with other space weather parameters. This additional information can be useful in finding explicit connection between parameters of solar wind and CR flux and can lead to better understanding of these complex processes.

2 CR data

In order to provide higher count rate, detector on Earth has to be omnidirectional and to detect integral flux over different range of energies. For the last seventy years secondary CRs are measured using standard ground-based neutron monitors (NMs) [6]. There is a worldwide network of NMs (<http://www01.nmdb.eu/>) that measures flux of secondary CRs originated from primary CRs with rigidity range approximately between 1 GV and 20 GV. Every node of the worldwide network of ground stations has its unique cut-off rigidity depending on its geomagnetic coordinates and height. The other type of widely used ground-based CR detectors are muon monitors. Muon monitors are sensitive to primary CRs of higher rigidity and complement NMs measurements [26]. Worldwide network of these muon stations is still rudimentary, but it can provide insight into flux variation of primary CRs with energies higher than CRs detected by NMs. Since both NMs and muon detectors are energy-integrating detectors and use entire atmosphere above it as a moderator, it is not trivial to relate count rate of these detectors to the flux or energy spectrum of primary CRs at the top of the atmosphere. One needs to know the response of a detector to a unit flux of CRs with the given energy, the so-called detector yield function. Yield functions can be calculated either theoretically, using a numerical simulation of the nucleonic cascade caused by energetic cosmic rays in the Earth's atmosphere, e.g., [8], or semi-empirically, for example based on a latitudinal survey [16].

As flux of secondary cosmic rays is also sensitive to varying properties of the atmosphere through which these CRs propagate, it is necessary to conduct flux correction of the measured flux for atmospheric parameters, where atmospheric pressure correction is the most important. In addition to atmospheric pressure, CR muons are sensitive to temperature variations in the atmosphere, starting from the top of the atmosphere all the way to the ground level. There are several procedures for corrections of these effects which are regularly used. Most commonly used are the integral method and the method of effective level of generation, but some novel techniques have also been introduced in recent years [25]. Correction for these atmospheric parameters is necessary in order to increase detector sensitivity to

Table 1 Properties of primary CR flux related to muons detected at Belgrade CR station

Detector	Muon flux 1/(m ² s)	$E_{0.05}$ (GeV)	E_{med} (GeV)	$E_{0.95}$ (GeV)	Cut-off rigidity (GV)
GLL	137(6)	11	59(2)	915	5.3
UL	45(2)	31	137(5)	1811	12

variations of primary CRs flux and more precisely study the influence of solar modulation on galactic CRs.

Belgrade CR station started collecting data with the current experimental set-up in 2009. The station consists of two separate detector units: one placed on ground level (GLL) and the other in shallow underground (UL), both utilising the same experimental set-up. Such configuration provides opportunity to monitor muon fluxes in two different energy ranges with all other external parameters (such as atmospheric parameters, geomagnetic location and experimental set-up) being the same. Underground part of the station detects muons originated from primary CRs with higher energy because of the layer of soil overburden (13 m of loess) which absorbs lower-energy muons. Details of the detector systems at the Belgrade CRs station as well as calculated response functions are presented in [29]. The station is situated at the Laboratory for Nuclear Physics at the Institute of Physics Belgrade, Serbia. The altitude of the station is 78 m above sea level. Its geographic coordinates are: 44°51' N and 20°23' E, with geomagnetic latitude of 39°32' N. Sensitivity of Belgrade CR detectors to galactic CRs is given in Table 1, where primary CRs with the energy below $E_{0.05}$ (and above $E_{0.95}$) contribute with 5% to the count rate of the corresponding detector, and E_{med} is median energy based on simulation. In preparation for the analysis, detected muon count rates are corrected for efficiency, as well as for barometric and atmospheric temperature effects. Temperature effect correction is done using integral method [24].

3 Satellite data

In recent years, satellites provide new direct measurements of primary CRs flux in the heliosphere and the geomagnetic field. Also, detectors mounted on spacecraft allow us to probe even further, as Voyager recently crossed heliospheric boundary and for the first time galactic CRs flux was measured outside the heliosphere. The problem with such measurements is limitation to the size of the detectors, due to constraints of the construction of the satellites. In order to have valid statistics and good resolution, only low-energy particle flux can be measured. These low-energy particles are sensitive to geomagnetic field, which can introduce additional perturbation. Also, measurements of low-energy CRs can be masked by the increased flux of low-energy solar energetic particles (SEPs) in the MeV energy range. FDs detected by ground-based detectors are measured in energy range several orders of

magnitude higher than the energy range available to satellites measurements. (NMs detect flux that originate from ~ 10 GeV, single muon detectors higher than that up to ~ 100 GeV, while solar weather satellite measurements range up to several 100 MeV.) SEP occurrence is sporadic and depends on which part of the solar cycle we are in, so long-term studies with stable data quality are necessary if we are to study solar modulation of CRs. Such long-term measurements have been performed with various spacecrafts during the last four decades. Data measured on different interplanetary locations are then used for modelling of the heliosphere, which is important for understanding and forecasting space weather. This is a relatively new and dynamic field that is still expanding. More in situ measurements that can be catalogued [17] and compared with data from ground based stations will improve our understanding of near space environment.

In this paper, we use proton data from ERNE (Energetic and Relativistic Nuclei and Electron experiment) detector at the SOHO (Solar and Heliospheric Observatory) (https://omniweb.gsfc.nasa.gov/ftpbrowser/flux_spectr_m.html), which has been performing measurements in Lagrangian point L1 for the last quarter of a century described in [13] and references therein. Experiments that collect in situ particles data are ERNE and COSTEP (Comprehensive SupraThermal and Energetic Particle analyser), where data are combined to meet requirements of the mission. ERNE detector provides proton flux data in relatively large energy range (1.6 to 131 MeV) separated in several energy channels (1.3–1.6, 1.6–2.0, 2.0–2.5, 2.5–3.2, 3.2–4.0, 4.0–5.0, 5.0–6.4, 6.4–8.0, 8.0–10, 10–13, 13–16, 16–20, 20–25, 25–32, 32–40, 40–50, 50–64, 64–80, 80–100, 100–130 MeV). Measurements are taken with two different detectors: LED (low-energy detector) covers lower-energy and HED (high-energy detector) which covers higher-energy channels [28]. Satellites, including SOHO, also measure in situ parameters of the space environment and gather data about magnetic field, solar wind and concentration and flux of various types of particles on the location. Satellite data relevant to heliospheric studies are, among other places, available at GSFC/Space Physics Data Facility, in the form of low- and high-resolution OMNI data (https://spdf.gsfc.nasa.gov/pub/data/omni/low_res_omni/). In this study, we used the low-resolution OMNI data that contain hourly data for the solar wind magnetic field and plasma parameters, energetic proton fluxes, and geomagnetic and solar activity indices for different regions in proximity to Earth [12].

4 Four prominent FD events during rising phase of solar cycle 24

Previous (24th) solar cycle started in December 2008 and ended in November 2019 (as available from Sunspot Index and Long-term Solar Observations database <http://www.sidc.be/silso/node/167>). It had an unusually weak maximum, with smoothed maximum international sunspot number of 116. For comparison, in cycles 22 and 23 this number was 214 and 180, respectively (as available from Sunspot Index and Long-term Solar Observations database <http://sidc.be/silso/home>). Same period was also characterised by smaller number of FDs, especially ones with larger amplitudes.

There were fifteen strong FDs (with magnitude of decrease larger than 5% for particles with 10 GV rigidity) recorded in the rising phase of solar cycle 24, however in this study we will limit our analysis to four events detected by the Belgrade Cosmic Ray Station (<http://www.cosmic.ipb.ac.rs/>). Other prominent FDs that occurred in this period have not being detected by either GLL or UL detector due to discontinuity of operation, so they have been omitted from this study. All four events followed ejections from an active region on the Sun, accompanied by a solar flare with interplanetary shock wave and sudden storm commencing (SSC), and disturbance in the geomagnetic field. All of these FDs were seen by the NM detector network as well.

First significant FD of solar cycle 24 was recorded on 18 February 2011 and has been caused by a CME heading directly towards Earth [20]. It has been detected by most ground stations around the world. Its morphology is influenced by the interaction of two CMEs, first slower and the second faster (with respective speeds of 390 km/s and 1020 km/s), that occurred a day apart [27]. Geomagnetic activity has been relatively weak due to orientation of the magnetic field of the ejecta [21].

Second event was observed on 7 March 2012. It included an X-class flare (X5.4), that occurred in NOAA AR 11429 with an intense halo CME, followed by several smaller flares and another partial CME. It caused one of the strongest FDs of the last solar cycle. Observed solar activity was also related to the intense geomagnetic storm that followed [15].

A strong SF (X1.6) was detected by several spacecrafts during 10 September 2014, originating from active region NOAA AR 2158. Based on the SOHO coronagraph images, this flare was associated with a CME that was aimed towards Earth, where it arrived on September 12. This activity resulted in a major geomagnetic storm, one of the strongest in 2014.

In the second half of June 2015, solar activity was very intense, since a number of CMEs and flares were produced from the powerful AR 12371, which dominated solar activity during that period [23]. The impact of these CMEs on the Earth's magnetosphere resulted in a moderate to severe G4-class geomagnetic storm that occurred on the summer solstice. The result was a very interesting and unusual modulation galactic CRs flux, which appeared as a series of FDs.

For the study of FD events and their relationship with IMF and geomagnetic disturbances, researchers from IZMIRAN (Pushkov Institute of Terrestrial Magnetism, Ionosphere and Radio Wave Propagation, Russian Academy of Sciences) created an FD database (<http://spaceweather.izmiran.ru/eng/dbs.html>) which contains various FD parameters, as well as their relationship with heliospheric and geomagnetic parameters covering several solar cycles [1]. Properties of the four selected FDs, taken from the IZMIRAN database, are given in Table 2.

5 Data analysis

In order to establish the usability of SOHO SEP flux data in the study of CR variations, we will first analyse how muon count rate time series compare with some of the IMF parameters more commonly used in the analysis of solar activity-induced CR variations. To this end, we compare hourly muon count rates (measured by Belgrade muon station and corrected for atmospheric effects) with time series for selected parameters from OMNI database. To give more weight to this qualitative analysis, we concentrate only on periods of extreme solar activity, in particular periods of the occurrence of four FD events described in Sect. 4. We then examine the relationship between measured muon count rates and the SOHO/ERNE SEP flux data and analyse any discerning features in comparison with the ones observed in OMNI data time series. The period selected for this analysis is approximately one solar rotation of 27 days. All probes at L1 are about an hour upstream of the magnetosphere so all their data are interspersed with data from spacecraft close to Earth (e.g., IMP 8). In order to compute hourly averages "at Earth" this time shift has to be taken into account (https://omniweb.gsfc.nasa.gov/html/ow_data.html).

Next, we investigate the short-term correlation between SEP flux and muon count rate data during time periods of four selected FDs. Muon time series for this procedure were selected for times where average muon flux was significantly lower than the background level. Background level was determined from moving averages for hourly count rates 10 days before the event. We then perform correlative analysis between SOHO SEP flux data and muon count rates for a period of one year (from 01.06.2010 to 31.05.2011), in order to establish the long-term relationship. For further insight, we also look into the correlation between these variables during the periods of reduced geomagnetic activity (International Quiet Days) and increased geomagnetic activity (International Disturbed Days).

Finally, we look in greater detail into SOHO SEP flux time series. In order to perform more quantitative analysis, time-integrated flux is calculated for SEP data for different SOHO energy bins and for the duration of selected FD events. In order to provide a parameter for characterisation for different FD events, calculated integral flux is plotted as a function of proton energy and

Table 2 Selected FD and interplanetary disturbance parameters (taken from IZMIRAN database)

Parameter	FD 1	FD 2	FD 3	FD 4	Parameter comment
Date of FD	18.2.2011.	8.3.2012.	12.9.2014.	22.6.2015.	
Date of parent solar event	15.2.2011.	7.3.2012.	10.9.2014.	21.6.2015.	
AR number	1158	11429	2158	12371	NOAA active region
V_{meanC}	584	1198	906	1040	The average ICME velocity between the Sun and the Earth, calculated using the time of the beginning of the associated CME observations (in km/s)
V_{max}	691	737	730	742	Maximal hourly solar wind speed in the event (in km/s)
B_{max}	31	23.1	31.7	37.7	Maximal hourly IMF strength in the event (in nT)
B_{zmin}	- 5.5	- 16.1	- 9.5	- 26.3	Minimal hourly Bz component of the IMF in the event (in nT)
R_{bulk}	72.25	146.2	131.35	171.25	An estimate of the maximum proton rigidity (in GV) that can be reflected by the total magnetic field, integrated from the event onset to the FD minimum
Magn	5.2	11.7	8.5	8.4	FD magnitude for particles with 10 GV rigidity, calculated as maximal range CRs density variations in the event, obtained by GSM from NM network data (in %)
MagnM	4.7	13.1	6.9	10.4	FD magnitude for particles with 10 GV rigidity, corrected on magnetospheric effect with Dst-index (in %)
TminM	7	20	9	11	Time from the FD onset to minimum, calculated from the data corrected for magnetospheric effect
Kp_{max}	5	8	6.33	8.33	Maximal Kp-index in the event
Ap_{max}	48	207	94	236	Maximal 3-hour Ap-index in the event
Dst_{min}	- 30	- 143	- 75	- 204	Minimal Dst-index in the event (in nT)
Flare class	X2.2	X5.4	X1.6	M2.6	Associated X-ray flare data
SSN	85	97	126	56	Number of sunspot at the FD onset day

fitted with a power function. Dependence of magnitude for selected FDs on the exponents obtained from fitted distributions is then analysed.

6 Results and discussion

Comparison between time series of selected IMF parameters from OMNI database and muon count rate time

series during the periods of four selected FD events is shown in Fig. 1. Observed anticorrelation between muon count rates and proton flux and temperature, as well as with the overall IMF magnetic field and detected plasma speed, is in agreement with previously stated evidence in the literature [30].

Similar comparison between muon count rate time series and selected channels of SOHO/ERNE proton flux data for the same time intervals is shown in Fig.

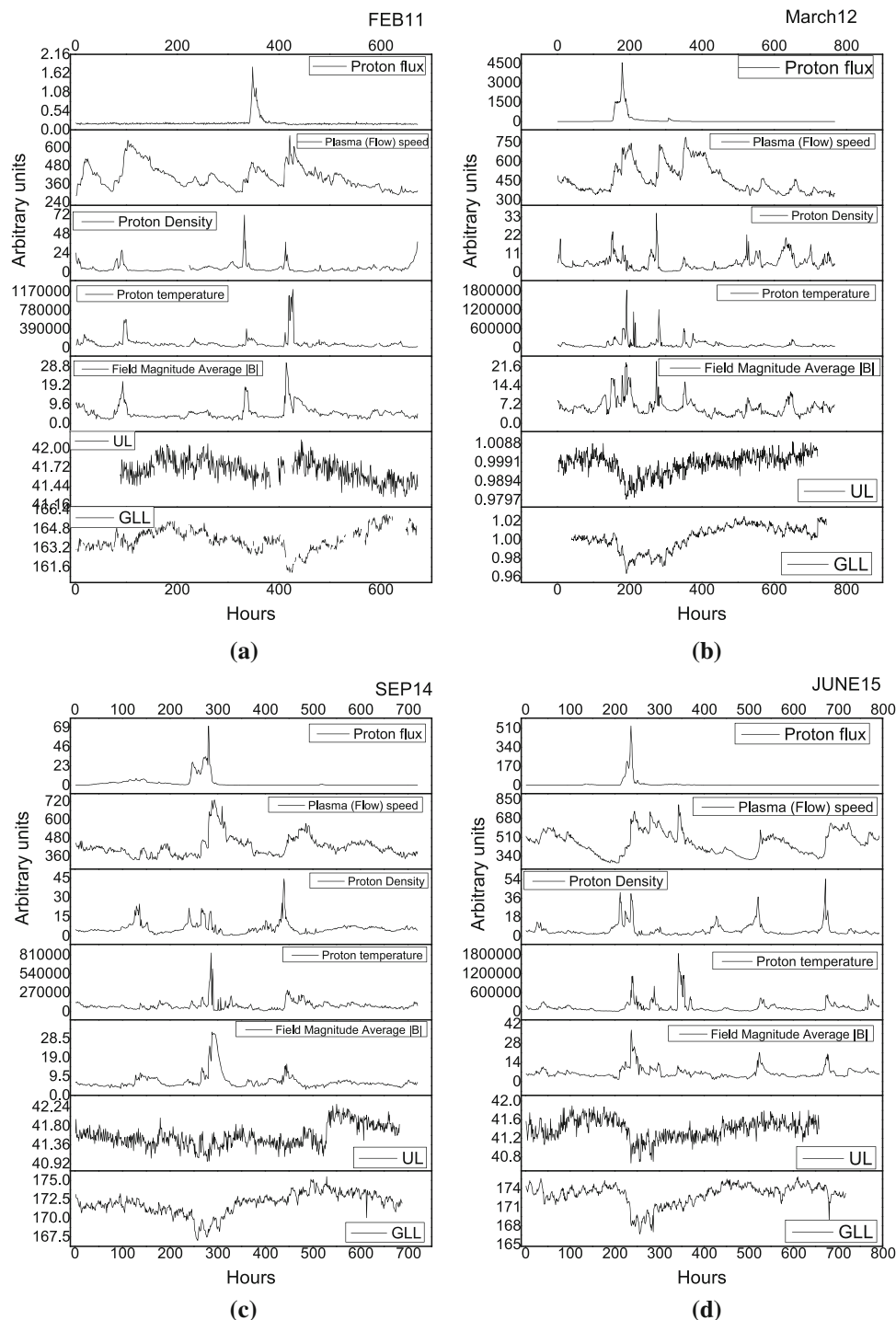


Fig. 1 Time series for particle and plasma parameters (taken from OMNI database) in the time interval of approximately one month around the occurrence of four selected FD events: **a** February 2011 (start of time interval on 1 February), **b** March 2012 (start of time interval on 1 March), **c** September 2014 (start of time interval on 1 September) and **d** June 2015 (start of time interval on 13 June)

2. For the sake of clarity, we chose three energy channels (1.6–2 MeV, 16–20 MeV, 100–130 MeV), approximately one order of magnitude apart, where first channel is measured with LED and the other two with HED detector on SOHO/ERNE instrument. In case of the

February 2011 event, there is an observable time lag (≈ 55 h) between the increase of measured proton flux at low-energy channels (1.6–2 MeV and 16–20 MeV energy channels) and the beginning of FD recorded at ground station. This time lag is also present between

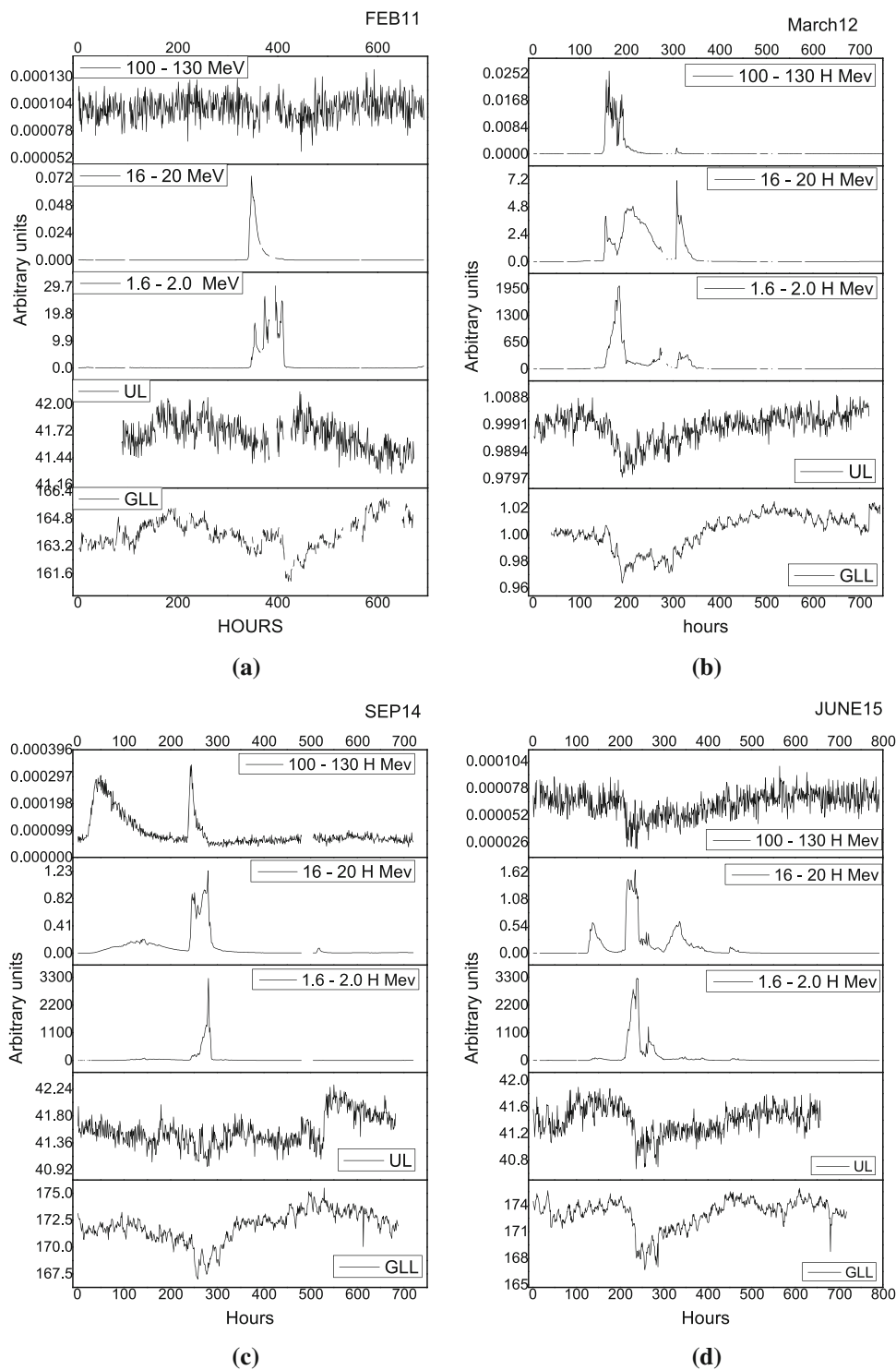


Fig. 2 Hourly time series for different proton channels from SOHO/ERNE and two muon detectors at Belgrade CR station, in the time interval of approximately one month around the occurrence of four selected FD events: **a)** February (start of time interval on 1 February) 2011, **b)** March 2012 (start of time interval on 1 March), **c)** September 2014 (start of time interval on 1 September) and **d)** June 2015 (start of time interval on 13 June)

OMNI proton flux data and ground station measurements for this FD alone. FD is a complex modulation of CR flux that depends on a lot of parameters, like magnitude of magnetic field and its components,

speed of solar wind and CMEs (with CME average speed ≈ 490 km/s), most of which are listed in Table 2. Parameter values for all four ICMEs are mostly comparable, but one difference that stands out is the discrep-

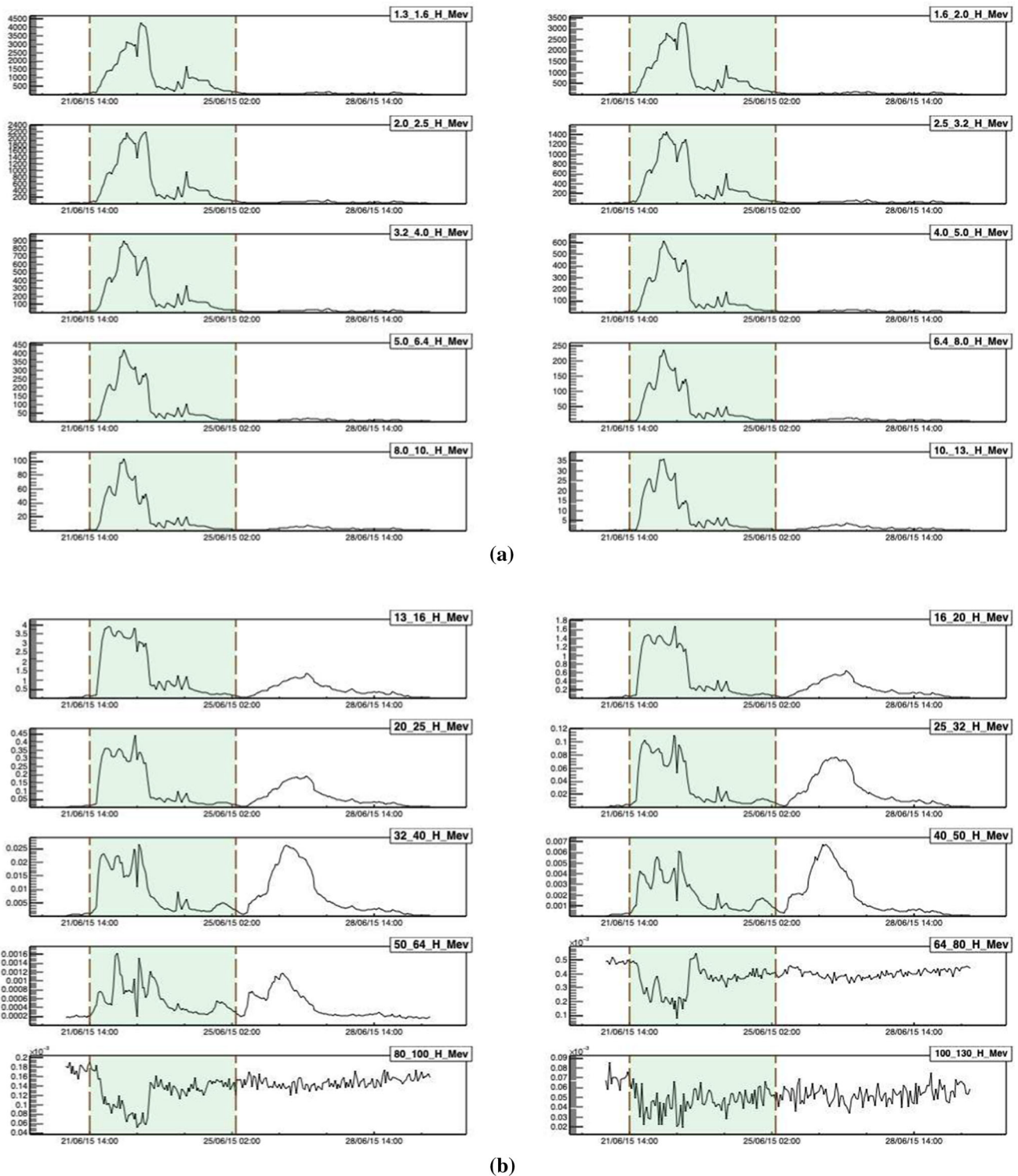


Fig. 3 Differential SEP fluxes during extreme solar event in June 2015, measured by SOHO/ERNE proton channels. Vertical dashed lines indicate the time for the start and the end of interval used to calculate the integral flux

ancy in average CME velocity (584 km/s from Table 2.) for the FD of February 2011, which can possibly explain the observed time lag for this particular FD.

Based on the observed time lag and other coincident features, we can establish good agreement between

SOHO low-energy channel data and OMNI data time series. As for high-energy channels, SEP time series in 100–130 MeV energy range for February 2011 and June 2015 events appear to correlate with muon count rate measurements on the ground. One possible explanation

Table 3 Statistical correlation between Belgrade CR station and SOHO/ERNE measurements during the periods of four selected FD events

FD	Energy range (MeV)	GLL		UL	
		Pearson coefficient	<i>P</i> value	Pearson coefficient	<i>P</i> value
FEB 11	1.6–2.0 H	– 0.10877	0.01	– 0.05285	0.2
	16–20 H	– 0.18384	2×10^{-5}	– 0.10732	0.01
	100–130 H	0.24204	$< 10^{-6}$	– 0.13212	0.02
MAR 12	1.6–2.0 H	– 0.48477	$< 10^{-6}$	– 0.43994	$< 10^{-6}$
	16–20 H	– 0.72033	$< 10^{-6}$	– 0.68221	$< 10^{-6}$
	100–130 H	– 0.29172	$< 10^{-6}$	– 0.27822	$< 10^{-6}$
SEP 14	1.6–2.0 H	– 0.2839	$< 10^{-6}$	– 0.48052	$< 10^{-6}$
	16–20 H	– 0.37814	$< 10^{-6}$	– 0.63735	$< 10^{-6}$
	100–130 H	– 0.04951	0.007	– 0.10466	0.2
JUN 15	1.6–2.0 H	– 0.3921	$< 10^{-6}$	– 0.27531	$< 10^{-6}$
	16–20 H	– 0.31229	$< 10^{-6}$	– 0.17113	$< 10^{-6}$
	100–130 H	0.48588	$< 10^{-6}$	0.39296	$< 10^{-6}$

could be that in addition to SEP these energy channels are also populated by very low-energy CRs.

We can further investigate this assumption by looking more closely into SOHO SEP flux time series for one of the two weaker FD events. We have selected June 2015 event, as time series for higher-energy channels appear to be slightly more informative. Figure 3 shows proton flux series for all energy channels measured by SOHO/ERNE detector. From these plots, it is apparent that proton fluxes for energies larger than 64 MeV exhibit different dynamic relative to fluxes of lower energies, and seem to be in anticorrelation with them. This indeed supports the assumption these channels are populated by low-energy CR.

Another way we can illustrate this observation more quantitatively is by performing correlative analysis. Firstly, we will look into short-term correlations between proton flux and muon count rate time series during four selected FD events. Correlation between respective time series was found using Pearson correlation coefficient. For significance two-tailed test is used. Correlation coefficient and its significance level between ground station and in situ measurement from SOHO/ERNE instrument is given in Table 3.

Due to higher energy of the primary CRs detected in UL, the correlation between SEPs and measured flux in UL is smaller than correlation between SEPs and flux measured in GLL. The greatest anticorrelation (i.e., between GLL and UL data and 16–20 MeV protons ≈ -0.7) is observed for the strongest ICME (and corresponding FD) of March 2012, and this anticorrelation is observed in all energy channels. However, for lower-intensity events of June 2015 and February 2011, correlations between detected CR flux in GLL and highest energy channel (100–130 MeV) are mostly positive. These observations further confirm the assumption about high-energy channels being populated by low-energy CR, which is especially evident in case of low-intensity FD events.

Table 4 Pearson correlation coefficient for the correlation between CR flux detected at Belgrade CR station (GLL detector) and flux of protons of different energies detected with SOHO/ERNE detector, for the period of one year (from June 2010 May 2011)

	GLL	
	Pearson coefficient	<i>P</i> value
H 1.3–1.6 MeV	– 0.02	0.13
H 1.6–2.0 MeV	– 0.02	0.16
H 2.0–2.5 MeV	– 0.02	0.20
H 2.5–3.2 MeV	– 0.01	0.27
H 3.2–4.0 MeV	– 0.01	0.36
H 4.0–5.0 MeV	– 0.01	0.57
H 5.0–6.4 MeV	< 0.01	0.75
H 6.4–8.0 MeV	< 0.01	1.00
H 8.0–10 MeV	< 0.01	0.78
H 10–13 MeV	0.01	0.57
H 13–16 MeV	0.01	0.41
H 16–20 MeV	0.01	0.31
H 20–25 MeV	0.01	0.26
H 25–32 MeV	0.01	0.24
H 32–40 MeV	0.01	0.27
H 40–50 MeV	0.01	0.46
H 50–64 MeV	< 0.01	0.80
H 64–80 MeV	0.05	< 0.01
H 80–100 MeV	0.12	< 0.01
H 100–130 MeV	0.07	< 0.01

Similar results, with even greater correlation between the entire time profile for flux measured with NMs and solar wind speed and magnetic field during ICME, are reported for stronger FDs during solar cycle 23 [5].

Next, we will analyse long-term correlations between SOHO proton flux and measured muon count rates. Pearson coefficients for this correlation over a period of one year (from June 2010 May 2011), when activity of the Sun was low at the commencement of the 11-years cycle, are presented in Table 4. Here we see very

Table 5 Pearson correlation coefficient for the correlation between CR flux detected at Belgrade CR station (GLL detector) and flux of protons of different energies detected with SOHO/ERNE detector, during international geomagnetically quiet and disturbed days for the period of one year (from June 2010 May 2011)

	GLL Quiet days		GLL Disturbed days	
	Pearson coefficient	<i>P</i> value	Pearson coefficient	<i>P</i> value
H 1.3–1.6 MeV	0.01	0.61	– 0.05	0.13
H 1.6–2.0 MeV	0.01	0.80	– 0.05	0.14
H 2.0–2.5 MeV	0.02	0.30	– 0.05	0.13
H 2.5–3.2 MeV	0.03	0.11	– 0.05	0.12
H 3.2–4.0 MeV	0.04	0.04	– 0.05	0.10
H 4.0–5.0 MeV	0.05	0.02	– 0.06	0.08
H 5.0–6.4 MeV	0.05	0.01	– 0.06	0.07
H 6.4–8.0 MeV	0.06	0.01	– 0.06	0.06
H 8.0–10 MeV	0.06	0.01	– 0.06	0.06
H 10–13 MeV	0.06	0.01	– 0.06	0.07
H 13–16 MeV	0.06	< 0.01	– 0.06	0.08
H 16–20 MeV	0.06	< 0.01	– 0.05	0.10
H 20–25 MeV	0.06	< 0.01	– 0.05	0.12
H 25–32 MeV	0.06	< 0.01	– 0.05	0.15
H 32–40 MeV	0.06	< 0.01	– 0.04	0.20
H 40–50 MeV	0.06	< 0.01	– 0.02	0.57
H 50–64 MeV	0.07	< 0.01	0.07	0.03
H 64–80 MeV	0.25	< 0.01	0.08	0.02
H 80–100 MeV	0.38	< 0.01	0.11	< 0.01
H 100–130 MeV	0.15	< 0.01	0.09	0.01

little correlation between CR and proton fluxes in all but the highest energy channels (above 64 MeV).

Table 5 shows the same correlation analysis if only data for 10 geomagnetically quietest or 5 geomagnetically most disturbed days of each month (http://isgi.unistra.fr/events_qdays.php) are used. The fact that we observe a significant increase of positive correlation coefficients in the case of geomagnetically quiet days, further corroborates the assumption about the mixed nature of particles that populate higher-energy channels. Consequentially, care should be taken how data from these channels are treated in analysis.

To provide further quantitative support for the use of SOHO SEP flux measurements in the analysis of FD events, we will calculate integral proton flux in all energy channels for the four selected FDs. Integration intervals are selected to include the period of increased proton flux that corresponds to a particular FD, but not to extend the interval to include potential follow-up structures that cannot be associated with the event. One such selection for all energy channels, for June 2015 event, is indicated by dashed lines in Fig. 3. In Fig. 4, we show thusly calculated integral flux as a function of particle energy (where lower boundary values from SOHO SEP energy bins are taken), using both linear and log scale for clarity.

One feature that can be noticed from plots in Fig. 4 is that integral flux drops off is more steeply in February 2011 than for others studied FDs, where a change in the trend between high-energy and low-energy range can be observed. FD that occurred in March 2012 was the longest and the most intensive of the four. Steepness of

the integral flux for this FD shows relatively more populated proton channels with higher energies compared to weaker FD. This is in agreement with strongest modulation of CRs flux during this FD. There is a discontinuity in the integral flux between proton energy channel 13–16 MeV and 16–20 MeV due to different acquisition method from different instruments, and possibly because of degradation of the detectors on board the spacecraft [13] and saturation of the instrument due to high intensity of solar protons [18].

One simple way to characterise relative abundance of SEP particles of different energies for a given event would be to fit described integral flux distribution with a power function, where (in a simple approximation) larger exponent would indicate greater relative abundance of lower-energy particles, while smaller exponent would point to greater relative abundance of higher-energy particles. Distributions were fitted with a power function given by the formula $I(E) = a * E^b$ (where I is the integral flux and E is particle energy), resulting fits represented by red lines in Fig. 4, while values for the exponents of power function fits are represented in Table 6.

If SOHO protons flux measurements are to be proved useful in the analysis of FD events, SEP flux characteristics should correlate with some of the FD and interplanetary disturbance parameters. To test this, we have analysed dependence of different FD parameters on the exponent of the integral proton flux power distribution (labelled b in the formula in previous paragraph). We have found some correlation for most tested parameters, most striking being one between the magnitude

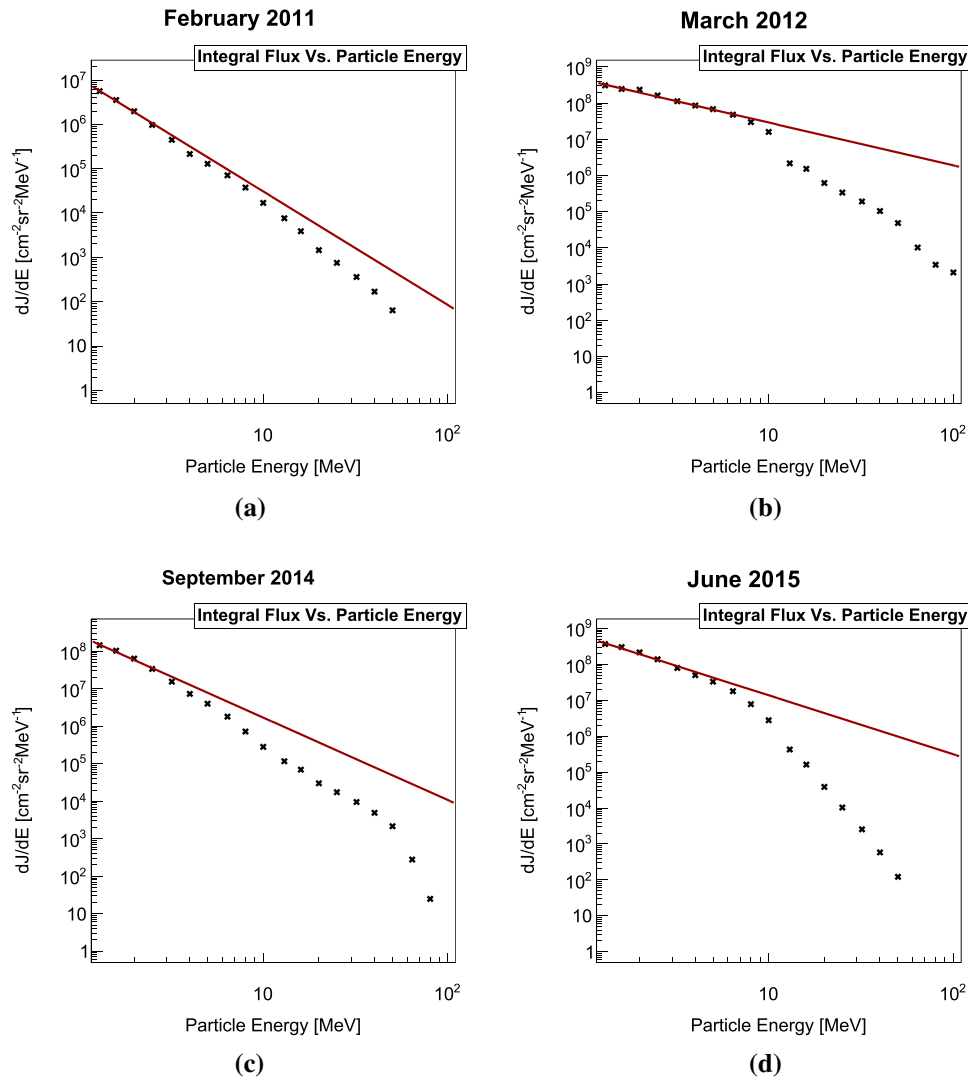


Fig. 4 Time-integrated flux of differential SEP fluxes during the four selected FD events: **a** February 2011, **b** March 2012, **c** September 2014 and **d** June 2015, in linear and logarithmic scale. Power function fits are represented by red lines

Table 6 Exponent values of power function fits of integral proton flux distributions

FD	Power function exponent values
FEB 2011	- 2.56
MAR 2012	- 1.18
SEP 2014	- 2.20
JUN 2015	- 1.64

of FD for particles with 10 GV rigidity (corrected for magnetospheric effect) and the exponent of the integral flux. This dependence (strictly for illustrative purposes fitted with linear fit) is shown in Fig. 5.

Observed strong dependence is potentially a very good indicator that SOHO SEP flux measurements can be a valid source of data to be used in the analysis of

interplanetary disturbances and their interaction with cosmic rays.

7 Conclusions

Analysing strong aperiodic variations of cosmic ray flux, such as Forbush decreases, allows us to study violent processes that occur on the Sun, and corresponding perturbations in the heliosphere, using Earth-based detectors. In addition to cosmic ray flux and magnetic field data commonly used to study such events, we have extended analysis to include proton flux measurements, obtained using spacecraft mounted detectors. Based on the analysis of four selected Forbush decrease events, we have found SOHO/ERNE proton flux measurements to be consistent with solar plasma parameters, as well as with observations by the ground-based muon detectors.

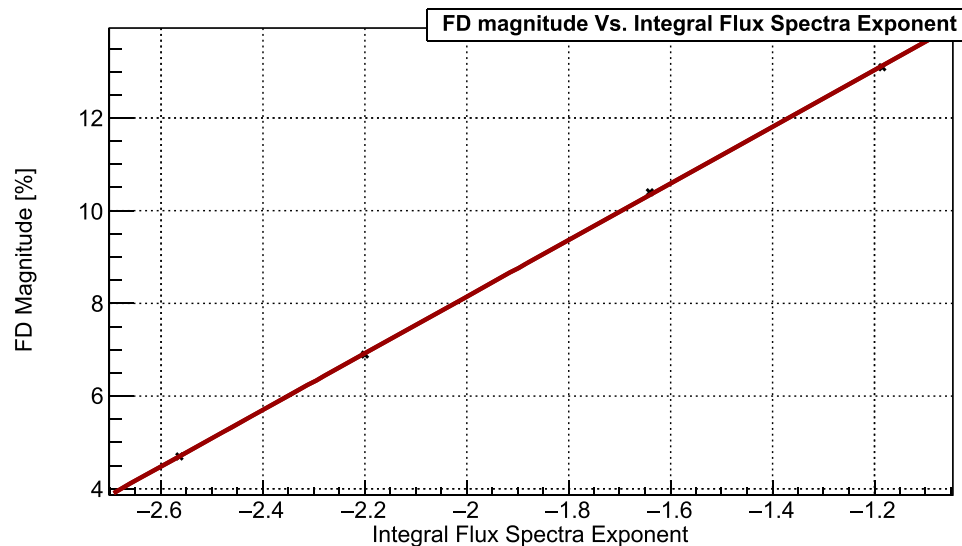


Fig. 5 Dependence of FD magnitude, corrected for magnetospheric effect with Dst-index for particles with 10 GV rigidity, on the power exponent of the integral SEP flux, four selected FD events: **a** February 2011, **b** March 2012, **c** September 2014 and **d** June 2015. Linear fit (for illustrative purposes) is indicated by the red line

We have concluded that during Forbush decrease events lower-proton-energy channels are dominated by SEP particles, while in higher-energy channels there is a contribution of low-energy cosmic rays, especially apparent during less intense events. We have found a clear correlation between Forbush decrease magnitude (corrected for magnetospheric effect with Dst-index for particles with 10 GV rigidity) and power exponent of the integral flux of SOHO/ERNE measurements. This result gives grounds to further pursue the analysis of heliospheric proton flux data, as it may yield additional valuable information. Such information can potentially help us to classify and study in greater detail the dynamics of interaction of cosmic rays in the heliosphere.

Acknowledgements The authors acknowledge funding provided by the Institute of Physics Belgrade, through the grant by the Ministry of Education, Science and Technological Development of the Republic of Serbia. We also acknowledge use of NASA/GSFC's Space Physics Data Facility's OMNIWeb (or CDAWeb or ftp) service and OMNI data as well as team behind SOHO, which is a project of international collaboration between ESA and NASA. We would also like to thank the referees for constructive and useful advice.


Data Availability Statement "This manuscript has data included as electronic supplementary material".

References

1. A.A. Abunin, M.A. Abunina, A.V. Belov, S.P. Gaidash, E.A. Eroshenko, I.I. Pryamushkina, L.A. Trefilova, E.I. Gamza, *J. Phys. Conf. Ser.* **1181**, 012062 (2019). <https://doi.org/10.1088/1742-6596/1181/1/012062>
2. K.P. Arunbabu, H.M. Antia, S.R. Dugad, S.K. Gupta, Y. Hayashi, S. Kawakami, P.K. Mohanty, T. Nonaka, A. Oshima, P. Subramanian, *A and A* **555**, A139 (2013). <https://doi.org/10.1051/0004-6361/201220830>
3. K.P. Arunbabu, H.M. Antia, S.R. Dugad, S.K. Gupta, Y. Hayashi, S. Kawakami, P.K. Mohanty, A. Oshima, P. Subramanian, *A and A* **580**, A41 (2015). <https://doi.org/10.1051/0004-6361/201425115>
4. C.R.A. Augusto, V. Kopenkin, C.E. Navia, K.H. Tsui, H. Shigueoka, A.C. Fauth, E. Kemp, E.J.T. Manganote, M.A. Leigui de Oliveira, P. Miranda, R. Ticona, A. Velarde, *ApJ* **759**, 143 (2012). <https://doi.org/10.1088/0004-637X/759/2/143>
5. A. Bhaskar, G. Vichare, K.P. Arunbabu et al., *Astrophys. Space Sci.* **361**, 242 (2016). <https://doi.org/10.1007/s10509-016-2827-8>
6. V. Belov, *SpaceSci. Rev.* **93**(1), 79–105 (2000). <https://doi.org/10.1023/A:1026584109817>
7. H.V. Cane, *Space Sci. Rev.* **93**, 55–77 (2000). <https://doi.org/10.1023/A:1026532125747>
8. J.M. Clem, L.I. Dorman, *Space Sci. Rev.* **93**, 335–359 (2000). <https://doi.org/10.1023/A:1026508915269>
9. E.S. Comedi, A.S. Elias, B.S. Zossi, S. Bruno, *JASTP* **211**, 105475 (2020). <https://doi.org/10.1016/j.jastp.2020.105475>
10. M. Duldig, *Science* **314**(5798), 429–430 (2006). <https://doi.org/10.1126/science.1134046>
11. M. Dumbović, B. Vršnak, J. Guo et al., *Sol. Phys.* **295**, 104 (2020). <https://doi.org/10.1007/s11207-020-01671-7>
12. J.H. King, N.E. Papitashvili, *J. Geophys. Res.* **110**, A02104 (2005). <https://doi.org/10.1029/2004JA010649>
13. P. Kühl, B. Heber, R. Gómez-Herrero, O. Malandraki, A. Posner, H. Sierks, *J. Space Weather Space Clim.* (2020). <https://doi.org/10.1051/swsc/2020056>
14. S.Y. Lee, *Accelerator Physics*, 2nd edn. (World Scientific, Singapore, 2004)

15. M. Livada, H. Mavromichalaki, C. Plainaki, *Astrophys. Space Sci.* **363**, 8 (2018). <https://doi.org/10.1007/s10509-017-3230-9>
16. R.A. Caballero-Lopez, H. Moraal, *JGR Space Phys.* **117**, A12 (2012). <https://doi.org/10.1029/2012JA017794>
17. R. Miteva, S.W. Samwel, M.V. Costa-Duarte, *JASTP* (2018). <https://doi.org/10.1016/j.jastp.2017.05.003>
18. R. Miteva, D. Danov, in *Proceedings of the tenth Workshop 'Solar Influences on the Magnetosphere, Ionosphere and Atmosphere', Primorsko, Bulgaria*, ed. by K. Georgieva, B. Kirov, D. Danov, 2018. <https://doi.org/10.31401/WS.2018.proc>
19. H. Moraal, *Space Sci. Rev.* **176**, 299–319 (2013). <https://doi.org/10.1007/s11214-011-9819-3>
20. S.Y. Oh, Y. Yi, *A Sol. Phys.* **280**, 197–204 (2012). <https://doi.org/10.1007/s11207-012-0053-2>
21. A. Papaioannou, A. Belov, H. Mavromichalaki et al., *J. Phys. Conf. Ser.* **409**, 012202 (2013). <https://doi.org/10.1088/1742-6596/409/1/012202>
22. A. Papaioannou, M. Belov, E. Abunina, A. Eroshenko, A. Abunin, S. Anastasiadis, Patsourakos, H. Mavromichalaki, *ApJ* **890**, 101 (2020). <https://doi.org/10.3847/1538-4357/ab6bd1>
23. E. Samara, A. Smponias, I. Lytrosyngounis et al., *Sol. Phys.* **293**, 67 (2018). <https://doi.org/10.1007/s11207-018-1290-9>
24. M. Savić, A. Dragić, N. Veselinović et al., *XXV ECRS 2016 Proceedings—eConf C16-09-04.3*, e-Print: 1701.00164 [physics.ins-det], [arXiv:1701.00164v1](https://arxiv.org/abs/1701.00164)
25. M. Savić, A. Dragić, D. Maletić et al., *Astropart. Phys.* (2019). <https://doi.org/10.1016/j.astropartphys.2019.01.006>
26. M. Savić, N. Veselinović, A. Dragić et al., *ASR* **63**, 4 (2019). <https://doi.org/10.1016/j.asr.2018.09.034>. ISSN 0273-1177
27. M. Temmer, A.M. Veronig, V. Peinhardt, B. Vršnak, *ApJ* **785**, 85 (2014). <https://doi.org/10.1088/0004-637X/785/2/85>
28. J. Torsti, E. Valtonen, M. Lumme et al., *Sol. Phys.* **162**, 505–531 (1995). <https://doi.org/10.1007/BF00733438>
29. N. Veselinović, A. Dragić, M. Savić, D. Maletić, D. Joković, R. Banjanac, V. Udovičić, *NIM A* **875**, 1 (2017). <https://doi.org/10.1016/j.nima.2017.09.008>. ISSN 0168-9002
30. L.-L. Zhao, H. Zhang, *ApJ* **827**, 13 (2016). <https://doi.org/10.3847/0004-637X>

Study on 2021 November 4 Forbush Decrease with Belgrade Muon Station

N.B. Veselinović¹ , M.B. Savić¹, D.M. Maletić¹, A.L. Dragić¹,
R.M. Banjanac¹, D.R. Joković¹, D.R. Joković¹, D. Knežević¹, M.
Travar¹ and V.I. Udovičić¹

*Institute of Physics Belgrade, University of Belgrade, Pregrevica 118, 11080
Belgrade, Serbia, (E-mail: veselinovic@ipb.ac.rs)*

Received: September 30, 2023; Accepted: July 28, 2020

Abstract.

The first significant Forbush decrease of rising phase of the solar cycle 25 was recorded on November 4, 2021. The Forbush decrease was observed with numerous ground based cosmic rays stations including Belgrade cosmic rays muons' station. Series of coronal mass ejections during October 28–November 4 2021. and their interplanetary counterparts, that also led to strong G3-class geomagnetic storm, auroras and even first Ground Level Enhancement of the cycle 25., produce conditions for this Forbush decrease. We discuss here the variation of cosmic rays' flux detected with ground-based detectors with different median rigidity during this recent event. Also, we compare conditions, measured in-situ, in interplanetary space around Earth, flux of solar wind protons measured with SOHO probe, at Lagrange Point 1 and properties of detected Forbush decrease in order to assess implication for solar-terrestrial coupling processes.

Key words: Cosmic rays – Forbush decrease – Space weather – muon detector – SOHO–ICME

1. Introduction

One of the methods of researching solar-terrestrial coupling processes is observing the response of the flux of cosmic rays (CR) to various types of disturbances (or drivers) in the heliosphere. CR are charged particles, mainly protons, originating mostly from outside the Solar system. These particles are modulated in the heliosphere and geomagnetic field before they reach Earth. Modulation in the heliosphere is related to solar activity and exhibits an inverse correlation with solar magnetic activity, represented by the number of sunspots. Transient phenomena detected in CR flux due to modulation in the heliosphere is the Forbush decrease: a sudden drop in CR flux followed by a gradual return to the previous level. It occurs CR interact with irregularities in the interplanetary magnetic field (IMF), usually connected with the emission of coronal plasma known as a coronal mass ejection (CME) and its interplanetary counterpart

(ICME). These drivers, and particularly sheath compression regions in front of fast ICMEs, have higher values for different parameters of the solar wind like density, temperature, solar wind speed, and magnetic field (Yermolaev *et al.*, 2021). In recent decades, space probes have measured these parameters in-situ but also provided data for particle flux. Due to the relatively small detector size on these probes, only low-energy particles in the MeV/n range can be measured with statistical significance. The detected particles can be fast-moving particles, known as solar energetic particles (SEPs), related to violent eruptions from the Sun such as X-ray solar flares and CMEs. These particles, with enough energy, can penetrate the geomagnetic field and cause a sudden increase in measured CR flux at the surface - a ground level enhancement (GLE) that can interfere with our technology and cause damage to infrastructure. The other particles detected with probes, aside from solar wind particles and SEPs, are energetic storm particles (ESP) accelerated locally by shocks driven by fast ICMEs (Desai & Giacalone, 2016) and low-energy CR (Veselinović *et al.*, 2021). It has been shown (Koldobskiy *et al.*, 2019; Savić *et al.*, 2023; Kolarski *et al.*, 2023) that parameters measured in-situ correlate with the magnitude and time evolution of FD. The present case-study combines in-situ measurements of solar wind parameters and proton flux in near-Earth space with measurements on the ground to analyze how these parameters affect parameters of the FD detected on November 4th, 2021. The end of October and the beginning of November 2021 marked extreme activity with a strong X-class solar flare (CIT), accompanied by the first Ground Level Enhancement (GLE) event in this cycle on October 28th, measured by several ground stations (Papaioannou, A. *et al.*, 2022). Activity continued during the beginning of November. On November 2nd, 2021, an M1.7-class solar flare originated from the sunspot region labeled AR2891 and was emitted, followed by a halo Coronal Mass Ejection (CME), a coronal plasma released outward from the Sun into the interplanetary medium, thus forming an Interplanetary Coronal Mass Ejection (ICME). There were several typical CMEs during this period, as detected with SOHO/LASCO C2 and STEREO-A/SECCHI COR2 coronagraphs onboard space probes in the vicinity of Earth (Li, 2022). Most pronounced were two halo CMEs on October 28th and November 2nd, with high velocities of 1519 km/s and 1473 km/s respectively (https://cdaw.gsfc.nasa.gov/CME_list/HALO_CME/1). The second halo CME, due to its speed, caught up with previous ICMEs and produced a CME-CME interaction, creating irregularities in the heliosphere. These disturbances created additional modulation of CR, producing the first strong FD in the present solar cycle, detected by multiple ground stations around the globe (Chilingarian *et al.*, 2022).

2. Ground level cosmic ray observations

The interaction of primary cosmic rays (CR) with molecules in the Earth's atmosphere produces a cascade of secondary cosmic rays that propagate further. The properties of this cascade are correlated with the energy and species of the primary CR particle. At the bottom of the atmosphere, these secondary cosmic rays can be detected using various techniques. The most widely used detectors are part of the worldwide network of Neutron Monitors (NM) (<https://www.nmdb.eu/nest/>).

2.1. Belgrade muon detector

One of the other species of these secondary CR that can be detected and used for monitoring primary CR are muons. The Belgrade muon station is a part of the Low-Background Laboratory for Nuclear Physics at the Institute of Physics, Belgrade, Serbia. The present setup consists of two separate detector units on two different levels, One is on the shallow underground level (UL) placed under 13m of loess overburden (25 m water equivalent), which absorbs lower-energy muons. The other is placed at ground level (GLL). This arrangement allows for the monitoring of secondary CR muon flux with different energy ranges of the primary CR under the same environmental parameters. The energy range of the observed primary CR extends and complements the energy ranges detected by the NM network, but is still sensitive to CR modulation of the heliosphere (N. et al., 2017). In this work we will address only GLL measurements because UL measured no statistical significant response to November 2021. FD. In the future, new technique for improving sensitivity of the detector will be applied. Details of the experimental setup, as well as the calculated response function of the detectors, are presented in (?).

2.2. Ground level data analysis

Both NM and muon detectors measure integral flux over different energy ranges, so the median energy of the detected primary CR is used in the analysis of the measured data. Rigidity is defined as $R = Br = pq$, where B is the magnetic field, r is the gyroradius of the particle due to this field, p is the particle momentum, and q is its charge. Cut-off rigidity is the minimal rigidity that the CR must have in order to penetrate the IMF and geomagnetic field. To determine the amplitude of the FD for each station, which differs in median energy and asymptotic direction, a baseline was established using the average hourly count rate during mid-October 2021 when solar activity was low. For this study, we utilized 1-hour time series of CR flux detected at 18 NM stations and GLL data (Table 1).

Median energy for NM was found using formula given in Li et al. (2023) and median energy for GLL was found using Monte Carlo method of CR transport.

Stations	Cut-off rigidity (GV)	Median Energy (GeV)
Belgrade muon station	5.3	63
Athens NM	8.53	17.8
Guadalajara NM	6.95	15.4
Baksan NM	5.6	13.7
Jungfrauoch IGY NM	4.5	12.6
Jungfrauoch NM64	4.5	12.6
Lomnický štít NM	3.84	12
Dourbes NM	3.18	11.5
Kiel NM	2.36	11
Yakutsk NM	1.65	10.6
Kerguelen NM	1.14	10.4
Oulu NM	0.8	10.3
Apatity NM	0.65	10.3
Norilsk NM	0.63	10.3
Tixie Bay NM	0.5	10.2
Fort Smith NM	0.3	10.2
Inuvik NM	0.3	10.2
South Pole bare NM	0.1	10.1
South Pole NM	0.1	10.1

Table 1. Cut-off rigidity and median energy of primary CR for several stations

Dependence of FD amplitude on CR median energy is given by power law (Cane, 2000)

$$\frac{\Delta N}{N} = E^{-a} \quad (1)$$

Here N is CR flux, E is median energy and a is power exponent that depends on heliospheric conditions.

A scatter plot of the selected event is given (Figure 1) plotted in log-log scale and it show clear median rigidity dependence of the amplitude of FD.

Steeper spectrum during this event shows greater modulation of primary CR. If GLL data is included the power exponent is not so large so that can be interpreted as stronger modulation of the lower energy CR due to CME-CME interaction. Linear regression is performed to found power indices correspond to November 2021 event. Power index for NM only is 1.23 ± 0.22 and for NM and GLL power index is 0.62 ± 0.10 . This is, in general, in good agreement with some previous studies (Lingri et al. (2016) and references within).

2.3. Relation to in-situ measured data

In this study we used measured in-situ parameters relevant for heliospheric studies which are available at GSFC/Space Physics Data Facility, in the form

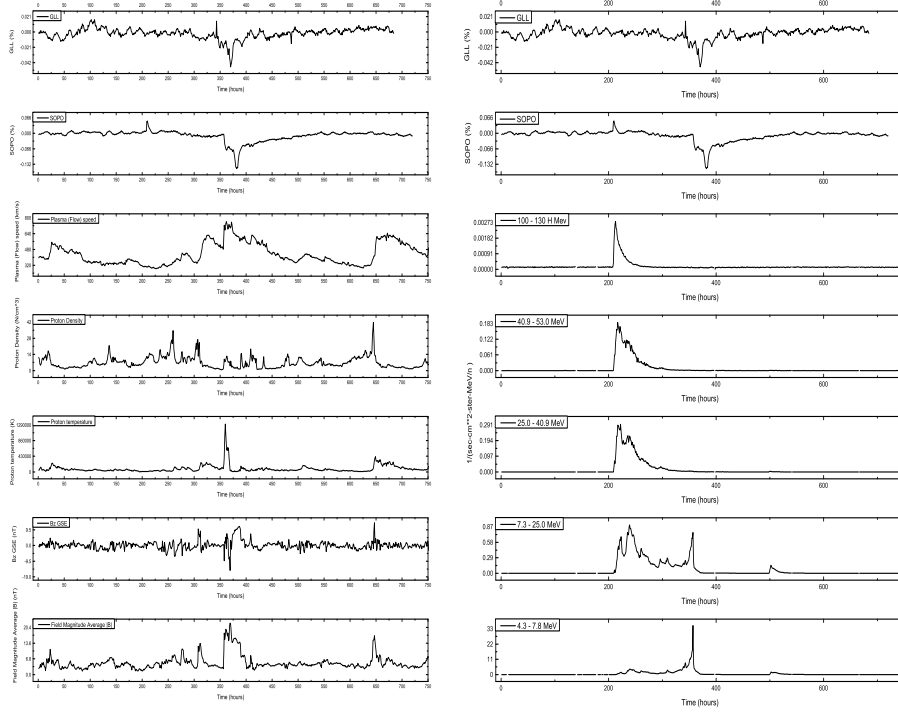


Figure 2. Left: Time series for plasma parameters (taken from OMNI database) and cosmic ray flux (measured at South Pole NM and GLL) from October 20th, 2021, until November 20th. Right: Hourly time series for different proton channels from SOHO/ERNE and SOHO/EPHIN and two CR detectors from October 20th, 2021, until November 20th, 2021.

3. Summary

In this work we studied the FD occurred in November 4th, 2021, using data from Belgrade muon station and other multiple sources. This rapid decrease was detected with CR detectors around the world and it was one of the consequences, along with the strong G3-class geomagnetic storm, auroras and GLE event, of series of overlapping CMEs. We showed that based on measured amplitude of FD of the range of ground station that higher energy CR was less affected with heliospheric disturbance. Cross correlations between time series of CR flux and IMF and solar wind characteristics during these strongly disturbed heliospheric conditions were presented. Lack of strong correlation is also apparent for higher

	SOPO		GLL	
	Pearson Corr.	p-value	Pearson Corr.	p-value
SOPO	1		0.52	$< 10^{-5}$
GLL	0.52	$< 10^{-5}$	1	
B Average	-0.55	$< 10^{-5}$	-0.48	$< 10^{-5}$
Bz	-0.4	$< 10^{-5}$	-0.15	$< 10^{-4}$
Proton temperature	-0.18	$< 10^{-5}$	-0.23	$< 10^{-5}$
Proton Density	0.23	$< 10^{-5}$	0.14	$< 10^{-4}$
Plasma (Flow) speed	-0.61	$< 10^{-5}$	-0.53	$< 10^{-5}$
7.3-25.0 MeV p	0.17	$< 10^{-5}$	-0.12	0.002
4.3-7.8 MeV p	0.01	0.67	-0.29	$< 10^{-5}$
25.0-40.9 MeV p	0.21	$< 10^{-5}$	0.02	0.5
40.9-53.0 MeV p	0.21	$< 10^{-5}$	0.03	0.45
80-100 H MeV p	0.22	$< 10^{-5}$	0.03	0.37

Table 2. Pearson correlation coefficients for the correlation between CR flux detected at Belgrade CR station (GLL), at South pole (SOPO), flux of protons of different energies from SOHO/ERNE and SOHO/EPHIN and plasma parameters (from OMNI database) for the period from October 20th until November 20th, 2021.

energy CR flux time series and time series of the heliospheric parameters and proton flux of certain energy ranges. This proves that, in order to better understand solar-terrestrial coupling processes, particularly its effect for higher energy particles requires more data from various sources and various probes and this analysis can be done in the future.

Acknowledgements. The authors acknowledge funding provided by the Institute of Physics Belgrade, through the grant by the Ministry of Education, Science and Technological Development of the Republic of Serbia. We also acknowledge use of NASA/GSFC's Space Physics Data Facility's OMNIWeb (or CDAWeb or ftp) service, and OMNI data as well as team behind SOHO, which is a project of international collaboration between ESA and NASA. We acknowledge the NMDB database, founded under the European Union's FP7 program (contract no.213007) for providing data.

References

- Cane, H. V., Coronal Mass Ejections and Forbush Decreases. 2000, *Space Science Reviews*, **93**, 55, DOI: 10.1023/A:1026532125747
- Chilingarian, A., Hovsepyan, G., Martoyan, H., et al. 2022, Forbush decrease observed by SEVAN particle detector network on November 4, 2021
- Desai, M. & Giacalone, J., Large gradual solar energetic particle events. 2016, *Living Reviews in Solar Physics*, **13**, 3, DOI: 10.1007/s41116-016-0002-5

- Kolarski, A., Veselinović, N., Srećković, V. A., et al., Impacts of Extreme Space Weather Events on September 6th, 2017 on Ionosphere and Primary Cosmic Rays. 2023, *Remote Sensing*, **15**, DOI: 10.3390/rs15051403
- Koldobskiy, S. A., Bindi, V., Corti, C., Kovaltsov, G. A., & Usoskin, I. G., Validation of the Neutron Monitor Yield Function Using Data From AMS-02 Experiment, 2011-2017. 2019, *Journal of Geophysical Research: Space Physics*, **124**, 2367, DOI: <https://doi.org/10.1029/2018JA026340>
- Kühl, P. & Heber, B., Revising More Than 20 Years of EPHIN Ion Flux Data-A New Data Product for Space Weather Applications. 2019, *Space Weather*, **17**, 84, DOI: <https://doi.org/10.1029/2018SW002114>
- Li, W.-h. et al., A study of Forbush Decreases effects with DAMPE experiment. 2023, *PoS*, **ICRC2023**, 1311, DOI: 10.22323/1.444.1311
- Lingri, D., Mavromichalaki, H., Belov, A., et al., Solar Activity Parameters and Associated Forbush Decreases During the Minimum Between Cycles 23 and 24 and the Ascending Phase of Cycle 24. 2016, *Solar Physics*, **291**, 1025, DOI: 10.1007/s11207-016-0863-8
- Papaioannou, A., Kouloumvakos, A., Mishev, A., et al., The first ground-level enhancement of solar cycle 25 on 28 October 2021. 2022, *A&A*, **660**, L5, DOI: 10.1051/0004-6361/202142855
- Savić, M., Veselinović, N., Dragić, A., et al., New insights from cross-correlation studies between solar activity indices and cosmic-ray flux during Forbush decrease events. 2023, *Advances in Space Research*, **71**, 2006, DOI: <https://doi.org/10.1016/j.asr.2022.09.057>, recent progress in the physics of the Sun and heliosphere
- Torsti, J., Mäkelä, P., Teittinen, M., & Laivola, J., SOHO/Energetic and Relativistic Nucleon and Electron Experiment Measurements of Energetic H, He, O, and Fe Fluxes during the 1997 November 6 Solar Event. 2000, *The Astrophysical Journal*, **544**, 1169, DOI: 10.1086/317219
- Veselinović, N., Dragić, A., Savić, M., et al., An underground laboratory as a facility for studies of cosmic-ray solar modulation. 2017, *Nuclear Instruments and Methods in Physics Research Section A: Accelerators, Spectrometers, Detectors and Associated Equipment*, **875**, 10, DOI: <https://doi.org/10.1016/j.nima.2017.09.008>
- Veselinović, N., Savić, M., Dragić, A., et al., Correlation analysis of solar energetic particles and secondary cosmic ray flux. 2021, *The European Physical Journal D*, **75**, 173, DOI: 10.1140/epjd/s10053-021-00172-x
- Yermolaev, Y. I., Lodkina, I. G., Dremukhina, L. A., Yermolaev, M. Y., & Khokhlachev, A. A., What Solar-Terrestrial Link Researchers Should Know about Interplanetary Drivers. 2021, *Universe*, **7**, DOI: 10.3390/universe7050138

Forbush decrease events associated with coronal mass ejections: Classification using machine learning

M.R. Savić[✉], N.B. Veselinović, A.L. Dragić, D.M. Maletić,
R.M. Banjanac, D.R. Joković, D.Knežević, M.Travar and
V.I. Udovičić

*Institute of Physics Belgrade, University of Belgrade, Pregrevica 118,
11080 Belgrade, Serbia (E-mail: msavic@ipb.ac.rs)*

Received: September 27, 2023; Accepted: October 22, 2023

Abstract. In presented work we further explore previously indicated possibility of the existence of two classes of Forbush decrease events, established by the prior analysis of the correlation between the shape of energetic proton fluence spectra and Forbush decrease properties. In an attempt to increase statistical robustness of the analysis and potentially reduce the uncertainties, we have developed an alternative classification procedure that employs machine learning and utilizes space weather parameters as input variables. Based on the overall performance, efficiency and flexibility of different machine learning methods we selected the best performing algorithm and established the optimal boundary value of Forbush decrease intensity to be used for class separation. A subset of good input variables was selected based on their predictive power.

Key words: cosmic rays – Forbush decrease – coronal mass ejection – solar energetic particles

1. Introduction

The dynamic activity of the Sun’s coronal magnetic field can give rise to complex space weather events. These events may include solar flares (SFs), coronal mass ejections (CMEs), their interplanetary counterparts known as interplanetary coronal mass ejections (ICMEs), the emission of solar energetic particles (SEPs), and similar phenomena (Kahler, 1992; Yashiro & Gopalswamy, 2008; Gopalswamy, 2022).

One such complex event can produce a number of effects in the heliosphere, one of which is the acceleration of solar wind particles. There is a distinction between particles accelerated by a SF in the lower Sun’s atmosphere and those accelerated locally by the CME shock. The later are often referred to as energetic storm particles (ESPs) (Desai & Giacalone, 2016).

Additionally, the passage of a CME can affect the primary cosmic rays (CRs) potentially resulting in a sudden drop in the observed CR flux, followed by a

recovery phase that takes place over the several following days. This effect is known as a Forbush decrease (FD) and can be observed by Earth-based CR detectors.

A previous study of the relationship between transient modulations in the fluxes of energetic protons and cosmic rays (measured near and at Earth respectively) indicated an existence of two classes of FD events (Savić et al., 2023). The main objective of this work is to expand this analysis and investigate whether a specific set of space weather (SW) parameters can be successfully used as input parameters for classification. The proposed procedure would aim to separate FD events into classes as indicated by the aforementioned analysis, while increasing the statistical significance and potentially the reliability of the analysis. Additional positive outcome of a successful classification would be the selection of a subset of SW parameters that prove to be good input variables. These variables could then be further used for the prediction of FD magnitudes utilizing some regression algorithm.

2. Motivation

As simultaneous ESP and FD events are very likely a consequence of the passage of an ICME, a relationship between them was assumed. To establish this possible connection, correlation of characteristics of proton fluence spectra and FD parameters was investigated (as described in more detail in Savić et al. (2023)).

The proton fluence spectra were calculated from in situ measurements at L1 by SOHO/ERNE instrument (Torsti et al., 1995), and fitted by a double-power law, as shown for one selected event on Figure 1.

Exponents obtained from these fits were used to parameterize the spectra shape, and some degree of correlation between these exponents and FD magnitudes was established. However, this analysis also indicated a possible existence of two classes of FD events, as illustrated in Figure 2. The plot shows the dependence of the FD magnitude corrected for the magnetospheric effect on one of the proton fluence spectra exponents. The green oval indicates a supposed class of events that exhibit a stronger correlation between these two variables, while the red oval indicates a class of events where this correlation is apparently weaker. One possible way to define the boundary between these two classes could be by introducing a cut on the intensity of the event.

Due to relatively low statistics of events where proton fluence can be reliably determined, one idea for extending this analysis is to try and utilize other space weather parameters in order to increase statistics and more strongly establish the assumed existence of two classes of FD events.

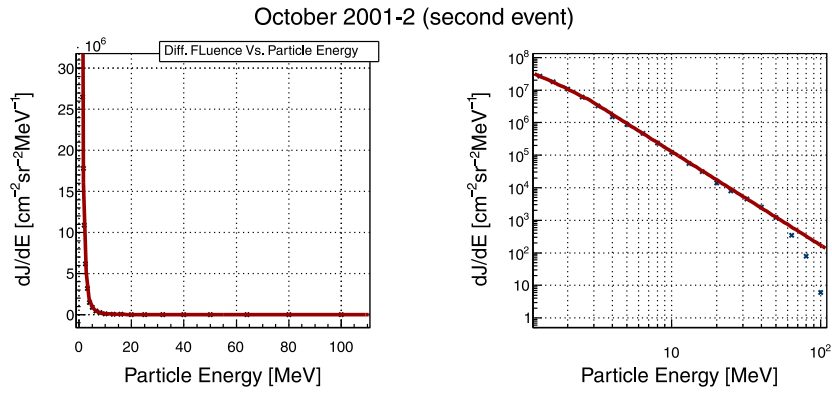


Figure 1. Proton fluence spectra at L1 for one event during October 2001, in linear (left) and logarithmic scale (right).

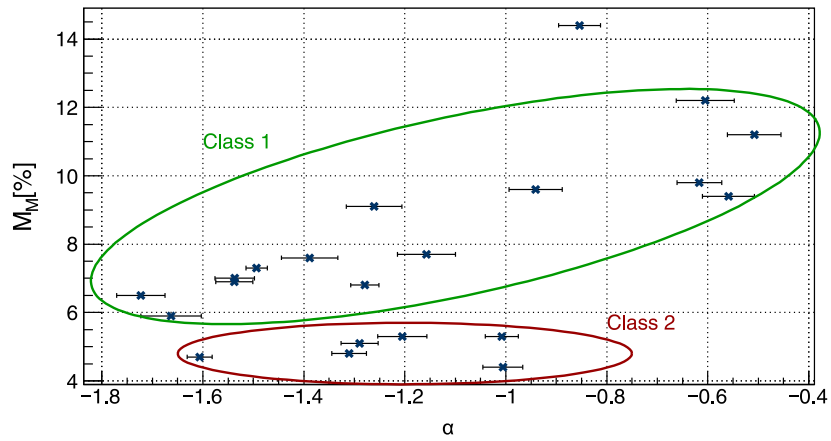


Figure 2. The dependence of the FD magnitude corrected for the magnetospheric effect (M_M) on one of the exponents used to parameterize the proton fluence spectra (α). Two assumed classes of FD events are indicated by the green and red ovals.

3. Methods and Results

IZMIRAN catalogue of Forbush effects (IZMIRAN, 2016) was used as the source of SW related data, as it contains an extensive list of FD events and associated SW parameters. The parameters selected from the IZMIRAN catalogue to be used in the analysis presented here fall into several categories: parameters describing the source (Otype, Stype) or the characteristics of the CME (Vmean, CMEwidth); solar wind parameters (Vmax, KTmax, KTmin); parameters describing interplanetary or geomagnetic field (Bzmin, Kpmax, Apmag, Dstmin); and parameters related to the associated solar flare (Xmagn, Sdur, SSN).

Several machine-learning-based classification methods implemented in the TMVA analysis network (Hoecker et al., 2007) were employed in order to establish the optimal FD magnitude for the separation of two classes (boundary criteria mentioned in Section 2), as well as to determine the optimal classification algorithm. Comparing the efficiency of various methods available in the TMVA (shown of Figure 3), it was found that the optimal separation between two classes is achieved with FD magnitude cut set to 6%, as separation efficiency seems to drop-off beyond that for most methods. Support vector machine (SVM) (Cortes & Vapnik, 1995) was identified as the overall best-performing algorithm.

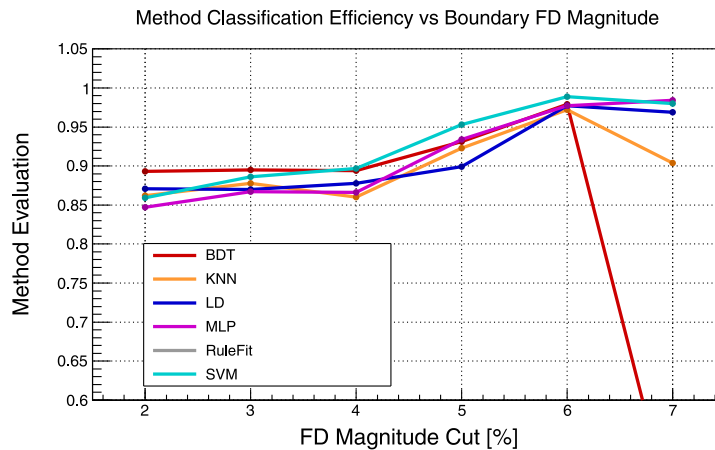


Figure 3. Comparison of the classification efficiency of various TMVA methods dependence on the FD magnitude cut used for class separation.

SVM implementation in the scikit-learn package (Pedregosa et al., 2011) was utilized to identify which of the SW parameters could reliably classify FD events. Third-degree polynomial kernel was found to have the most flexible and efficient performance.

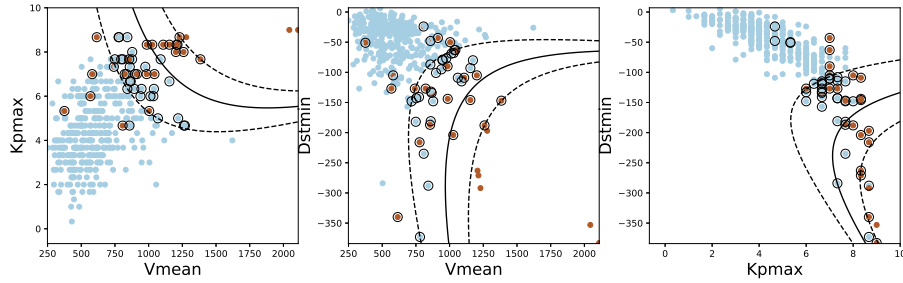


Figure 4. Example of SVM classification using some of SW parameters (mean CME velocity, maximum Kp index and minimal Dst index over the event's duration) that proved to be good input variables for FD classification.

Obtained results appear to confirm the assumption regarding the existence of two classes of FD events. Furthermore, a subset of SW parameters that provide a more reliable classification of FD events was determined. These include mean CME velocity (V_{mean}) and geomagnetic indices (K_{pmax} , A_{pmax} , D_{stmin}), with a possible inclusion of the solar wind speed (V_{max}) and minimal hourly component of the interplanetary magnetic field (B_{zmin}). Decision boundaries between some pairs of mentioned good input variables are showed on Figure 4. Other SW variables proved to be less well suited for classification (as illustrated in Figure 5, for K_{Tmin} and K_{Tmax}).

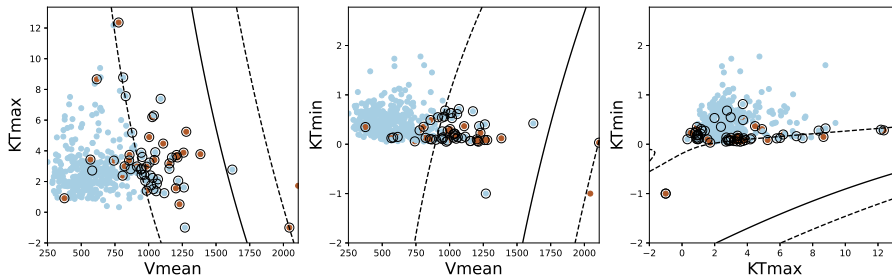


Figure 5. Example of SVM classification using some of SW parameters (K_{Tmax} , K_{Tmin}) that proved to be less well suited input variables for FD classification.

The identified good variables could prove useful in a potential future extension of the analysis. More specifically, they could serve as an input for a regression procedure that would potentially allow the prediction of FD magnitudes.

This prediction would provide either estimates of FD magnitude as measured by Earth-based detectors or, more importantly, estimates of FD magnitudes corrected for the magnetospheric effect.

4. Conclusions

The potential existence of two classes of FD events was investigated. To increase statistical robustness and reduce uncertainties, the analysis was expanded to include a wider set of various space weather parameters. Machine learning techniques were employed in an attempt to separate FD events into two assumed classes, using a number of selected SW parameters as input variables. We compared the efficiency of different machine learning algorithms, and established the optimal boundary value of FD intensity to be used for class separation. The SVM algorithm was selected for the analysis based on its overall performance, efficiency and flexibility, and used to select a subset of space weather variables to be used for reliable classification of FD events. This subset of good variables could prove useful for a future extension of the analysis, where they would provide an input for a regression procedure used to predict FD magnitudes.

Acknowledgements. This work was funded by the Institute of Physics Belgrade, University of Belgrade, through a grant by the Ministry of Science, Technological Development and Innovations of the Republic of Serbia.

We kindly acknowledge the usage of data from the SOHO experiment, as well as data from the catalogue of Forbush effects and interplanetary disturbances provided by the IZMIRAN Space Weather Prediction Center.

References

- Cortes, C. & Vapnik, V., Support Vector Networks. 1995, *Machine Learning*, **20**, 273
- Desai, M. & Giacalone, J., Large gradual solar energetic particle events. 2016, *Living Reviews in Solar Physics*, **13**, 3, DOI: 10.1007/s41116-016-0002-5
- Gopalswamy, N., The Sun and Space Weather. 2022, *Atmosphere*, **13**, DOI: 10.3390/atmos13111781
- Hoecker, A., Speckmayer, P., Stelzer, J., et al., TMVA - Toolkit for Multivariate Data Analysis. 2007, *arXiv e-prints*, physics/0703039, DOI: 10.48550/arXiv.physics/0703039
- IZMIRAN. 2016, Space weather prediction center (IZMIRAN), <http://spaceweather.izmiran.ru/eng/index.html>
- Kahler, S. W., Solar flares and coronal mass ejections. 1992, *Annual Review of Astronomy and Astrophysics*, **30**, 113, DOI: 10.1146/annurev.aa.30.090192.000553
- Pedregosa, F., Varoquaux, G., Gramfort, A., et al., Scikit-learn: Machine Learning in Python. 2011, *Journal of Machine Learning Research*, **12**, 2825

- Savić, M., Veselinović, N., Dragić, A., et al., New insights from cross-correlation studies between solar activity indices and cosmic-ray flux during Forbush decrease events. 2023, *Advances in Space Research*, **71**, 2006, DOI: 10.1016/j.asr.2022.09.057
- Torsti, J., Valtonen, E., Lumme, M., et al., Energetic Particle Experiment ERNE. 1995, *Solar Physics*, **162**, 505, DOI: 10.1007/BF00733438
- Yashiro, S. & Gopalswamy, N., Statistical relationship between solar flares and coronal mass ejections. 2008, *Proceedings of the International Astronomical Union*, **4**, DOI: 10.1017/S1743921309029342

New empirical methods for correction of meteorological effects on cosmic ray muons

M. Savić,^{a,*} A. Dragić,^a D. Maletić,^a N. Veselinović,^a D. Joković,^a R. Banjanac,^a V. Udovičić^a and D. Knežević^a

^a*Institute of Physics Belgrade,
Pregrevica 118, 11080 Belgrade, Serbia
E-mail: msavic@ipb.ac.rs*

Flux of muon component of secondary cosmic rays is affected by varying conditions in the atmosphere. Dominant effects are barometric and temperature effect, which reflect variations of atmospheric pressure and atmospheric temperature respectively. Precise modelling and correction for these meteorological effects significantly increases sensitivity of Earth-based muon detectors to variations of primary cosmic ray flux. We are presenting two recently developed empirical methods for correction of meteorological effects on cosmic ray muons. First method is based on principal component analysis, while second employs multivariate analysis using machine learning techniques. Both methods are applied for correction of barometric and temperature effects, but can easily be generalised to take more atmospheric parameters into account. We apply these corrections to muon count rates measured by Belgrade cosmic ray station and study their effect on sensitivity of detection of periodic and aperiodic flux variations of primary cosmic rays. Comparison with the most widely used method for correction of meteorological effects – integral method, as well as with neutron monitor data, demonstrates very high effectiveness of presented methods.

*37th International Cosmic Ray Conference (ICRC 2021)
July 12th – 23rd, 2021
Online – Berlin, Germany*

*Presenter

1. Introduction

Cosmic ray muons (hard component of secondary cosmic rays) are affected by variations of atmospheric parameters as they propagate toward Earth. There are a number of meteorological effects that affect cosmic ray muon flux, most prominent being the *barometric (pressure) effect* and the *temperature effect*, which depend on atmospheric pressure and atmospheric temperature respectively. Apart from fundamental, precise modelling of these effects also has practical importance, as it allows for correction that significantly increases the sensitivity of ground based muon monitors to variations of primary cosmic rays.

A number of methods for correction of barometric and temperature effect have been developed over the years. Some (i.e. method of effective level of generation [1]) are empirical in nature, while others (most notably integral method) rely on the theory of meteorological effects, developed by Dorman [2] among others. All these methods are at least in some part approximative, but for all intents and purposes we have decided to use the integral method as a reference in our analysis, as it gives the most complete treatment of the problem.

The idea behind the work presented here is to try and develop a new, easy to use empirical method, less approximative in nature, compare it to the reference integral method, and investigate whether a more precise model of meteorological effects can be constructed, and possibly some additional information extracted. In order to most completely treat the meteorological effects, both atmospheric pressure and full atmospheric temperature profile need to be taken into account. For analysis that involves that many potentially highly correlated input variables, we have decided to employ modern techniques used for decorrelation and dimensionality reduction, and introduce two new methods for modelling and correction of meteorological effects - *PCA method* based on principal component analysis (PCA), and *MVA method* based on multivariate analysis (MVA) via use of machine learning. Though these two are somewhat similar in nature, a more "hands on" approach of the PCA method can offer a somewhat different insight than the more "blackbox" machine learning approach.

2. Data

2.1 CR data

Muon count rates used in this analysis were measured in the Ground Level Laboratory (GLL) of the Low Background Laboratory for Nuclear Physics, at the Institute of Physics Belgrade [3]. More detailed description of the laboratory and current detector system can be found in some of our previous work [4]. Muon count rates can have arbitrary time resolution but five-minute and hour sums were used in the analysis. For quality and consistency of data reasons, and to remove potential biases due to annual variation, data for a period of one year (from 01.06.2010 to 31.05.2011) were selected.

2.2 Meteo data

This analysis requires information about both atmospheric pressure and vertical atmospheric temperature profile. Data about atmospheric pressure is readily available from the Republic Hydro-meteorological Servis of Serbia. As for the vertical temperature profile data, temperatures for 24

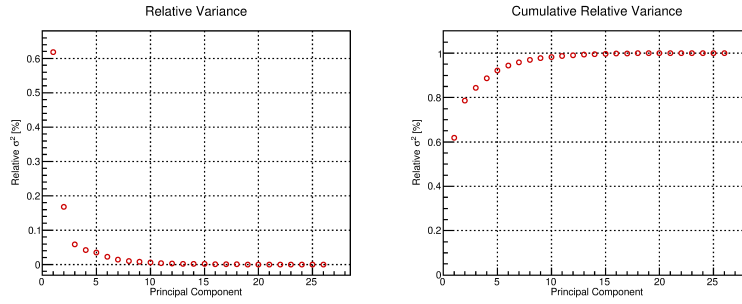


Figure 1: Relative variance (left) and cumulative relative variance (right) for all 26 principal components.

isobaric levels modelled by the Global Forecast System (GFS) [5] were used, starting from the top layer of the atmosphere (10 mb), to the level just above ground level (975 mb). For the above ground layer, locally measured temperature was used as the model was performing poorly there. More details about the preparation of meteorological data is available elsewhere [7].

3. Methodology

3.1 PCA method

Principal component analysis is a well established technique for dimensionality reduction of complex problems that involve large number of correlated variables, and as such very well suited for application to our problem. Using principal component decomposition we have transformed the initial set of correlated meteorological variables (locally measured atmospheric pressure, 24 modelled temperatures, and locally measured ground temperature) to a set of 26 uncorrelated principal components.

Using a series of tests typically used in such analysis (cumulative percentage rule, modified Kaiser's rule, mean eigenvalue rule, ...), we have determined that the first six components (responsible for close to 95% of total variance, as seen on Figure 1) are significant. Composition of the these components is shown on Figure 2, where variables on the x-axis are atmospheric pressure followed by atmospheric temperatures, starting from the top layer of the atmosphere.

Correlative analysis of muon count rate and significant principal components showed practically no correlation between measured muon count rate and the second principal component, further reducing the set of principal components to five. This is an interesting results as this component, mainly composed of lower stratosphere and upper troposphere temperatures, is responsible for close to 17% of total variation of meteorological variables.

Finally, we have determined the muon count rate corrected for meteorological effects according to formula:

$$N_{\mu}^{(corr)} = N_{\mu} - \langle N_{\mu} \rangle \sum_i k_i PC_i, \quad i = 1, 3, 4, 5, 6 \quad (1)$$

where $N_{\mu}^{(corr)}$ is corrected, N_{μ} measured and $\langle N_{\mu} \rangle$ mean muon count rate, while k_i , that correspond to principal components PC_i , are coefficients determined by linear regression, as shown on Figure 3. Full analysis and results are presented in more detail in our other work [8].

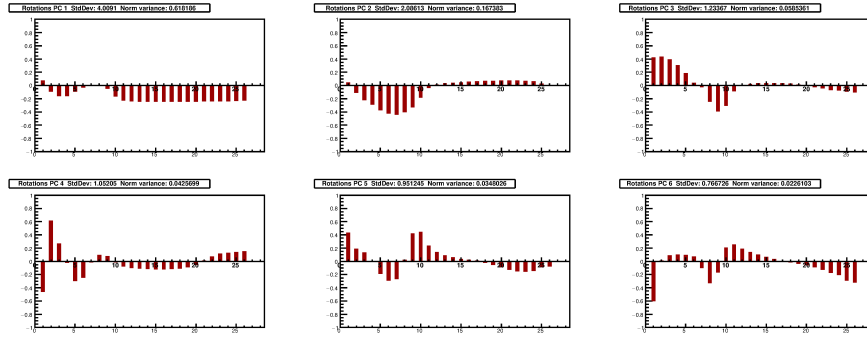


Figure 2: Composition for six most significant principal components. Meteorological variables are on the x-axis, first one being atmospheric pressure, followed by atmospheric temperatures (starting with the top layer of the atmosphere and ending with the ground level).

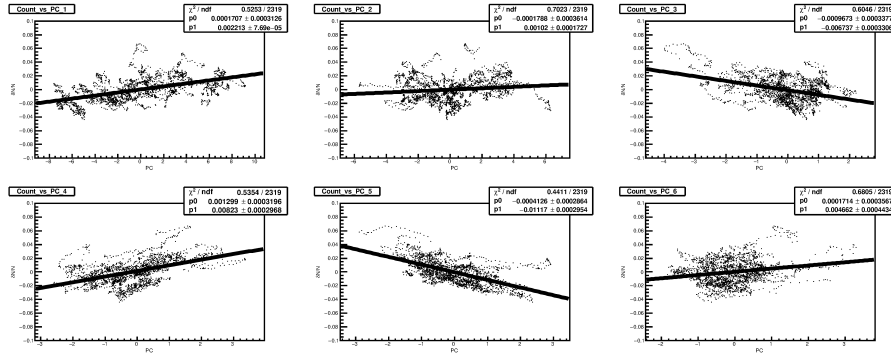


Figure 3: Muon count rate dependence on principal components for six most significant components, distributions fitted with linear function.

3.2 MVA method

Multivariate analysis utilising machine learning techniques can be a powerful tool for modelling of highly correlated systems. We have tested a number of algorithms implemented in Toolkit for Multivariate Data Analysis (TMVA), which has been successfully used for classification and regression problems in particle physics. For us, regression application is of greater interest, as the idea is to train and test multivariate algorithms on a subset of data (for geomagnetically quiet days), where most of the variation can be attributed to atmospheric effects, using meteorological variables as input and muon count rate as the target value. Trained algorithms can be then used on a full data set to predict the muon count rate (which would ideally depend only on meteorological parameters), and corrected muon count rate can be calculated using the formula:

$$N_{\mu}^{(corr)} = \Delta N_{\mu} + \langle N_{\mu} \rangle, \quad \Delta N_{\mu} = N_{\mu}^{(mod)} - N_{\mu}, \quad (2)$$

where $N_{\mu}^{(corr)}$ is corrected, N_{μ} measured, $N_{\mu}^{(mod)}$ modelled, and $\langle N_{\mu} \rangle$ is mean muon count rate.

Minimal average quadratic deviation of modelled from measured value was the only criterion used for optimisation of algorithm parameters in the training phase, so a series of tests have been

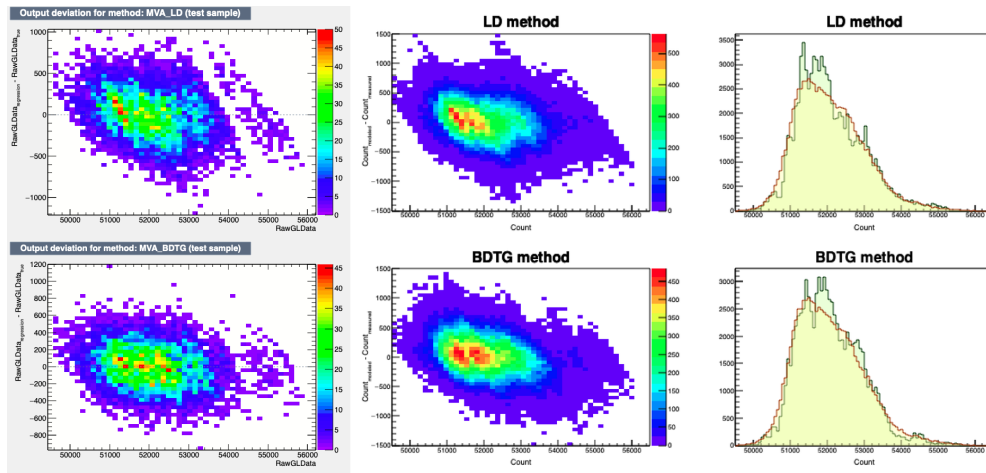


Figure 4: Modelled count rate and its deviation from measured count rate as a function of measured count rate for LD (top) and BDTG (bottom) algorithms. Deviation distributions for test data set are on left, for the full data set are in the middle, while distributions of modelled count rate (compared with the measured one) are on the right.

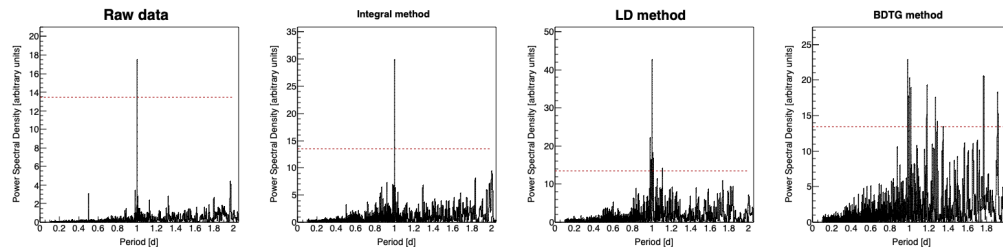


Figure 5: Power spectra for periods in the interval $[0, 2]$ days, for measured data (far left), and data corrected using integral (central left), LD (central right) and BDTG (far right) methods.

devised in order to investigate the consistency of application of trained algorithms and minimise the possibility of artificial features being introduced.

Some of the tests included comparison of distributions of residual deviation of modelled from measured data for the test and full data set, or looking for anomalous features in distributions of modelled count in comparison with measured count distribution (both types of distributions for selected algorithms shown in Figure 4).

Based on these tests, the best performing algorithm proved to be LD (Linear Discriminant method), which is closely related to PCA approach. The second best potential candidate was BDTG (Gradient Boosted Decision Tree method), but there are probably some limits to its applicability, as indicated by spectral analysis (Figure 5). From the remaining tested methods, algorithms based on probability density techniques performed more poorly, which was not that surprising as the problem analysed here involves highly linear dependencies, but poor performance of methods based on neural networks was not expected, and possibly some improvement can be made there.

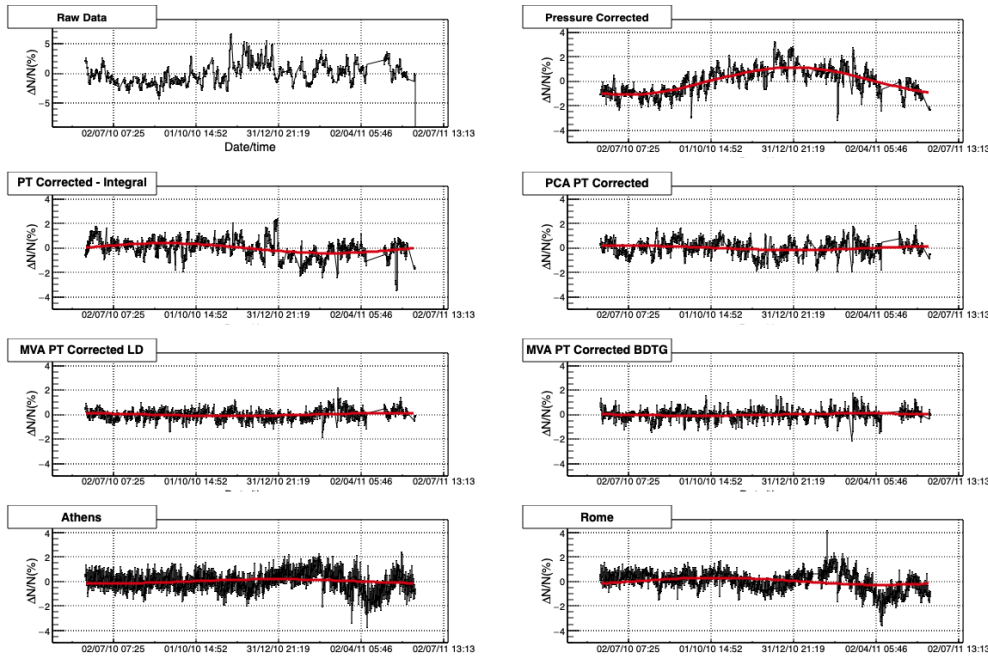


Figure 6: Muon count rate time series and reference neutron monitor data for the period of one year (01.06.2010-31.05.2011), fitted with sine function with a period of one year.

4. Results

4.1 Effect of corrections on periodic CR variations

One way to assess the performance of different methods for correction of meteorological effects could be to compare the efficiency with which they remove the annual variation due to temperature variation. In order to determine this variation, we have fitted pressure corrected data with a sine function, with a period of one year. Amplitude determined from such fit is then used as an estimate of magnitude of the annual variation. The same procedure was used to determine the residual annual variation after the correction via use of different methods (Figure 6). As neutron monitor count rates are usually considered to negligibly depend on atmospheric temperature (at least in the first approximation), we can treat their time series the same way in order to estimate the expected annual variation magnitude.

Table 1 shows amplitudes for the annual variation calculated based on plots in Figure 6, as well as reduction in annual variation relative to pressure corrected data. As can be seen, values for PCA and LD methods are closer to the estimates based on the neutron monitor data than the integral method value, while for BDTG method the value is somewhat smaller.

4.2 Effect of corrections on aperiodic CR variations

To study the effect of corrections on aperiodic variations we have selected the most intense Forbush decrease event in the one year period used for the analysis. For the event that occurred on 18.02.2011, we determined the amplitude of decrease for data corrected via different methods and reference neutron monitors, using procedure suggested by Barbashina et al. [9] (as shown on

Method/ Neutron monitor	P corr.	Integral	PCA	LD	BDTG	Athens	Rome
Annual amplitude [%]	1.11(9)	0.40(3)	0.18(5)	0.11(3)	0.086(9)	0.17(5)	0.29(1)
Relative reduction [% of P corrected]	-	64(10)	84(28)	90(30)	92(30)	-	-

Table 1: Amplitude and reduction of the amplitude of annual variation relative to pressure corrected data (P corr.) for pressure and temperature corrected data (using integral and selected multivariate methods). Athens and Rome neutron monitor data also included for reference

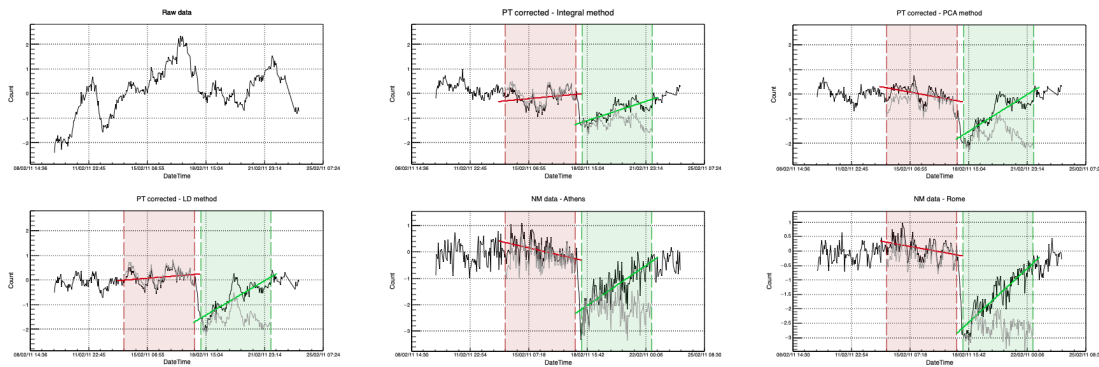


Figure 7: Muon count rate time series and reference neutron monitor data for the period around the Forbush decrease event of 18.02.2011. Highlighted intervals are used for detrending and calculation of decrease amplitude.

Method/ Neutron monitor	Integral	PCA	LD	BDTG	Athens	Rome
FD amplitude [%]	1.38(14)	1.52(21)	1.96(18)	1.10(13)	1.97(15)	2.68(15)
Relative FD amplitude	4.31(44)	4.90(66)	7.09(65)	4.78(56)	5.30(40)	8.65(48)

Table 2: Amplitudes and relative amplitudes for the Forbush decrease event of 18.02.2011 for pressure and temperature corrected muon data and reference neutron monitors

Figure 7). Additionally, as a measure of sensitivity to such events, we have introduced amplitude calculated relative to standard deviation of count rates leading up to the event.

Values for thusly calculated amplitudes and relative amplitudes are shown in Table 2. LD algorithm has values comparable to neutron monitor values, but that is at least in part due to somewhat larger calculated amplitude. This is most likely a feature pertaining to the specific event, as preliminary results for other events outside the interval used in this work show values closer to expected.

5. Conclusions

Two new methods for correction of meteorological effects on cosmic ray muons are introduced. Both are fully empirical, require knowledge about the atmospheric pressure and atmospheric temperature profile and can be applied to any muon monitor. The effect on reduction of the annual variation of CR data, as well as the effect on sensitivity of FD event detection was compared to the integral method and reference neutron monitor data. Their effectiveness was comparable or possibly better than for the integral method, allowing for the possibility that a part of meteorological effects is not taken into account by theory.

References

- [1] A Duperier, "The Meson Intensity at the Surface of the Earth and the Temperature at the Production Level", in Proceedings of the Physical Society. Section A, volume 62, number 11, pages 684, year 1949, doi: 10.1088/0370-1298/62/11/302
- [2] Dorman, L. I., "On the temperature effect of the hard component of cosmic rays", in Reports of Academy of Sciences of USSR (DAN SSSR), volume 95, issue 1, pages 49 - 52, year 1954b
- [3] Low Background Laboratory for Nuclear Physics, url: <http://www.cosmic.ipb.ac.rs/>
- [4] Dragic Aleksandar, Udovicic Vladimir, Banjanac Radomir, Jokovic Dejan, Maletic Dimitrije, Veselinovic Nikola, Savic Mihailo, Puzovic Jovan, Anicin Ivan, "The New Set-Up in the Belgrade Low-Level and Cosmic-Ray Laboratory", in NUCLEAR TECHNOLOGY AND RADIATION PROTECTION, volume 26, number 3, pages 181-192, year 2011, doi: 10.2298/NTRP1103181D
- [5] GFS, url: <https://www.ncdc.noaa.gov/data-access/model-data/model-datasets/global-forecast-system-gfs>
- [6] Berkova M., Belov A., Eroshenko E., Yanke Victor, "Temperature effect of muon component and practical questions of how to take into account in real time", in Astrophysics and Space Sciences Transactions, year 2012, pages 41-44, volume 8, doi: 10.5194/astra-8-41-2012
- [7] Savic Mihailo, Dragic Aleksandar, Veselinovic Nikola, Udovicic Vladimir, Banjanac Radomir, Jokovic Dejan, Maletic Dimitrije, "Effect of pressure and temperature corrections on muon flux variability at ground level and underground", in "25th European Cosmic Ray Symposium", Torino, Italy, eprint: 1701.00164, year 2016
- [8] Savic Mihailo, Dragic Aleksandar, Maletic Dimitrije, Veselinovic Nikola, Banjanac Radomir, Jokovic Dejan, Udovicic Vladimir, "A novel method for atmospheric correction of cosmic-ray data based on principal component analysis", in ASTROPARTICLE PHYSICS, volume 109, pages 1-11, year 2019, doi: 10.1016/j.astropartphys.2019.01.006
- [9] Barbashina N., Dmitrieva Anna, Kompaniets K., Petrukhin A., Timashkov D., Shutenko V., Yakovleva Elena, Yashin, Igor, "Specific features of studying Forbush decreases in the muon flux", in Bulletin of The Russian Academy of Sciences: Physics, year 2009, pages 343-346, volume 73, doi: 10.3103/S1062873809030198

CORRELATION ANALYSIS OF SOLAR WIND PARAMETERS AND SECONDARY COSMIC RAYS FLUX

NIKOLA VESELINović, MIHAILO SAVIĆ, ALEKSANDAR DRAGIĆ,
DIMITRIJE MALETIĆ, DEJAN JOKOVIĆ, RADOMIR BANJANAC,
VLADIMIR UDOVIČIĆ and DAVID KNEŽEVIĆ

*Institute of Physics Belgrade
Pregrevica 118, Belgrade, Serbia
E-mail veselinovic@ipb.ac.rs*

Abstract. Galactic cosmic rays (GCRs) entering the heliosphere are disturbed by solar wind and Sun's magnetic field, see Potgieter 2013 Coronal mass ejections (CMEs) structure and shockwave can additionally modulate GCRs, which could result in a transient decrease followed by a gradual recovery in the observed galactic cosmic ray intensity, known as Forbush decrease (FD) see Maričić et al.2014. CMEs are regularly observed via in-situ measurements of plasma and magnetic field in near-Earth space so it is important to understand the relationship between the FDs and near-Earth particles flux associated with these CMEs.

During last 24th Solar cycle, unprecedented extent of heliospheric observations has been achieved thanks to the several new satellites in orbit and CMEs can be observed throughout the heliosphere from the Sun to the Earth, allowing us to relate ground observations to remote sensing data, for Mars see Freiherr von Forstner et al. 2019. We analyzed the dynamics of the variation of galactic cosmic rays (GCR) combining in situ measurement of the particles species present in solar wind with ground observations (worldwide neutron monitor (NM) network and Belgrade's muon detector). This dynamics compared for several CMEs induced FD events. Variations in interplanetary plasma and field parameters during, before, and after the Forbush decreases were examined. Correlation between the 1-hour variations of GCR and several different one-hour averaged particle fluxes was found during FDs and it depends on energy of the particles of the solar wind as well as cut-off rigidities of secondary cosmic rays detectors on ground. These correlations were compared with correlation between same parameters during quiet period of the solar activity. This cross-correlation analysis can help in better understanding of Earth-affecting CMEs and space weather but also to predict GCR flux during extreme solar events.

References

- Freiherr von Forstner, J. L. et al. : 2019, *Space Weather*, **17**, 586– 598.
Maričić, D., Vršnak, B., Dumbović, M. et al. : 2014, *Sol Phys* **289**, 351–368.
Potgieter, M. S.: 2013, *Living Rev. Sol. Phys.* **10**, 3 (2013).

Invited lecture

COSMIC RAY FLUX MEASUREMENTS AT BELGRADE COSMIC RAYS STATION DURING SOLAR CYCLE 24

**N. Veselinović, M. Savić, A. Dragić, D. Maletić, D. Joković, V. Udovičić,
R. Banjanac and D. Knežević**

Institute of Physics, University of Belgrade, Pregrevica 118, Belgrade, Serbia
E-mail: veselinovic@ipb.ac.rs

It has been well known for more than half a century that solar activity is responsible for modulation of galactic cosmic ray reaching Earth (Potgieter 2013). Low-background Laboratory for Nuclear Physics at the Institute of Physics, Belgrade is dedicated to low-background spectroscopy and cosmic rays measurement. Measurements are performed at interconnected spaces: at the surface level (78m a.s.l.) and in the underground laboratory at the depth of 25 m.w.e. with identical sets of detectors and analyzing electronics thus creating opportunity to monitor simultaneously muon flux at different energies. The cosmic-ray muon count rate and energy loss spectra in plastic scintillator detectors are recorded and from experimental data and with the use of GEANT4 computer simulation the flux and vertical intensities have been determined (Veselinović *et al.* 2017). The aim of the present work is to present study of energy dependent solar modulation process during Solar cycle 24 utilizing a shallow underground laboratory with detector configuration sensitive to primaries in the energy region exceeding sensitivity of neutron monitors (Savić *et al.* 2019).

References

- Potgieter, M.S.:2013, *Living Rev. Sol. Phys.* **10**, 3.
Savić, M. et al.: 2019, *Advances in Space Research*, **63**, 4.
Veselinović, N. et al. :2017, *Nuclear Instruments and Methods in Phy. Res. A*,
875.

RADON VARIABILITY DUE TO FLOOR LEVEL IN THE TWO TYPICAL RESIDENTIAL BUILDINGS IN SERBIA

Vladimir Udovičić¹, Nikola Veselinović¹, Dimitrije Maletić¹, Radomir Banjanac¹, Aleksandar Dragić¹, Dejan Joković¹, Mihailo Savić¹, David Knezević¹, Maja Eremić Savković²

¹Institute of Physics Belgrade, University of Belgrade, Belgrade, Serbia

²Serbian Radiation and Nuclear Safety and Security Directorate, Belgrade, Serbia

E-mail: udovicic@ipb.ac.rs

It is well known that one of the factors that influences the indoor radon variability is the floor level of the buildings. Considering the fact that the main source of indoor radon is radon in soil gas, it is expected that the radon concentration decreases at higher floors. Thus, at higher floors the dominant source of radon is originating from building materials and in some cases there may be deviations from the generally established regularity. On the other hand, the radon variability due to floor level, especially in big cities with a much higher number of high-rise buildings and population density compared with rural environments, may have an impact on the assessments of collective dose from radon.

According to the national typology [1], there are six types of residential buildings in Serbia; two for family housing: Freestanding single-family house and single-family house in a row, and four for multi-family housing: Freestanding residential building, residential building - lamela (apartment block with repeated multiple – lamellar – cores and separate entrances), residential building in a row and high-rise residential building. Distribution of buildings by type at national level shows that 97.23% of all residential buildings are family housing. Also, for all defined types of buildings number of floors ranges from one to eight above the ground level. Freestanding family houses are mostly ground floor (37%) or ground floor with loft in use (26%), while there is a very low representation of houses that have more than two floors (5%), with average height of family buildings of 1.4. In that sense, we chose one freestanding single-family house with loft with well-known radon characteristics [2] and one sixteenth floor high-rise residential building for this study.

The indoor radon measurements are performed with two active devices. One was fixed in the living room at the ground level and the second one was moved through the floors of the residential building. Every measuring cycle at the specified floor lasted seven days with the sampling time of the two hours. In this work, the analysis of the obtained results is shown in details.

Ref.

- [1] Jovanović Popović M., Ignjatović D., Radivojević A., Rajčić A., Čuković Ignjatović N., Đukanović Lj. & Nedić M. (2013), National Typology of Residential Buildings in Serbia, Faculty of Architecture University of Belgrade, Belgrade (2013), ISBN 978-86-7924-102-3.
- [2] Udovičić V., Maletić D., Banjanac R., Joković D., Dragić A., Veselinović N., Živanović J., Savić M., Forkapić S. Multiyear Indoor Radon Variability in a Family House – a Case Study in Serbia, Nuclear Technology and Radiation Protection Vol. XXXIII, No. 2 (2018), pp. 174-179.

New insights from cross-correlation studies between solar activity indices and cosmic-ray fluxes during Forbush decreases

Nikola Veselinović, Mihailo Savić, Aleksandar Dragić, Dimitrije Maletić, Radomir Banjanac, Dejan Joković, David Knežević and Vladimir Udovičić

*Institute of Physics Belgrade, University of Belgrade, Pregrevica 118,
11080 Belgrade, Serbia*

Observed galactic cosmic rays intensity can be subjected to transient decrease, called Forbush decreases, which can be driven by solar activity and shockwaves in Heliosphere with solar origin, in terms of flares and coronal mass ejections (Miteva et al., 2018 [1]). By combining in-situ measurements, using space borne instruments, of solar energetic particles with ground-based observations we investigate the relationship between solar activity indices, as well as event-integrated spectra of solar energetic particles (Belov et al, 2021 [2]) with intensity measurements of cosmic rays during these strong transient decreases. We present cross-correlation studies (Veselinović et al, 2021 [3]) using data from the SOHO/ERNE measurements at 19 energy thresholds between 1.6 and 90 MeV/n, neutron monitors and solar observatories collected during strongest Forbush decreases over last two solar cycles.

References

- [1] Miteva, R., Samwel, S.W. & Costa-Duarte, M.V. The *Wind*/EPACT Proton Event Catalog (1996 – 2016). *Sol Phys* **293**, 27 (2018).
<https://doi.org/10.1007/s11207-018-1241-5>
- [2] Belov A. *et al* 2021 *ApJ* **908** 5. <https://doi.org/10.3847/1538-4357/abd724>
- [3] Veselinović, N., Savić, M., Dragić, A. *et al*. Correlation analysis of solar energetic particles and secondary cosmic ray flux. *Eur. Phys. J. D* **75**, 173 (2021). <https://doi.org/10.1140/epjd/s10053-021-00172-x>

Nucleosynthesis

80

The radiogenic heating of planets and the 40K question**Author:** Georgios Perdikakis¹¹ *Central Michigan University***Corresponding Author:** perdi1g@cmich.edu

The quantity of radioactive isotopes in a planet's mantle and the evolution of its heating due to the isotopes' radioactive decay determines the capability of that planet to develop geological features associated with a habitable environment, such as surface crust and plate tectonics. When our solar system was formed, large quantities of Potassium (K), a major element available in the interstellar medium at the time, got subsequently deposited inside our planet's mantle and crust. Potassium's long-lived radioactive isotope ⁴⁰K is still present in large quantities inside the planet. The beta particles that it emits heat up earth's mantle for the last several billions of years and largely contribute to the habitable nature of Earth. Predicting the amount of ⁴⁰K enrichment in the solar system of a given exoplanet would be fundamental for a reliable calculation of the planet's heating evolution and would allow us to make estimates on the likely existence of a habitable environment. Potassium, however, has a complex production and (destruction) mechanism in the cosmos. From a nucleosynthesis point of view, the uncertainty in the abundance of ⁴⁰K is associated with the reactions that create and destroy 40K in stellar nucleosynthesis processes and the corresponding reaction rates. In my talk, I will discuss the importance of potassium in the context of exoplanet-related research, the origin of potassium in stars, the nuclear physics aspects that affect the existence of ⁴⁰K, and current experimental efforts to constrain the relevant reaction rates.

Length of presentation requested:

Oral presentation: 25 min + 5 min questions (Review-type talk)

Please select between one and three keywords related to your abstract:

Nuclear physics - experimental

2nd keyword (optional):

Nucleosynthesis

3rd keyword (optional):

Habitability, Exoplanets

81

Simulation of production of the cosmogenic radionuclides in loess

Authors: Nikola Veselinovic^{None}; Dimitrije Maletic^{None}; Mihailo Savic¹; Aleksandar Dragić¹; Dejan Jokovic²; Radomir Banjanac³; David Knežević⁴; Vladimir Udovičić⁵

¹ *Institute of Physics Belgrade*² *Institute of Physics, University of Belgrade*³ *Institute of physics Belgrade*⁴ *Institute of physics Belgrade*

⁵ *Institute of Physics Belgrade*

Corresponding Authors: veselinovic@ipb.ac.rs, maletic@ipb.ac.rs, yokovic@ipb.ac.rs, banjanac@ipb.ac.rs, davidk@ipb.ac.rs, udovicic@ipb.ac.rs, dragic@ipb.ac.rs, msavic@ipb.ac.rs

Development of a Geant4 application which models propagation and interaction of cosmic rays with the soil - loess, including the simulation of creation of cosmogenic radionuclides in soil is reported. CORSIKA is used to simulate the propagation of cosmic rays through atmosphere to the ground. The distribution of concentration of produced radionuclides by depth from simulation is presented thus allowing alternative method of study loess geomorfology but also to study cosmic ray flux modulated by the sun activity on long-term scale. The possibility of detection using laboratory equipment of these cosmogenic radionuclides created in soil is discussed.

Length of presentation requested:

Oral presentation: 8 min + 2 min questions (Poster-type talk)

Please select between one and three keywords related to your abstract:

Cosmic Rays

2nd keyword (optional):

Nuclear physics - experimental

3rd keyword (optional):

82

Spectroscopy of ^{48}Cr by the $^{50}\text{Cr}(p, t)^{48}\text{Cr}$ reaction

Authors: Philip Adsley¹; Sifundo Binda²

¹ *Texas A&M University*

² *WITS/iTL*

Corresponding Authors: padsley@tamu.edu, 1395463@students.wits.ac.za

The radioactive nucleus ^{44}Ti is thought to be produced in Core-Collapse Supernovae (CCSNe) with the amount produced being sensitive to internal dynamics of the explosion. As such, ^{44}Ti is a potential diagnostic tool for understanding the behaviour of these stellar explosions.

The amount of ^{44}Ti produced depends not only on the production reactions but also on the destruction reactions, most notably the $^{44}\text{Ti}(\alpha, p)^{47}\text{V}$ reaction which proceeds through states in the compound nucleus ^{48}Cr . This reaction is usually treated through statistical models (see, for example, the recent study by Chipps and collaborators Phys. Rev. C 102, 035806) but it is not clear that this is valid given the limitations of the levels which can be populated in $^{44}\text{Ti}+\alpha$ fusion (natural parity, isoscalar) and the influence of α -particle clustering behaviour on other α -particle induced reactions.

Spectroscopy in the Gamow Window of the $^{44}\text{Ti}(\alpha, p)^{47}\text{V}$ reaction has been performed using the $^{50}\text{Cr}(p, t)^{48}\text{Cr}$ reaction with the K600 magnetic spectrometer at iThemba LABS in South Africa. A number of excited states have been observed, many for the first time, giving insights into the validity of statistical models for the $^{44}\text{Ti}(\alpha, p)^{47}\text{V}$ reaction.

Length of presentation requested:

Oral presentation: 8 min + 2 min questions (Poster-type talk)

Please select between one and three keywords related to your abstract:

Nuclear physics - experimental

The study of atmospheric effects on cosmic ray muons in the Low Background Laboratory for Nuclear Physics at the Institute of Physics Belgrade

**Mihailo Savić, Nikola Veselinović, Aleksandar Dragić, Dimitrije Maletić,
Dejan Joković, Vladimir Udovičić, Radomir Banjanac and David Knežević**

*Institute of Physics Belgrade, University of Belgrade, Pregrevica 118, 11080
Belgrade, Serbia*

Email: msavic@ipb.ac.rs

Galactic cosmic rays are being modulated in the heliosphere by different processes on the Sun. Upon arriving at Earth, they interact with nuclei in the atmosphere and produce secondary cosmic rays. Changing conditions in the atmosphere affect the propagation of secondary cosmic rays, especially the muon component. To increase the effectiveness of ground-based muon detectors these atmospheric effects need to be decoupled from non-atmospheric ones, and corrected for. To this end, in the Low Background Laboratory for Nuclear Physics at the Institute of Physics Belgrade, we are using several existing techniques but have also developed two new empirical methods for modeling and correction of barometric and temperature effects on cosmic ray muons. Newly developed methods proved to be equally or more effective than the most widely used ones. Such results allow for more precise study of solar modulation and more reliable long term monitoring of galactic cosmic ray flux, and could provide further insight into the relationship between atmospheric parameters and propagation of secondary cosmic rays in the atmosphere.

CORRELATION OF SOLAR WIND PARAMETERS WITH COSMIC RAYS OBSERVED WITH GROUND STATION

Nikola Veselinović¹, Mihailo Savić¹, Aleksandar Dragić¹, Dimitrije Maletić¹, Dejan Joković¹, Radomir Banjanac¹, Vladimir Udovičić¹, David Knežević¹

¹Institute of Physics, University of Belgrade, Pregrevica 118, 11080 Belgrade, Serbia;
e-mail: nikola.veselinovic@ipb.ac.rs, mihailo.savic@ipb.ac.rs, aleksandar.dragic@ipb.ac.rs,
dimitrije.maletic@ipb.ac.rs, dejan.jokovic@ipb.ac.rs, radomir.banjanac@ipb.ac.rs, vladimir.udovicic@ipb.ac.rs,
david.knezevic@ipb.ac.rs

Solar activity and conditions in heliosphere can be a critical driver of human impact space weather as they can damage electronics and threaten the lives of astronauts as well as increase radiation hazards to high-altitude, high-latitude aviation. It has been well known for more than half a century that solar activity has a strong influence of cosmic ray flux reaching to the Earth (anti-correlation). Solar wind, by both particle drift patterns and structures is responsible for galactic cosmic ray flux modulation, hence the flux of observed galactic cosmic rays varies (GCR) with the solar wind reflecting the solar activity so one could use cosmic ray flux measured at the surface of the earth and in space to monitor the space weather and solar activity. Drops of a few percent in near-Earth GCR flux (Forbush decreases) are well known to be associated with the near-Earth passage of solar wind structures resulting from corotating interaction regions (CIRs) and transient coronal mass ejections (CMEs). We investigated how FDs vary with the properties of the driving solar wind structure. In this context, we study correlations between galactic cosmic rays (GCR) and particles of different species and energies of the solar wind based on the analyses of observational data from our muon detector, worldwide network of neutron detectors and satellites. We perform comparative analysis of Forbush events during Solar cycle 24, which happens during *STEREO* era, enabling in situ and remote observations of solar wind particles' flux from three well-separated heliospheric locations.

Heliospheric and atmospheric parameters affecting cosmic rays flux measured at Belgrade muon station

Nikola VESELINOVIĆ, Mihailo Savić, Aleksandar Dragić, Dimitrije Maletić, Dejan Joković, Radomir Banjanac, David Knežević, Vladimir Udovičić
The Low-background Laboratory for Nuclear Physics, Institute of Physics, University of Belgrade
veselinovic@ipb.ac.rs

Belgrade Muon station monitor secondary cosmic ray flux for two decades. It is a part of The Low-background Laboratory for Nuclear Physics (LBLNP) at the Institute of Physics, Belgrade, Serbia. Measurements are done simultaneously at ground level and at shallow-underground level which is suitable for studies of energy dependence of cosmic-ray variations. Overview of laboratory's activity and research is given. Progress in several different research topics studied, ranging from correction of secondary cosmic rays flux on atmospheric parameters using multivariate analysis, upgrade of instrumental setup and determining concentration of in situ cosmogenic radionuclides based on simulation, to studying correlation between solar wind parameters and measured muon flux during transient or quasi-periodic cosmic-ray variations like Forbush decreases. Also a planned future collaboration is discussed with goal of developing and using worldwide network of novel, low-cost and portable detectors for cosmic ray muon and neutron flux measurements and its application in studying heliospheric and environmental parameters.

KEYWORDS: cosmic rays, measured flux, ground and underground station

MULTI-INSTRUMENTAL INVESTIGATION OF THE POWERFUL SOLAR FLARES IMPACT ON THE IONOSPHERE: CASE STUDY

A. Kolarski¹, N. Veselinović¹, V. A. Srećković¹, Z. Mijić¹,
M. Savić¹ and A. Dragić¹

¹*Institute of Physics Belgrade, UB, Pregrevica 118, 11080 Belgrade, Serbia*

*E-mail: aleksandra.kolarski@ipb.ac.rs, nikola.veselinovic@ipb.ac.rs,
vlada@ipb.ac.rs, zoran.mijic@ipb.ac.rs, mihailo.savic@ipb.ac.rs,
aleksandar.dragic@ipb.ac.rs*

Case study of energetic solar events which included strongest solar flare of the previous solar cycle, X9.3 from 6 September 2017 and accompanying Coronal Mass Ejections (CMEs) directed towards Earth is presented through ionospheric and primary cosmic rays implications. Conducted analysis and numerical simulations were done both on data from ground-based Belgrade Very Low Frequency (VLF) and Cosmic Ray (CR) stations and space-borne satellite platforms of GOES and SOHO missions. Some of the main findings regarding related disturbances of ionospheric parameters and on primary cosmic rays are presented in this work.

Study on 2021 November 4 Forbush decrease with Belgrade muon station

**Dimitrije M. Maletić, Nikola B. Veselinović, Mihailo R. Savić,
Aleksandar L. Dragić, Radomir M. Banjanac, Dejan R. Joković,
David Knezević, Miloš Travar and Vladimir I. Udovičić**

*Institute of Physics Belgrade, Pregrevica 118, 11080 Belgrade, Serbia
E-mail: maletic@ipb.ac.rs*

The first significant Forbush decrease of rising phase of the solar cycle 25 was recorded on November 4, 2021. It was detected with numerous ground based cosmic rays stations around the world (Chilingarian et al. 2022). including Belgrade cosmic rays muons' station. Belgrade cosmic rays' muon station is located at the Institute of Physics Belgrade and it constantly measures muon flux during cycle 24 (and 25) originated from primary cosmic rays with higher median energy than neutron monitors (Veselinović et al. 2017). This rapid decrease in the observed galactic cosmic ray intensity was the result of a series of coronal mass ejections during October 28–November 2. (Li et al. 2022), and their interplanetary counterparts (ICME) that led to strong G3-class geomagnetic storm, auroras and even first Ground Level Enhancement of the cycle 25 (Papaioannou et al. 2022). We discuss here the variation of cosmic rays' flux detected with ground-based detectors with different median rigidity during this recent event. Also, we compare conditions, measured in-situ, in interplanetary space around Earth, flux of solar wind protons measured with SOHO/ERNE probe, at Lagrange Point 1 and properties of detected Forbush decrease in order to asses implication for solar-terrestrial coupling processes.

References

- Chilingarian, A., Hovsepyan, G., Martoyan, H., Karapetyan, T., et al., 2022
<https://arxiv.org/abs/2212.13514>
Li, X., Wang, Y., Guo, J., Lyu, S., 2022 *ApJL* 928 L6
Papaioannou, A., Kouloumvakos, A., Mishev, A., Vainio R., et al., 2022, *A&A*, 660 L5
Veselinović, N., Dragić, A., Savić, M., Maletić, D., et al. 2017, *NiM A*, 875

Multi-instrumental investigation of extreme space weather events in September 2017: Data and modeling

**Nikola B. Veselinović, Aleksandra Kolarski, Vladimir A. Srećković,
Zoran R. Mijić, Mihailo R. Savić and Aleksandar L. Dragić**

*Institute of Physics Belgrade, Pregrevica 118, 11080 Belgrade, Serbia
E-mail: veselinovic@ipb.ac.rs*

Strong Solar activity during September 2017, despite being in the declining phase of cycle 24, produced several solar flares, accompanied by a series of coronal mass ejections that led to complex and geoeffective plasma structures in the heliosphere (Luhmann et al., 2020). These events, involving interactions between plasma structures (Albert et al., 2020), as well as their influence on Earth's environment are very difficult to forecast.

A number of studies used different approaches to analyze influence of Solar activity on particular phenomena either in heliosphere (Kozev et al., 2022, Savić et al., 2023) or ionosphere responses (Kolarski et al., 2022, Srećković et al., 2021). Recently, several investigations based on multi-instrumental measurements and numerical simulations show more comprehensive insight into the ionospheric responses and change of primary cosmic rays' flux due to the extreme Solar activity (Kolarski et al., 2023, Barta et al., 2022).

The focus of this research is to investigate the phenomena induced by the extreme event in near-Earth space and Earth's atmosphere during September 2017, with an emphasis on studying and modeling the variations in cosmic ray flux and disturbances in the lower ionosphere in correlation with Solar activity. The investigation is based on ground-based measurements such as from neutron monitors, very low-frequency (VLF) radio wave stations, and cosmic ray detectors, as well as in situ measurements from different space probes.

The results of this study show that the ionospheric atomic and molecular data like sharpness and effective reflection height and electron density obtained from Belgrade VLF data measurements, are in correlation with incident X-ray flux while time series of cosmic rays' flux measured at Belgrade muon station correspond to disturbance of near-Earth heliospheric conditions.

The multi-instrumental approach accompanied with numerical modeling of specific space weather events additionally contribute to better understanding of solar-terrestrial coupling processes.

References

- Albert, D., Antony, B., Ba, Y. A., Babikov, Y. L., et al., 2020, *Atoms*, 8, 76
- Barta, V., Natras, R., Srećković, V., Koronczay, D., et al., 2022, *Front. Environ. Sci.* 10:904335.
- Kolarski, A., Veselinović, N., Srećković, V. A., Mijić, Z., et al., 2023, *Remote Sens.* 15, 1403
- Kolarski, A., Srećković, V. A., Mijić, Z. R., 2022, *Appl. Sci.* 12, 582
- Kozarev, K., Nedal, M., Miteva, R., Dechev, M. and Zucca, P., 2022, *Front. Astron. Space Sci.* 9:801429.
- Luhmann, J. G., Gopalswamy, N., Jian, L. K. et al., 2022, *Sol Phys* 295, 61
- Savić, M., Veselinović, N., Dragić, A., et al., 2023, *Adv. Sp. Research*, 71,4
- Srećković, V. A., Šulić, D. M., Vujčić, V., Mijić, Z. R., et al., *Appl. Sci.* 2021, 11, 11574

Classification of Forbush decrease events utilizing machine learning

**Mihailo R. Savić, Nikola B. Veselinović, Aleksandar L. Dragić,
Dimitrije M. Maletić, Radomir M. Banjanac, Dejan R. Joković,
David Knežević, Miloš Travar and Vladimir I. Udovičić**

*Institute of Physics Belgrade, Pregrevica 118, 11080 Belgrade, Serbia
E-mail: msavic@ipb.ac.rs*

The potential existence of two classes of Forbush Decrease (FD) events has already been suggested by the analysis of energetic proton fluence spectra measured at L1 (Savić et al. 2023). We further explore this assumption in the work presented herein.

The most powerful coronal mass ejections, which can lead to Forbush Decreases, often occur during periods of increased solar activity. Coincidentally, such intense phenomena can also result in complex interactions in the heliosphere, where accurate determination of energetic proton fluence may become more difficult. Therefore, in order to increase statistical robustness and reduce uncertainties, we try to expand the classification procedure to include a wider set of various space weather parameters, that are more reliably determined.

The IZMIRAN database of Forbush decreases (IZMIRAN 2021) serves as an online repository, and contains an extensive list of FD events, along with a large number of associated space weather parameters. The idea for the presented analysis is to employ machine learning techniques in an attempt to separate FD events into two assumed classes, using a number of selected parameters from the IZMIRAN database as input variables. We compared the efficiency of different machine learning algorithms using the TMVA package integrated in the ROOT analysis framework (Hocker 2007), and tried to establish the optimal boundary value of FD intensity to be used for separation. The Support Vector machine algorithm (SVM, Cortes 1995) was selected for the analysis based on its overall performance, efficiency and flexibility. Finally, a subset of space weather variables to be used for classification was selected based on their predictive power.

References

- Cortes, C., Vapnik, V., 1995, Mach Learn, 20, 273–297.
Hocker, Andreas; 2007, CERN-OPEN-2007-007.
IZMIRAN Space Weather Prediction Center, 2021
Savić, Mihailo; Veselinović, Nikola; Dragić, Aleksandar, Maletić, Dimitrije; Joković, Dejan; Udovičić, Vladimir; Banjanac, Radomir; Knežević, David; 2023, ASR, 71, 4, 2006-2016.

Serbian space weather research activities

*Nikola VESELINOVIĆ
Institute of Physics Belgrade
veselinović@ipb.ac.rs*

Strong variation of solar activity and accompanied space weather phenomena can affect Earth's environment and our civilization. Cosmic rays, originated from outside of the Solar system are also sensitive to properties of interplanetary medium and violent energetic events originated from the Sun that can additionally modulate cosmic rays. Here, a correlation between various space weather indices and energetic particles flux measured in-situ at L1 and measured ground-level cosmic ray muon flux is investigated. Found connection between proton flux fluence spectra and selected parameters of associated Interplanetary coronal mass ejections and variation of primary cosmic rays can improve analysis of how violent energetic events, with irregular sporadic occurrence, affect space weather and induce primary cosmic ray variations but also affect Earth's magnetosphere and upper atmosphere. These events can produce Forbush decreases, a transient decrease in the observed galactic cosmic ray intensity that can be detected by ground-based cosmic ray detectors. Ground-based muon detectors are sensitive to higher energies of primary cosmic rays than the network of standard devices like neutron monitors and can expand the range of energy of monitored cosmic rays. Plans for a worldwide network of ground muon detectors are discussed as well as plans and goals of space weather related Serbian CUBESAT project. The goal of CUBESAT project, still in the initial phase, is to study solar activity from LEO and to correlate acquired data with VLF measurements of the ionosphere and CR measurements conducted at the Institute of Physics. These projects will have strong educational and outreach components because of the necessity to develop research capacity in study of the integrated Sun-Earth system.

KEYWORDS: solar energetic particles; secondary cosmic ray muon flux; ground-based and satellite observations

SIMULACIJA PRODUKCIJE NEUTRONA MIONIMA IZ KOSMIČKOG ZRAČENJA U OLOVNOJ ZAŠTITI GERMANIJUMSKOG DETEKTORA

**Dejan JOKOVIĆ, Dimitrije MALETIĆ, Vladimir UDOVIČIĆ,
Radomir BANJANAC, Aleksandar DRAGIĆ, Mihailo SAVIĆ,
Nikola VESELINOVIĆ i David KNEŽEVIĆ**

*Institut za fiziku u Beogradu, Univerzitet u Beogradu, Beograd, Srbija,
yokovic@ipb.ac.rs, maletic@ipb.ac.rs, udovicic@ipb.ac.rs, banjanac@ipb.ac.rs,
dragic@ipb.ac.rs, msavic@ipb.ac.rs, veselinovic@ipb.ac.rs, davidk@ipb.ac.rs*

SADRŽAJ

Zbog svojih osobina, olovo se uobičajeno koristi kao materijal za zaštitu germanijumskih detektora. Mioni iz kosmičkog zračenja u interakcijama sa olovom proizvode sekundarno zračenje, koje doprinosi ukupnom fonu detektora. Značajan deo ove komponente fona čine neutroni proizvedeni u interakcijama miona u olovnoj zaštiti. Neutroni mogu biti poseban problem u eksperimentima u dubokim podzemnim laboratorijama. U podzemnoj laboratoriji u Institutu za fiziku u Beogradu, germanijumski detektor, koji se nalazi u olovnoj zaštiti, može raditi u koincidenciji sa mionskim detektorom. U ovom režimu rada mogu se proučavati različiti efekti u germanijumskom detektoru izazvani mionima, posebno efekti koji potiču od neutrona proizvedenih mionima. Ovde su predstavljeni rezultati Geant4 simulacija produkcije neutrona u olovu mionima iz kosmičkog zračenja. Rezultat ovih simulacija je procena prinosa neutrona – broja proizvedenih neutrona u olovu po jedinici dužine puta – u interakcijama miona. Pored toga, određena je raspodela multipliciteta neutrona, kao broja proizvedenih neutrona u jednoj interakciji.

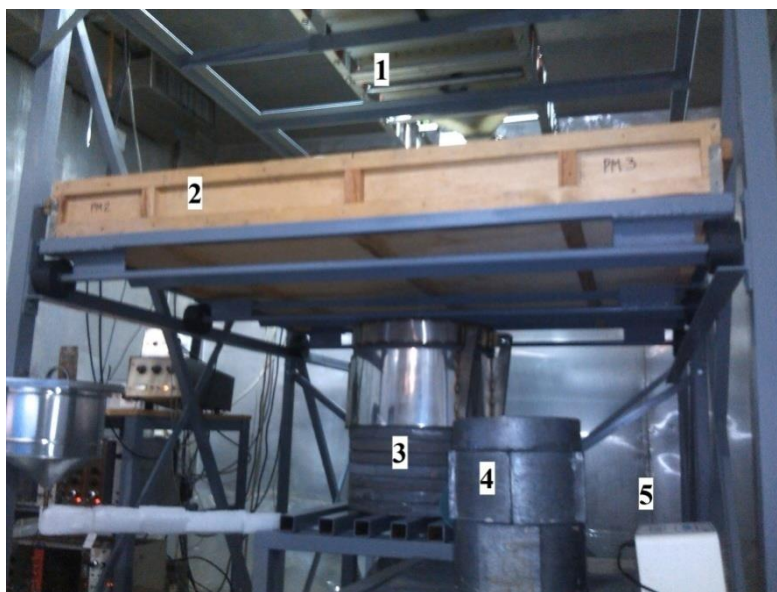
1. Uvod

U eksperimentima u kojima se traže retki događaji glavni problem je redukcija fonskog zračenja. Zato se ovi eksperimenti vrše u podzemnim laboratorijama, gde je fon u odnosu na površinu Zemlje znatno niži. Međutim, mioni iz kosmičkog zračenja su veoma prodorne čestice, prisutne i u dubokim podzemnim laboratorijama, i zato čine važan izvor fonskog zračenja u ovakvim osetljivim eksperimentima. Poseban problem je mionima indukovano sekundarno zračenje u detektorima i njihovoj okolini (detektorskoj zaštiti, zidovima, itd). Značajan doprinos fonu potiče od neutrona proizvedenih u interakcijama miona sa materijalom u okolini detektora [1].

U Niskofonskoj laboratoriji Instituta za fiziku u Beogradu intenzitet kosmičkog zračenja kontinuirano se meri od 2002. godine [2,3]. Geografski položaj laboratorije je takav da se kosmičko zračenje koje se detektuje u osnovi sastoji od mionske tvrde komponente, uz izvestan procenat meke elektromagnetne komponente. Laboratorija se sastoji od nadzemnog i plitko ukopanog podzemnog dela na dubini od 12 m ispod površine. Zemljište (les) iznad podzemne laboratorije ima gustinu približno $2,0 \text{ g/cm}^3$ – efektivni apsorpcioni sloj iznosi približno 25 hg/cm^3 (25 m.w.e.). Na toj dubini prisutna je praktično samo mionska komponenta kosmičkog zračenja. Zbog svojih niskofonskih karakteristika, laboratorija je osposobljena za izučavanja različitih pojava generisanih kosmičkim zračenjem, pre svega događaja indukovanih mionima iz kosmičkog zračenja u germanijumskim detektorima, kao i u pasivnoj zaštiti detektora.

U podzemnoj laboratoriji nalazi se HPGe detektor deklarisan aktivne zapremine 149 cm^3 i relativne efikasnosti 35 %. Podzemna pozicija detektora, zajedno sa olovnom

zaštitom debljine 12 cm, daje značajno smanjenje fonskog zračenja. Pored pasivne zaštite, za aktivnu veto zaštitu germanijumskog detektora mogu se koristiti postojeći scintilacioni detektori kosmičkog zračenja. Plastični scintilacioni detektor nalazi se neposredno iznad olovne zaštite; dimenzije detektora su 100 cm × 100 cm × 5 cm. Oba detektora – HPGe i scintilacioni – vezani su za analogno-digitalni konvertor, koji omogućava snimanje i čuvanje svih detektovanih događaja. Svi događaji analiziraju se *off-line*. Uz odgovarajuće selekzione kriterijume mogu se izdvojiti svi koincidentni i/ili antikoincidentni događaji u scintilacionom i HPGe detektoru [4,5].



Slika 1. Ekperimentalna konfiguracija u podzemnoj laboratoriji: scintilacioni detektori (1,2) i germanijumski detektor u olovnoj zaštiti (3).

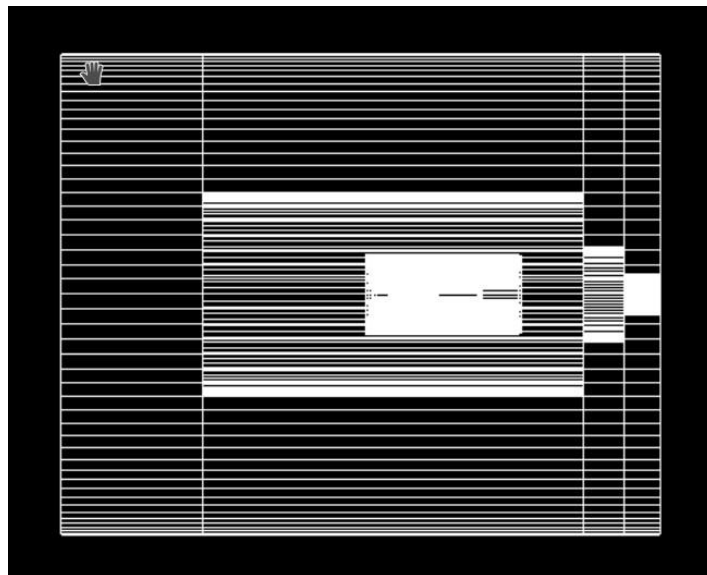
Prvi rezultati merenja produkcije neutrona mionima iz kosmičkog zračenja u olovnoj zaštiti HPGe detektora objavljeni su 2013. godine. Podaci su snimani tokom više od 400 dana merenja, u koincidentnom režimu rada scintilator-HPGe detektor. Analizom ovih podataka dobijen je rezultat za fluks neutrona proizvedenih mionima, na dubini naše podzemne laboratorije [6]. Merenja su kontinuirano nastavljena, sa većom statistikom snimljenih događaja; analiza ovih podataka je u toku. Pored eksperimentalnih merenja, uporedo su urađene Monte Carlo simulacije produkcije neutrona u olovnoj zaštiti, bazirane na Geant4 *framework*-u. Ovde su predstavljeni prvi rezultati simulacija: procena prinosa neutrona (broj neutrona po jedinici dužine) u interakcijama miona, kao i raspodela multipliciteta proizvedenih neutrona.

2. Metod

Geant4 je softverski paket za Monte Carlo simulacije transporta i interakcija čestica sa materijom [7]. On sadrži kompletan alat za modelovanje geometrije detektora, fizičkih procesa, primarnih i sekundarnih događaja, kao i odziva detektora. Na osnovi Geant4 platforme razvijena je posebna aplikacija za simulacije odziva germanijumskog i scintilacionih detektora u laboratoriji. Aplikacija je fleksibilna i omogućuje simulacije pojedinačnih i koincidentnih režima rada detektora. Prethodno je korišćena u različitim

slučajevima koji su zahtevali precizne simulacije scintilacionih i germanijumskih detektora [2,4,8,9].

Olovna zaštita je geometrije šupljeg cilindra, unutar kojeg se nalazi germanijumski detektor. Visina cilindra je 51 cm, prečnik osnove 41 cm, a debljina olovnog zida je 12 cm. Detektor je konstruisan prema specifikaciji proizvođača. Skica detektora i olovnog cilindra prikazana je na slici 2.



Slika 2. Skica olovne zaštite germanijumskog detektora.

Primarni događaji generisani su definisanjem incidentne čestice, njene pozicije, pravca kretanja i energije. Incidentne čestice su pozitivni i negativni mioni; odnos broja pozitivnih i broja negativnih miona je 1,3. Početne pozicije miona na površini olovnog cilindra određene su na sledeći način: prvo se odabere gornja horizontalna strana ili vertikalna strana cilindra, prema verovatnoći da kosmički mion pogodi horizontalnu ili vertikalnu stranu, a zatim se odabere pozicija na datoj površini iz uniformne raspodele. Pravac kretanja miona simpliran je iz raspodele miona po pravcima, u funkciji od zenitnog ugla θ , koja je proporcionalna $\cos^{1.55}\theta$. Energija miona određena je iz energijske raspodele miona na površini Zemlje, pri čemu se uzimaju oni mioni koji uspeju da prođu kroz 12 m zemljišta. Detaljnija procedura generisanja primarnih događaja i izvođenje raspodele miona po pravcima i energijama može se videti u [4].

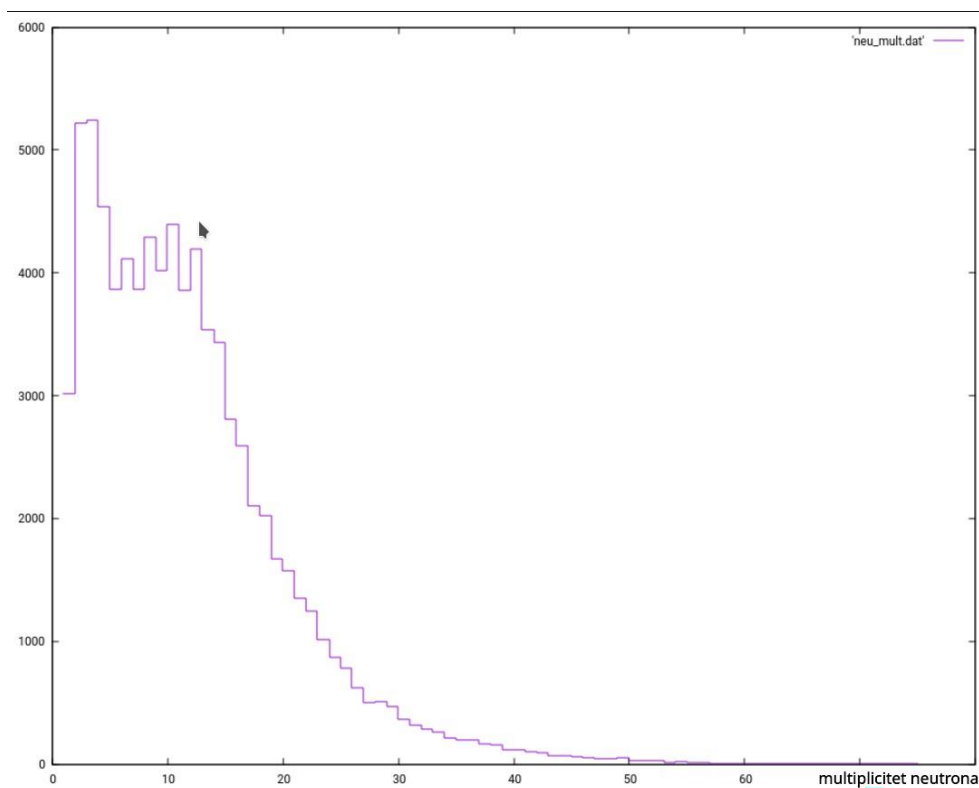
Fizički procesi u kojima učestvuju mioni – elektromagnetni i nuklearni – uključeni su u simulaciju kroz predefinisane Geant4 klase QGSP_BERT_HP; ova klasa omogućava simulacije interakcija čestica sa velikom preciznošću.

3. Rezultati i diskusija

Prvi cilj simulacije bio je da se odredi broj proizvedenih neutrona u interakcijama miona sa jezgrom olova, po jedinici dužine puta, pri njihovom prolasku kroz olovnu zaštitu germanijumskog detektora. Generisanih primarnih događaja bilo je 10^8 ; ovaj broj može biti povezan sa vremenom eksperimentalnih merenja, uzimajući u obzir fluks miona u podzemnoj laboratoriji.

Ukupan broj proizvedenih neutrona bio je 934 000. Odavde je određen prinos neutrona, kao odnos broja neutrona i proizvoda gustine olova i srednje dužine puta miona kroz

olovo. Srednja dužina puta miona je 26,6 cm, a proizvod gustine olova i srednje dužine puta iznosi 302 g/cm^3 . Dobijena vrednost za prinos neutrona je $3,1 \times 10^{-5} \text{ neut.}/(\text{gcm}^{-2})$. Pored prinosa neutrona, određena je raspodela multipliciteta neutrona – broja neutrona proizvedenih u interakciji jednog miona sa olovom. Mion može proizvesti više od jednog neutrona na svom putu kroz olovo, što za rezultat ima više neutronske fonske događaja u detektoru koji potiču od jednog miona. Događaji su vremenski razdvojeni, odnosno detektuju se sa vremenskim razmakom, u zavisnosti od trenutka i mesta produkcije neutrona. Ovi događaji registruju se u detektoru kao signali sa vremenskim kašnjenjem, unutar definisanog vremenskog prozora mionskog događaja. To može poslužiti za selekciju fonskih događaja koji potiču od neutrona indukovanih mionima. Raspodela multipliciteta neutrona prikazana je na slici 3. Najveći broj miona proizvede manje od 10 neutrona u kaskadi, dok srednji multiplicitet neutrona iznosi 11,5. Dobijena raspodela slaže se sa rezultatima ranijih sličnih simulacija [10].



Slika 3. Raspodela multipliciteta neutrona proizvedenih mionima iz kosmičkog zračenja u olovnoj zaštiti HPGE detektora.

Rezultati simulacije pokazali su da ovaj metod može biti koristan za procenu produkcije neutrona mionima iz kosmičkog zračenja. On može dati detaljniji uvid u mehanizam produkcije neutrona. Osim toga, rezultati simulacije mogu pomoći u analizi podataka eksperimentalnih merenja, njihovom boljem razumevanju i evaluaciji.

4. Zahvalnica

Ovaj rad finansiran je od Instituta za fiziku u Beogradu kroz projekat Ministarstva prosvete, nauke i tehnološkog razvoja Republike Srbije.

5. Literatura

- [1] D. Mei, A. Hime. Muon-induced background study for underground laboratories. *Phys. Rev. D* 73, 2006, 053004.
- [2] A. Dragić, D. Joković, R. Banjanac, V. Udovičić, B. Panić, J. Puzović, I. Aničin. Measurement of cosmic ray muon flux in the Belgrade ground level and underground laboratories. *Nucl. Instr. Meth. A* 591, 2008, 470-475.
- [3] M. Savić, A. Dragić, D. Maletić, N. Veselinović, R. Banjanac, D. Joković, V. Udovičić. A novel method for atmospheric correction of cosmic-ray data based on principal component analysis. *Astropart. Phys.* 109, 2019, 1-11.
- [4] D. Joković, A. Dragić, V. Udovičić, R. Banjanac, J. Puzović, I. Aničin. Monte Carlo simulations of the response of a plastic scintillator and an HPGe spectrometer in coincidence. *Appl. Radiat. Isot.* 67, 2009, 719-722.
- [5] A. Dragić, V. Udovičić, R. Banjanac, D. Joković, D. Maletić, N. Veselinović, M. Savić, J. Puzović, I. Aničin. The new set-up in the Belgrade low-level and cosmic-ray laboratory. *Nucl. Techn. Radiat. Prot.* 26, 2011, 181-192.
- [6] A. Dragić, I. Aničin, R. Banjanac, V. Udovičić, D. Joković, D. Maletić, M. Savić, N. Veselinović, J. Puzović. Neutrons produced by muons at 25 mwe. *J. Phys.: Conf. Ser.* 409, 2013 012054.
- [7] S. Agostinelli et al. Geant4 – a simulation toolkit. *Nucl. Instr. Meth. A* 506, 2003, 250-303.
- [8] M. Krmar, J. Hansman, N. Jovančević, N. Lalović, J. Slivka, D. Joković, D. Maletić. A method to estimate a contribution of Ge(n,n') reaction to the low-energy part of gamma spectra of HPGe detectors. *Nucl. Instr. Meth. A* 709, 2013, 8-11.
- [9] J. Nikolić, T. Vidmar, D. Joković, M. Rajačić, D. Todorović. Calculation of HPGe efficiency for environmental samples: comparison of EFFTRAN and GEANT4. *Nucl. Instr. Meth. A* 763, 2014, 347-353.
- [10] L. Reichhart et al. Measurement and simulation of the muon-induced neutron yield in lead. *Astropart. Phys.* 47, 2017, 67-76.

MONTE CARLO SIMULATION OF THE COSMIC RAY MUON INDUCED NEUTRON PRODUCTION IN THE LEAD SHIELD OF THE GERMANIUM DETECTOR

**Dejan JOKOVIĆ, Dimitrije MALETIĆ, Vladimir UDOVIČIĆ,
Radomir BANJANAC, Aleksandar DRAGIĆ, Mihailo SAVIĆ,
Nikola VESELINOVIĆ and David KNEŽEVIĆ**

*Institute of Physics Belgrade, University of Belgrade, Belgrade, Serbia,
yokovic@ipb.ac.rs, maletic@ipb.ac.rs, udovicic@ipb.ac.rs, banjanac@ipb.ac.rs,
dragic@ipb.ac.rs, msavic@ipb.ac.rs, veselinovic@ipb.ac.rs, davidk@ipb.ac.rs*

ABSTRACT

Lead is usually used as a common shielding material for germanium detectors. Cosmic ray muons produce secondary particles in their interactions with lead nuclei, which contribute to overall background radiation detected by germanium detectors. Neutrons produced in muon interactions in lead shield make a significant part of this background component. Cosmic ray induced neutrons are a particular problem in experiments carried out in deep underground laboratories.

In the low-level underground laboratory at Institute of Physics Belgrade, a germanium detector and a muon detector operate in coincidence. This provides studying of different effects in the germanium detector induced by cosmic rays, especially effects originated from the cosmic ray induced neutrons.

Here, the results of Geant4 simulations of the cosmic ray muon induced neutron production in the lead shield of the germanium detector are presented. Estimate of the neutron yield – number of neutrons produced per unit path length – in muon interactions is obtained. The result is 3.1×10^{-5} neutrons/(gcm⁻²). Also, the neutron multiplicity distribution is determined, as a distribution of number of neutrons produced per muon interaction. The average multiplicity is 11.5.

DISTRIBUCIJA KONCENTRACIJE RADONA PO SPRATNOSTI STAMBENIH ZGRADA

Vladimir UDOVIČIĆ¹, Dimitrije MALETIĆ¹, Aleksandar DRAGIĆ¹,
Radomir BANJANAC¹, Dejan JOKOVIĆ¹, Nikola VESELINOVIĆ¹,
Mihailo SAVIĆ¹, David KNEŽEVIĆ¹ i Maja EREMIĆ-SAVKOVIĆ²

- 1) Institut za fiziku u Beogradu, Institut od nacionalnog značaja za Republiku Srbiju, Beograd, Srbija, udovic@ipb.ac.rs, maletic@ipb.ac.rs, dragic@ipb.ac.rs,
banjanac@ipb.ac.rs, yokovic@ipb.ac.rs, veselinovic@ipb.ac.rs,
msavic@ipb.ac.rs, davidk@ipb.ac.rs
- 2) Direktorat za radijacionu i nuklearnu sigurnost i bezbednost Srbije, Beograd, Srbija, eremic.savkovic@srbatom.gov.rs

SADRŽAJ

Dobro je poznato da je jedan od faktora koji utiče na varijabilnost radona u zatvorenom prostoru spratnost stambenih zgrada. Imajući u vidu činjenicu da glavni izvor radona u zatvorenim prostorijama potiče iz zemljišta, očekuje se smanjenje koncentracije radona na višim spratovima. Na višim spratovima dominantan izvor radona potiče od građevinskog materijala, a u nekim slučajevima može doći do odstupanja od ove opšte utvrđene pravilnosti. S druge strane, varijabilnost radona zbog spratnosti, posebno u velikim gradovima, sa mnogo većim brojem visokih zgrada i gustom naseljenosti u poređenju sa ruralnim sredinama, može uticati na procenu kolektivne doze koja potiče od radona. U tom smislu, a u svrhu naših istraživanja, izabrali smo jednu tipičnu porodičnu kuću sa potkrovljem i jedan šesnaestospratni soliter. Merenje koncentracije radona u odabranim stambenim objektima izvršeno je sa dva aktivna uređaja. Jedan je bio fiksiran u dnevnoj sobi u prizemlju, a drugi je menjao poziciju po spratovima u stambenim zgradama. Svaki merni ciklus na datom spratu trajao je sedam dana uz vreme uzorkovanja od dva sata. U ovom radu detaljno je urađena analiza dobijenih rezultata.

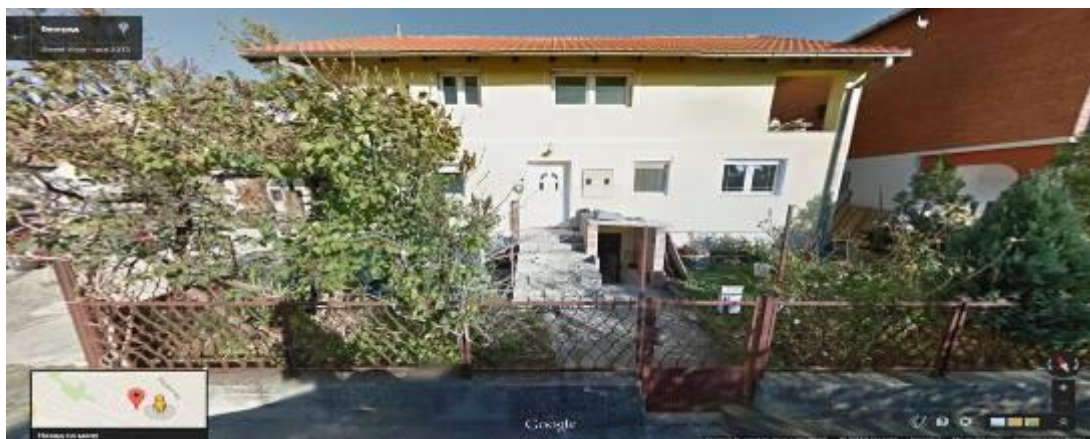
1. Uvod

Izvori radona u stambenim i poslovnim zgradama su, pre svega iz zemljišta, građevinskog materijala i vode. S obzirom na prirodu nastanka i svih pomenutih izvora, koncentracija radona je veća u prizemnim prostorijama u odnosu na stanove na višim spratovima stambenih objekata. U literaturi se može pronaći dosta radova koji se bave uticajem raznih faktora na nivo i varijabilnost radona u zatvorenim prostorijama, pa između ostalih i uticajem spratnosti [1-4]. U slučaju velikih stambenih objekata sa većim brojem spratova, može se uočiti odstupanje od opšte pravilnosti, jer je na višim spratovima dominantan izvor radona građevinski materijal, te se mogu uočiti povećane koncentracije radona u odnosu na situaciju na nižim spratovima. U tom smislu, urađena su merenja radona u dva tipična stambena objekta. Izbor zgrada je baziran na rezultatima iz monografije „Nacionalna tipologija stambenih zgrada Srbije“ grupe autora sa Arhitektonskog fakulteta [5]. S obzirom na specifičnosti gradnje u Srbiji, broj

tipova zgrada je tako sveden na šest kategorija, dve za porodično stanovanje i četiri kategorije za kolektivno stanovanje; porodično stanovanje: 1. slobodnostojeća kuća, 2. kuća u nizu i kolektivno stanovanje: 3. slobodnostojeća zgrada, 4. zgrada u nizu, 5. zgrada u nizu tipa lamele (ponavlja se više zgrada rađenih po istom projektu, zgrada sa više ulaza...) i 6. soliter (slobodnostojeća zgrada velike spratnosti). Pokazuje se da više od 97% svih stambenih zgrada čine samostojeće porodične kuće. Takođe, za sve definisane tipove zgrada broj spratova se kreće od jednog do osam, pri čemu su samostojeće porodične kuće uglavnom prizemne (37%) ili prizemne sa potkrovljem (26%), dok je veoma niska zastupljenost kuća koje imaju više od dva sprata (5%), sa prosečnom visinom porodičnih zgrada od 1,4 [5].

2. Eksperimentalna postavka

Izabrana su dva stambena objekta, jedan iz grupe za porodično stanovanje i jedan soliter iz grupe za kolektivno stanovanje. Porodična kuća (slika 1) ima karakterističan stil gradnje u kome se kuća gradi više godina uz konstantno dograđivanje i nadogradnju, što potencijalno može biti izvor ulaska radona u takve kuće. Kuća ima podrum i izgrađena je od standardnih materijala (cigla-blok, beton, malter). Na kraju je urađena i izolacija korišćenjem stiropora debljine 5 cm. U kući su već vršena višegodišnja merenja koncentracije radona različitim metodama, o čemu je do sada publikovano nekoliko naučnih radova [6-8].



Slika 1. Tipična porodična kuća u Beogradu.

Iz grupe stambenih zgrada za kolektivno stanovanje izabran je soliter na Novom Beogradu (slika 2). Izgrađen je šezdesetih godina prošlog veka, blokovskog tipa. Soliter ima podrum, dok se u prizemlju nalaze lokali i poslovne prostorije. Stanovi se nalaze od prvog sprata pa naviše. Soliter ima 16. spratova.



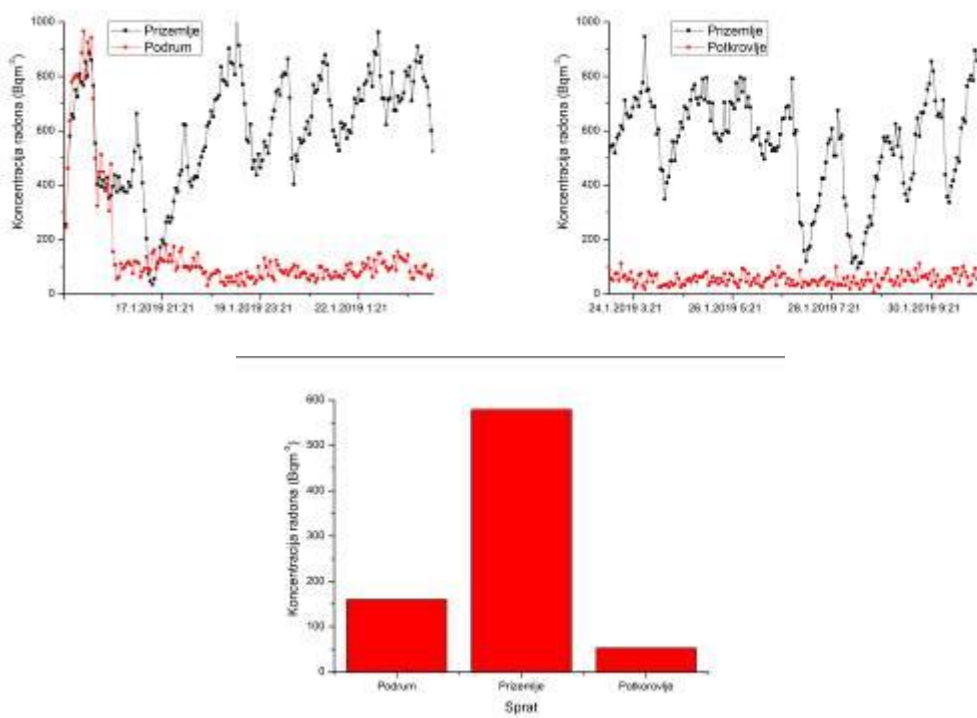
Slika 2. Soliter na Novom Beogradu.

Vremenske serije merenih koncentracija radona u ispitivanim stambenim objektima dobijene su pomoću dva aktivna uređaja SN1029 i SN1030 (proizvođača Sun Nuclear Corporation). To su merni uređaji jednostavne konstrukcije i primene u praksi. U suštini, radi se o brojaču sa dodatkom senzora za merenje meteoroloških parametara. Nedostatak uređaja je nemogućnost merenja koncentracije radona u zemljištu i vodi. Operater može podesiti vremenske sekvence od 0,5 do 24 sati. Jedan ciklus merenja može trajati 1000 sati ili ukupno 720 vremenskih sekvenci (broj sukcesivnih merenja, odnosno tačaka u vremenskoj seriji). Uređaji su bili podešeni da rade u vremenskoj sekvenci od 2 sata. Jedan je bio fiksiran u dnevnoj sobi u prizemlju, a drugi je menjao poziciju po spratovima u stambenim zgradama. Svaki merni ciklus na datom spratu trajao je sedam dana.

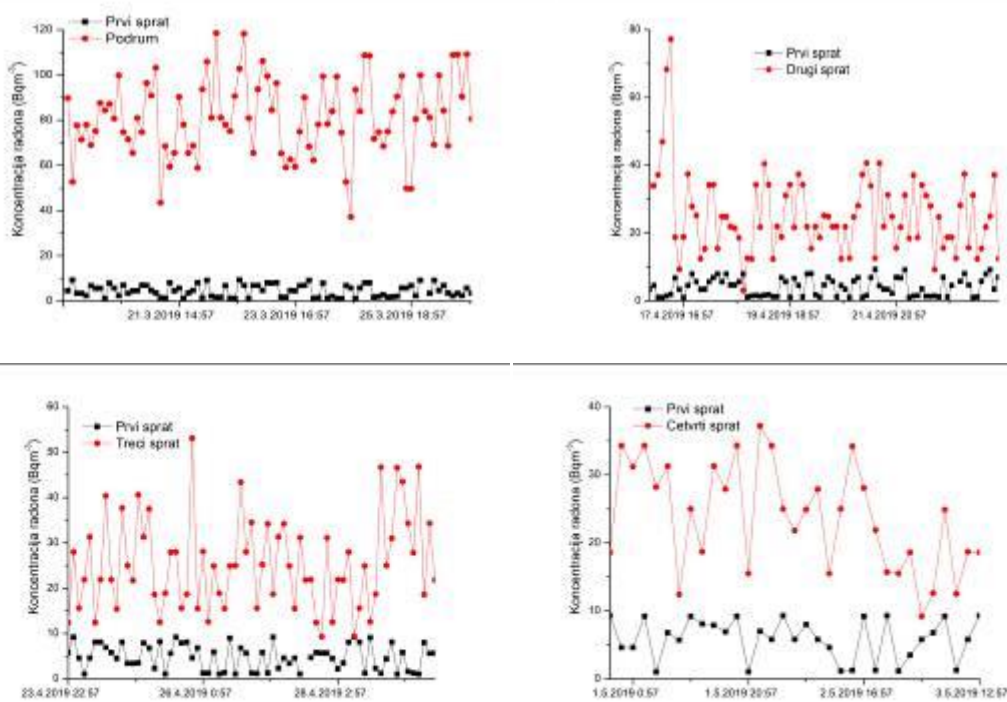
3. Rezultati i diskusija

Na slikama 3 i 4 su prikazani dobijeni rezultati merenja, kako vremenske serije tako i usrednjene koncentracije radona u ispitivanim stambenim objektima za zadati ciklus merenja od sedam dana.

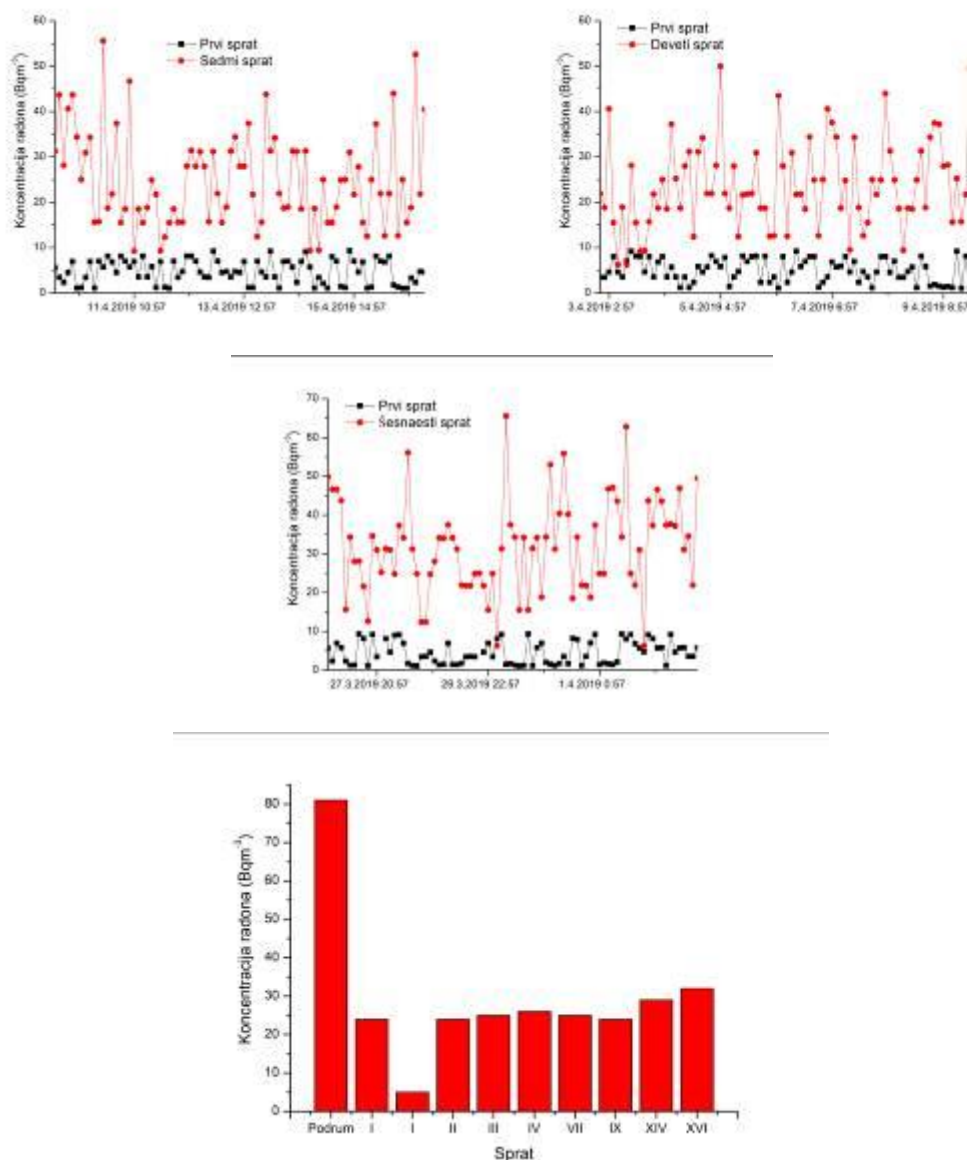
S obzirom da je detektor koji je sve vreme stajao u prizemlju solitera pokazao neobično niske vrednosti za koncentraciju radona, uradili smo uporedno merenje sa drugim detektorom u susednom, kao i u stanu u kome se nalazio fiksirani detektor. Dobijeni rezultati pokazuju izvesnu razliku, ali s obzirom da se radi o domenu izrazito niskih nivoa radona, pretpostavka je da su i merne nesigurnosti velike.



Slika 3. Vremenske serije i srednja koncentracija radona po spratovima u porodičnoj kući.



Slika 4. Vremenske serije i srednja koncentracija radona po spratovima u soliteru.



Slika 4. Nastavak.

4. Zaključak

Dobijeni rezultati pokazuju da je ponašanje radona u dva različita stambena objekta dijametralno suprotno. U porodičnoj kući je moguće uočiti izrazite varijacije koncentracije radona uz jednodnevnu periodiku. Takođe, interesantan je odnos koncentracije radona u prizemlju, u odnosu na podrum kuće, koji je suprotan od uobičajene situacije kod kuća sa podrumom. Ovo inverzno ponašanje može se protumačiti činjenicom da podrum ne prekriva celo prizemlje već njegov manji deo. Ostali deo prizemlja je pokriven betonskom pločom kao podlogom, ali sa pukotinama i lošim spojem sa zidovima predstavlja potencijalni izvor povišenog radona. Kod solitera je situacija suprotna i može se smatrati da već od prvog sprata dominantan izvor radona je građevinski materijal. Čak se može uočiti blagi rast srednje koncentracije radona na

višim spratovima. No, dobijeni rezultati u soliteru se mogu predvideti, a na osnovu rada grupe autora koji su odredili interno izlaganje iz građevinskog materijala, koji se koristi u Srbiji, a koje potiče od eshalacije radona i torona [9].

5. Zahvalnica

Ovaj rad je realizovan uz podršku Ministarstva prosvete, nauke i tehnološkog razvoja Republike Srbije u okviru projekta pod brojem III43002.

6. Literatura

- [1] F. Bochicchio, G. Campos-Venuti, S. Piermattei, C. Nuccetelli, S. Risica, L. Tommasino, G. Torri, M. Magnoni, G. Agnesod, G. Sgorbati, M. Bonomi, L. Minach, F. Trotti, M.R. Malisan, S. Maggiolo, L. Gaidolfi, C. Giannardi, A. Rongoni, M. Lombardi, G. Cherubini, S. D'Ostilio, C. Cristofaro, M. Pugliese, V. Martucci, A. Crispino, P. Cuzzocrea, A. Sansone Santamaria, M. Cappai. Annual average and seasonal variations of residential radon concentration for all the Italian Regions. *Radiat. Meas.* 40, 2005, 686-694.
- [2] H. Friedmann. Final Results of the Austrian Radon Project. *Health Phys.* 89(4), 2005, 339-348.
- [3] R. Borgoni, D. De Francesco, D. De Bartolo, N. Tzavidis. Hierarchical modeling of indoor radon concentration: how much do geology and building factors matter? *J. Environ. Radioact.* 138, 2014, 227-237.
- [4] M. Lorenzo-González, A. Ruano-Ravina, J. Peón, M. Piñeiro, J. Miguel Barros-Dios. Residential radon in Galicia: a cross-sectional study in a radon-prone area. *J. Radiol. Prot.* 37(3), 2017, 728-741.
- [5] M. Jovanović Popović, D. Ignjatović, A. Radivojević, A. Rajčić, N. Ćuković Ignjatović, Lj. Đukanović, M. Nedić. National Typology of Residential Buildings in Serbia, Faculty of Architecture University of Belgrade, Belgrade, 2013, ISBN 978-86-7924-102-3.
- [6] V. Udovičić, D. Maletić, R. Banjanac, D. Joković, A. Dragić, N. Veselinović, J. Živanović, M. Savić, S. Forkapić. Multiyear Indoor Radon Variability in a Family House – a Case Study in Serbia. *Nucl. Tech. Radiat. Protect.* XXXIII (2), 2018, 174-179.
- [7] D. Maletić, V. Udovičić, R. Banjanac, D. Joković, A. Dragić, N. Veselinović, J. Filipović. Comparison of multivariate classification and regression methods for indoor radon measurements. *Nucl. Tech. Radiat. Protect.* 29, 2014, 17-23.
- [8] J. Filipović, D. Maletić, V. Udovičić, R. Banjanac, D. Joković, M. Savić, N. Veselinović. The use of multivariate analysis of the radon variability in the underground laboratory and indoor environment. *Nukleonika* 61(3), 2016, 357-360.
- [9] P. Ujić, I. Ćeliković, A. Kandić, I. Vukanac, M. Đurašević, D. Dragosavac, Z. S. Žunić. Internal exposure from building materials exhaling ^{222}Rn and ^{220}Rn as compared to external exposure due to their natural radioactivity content. *Appl. Radiat. Isot.* 68, 2010, 201–206.

INDOOR RADON DISTRIBUTION DUE TO FLOOR LEVEL IN THE RESIDENTIAL BUILDINGS

**Vladimir UDOVICIC¹, Nikola VESELINOVIC¹, Dimitrije MALETIC¹,
Radomir BANJANAC¹, Aleksandar DRAGIC¹, Dejan JOKOVIC¹,
Mihailo SAVIC¹, David KNEZEVIC¹ and Maja EREMIC-SAVKOVIC²**

*1) Institute of Physics Belgrade, University of Belgrade, Belgrade, Serbia,
udovicic@ipb.ac.rs, maletic@ipb.ac.rs, dragic@ipb.ac.rs, banjanac@ipb.ac.rs,
yokovic@ipb.ac.rs, veselinovic@ipb.ac.rs, msavic@ipb.ac.rs, davidk@ipb.ac.rs*

*2) Serbian Radiation and Nuclear Safety and Security Directorate, Belgrade,
Serbia, eremic.savkovic@srbatom.gov.rs*

ABSTRACT

It is well known that one of the factors influencing indoor radon variability is the floor level of residential buildings. Bearing in mind the fact that the main source of indoor radon is from radon in soil gas, a radon concentration on upper floors is expected to decrease. On the upper floors, the dominant source of radon originates from building materials, and in some cases there may be deviations from this generally established regularity. On the other hand, radon variability due to floor level, especially in large cities, with a much larger number of high buildings and density of population compared to rural areas, can affect the estimation of the collective dose derived from radon. In this sense, and for the purpose of our research, we chose a typical family house with a loft and sixteen high-rise building. Indoor radon measurements in selected residential buildings were done with two active devices. One was fixed in the living room on the ground floor, while the other was changing the position on the floors in residential buildings. Each measuring cycle on the floor lasted for seven days with a sampling time of two hours. In this paper, an analysis of the obtained results has been done in detail.

PROCENA TEMPERATURSKOG PROFILA ATMOSFERE NA OSNOVU DETEKTOVANOG FLUKSA KOSMIČKIH MIONA

Mihailo SAVIĆ, Vladimir UDOVIČIĆ, Dimitrije MALETIĆ, Aleksandar DRAGIĆ, Radomir BANJANAC, Dejan JOKOVIĆ, Nikola VESELINOVIĆ i David KNEŽEVIĆ

Institut za fiziku u Beogradu, Institut od nacionalnog značaja za Republiku Srbiju, Beograd, Srbija, msavic@ipb.ac.rs

SADRŽAJ

Uticaj atmosferskih parametara na intenzitet mionske komponente sekundarnog kosmičkog zračenja dobro je poznat. Dominantan doprinos varijaciji fluksa kosmičkih miona usled atmosferskih parametara daju dva meteorološka efekta - barometarski (usled varijacije atmosferskog pritiska) i temperaturski (usled varijacije temperature atmosfere). Postoji više teorijskih i empirijskih modela koji dobro opisuju ove zavisnosti. Obično se na osnovu ovih modela vrši korekcija kako bi se eliminisala varijacija fluksa kosmičkih miona atmosferskog porekla.

Obrnuto, osetljivost mionskih detektora na varijacije atmosferskih parametara može se iskoristiti da se na osnovu poznatih parametara modela i poznatog odbroja kosmičkih miona odredi temperatura različitih nivoa atmosfere. U ovom radu ćemo demonstrirati ovaj pristup na osnovu podataka merenih mionskim monitorima Niskofonske laboratorije za nuklearnu fiziku Instituta za fiziku u Beogradu i primenom empirijskog modela meteoroloških efekata, zasnovanog na tehnici dekompozicije na osnovne komponente.

1. Uvod

Intenzitet pljuskova sekundarnog kosmičkog zračenja zavisi od atmosferskih meteoroloških parametara. To se naročito odnosi na mionsku komponentu sekundarnog kosmičkog zračenja. Dva efekta dominantno utiču na fluks sekundarnih miona: barometarski koji opisuje antikorelaciju fluksa kosmičkih miona sa atmosferskim pritiskom [1] i temperaturski koji se odnosi na uticaj varijacije atmosferske temperature na detektovani intenzitet miona [2].

Osim fundamentalnog, detaljno poznavanje meteoroloških efekata ima značaj u proceduri korekcije na date efekte, čime se povećava osetljivost zemaljskih detektora kosmičkog zračenja na varijacije neatmosferskog porekla. Alternativno, dobar model meteoroloških efekata bi u principu omogućio predviđanje atmosferskih parametara na osnovu merenja fluksa miona. Ovo je potencijalno značajno za određivanje temperatura pojedinih slojeva atmosfere u slučaju da su druge metode nedostupne.

Postoji više predloženih metoda za predikciju atmosferskih meteoroloških parametara na osnovu merenja intenziteta kosmičkog zračenja zemaljskim detektorima. Mogu se bazirati na merenju različitih komponenti fluksa kosmičkih miona [3, 4], simultanom merenju neutronske i mionske komponente [5] ili upotrebi mionskog teleskopa sposobnim da meri ugaonu distribuciju intenziteta [6]. Sve pomenute metode karakteriše relativna kompleksnost eksperimentalne postavke i analize. Takođe, zajedničko svim pomenutim metodama je da se u proceduri određivanja atmosferskih temperatura oslanjaju na teorijski izračunate koeficijente za opisivanje zavisnosti inenziteta miona od temperaturskog profila atmosfere. Ovaj pristup ima određenih ograničenja usled nužno aproksimativnog karaktera i neprilagođenosti konkretnom

detektorskom sistemu.

U ovom radu, mi ćemo demonstrirati upotrebljivost jednostavnije eksperimentalne postavke i primenu empirijskog modela meteoroloških efekata na određivanje temperaturskog profila atmosfere.

2. Eksperimentalni podaci i obrada

U Niskofonskoj laboratoriji za nuklearnu fiziku Instituta za fiziku u Beogradu mionski fluks se meri kontinualno od 2009. godine, na nivou zemlje i na dubini od 25 m.w.e. Eksperimentalna postavka se sastoji od scintilacionog detektora i sistema za akviziciju. Detektor je plastični scintilator dimenzija $100\text{cm}\times 100\text{cm}\times 5\text{cm}$ sa četiri fotomultiplikatora postavljena na čoškove. U srcu sistema za akviziciju nalazi se brzi analogno-digitalni konverter sposoban da u realnom vremenu precizno određuje vreme detekcije i amplitudu signala [7]. U ovoj analizi korišćeni su podaci snimljeni detektorom na nivou zemlje u periodu od 01.06.2010. do 31.05.2011. godine.

Za opisivanje meteoroloških efekata na kosmičke mione, u okviru Niskofonske laboratorije razvijen je empirijski model baziran na tehnici dekompozicije na osnovne komponente (Principal Component Analysis - PCA) [8]. Metod se zasniva na ideji da se u analizi meteoroloških efekata sa skupa visoko korelisanih meteoroloških parametara pređe na skup linearno nezavisnih promenljivih, kao i potencijalno smanji dimenzionalnost problema zadržavanjem samo statistički značajnih osnovnih komponenti u analizi. Koeficijenti zavisnosti detektovanog odbroja miona od tako određenih osnovnih komponenti su pouzdaniji, jer su manje podložni statističkim fluktuacijama. Ovde ćemo primeniti ovaj model kako bismo na osnovu odbroja miona merenog u nadzemnoj laboratoriji odredili temperature različitih nivoa atmosfere.

Neka je C_X matrica tipa $n\times m$ koja predstavlja m merenja n različitih meteoroloških parametara. Dekompozicijom na osnovne komponente se sa skupa n meteoroloških varijabli prelazi na skup n osnovnih komponenti, čije vrednosti su reprezentovane matricom C_Y , takođe tipa $n\times m$. Ova relacije se može predstaviti jednačinom:

$$C_Y = PC_X, \quad (1)$$

gde je P matrica transformacije čiji redovi predstavljaju kompoziciju osnovnih komponenti.

Na slici 1 prikazana je kompozicija prvih 9 osnovnih komponenti. Na x-osi su meteorološke promenljive: pritisak, temperature 24 izobarna nivoa (10, 20, 30, 50, 70, 100, 150, 200, 250, 300, 350, 400, 450, 500, 550, 600, 650, 700, 750, 800, 850, 900, 925 i 975 mb) i temperatura na nivou tla. Na y-osi su prikazane vrednosti kosinusa uglova rotacije pri prelasku sa skupa meteoroloških varijabli na skup osnovnih komponenti.

Na osnovu statističke i korelacione analize zaključeno je da su za meteorološke efekte od značaja samo pet osnovnih komponenti, i to komponente 1, 3, 4, 5 i 6 [8].

Zavisnost varijacije detektovanog odbroja miona od ovih komponenti, usled meteoroloških efekata, data je jednačinom:

$$\delta N_{PC} = \sum_i k_i PC_i, \quad i = 1, 3, 4, 5, 6 \quad (2)$$

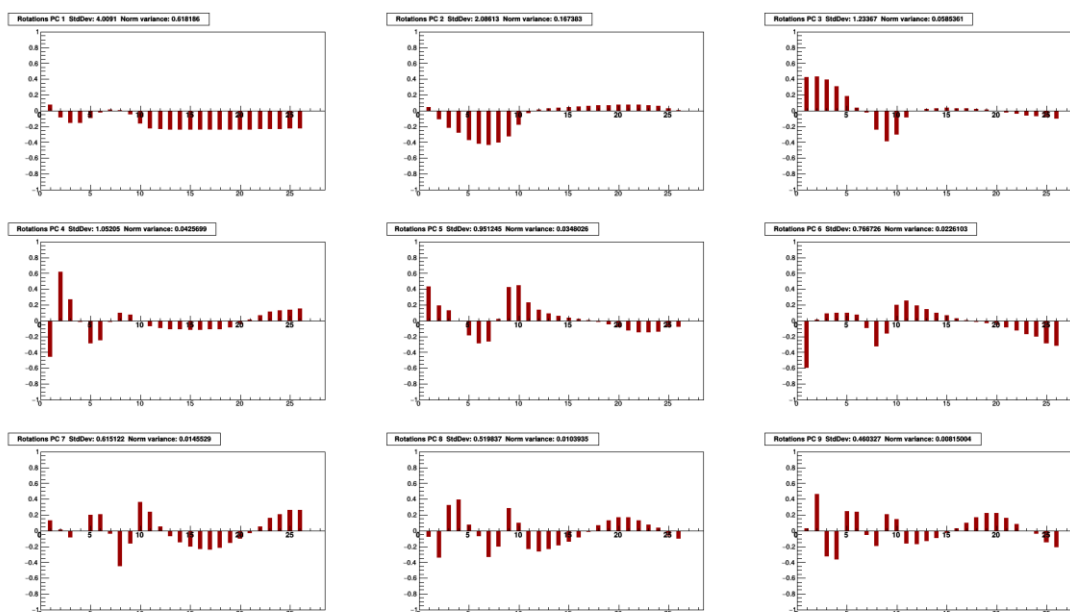
gde su PC_i osnovne komponente a k_i odgovarajući koeficijenti.

Pomoću ove relacije u principu je moguće proceniti vrednosti osnovnih komponenti na osnovu poznatog odbroja.

Dalje, transformišući jednačinu 1 kao:

$$C_X = P^{-1} C_Y = P^T C_Y \quad (3)$$

na osnovu procenjenih vrednosti osnovnih komponenti sada je moguće odrediti procenjene vrednosti meteoroloških parametara.



Slika 1. Kompozicija prvih devet osnovnih komponenti. Na x-osi su meteorološke promenljive: pritisak, temperature 24 izobarna nivoa (10, 20, 30, 50, 70, 100, 150, 200, 250, 300, 350, 400, 450, 500, 550, 600, 650, 700, 750, 800, 850, 900, 925 i 975 mb) i temperatura na nivou tla. Na y-osi su prikazane vrednosti uglova rotacije.

3. Rezultati i diskusija

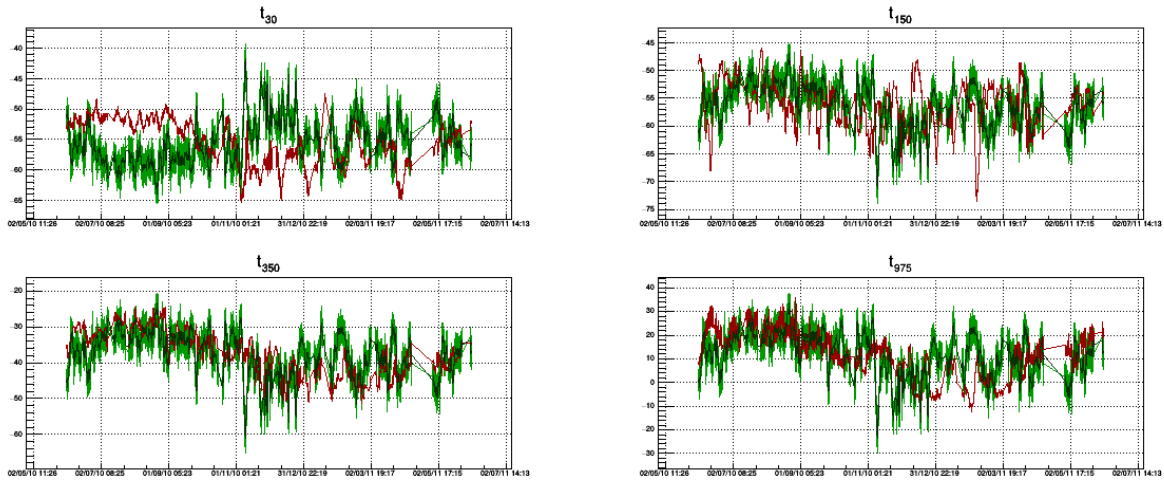
Za pomenuti referentni period određeni su koeficijenti u jednačini 2, uzimajući u obzir samo geomagnetno mirne dane [8]. Pomoću ovako određenih koeficijenata i merenog odbroja određene su procenjene vrednosti za pet signifikantnih osnovnih komponenti za ceo referentni period. Zatim su na osnovu jednačine 3 određene procenjene vrednosti meteoroloških parametara. Na slici 2 prikazane su vremenske serije merenih i procenjenih vrednosti meteoroloških parametara za izabrane izobarne nivoe.

Zbog preglednosti, prikazani su grafici za četiri različita nivoe. Kao referentni izabrani su nivoe od 30 mb (stratosfera), 150 mb (tropopauza/gornja troposfera), 350 mb (troposfera) i 975 mb (u blizini zemlje). Na plotovima crvenom linijom prikazane su merene vrednosti a svetlo zelenom vrednosti procenjene na osnovu merenog odbroja miona. Takođe, kako bi se dala jasnija slika i smanjio efekat fluktuacija merenog odbroja, vremenska serija predviđenih vrednosti je smutovana (*smoothing*) i prikazana na graficima tamno zelenom bojom.

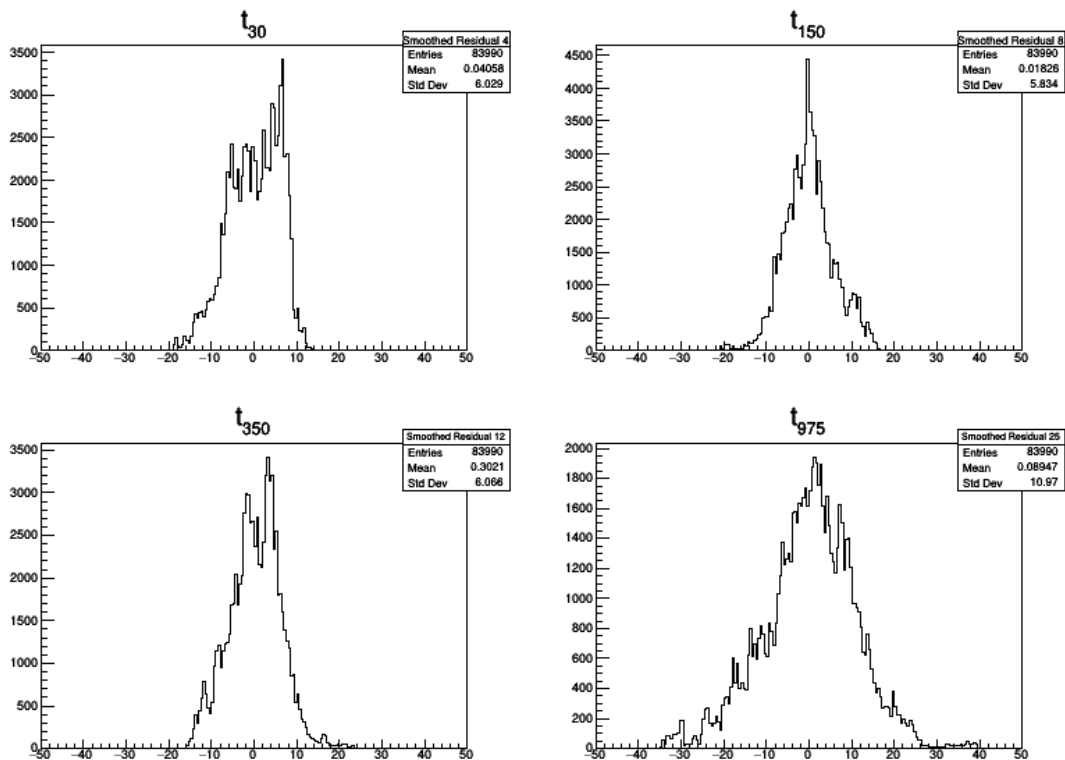
Na slici 3 prikazana je raspodela razlika merenih i procenjenih vrednosti meteoroloških parametara.

Osim analize vremenskih serija, još jedan kriterijum za određivanje efikasnosti predviđanja temperature pojedinih nivoe mogao bi biti na osnovu širine prikazanih raspodela. Međutim, varijacija temperatura različitih nivoe nije ista tako da ovo može dati nepotpunu sliku. Stoga su u tabeli 1 prikazane vrednosti standardnih devijacija ovih raspodela, standardnih devijacija merenih vrednosti, kao i relativan odnos ove dve

veliĉine koji daje bolji uvid u efikasnost predikcije temperatura pojedinih nivoa atmosfere.



Slika 2. Vremenske serije merenih i procenjenih vrednosti meteoroloških parametara za izobrne nivoe od 30, 150, 350 i 975 mb. Merene vrednosti - crvena linija, procenjene - svetlo zelena linija i smutovane procenjene - tamno zelena linija.



Slika 3. Raspodela razlika merenih i procenjenih vrednosti meteoroloških parametara za izobarne nivoe od 30, 150, 350 i 975 mb.

Tabela 1. Standardna devijacija raspodela razlika merenih i procenjenih vrednosti (σ_r), raspodele vrednosti merenih temperatura (σ_t) i relativan odnos ove dve vrednosti (σ_r/σ_t).

	t_{10}	t_{20}	t_{30}	t_{50}	t_{70}	t_{100}	t_{150}	t_{200}	t_{250}	t_{300}	t_{350}	t_{400}
σ_r	9.314	5.246	6.029	3.645	3.940	4.032	5.834	7.455	5.761	5.679	6.066	6.297
σ_t	7.154	4.844	3.669	3.320	2.862	3.055	4.012	5.754	5.111	5.658	6.237	6.460
σ_r/σ_t	1.302	1.083	1.643	1.098	1.377	1.320	1.454	1.296	1.127	1.004	0.973	0.975

t_{450}	t_{500}	t_{550}	t_{600}	t_{650}	t_{700}	t_{750}	t_{800}	t_{850}	t_{900}	t_{925}	t_{975}	t_{ground}
6.386	6.415	6.389	6.387	6.504	6.863	7.340	8.085	8.985	9.956	10.40	10.97	11.20
6.518	6.510	6.466	6.415	6.428	6.616	6.841	7.253	7.793	8.456	8.810	9.444	9.523
0.980	0.985	0.988	0.996	1.012	1.037	1.073	1.115	1.153	1.177	1.181	1.161	1.176

Na osnovu predstavljenih grafika i tabela možemo videti da se najbolje slaganje dobija za sloj atmosfere od 300 do 600 *mb*. Nešto slabije slaganje dobija se za nivoe u blizini tla, što je u skladu sa kompleksnijom dinamikom temperatura u ovih slojevima, kao i za slojeve od 100 do 200 *mb*, u kojima dominantno dolazi do produkcije miona. Ovaj drugi podatak je moguća posledica činjenice da je za mione detektovane na površini zemlje značajniji negativni temperaturski efekat, asociiran sa jonizacionim gubicima i verovatnoćom raspada miona u nižim slojevima atmosfere, dok pozitivni temperaturski efekat u vezi sa verovatnoćom nastanka miona u sloju između 100 i 200 *mb* ima manji doprinos. Najslabije slaganje dobija se za neke od nivoe u stratosferi i tropopauzi, što se može videti na primeru temperature nivoe od 30 *mb* koji je u značajnom delu godine antikorelisan sa procenjenom temperaturom. Ovo je možda uslovljeno manjim varijacijama temperature na ovim nivoima kao i činjenicom da postoji značajna varijacija temperature ovih nivoe koja nije korelisana sa intenzitetom kosmičkih miona, sadržana u osnovnoj komponenti 2 (slika 1).

4. Zaključak

Preliminarna analiza je pokazala da postoji dosta dobro slaganje merenih i procenjenih atmosferskih temperatura za veći broj nivoe. Procenjene temperature imaju uglavnom konzistentne vremenske serije i dobro opisuju godišnju varijaciju. Najbolje slaganje sa merenim vrednostima dobija se u višim slojevima troposfere. Stoga, prikazani rezultati predstavljaju dobru polaznu osnovu za dalju analizu.

5. Zahvalnica

Ovaj rad je realizovan uz podršku Ministarstva prosvete, nauke i tehnološkog razvoja Republike Srbije u okviru projekta pod brojem OI 171002.

Literatura

- [1] L. Myssowsky and L. Tuwim. "Unregelmäßige Intensitätsschwankungen der Höhenstrahlung in geringer Seehöhe". *Zeitschrift für Physik* 39.2-3 (1926).
- [2] A Duperier. "The Temperature Effect on Cosmic-Ray Intensity and the Height of

- Meson Formation". *Proceedings of the Physical Society* 61.1 (1948), ñ. 34.
- [3] Miyazaki Y. and M. Wada. "Simulation of cosmic ray variation due to temperature effect", *Acta phys. Acad. Sci. hung.*, 29, Suppl. 2, 591-595 (1970).
- [4] Kohno, T., Imai, K., Inue, A., Kodama, M., & Wada, M. "Estimation of the Vertical Profile of Atmospheric Temperature from Cosmic-Ray Components". *Proceedings of the 17th International Cosmic Ray Conference, held in Paris, France*. Volume 10., p.289
- [5] L.I.Dorman, *Cosmic Rays in the Earth's Atmosphere and Underground*, Springer 2004.
- [6] V.V. Borog, O.V. Belonosova, A.S. Davydov, G.M. Kruchenitskii, S.P. Perov and V.G. Yanke. "Study of Atmospheric Temperature at Different Altitudes using Muon Angular Distribution at Sea Level". *29th International Cosmic Ray Conference Pune (2005)* 2, 381-384
- [7] Aleksandar Dragic, Vladimir Udovicic, Radomir Banjanac, Dejan Jokovic, Dimitrije Maletic, Nikola Veselinovic, Mihailo Savic, Jovan Puzovic. "The New Setup in the Belgrade Low-Level and Cosmic-Ray Laboratory". *Nuclear Technology & Radiation Protection: Year 2011*, Vol. 26, No. 3, pp.181-192
- [8] M Savic at al. "A novel method for atmospheric correction of cosmic-ray data based on principal component analysis". *Astroparticle Physics* **109** (2019).

ATMOSPHERIC TEMPERATURE PROFILE ESTIMATION BASED ON MEASURED COSMIC RAY MUON FLUX

Mihailo SAVIĆ, Vladimir UDOVIČIĆ, Dimitrije MALETIĆ, Aleksandar DRAGIĆ, Radomir BANJANAC, Dejan JOKOVIĆ, Nikola VESELINOVIĆ i David KNEŽEVIĆ

*Institute of Physics Belgrade, University of Belgrade, Belgrade, Serbia,
msavic@ipb.ac.rs*

ABSTRACT

The effect of atmospheric parameters in secondary cosmic ray muon component is well known. This is mainly through two dominant meteorological effects - barometric (due to atmospheric pressure variation) and temperature (due to atmospheric temperature variation). There are several theoretical and empirical models that describe these effects well. Usually this knowledge is used to correct for secondary cosmic ray variations due to atmospheric effects.

Alternatively, once model parameters are established, sensitivity of cosmic ray muon detectors to variations of atmospheric origin can be used to estimate temperatures for different layers of the atmosphere. In this work we will demonstrate this procedure using cosmic ray data measured in Low Background Laboratory for Nuclear Physics at Institute of Physics Belgrade, combined with parameters of empirical model for meteorological effects based on principal component analysis.